

Integration of seismic data with well-log data

Proefschrift



ter verkrijging van de graad van doctor
aan de Technische Universiteit Delft,
op gezag van de Rector Magnificus prof. ir. K. F. Wakker,
voorzitter van het College voor Promoties,
in het openbaar te verdedigen op maandag 18 december 2000 om 16:00 uur

door

**Frédérique (Frédéric) José Paul Christian Marie Ghislain
VERHELST**

Burgerlijk Mijningenieur aan de Katholieke Universiteit te Leuven, België
geboren te Sint-Niklaas, België.

Dit proefschrift is goedgekeurd door de promotoren:

Prof. dr. ir. A. J. Berkhout

Prof. dr. ir. C. P. A. Wapenaar

Samenstelling Promotiecommissie:

| | |
|--|--|
| Rector Magnificus | <i>voorzitter</i> |
| 7 Prof. dr. ir. A. J. Berkhout | <i>Technische Universiteit Delft, promotor</i> |
| 6 Prof. dr. ir. C. P. A. Wapenaar | <i>Technische Universiteit Delft, promotor</i> |
| 5 Prof. dr. ir. J. T. Fokkema | <i>Technische Universiteit Delft</i> |
| 4 Prof. em. ir. K. J. Weber | <i>Technische Universiteit Delft</i> |
| 3 Prof. dr. R. Swennen | <i>Katholieke Universiteit Leuven</i> |
| 2 Dr. ir. F. J. Herrmann <i>Ned.</i> | <i>Massachusetts Institute of Technology</i> |
| 1 Mevr. dr. I. Magnus <i>geheel Engels</i> | <i>04 Norsk Hydro ASA</i> |
| ISBN 90-9014386-6 | <i>2 paranijsen: o*</i> <i>v. Verhelst.</i> <i>Stellingen tegenover Engels</i> |
| | <i>Sheets gamer fotografie</i> |

Copyright ©2000, by F. Verhelst, Laboratory of Seismics and Acoustics, Faculty of Applied Sciences, Delft University of Technology, Delft, The Netherlands.

All rights reserved. No part of this publication may be reproduced, stored in a retrieval system or transmitted in any form or by any means, electronic, mechanical, photocopying, recording or otherwise, without the prior written permission of the author.

SUPPORT

The research for this thesis was financially supported by the DELPHI consortium.

TOOLS

Typesetting system: *LATEX 2_E*

Technical computing environment: *MATLAB 5.3*

Postscript editor: *Tailor, 2.0d for NeXTSTEP*

Operating system workstation: *NeXTSTEP 3.3*

Printed in The Netherlands by: DocVision - Technische Universiteit Delft

Aan mijn moeder en Olivier

en

Aan Liesbeth

Contents

| | | |
|----------|--|-----------|
| 1 | Introduction | 1 |
| 1.1 | A brief introduction to some petroleum geological concepts | 1 |
| 1.1.1 | Three main groups of rocks | 1 |
| 1.1.2 | Sedimentological environments | 3 |
| 1.1.3 | A further subdivision of environments: facies | 5 |
| 1.1.4 | Scales in clastic sedimentary deposits | 5 |
| 1.2 | Exploration geophysics | 7 |
| 1.2.1 | Introduction to seismic exploration | 7 |
| 1.2.2 | Conceptual framework | 9 |
| 1.3 | Outline of this thesis | 10 |
| 1.4 | Notational conventions | 11 |
| 2 | <i>P</i>-wave propagation at different scales | 13 |
| 2.1 | Introduction | 13 |
| 2.2 | Short and long wavelength limits | 14 |
| 2.2.1 | Short wavelength limit: ray theory | 14 |
| 2.2.2 | Long wavelength limit: effective medium theory | 15 |
| 2.3 | Full waveform synthetic seismograms | 15 |
| 2.4 | Stationary medium parameters: stratigraphic filter | 17 |
| 2.5 | Laboratory experiments | 20 |
| 2.5.1 | Stationary media | 20 |
| 2.5.2 | Non-stationary media | 22 |
| 2.6 | Composite ray and effective media theory | 23 |
| 2.6.1 | Choice of window function | 26 |

| | | |
|----------|--|-----------|
| 2.6.2 | Regularized velocity at a certain scale | 26 |
| 2.6.3 | Characterizing events | 32 |
| 2.7 | Catch-22 problem | 36 |
| 2.8 | Solution: iterative procedure | 37 |
| 2.8.1 | Simplest case: constant wavelength in time λ_t | 37 |
| 2.8.2 | Non-constant wavelength in time $\lambda_t(t)$ | 39 |
| 2.9 | Application on the Saga-well | 41 |
| 2.10 | Conclusions | 44 |
| 3 | <i>P</i>-wave propagation at an oblique angle | 45 |
| 3.1 | Introduction | 45 |
| 3.2 | Theory of elasticity | 46 |
| 3.3 | Long wavelength limit: anisotropic equivalent medium | 50 |
| 3.3.1 | Special case: isotropic individual layers | 55 |
| 3.3.2 | Another special case: relationship between c_P and c_S | 57 |
| 3.4 | Thomsen anisotropic parameters | 59 |
| 3.5 | <i>P</i> -wave velocities assuming weak anisotropy | 60 |
| 3.6 | Thomsen anisotropic parameters at a certain scale | 64 |
| 3.7 | Extended catch-22 problem | 68 |
| 3.8 | Solution: extension of iterative method | 72 |
| 3.9 | Application on the Saga-well | 73 |
| 3.10 | Influence of background velocity on inversion results | 77 |
| 3.11 | Conclusions | 78 |
| 4 | Characterizing local wavelet shapes using Gabor-atoms | 81 |
| 4.1 | Introduction | 81 |
| 4.2 | Geological sequences at layer scale | 82 |
| 4.2.1 | Petrophysical interpretation at layer scale | 82 |
| 4.2.2 | From gamma-ray log signatures to acoustic impedance trends | 83 |
| 4.2.3 | Seismic modelling for the typical sequences | 86 |
| 4.3 | Analysis of the seismic measurement | 88 |
| 4.3.1 | Instantaneous and response attributes | 88 |

| | | |
|----------|--|------------|
| 4.3.2 | Deriving amplitude, phase and scale using Matching Pursuit | 91 |
| 4.3.3 | Characterization of typical sequences using phase | 97 |
| 4.3.4 | Influence of noise: comparison with response phase | 103 |
| 4.3.5 | The effect of pore fill | 106 |
| 4.3.6 | Application to a synthetic seismic trace | 106 |
| 4.4 | Application to 3-D migrated data-sets | 109 |
| 4.4.1 | Description of the first data-set: Gulf of Mexico | 110 |
| 4.4.2 | Characterization of a delta front system | 112 |
| 4.4.3 | Characterisation of a sub-marine fan system | 120 |
| 4.4.4 | Description and results for the second data-set: Northern Europe | 126 |
| 4.5 | Geological classification by means of wavelet shape attributes | 128 |
| 4.6 | Comparison with other techniques | 132 |
| 4.7 | Discussion and conclusions | 134 |
| 5 | Conclusions | 135 |
| A | Anelastic media | 137 |
| A.1 | Introduction | 137 |
| A.2 | Constant phase velocity: no dispersion | 137 |
| A.3 | Non-constant phase velocity: dispersion | 138 |
| A.3.1 | Constitutive relationships | 139 |
| A.3.2 | Harmonic stimulation | 140 |
| A.3.3 | Cauchy's integral theorem and Kramers-Kronig relations . . . | 142 |
| A.3.4 | Quality factor Q and energy dissipation | 145 |
| A.3.5 | Constant Q -behaviour | 146 |
| A.3.6 | Phase and group velocity | 148 |
| B | Geological description of Saga-well | 153 |
| B.1 | Regional geological and structural setting | 153 |
| B.2 | Well description | 154 |
| B.2.1 | Short lithologic description of the formations | 154 |
| C | Geological description of well A from the Mobil AVO data set | 157 |

| | |
|---|------------|
| C.1 Regional geological setting | 157 |
| C.2 Well description | 158 |
| Bibliography | 161 |
| Summary | 171 |
| Samenvatting | 175 |
| Curriculum vitae | 179 |
| Acknowledgment/Dankwoord | 181 |

Chapter 1

Introduction

In this chapter a brief introduction is given to some of the concepts that will be used at a later stage in this thesis. First a very brief introduction is given to geology, focussed on sedimentary rocks. Afterwards the typical scales encountered in a sedimentary basin are discussed and exploration geophysics is introduced. Finally the outline of this thesis is given.

1.1 A brief introduction to some petroleum geological concepts

The focus in this section is on sedimentology, the geologic discipline dealing with sedimentary rocks. But first, a larger picture is given of the different locations where rocks may form.

1.1.1 Three main groups of rocks

Three main groups of rocks are formed at different places in the earth (Figure 1.1). These three groups are:

- igneous rocks,
- sedimentary rocks,
- metamorphic rocks.

Igneous rocks form by crystalization from a magma, a mass of melted rock that originates deep in the crust or the upper mantle. At these depths temperatures reach 700°C or more. When the magmas rise and cool down, they start to crystalize, forming igneous rocks (Press and Siever, 1997). There are a few typical plate tectonic locations where igneous rocks form (see Figure 1.1). One location is

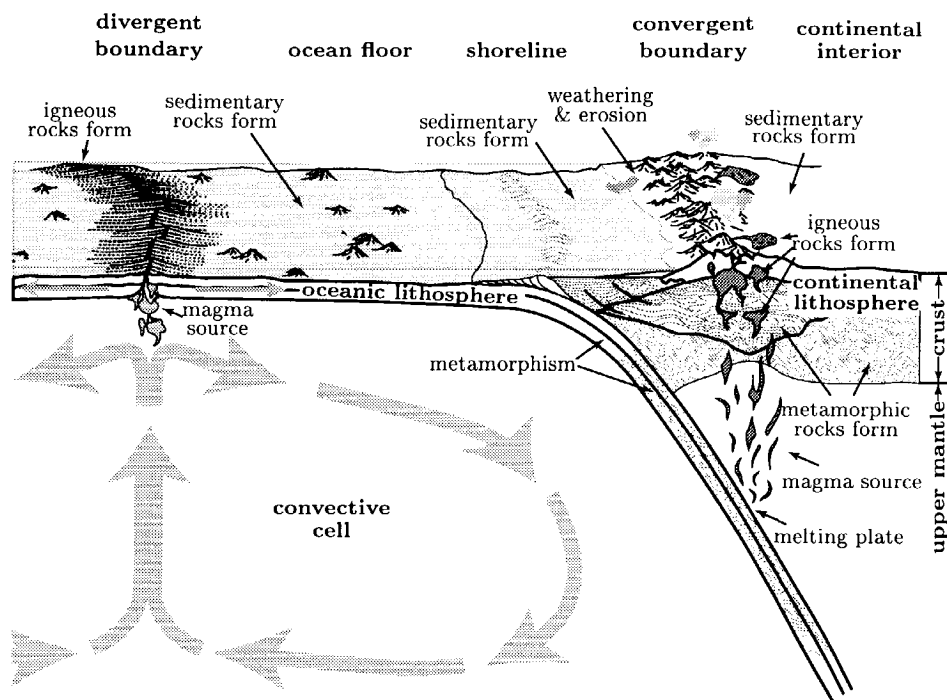


Fig. 1.1 The rock cycle in a plate tectonic setting. Modified after a public domain figure from US Geological Survey (2000).

at mid ocean ridges, i.e. divergent boundaries of two plates where new oceanic crust is formed by rising magmas. Another location is at convergent boundaries, where an oceanic and a continental plate collide. The oceanic plate descends into the mantle and melts. The this location magmas are generated which eventually rise and give form to volcanic activity and igneous intrusions.

Sediments, the precursors of sedimentary rocks, are found on the earth's surface as layers of loose particles. Two processes play a role in the creation of sediment deposits: weathering (i.e. the breaking up of a rock due to different physical, chemical and biological processes) and erosion (i.e. the transportation of the particles). Weathering and erosion produce two main types of sediments:

- clastic sediments that are physically deposited. These sediments include quartz, feldspar and clay particles, and are commonly forming layers of (from coarse to small particles) gravel, sand, silt and clay,
- chemical and biochemical sediments that are formed by precipitation from a

dissolved solution. These sediments include minerals such as halite and calcite (e.g. in the form of limestone).

By lithification, the sediments are converted into a solid, sedimentary rock. This occurs by compaction and cementation processes during the burial of a sediment (Press and Siever, 1997). Typical locations where sediments are deposited are on continents and ocean floors, and at the transition zone between both, i.e. the shoreline (see Figure 1.1).

Methamorphic rocks are produced when any kind of rock changes its mineralogy, texture or chemical composition under the influence of high temperatures and pressures, while still maintaining its solid form. Commonly, this happens by burial deep in the earth, at temperatures typically above 250°C, but below the melting point for rocks (around 700°C). Methamorphism occurs also around intrusions of igneous rocks in the crust, the so-called contact metamorphism (Press and Siever, 1997). Convergent boundaries are typical locations where metamorphic rocks are formed (Figure 1.1).

Due to the plate tectonic processes (plate movement in the earth's crust under the influence of convection in the ductile mantle), a cycle occurs, linking the three groups of rocks. This cycle is also called the rock cycle, and was proposed by Hutton (1788) some 200 years ago. Figure 1.1 gives an overview of a typical tectonic cycle. Igneous rocks form from a cooling magma. Due to volcanic processes and by orogeny (mountain building at convergent boundaries), rocks are uplifted. Subjected to weathering and erosion, the rocks form sediments. Subsequently these sediments are deposited, buried and lithified, forming sedimentary rocks. After deep burial, the rocks undergo metamorphism and/or melting, and are recycled again.

Almost all known hydrocarbon reservoirs are situated in sedimentary rocks. Because of this, in the remaining of this chapter the focus will be on sedimentary rocks only.

1.1.2 Sedimentological environments

At the different plate tectonic settings separate sedimentological environments are distinguished. These environments are geographic locations characterised by a particular combination of geological processes and environmental conditions with limited variation (Reading, 1996; Press and Siever, 1997). Environmental conditions include:

- the kind and the amount of water available (e.g. desert, river, lake, ocean),
- the topography (e.g. mountain, low land, coastal plain, shallow ocean, deep

ocean),

- the biological activity.

Geological conditions include:

- the nature of the currents (e.g. water, wind, ice) that control transport and deposit of sediments,
- the tectonic activity that may affect sedimentation and burial,
- presence of volcanic activity.

Sedimentological environments are often grouped by their location on the continents, in the ocean, or in the transition zone, i.e. the shoreline.

Four main environments can be found on the continents. These environments are respectively built around rivers, deserts, lakes and glaciers. The main continental environments are:

- the alluvial environment: composed of a river channel and its borders. Also the flood plains, flat valley floors on either side of the channel that is inundated when the river floods, are included in the environment,
- a desert environment: the sediments are mainly formed under arid conditions by wind action and by the action of ephemeral rivers that only flow very intermittently,
- a lake environment: controlled by relatively small water currents and wave action. Both fresh water lakes and saline lakes exist,
- a glacial environment: controlled by the movement of masses of ice.

At the shoreline, the transportation and deposition of sediments is dominated by the interaction of waves, tides and currents on sandy shores. The main shoreline environments are:

- deltaic environments where the rivers enter lakes or the sea,
- tidal flat environments, dominated by tidal currents and often exposed at low tide,
- beach environments, controlled by waves approaching and breaking on the shore.

The depth of water is an important factor in the subdivision of the marine environments, since depth controls the kinds of currents. The main marine environments are:

- continental shelf environments: a relative shallow, gently seaward-dipping surface extending from the shore to the continental slope, on average 70 km out the coast (Allaby and Allaby, 1999). Sedimentation is controlled by relatively gentle currents,
- continental slope environments: on average situated at 70 km out the coast, and is characterised by a relatively steeply sloping sea floor. Sediments are mainly deposited by turbiditic currents,
- organic reefs, which are composed of carbonate structures formed by carbonate-secreting organisms. An example is a coral reef that are built on continental shelves,
- deep-sea environments, which include all the floors of the deep ocean, far away from the continents.

1.1.3 A further subdivision of environments: facies

The controlling geological processes and the environmental conditions that were specific for the environments as described in the previous section, still allow for a range of sediments to occur. A further subdivision of environments can be made in different facies. Bedding characteristics often reflect very accurately a depositional process (Miall, 1999). The evolution of mineral composition and sedimentary structures in a bedding sequence is often very characteristic for a facies.

1.1.4 Scales in clastic sedimentary deposits

Deposition of clastic material in a sedimentary system is governed by the local energy available for the transportation of detrital particles¹ (Press and Siever, 1985). Usually at any location in a sedimentary system a distribution of particle sizes and shapes is available. These distributions of sizes and shapes of the particles in transportation depend upon the type of source material (source distribution, composition, susceptibility to alteration and cleavage) and on characteristics of the transport system (type, energy and length of system).

A dynamic equilibrium between deposition and transportation exists at all times in the transport system. The coarser particles (e.g. gravel and sand) are commonly deposited in high energetic situations, whereas the finer particles (e.g. clays) can only be deposited in low energetic regimes. Also the width of the particle size distribution (related to the degree of sorting) can change considerably. A poor sort-

¹Note that only clastic systems are described here. Chemical and biochemical sediments (e.g. coral-algal reefs), are explicitly not meant.

| | Dimensions | | |
|------------------------------|------------------|------------------|-----------------|
| | x | y | z |
| Basin | 100-1000 km, | 100-1000 km, | 1-10 km |
| Formation | 1-10 km, | 1-10 km, | 10-1000 m |
| Layer | 100-1000 m, | 100-1000 m, | 5-50 m |
| Intra layer | 1-10 m, | 1-10 m, | 1-10 m |
| Intra-bed sediment structure | 1-10 cm, | 1-10 cm, | 1-10 cm |
| Grains and pores | 10-2000 μ m, | 10-2000 μ m, | 10-2000 μ m |

Table 1.1 *Different scales in reservoir description.*

ing (a wide size distribution) severely reduces permeability.

The evolution of the energy in the depositional system is governed by processes at a wide variety of scales. Some processes are mostly relatively small scale, like for instance small scale ripples and some bedding types. They are a result of energy fluctuations related to tidal and wave phenomena. An example of a larger scale process is the abandonment of a channel by avulsion. This means that the channel is breaking through its natural levees, creating another channel-bed. Other processes are commonly large scale like for instance the well-known global Milankovitch-cycles related to the orbit of the earth around the sun (Payton, 1977; Emery and Myers, 1996).

All these phenomena on different scales are in some sense recorded in the current sedimentological column observed in a borehole². Due to the interplay of different types of phenomena acting on different scales, a sedimentological column will also exhibit a wide variety of scales (Table 1.1 and Figure 1.2), starting at the scale of grains and pores up to basin scale.

Most often the phenomena governing sedimentation change through time, for instance due to a relative change in the sea level as nicely described by the theory of sequence stratigraphy (Vail et al., 1977; Emery and Myers, 1996). Because of this, the resulting geological column will most often not be stationary along the depth direction.

²Note that a geological column is typically only a partial record of the geological history. Times of non-deposition ("hiatus") and of erosion lead to a partial record.

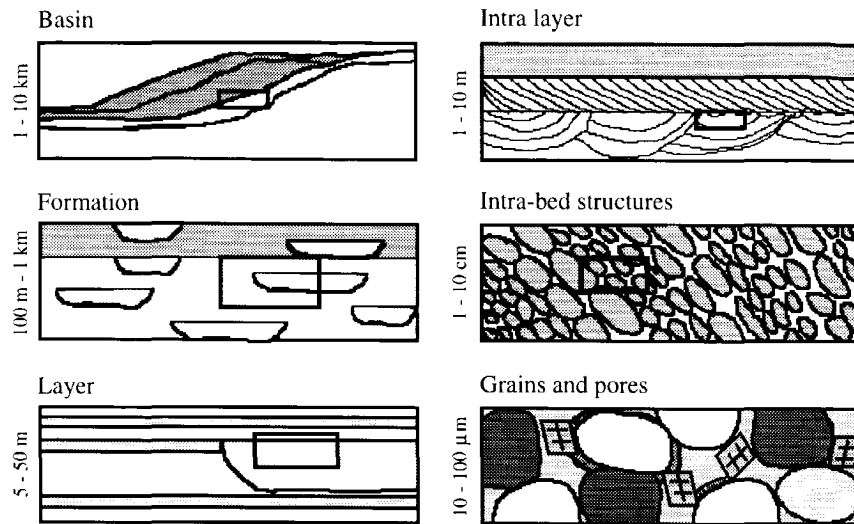


Fig. 1.2 *Different scales in reservoir description. The largest scale is sketched on the upperleft corner. Descending on the left-hand side, the scales become smaller. The trend is continued on the right-hand side. Modified after Weber (1986).*

1.2 Exploration geophysics

1.2.1 Introduction to seismic exploration

In the search for new oil and gas resources, the earth with its wide variety of scales is investigated by a remote sensing technique: the seismic exploration method.

The seismic method is schematically explained in Figure 1.3. Using measurements at or near the surface or in a borehole, information about the subsurface is obtained. Elastodynamic waves are generated by a seismic source. On land, this source can be some explosive or a seismic vibrator, while at sea the seismic wave field typically is generated by an air gun. By injecting a bubble of highly compressed air into the water, a wave is generated. A part of the created wave travels into the subsurface as a body wave. Due to contrasts in the elastic parameters of the subsurface, a part of the wave gets reflected, and propagates up again. At the surface, the wave is measured by receivers. In land acquisition the receivers are called geophones, in marine acquisition hydrophones. The measurement recorded in one receiver is called a seismic trace. Each generated wave is recorded by a multitude of receivers. The

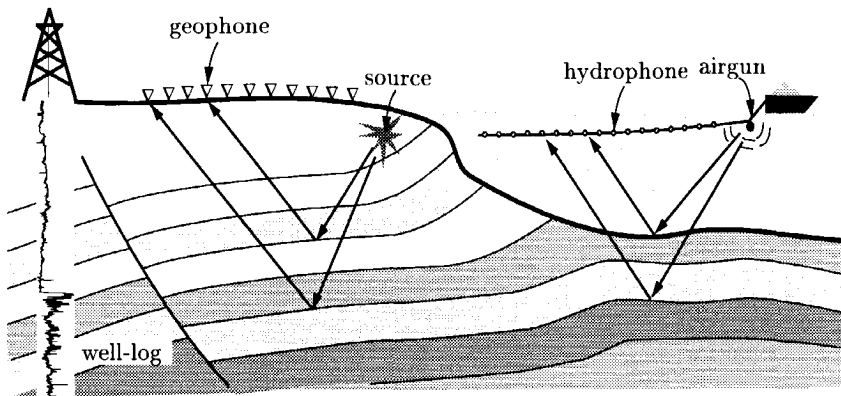


Fig. 1.3 A schematic overview of the acquisition of a seismic survey. To the right a marine acquisition, in the middle a land acquisition. On the left-hand side, a borehole with a well-log measurement is shown.

receivers are placed in a more or less regular grid, extending up to a few kilometers away from the source location. The combination of the recordings of all receivers due to one source, is called a shot record. A seismic survey consists of a large number of shot records at different locations. The data volumes involved with a modern seismic survey are in the order of Tb's.

The measured seismic reflections for the entire seismic survey are subsequently processed to obtain an accurate structural and lithologic image of the subsurface. The process to generate a structural image is called imaging or migration. In structural imaging, an image of the average reflection strength of the subsurface is obtained. When more information of the subsurface is required, the reflection strength is obtained for waves reflecting at various angles in the subsurface. This is called pre-stack migration. From the resulting angle-dependent reflection strength lithological parameters can be estimated using an inversion process. A typical resolution of the seismic method in the depth direction is in the order of 25 meter at shallow depths to 100 meter at deeper intervals.

When direct measurements in a borehole are available, these can be used to constrain and verify the imaging process. The direct measurements are performed by lowering a logging tool in the borehole. The measurements are also known as well-log measurements, and represent a multitude of subsurface parameters very lo-

cally, and very detailed. Some of the most frequently used well-log measurements include density, sonic velocity and natural radioactivity (known as the gamma-ray log) of the rocks in the immediate vicinity of the borehole. The resolution of well-log measurements along the depth dimension is in the order of 10 to 30 centimeters. Some more recent well-log measurements, like the Formation MicroImager (FMI) and the Circumferential Borehole Imaging Log (CBIL), have a resolution upto 1 centimeter.

A combination of a seismic survey and a well-log measurement is a Vertical Seismic Profile (VSP). In a VSP, the response for seismic sources at the surface is recorded by receivers in a borehole. The resolution of a VSP recording is typically about two times better than for a seismic survey.

1.2.2 Conceptual framework

The *WRW*-model is presented in Figure 1.4, and gives an overview of the most relevant aspects of seismic wave propagation. It was developed in the early eighties by Berkhout (1982, 1984b). Since more than a decade now, work within the DELPHI consortium has been embedded in the philosophy of the *WRW*-model (Berkhout, 1989; Berkhout and Wapenaar, 1990a,b).

The factor $S(z_0)$ represents the source characteristics. The operator $D^+(z_0)$ converts the source properties into a downgoing wave field, and can also be used to represent the actual configuration of the sources at or near the surface. Propagation from the surface z_0 into the subsurface to depth level z is represented by the propagation operator $W^+(z, z_0)$. Reflection occurs at depth z , which is described by operator $R^+(z)$. This operator is related to changes in lithology. The propagation operator $W^-(z_0, z)$ describes propagation of the upgoing wave to the surface. At the surface, the wave is reflected down again, which is described by the reflection operator $R^-(z_0)$. This operator is responsible for the surface related multiples. Finally, $D^-(z_0)$ converts the upgoing wave fields into the signals measured by the receivers. It represents the measurement process at the surface, also representing the receiver configuration. This yields the seismic reflection data $P(z_0, z_0)$. All operators are multidimensional and, in the discrete situation, they are represented by matrices.

The *WRW*-model was found to be very suitable for the description of the seismic acquisition process. It is also a good platform for the the imaging and the subsequent lithologic inversion process.

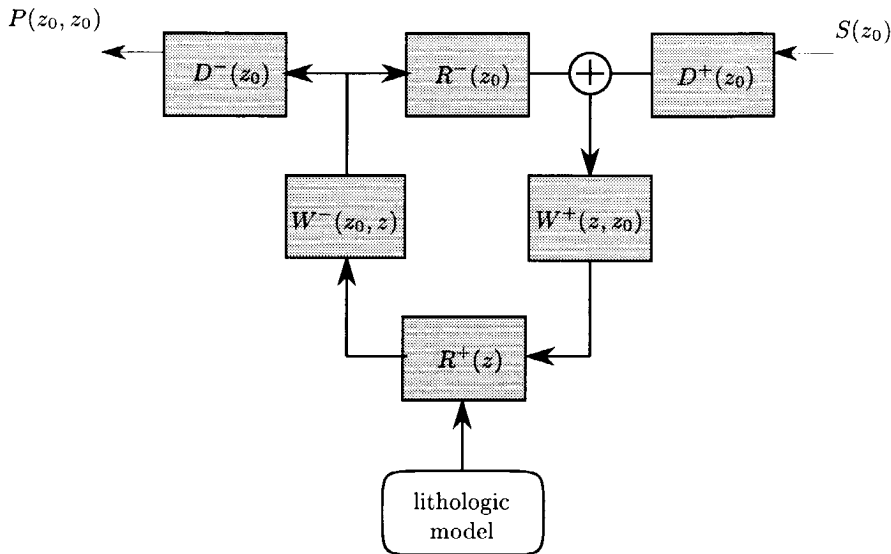


Fig. 1.4 The WRW-model after Berkhout (1982). The reflection operator $R^+(z)$ forms the link with the lithology.

1.3 Outline of this thesis

In this thesis two main topics are discussed.

A first topic discusses the effect of non-stationary small scale layering on the propagation of a seismic wave at intermediate frequencies. This is represented by the propagation operators $W^+(z, z_0)$ and $W^-(z_0, z)$ in Figure 1.4. Due to the effect of multiple reflections at this small scale, the seismic wave will be briefly delayed. This delay is often observed in well-tieing, when a discrepancy occurs between the traveltimes from the seismic measurement and the traveltimes computed from the P -wave velocity measurements in the well. Commonly this difference is in the order of a few percents, but can occasionally reach five up to ten percent. The methods currently available all start with a stringent assumption on the stationarity of the medium parameters in depth. In section 1.1.4 it was stated that sedimentary deposits are often non-stationary. In this thesis, a method is developed to describe the effect of small scale multiples in non-stationary media. From a review of laboratory measurements, a method is derived to average the medium properties in a way similar to the way the seismic wave experiences the medium. By means of a windowed averaging procedure, an effective velocity with a reference to scale will be calculated.

The scale-dependency of the derived velocity will be analysed using methods similar to the wavelet transform. An important scale dependency was observed. In Chapter 2 the method will be discussed for the propagation of plane waves perpendicular to the layering. In Chapter 3 the method is extended to plane waves propagating at an oblique angle with the fine layering. A method to derive the Thomsen anisotropy parameters (Thomsen, 1986) in a non-stationary medium is proposed as well.

In Chapter 4 a second main topic will be discussed. This topic is in the field of seismic characterization, and is represented by the reflection operator $R^+(z)$ in Figure 1.4. The need for more detailed interpretations in the reservoir management stage of the reservoir is increasing. A few of the driving forces for this increasing need are the increasing sedimentological complexity of the petroleum reservoirs under production, the increased use of advanced production methods (e.g. horizontal wells, gas and/or water injection) and the fact that a large number of the important fields in for instance the North Sea are at the end of the plateau stage and about to decline in production. All these factors lead to an increased need for detailed interpretations at the scale of individual sandbodies or stacks of sandbodies. A method to derive robust attributes and relate those attributes in some favourable cases to the type of sandbody is discussed in this thesis (Chapter 4). Using the matching pursuit method, attributes for geological characterization will be extracted. When some conditions are favourable, the phase attribute will prove to be able to distinguish between different types of sequences at the layer scale. For instance channel sands, with their blocky sequence type will be distinguished from point bars with a bell sequence.

1.4 Notational conventions

Some notational conventions that will be used in this thesis are introduced below.

Any scalar function in the space time domain is denoted by a lower case symbol, e.g. $f(z, t)$. The spatial variable z indicates the depth coordinate, and is taken positive for increasing depths. The variable t indicates the time coordinate. The corresponding function in the space frequency domain is denoted by an upper case symbol $F(z, \omega)$. The forward temporal Fourier transformation of a time dependent function is defined as:

$$F(z, \omega) = \int_{-\infty}^{+\infty} f(z, t) e^{-j\omega t} dt, \quad (1.1)$$

and the inverse transformation is defined as:

$$f(z, t) = \frac{1}{2\pi} \int_{-\infty}^{+\infty} F(z, \omega) e^{j\omega t} d\omega. \quad (1.2)$$

Vector quantities are denoted by an arrow above the symbol, e.g. $\vec{f}(z, t)$. Matrix quantities are denoted with a bold symbol, e.g. $\mathbf{f}(z, t)$.

The complex conjugate of a complex quantity is denoted by a superscript *. The symbol \Re indicates that the real part of a complex quantity, while \Im indicates that the imaginary part is taken.

Chapter 2

P-wave propagation at different scales

Often a discrepancy is observed between primary traveltimes derived from well-log velocities and traveltimes observed in the seismic experiment. Relative traveltime differences over a reservoir zone in the order of a few percents are common. Occasionally this can reach five up to ten percent. One of the most important reasons for this difference is the different frequency range at which both measurements are performed; well-log measurements are performed using acoustic signals with a much broader frequency spectrum compared to a seismic experiment. Small scale internal multiples will have a different effect at these different frequencies. Laboratory measurements found in literature showed that the ratio between the scale of measurement and the scale of the heterogeneities in the earth is an important factor. A problem is that the heterogeneities in the earth show a broad range of scales, i.e. they are multiscale. In this chapter a first order correction is used to compensate for this effect of scale-differences between measurements. The method was first described by Sams and Williamson (1994) and Rio et al. (1996), but the results will be analysed in more depth in this study. Mainly the scale dependency of the derived velocities will be analysed.

2.1 Introduction

In this chapter the effects of layering at different scales on the *P*-wave propagation properties are discussed. Acoustic properties measured in a wellbore are used in the derivations. The assumption of a transversely isotropic medium is made. Only propagation perpendicular to the layering is discussed. Propagation under an

oblique angle with respect to the layering will be discussed in Chapter 3. Of course, the full waveform response could be calculated, but that is rather resource intensive and complex. In this study, a simplified method will be described to derive the first break traveltimes at different scales. The method will allow to derive a localized, space variant velocity, and not like other methods a statistical average velocity over a long path. This method will be used to investigate the scale dependence of the first break velocities. Following the observation of scale dependance, an iterative procedure is developed to calculate the first break velocities at a scale matching the scales observed locally on the seismic trace.

The results from this method can be used for time-to-depth or depth-to-time conversion in sophisticated inversion methods or in well-tieing.

For the moment, the methodology is described using elastic materials. Only the effect of scattering is studied. In reality, losses caused by intrinsic anelasticity also play a role. When studying a real well-log at a later stage in this chapter, anelasticity will be introduced “ad hoc”. In Appendix A the theory of anelasticity is described for the sake of completeness.

2.2 Short and long wavelength limits

There are two main limiting theories of the interaction of seismic waves with heterogeneities.

2.2.1 Short wavelength limit: ray theory

In the short wavelength limit (this is when wavelength λ is much smaller than the layering thickness d , $\lambda \ll d$) the P -wave velocity c_{Prt} for plane waves traveling perpendicular to the layers of a stratified medium is given by the harmonic average:

$$\frac{1}{c_{Prt}} = \sum_{i=1}^N \frac{f_i}{c_{Pi}} = \left\langle \frac{1}{c_P} \right\rangle, \text{ with } \sum_{i=1}^N f_i = 1, \quad (2.1)$$

f_i the volume fraction and c_{Pi} being the P -wave velocity of the individual layers. $\langle \cdot \rangle$ denotes the averaging of the property in between the brackets. Equation (2.1) can also be written in terms of the compressibility $\kappa = \frac{1}{\rho c_P^2}$, and thus reads:

$$\frac{1}{c_{Prt}} = \left\langle \kappa^{\frac{1}{2}} \rho^{\frac{1}{2}} \right\rangle. \quad (2.2)$$

Equation (2.1) can also be written continuously:

$$\frac{1}{c_{Prt}} = \frac{1}{l} \int_0^l \frac{1}{c_P(z)} dz = \frac{1}{l} \int_0^l s_P(z) dz, \quad (2.3)$$

with $s_P = \frac{1}{c_P}$ the slowness. The P -wave velocity in the short wavelength limit, c_{Prt} , is defined by the velocity of the primary wave, as can be seen from Equations (2.1) and (2.3).

In this limit the wavelength λ is much smaller than the layering thickness d , so the multiple reflections will not interfere with the main lobe of the primary. Thus, the multiple reflections will not change the form of the wavelet. This also makes that the wavelet will not be dispersive and that the phase, group and first break velocities will all be the same and equal to c_{Prt} (see Appendix A for a discussion on the different velocities, although for anelastic materials).

2.2.2 Long wavelength limit: effective medium theory

In the long wavelength or the effective medium limit ($\lambda \gg d$), the material behaves as a homogeneous effective medium with velocities for plane-wave propagation normal to the layering c_{Pe} given by (Levin, 1979; Mavko et al., 1998):

$$\begin{aligned} \kappa_e &= \sum_{i=1}^N f_i \kappa_i = \langle \kappa \rangle \\ \text{or, } \frac{1}{\rho_e c_{Pe}^2} &= \sum_{i=1}^N \frac{f_i}{\rho_i c_{Pi}^2} = \langle \frac{1}{\rho c_P^2} \rangle \\ \text{with } \rho_e &= \sum_{i=1}^N f_i \rho_i = \langle \rho \rangle. \end{aligned} \quad (2.4)$$

This is a weighted average of compressibility κ_i , resulting in the effective medium velocity always being lower than the ray theory velocity.

Due to the effect of internal multiples or reverberations, the wave becomes delayed, as will be discussed in more detail in Section 2.3.

2.3 Full waveform synthetic seismograms

In section 2.2.1 the velocity of the primary wave was discussed. This is also called the ray theory limit or short wavelength limit. In that case, the multiples are arriving as separate events. When the multiples are not arriving as separate events, the primary wave interferes with the small-scale multiples, which can lead to a delay of the arrival.

Different methods are described for the calculation of the full waveform seismogram (Kennett, 1974; Aki and Richards, 1980; Kennett, 1983). Here we will give a description in the framework of the *WRW*-model as introduced by Berkhout (1982, 1984a) for acoustic one-way wave fields, and extended by Wapenaar and Berkhout (1989) for elastodynamic one-way wave fields. For more than a decade now, the *WRW*-model acts as the underlying philosophy for the integration of research within the *DELPHI* consortium (Berkhout, 1989; Berkhout and Wapenaar, 1990a,b).

The *WRW*-models are based on “one-way wave theory”, this means that it explicitly distinguishes between downward and upward propagation¹. Downward propagation is described by a propagator W^+ (the + sign denotes the propagation along the positive z -axis, which is pointing downward), and upward propagation is described by a propagator W^- . The reflection operator R^+ transforms downward propagating into upward propagating waves. The reflector operator R^- on the other hand, describes the transformation from upward into downward propagating waves.

In the case of a 1-D medium, and with a plane wave propagating perpendicular to the layering, the propagator W^+ for a medium imbedded in two homogeneous scatter-free half-spaces, becomes²:

$$\begin{aligned} W_g^+(z, z_0) &= W_p^+(z, z_0) \\ &+ \int_{z_0}^z dz' \int_{z'}^z W_p^+(z, z') R^-(z') W_p^-(z', z'') R^+(z'') W_p^+(z'', z_0) dz'' \\ &+ \dots, \end{aligned} \quad (2.5)$$

defining the so-called flux-normalized generalized primary propagator W_g^+ (Hubral et al., 1980; Resnick et al., 1986). Here z_0 belongs to the upper half-space and z to the lower one. The W_g^+ -propagator includes the effects of internal multiples. W_p^\pm are the so-called primary propagators, which are defined as follows:

$$W_p^\pm(z_a, z_b) = \exp \left(\mp j\omega \int_{z_a}^{z_b} \frac{dz'}{c_P(z')} \right), \quad (2.6)$$

with $j = \sqrt{-1}$ and ω the angular frequency. The reflection operators R^\pm (in this 1-D medium under normal incidence) are defined as:

$$R^\pm(z) = \pm \frac{1}{2Z} \frac{dz}{dz}, \quad (2.7)$$

where $Z = \rho c_P$ is the acoustic impedance. Equation (2.5) is also known as a Bremmer series expansion (Mendel, 1978). The first term on the right-hand side, W_p^+ , describes the primary, the second term on the right-hand side fully describes the first order multiple. Each order of multiples is described by one term in the Bremmer series as illustrated by Figure 2.1.

¹The *WRW*-model is well suited for any acoustic discipline where there is a preferred direction of propagation. In seismic exploration, this is the vertical direction. Since we are discussing the seismic exploration case, the upward and downward directions are used.

²All the properties in Equation (2.5) are also function of angular frequency ω . For notational convenience, ω will be omitted whenever there is no risk of confusion.

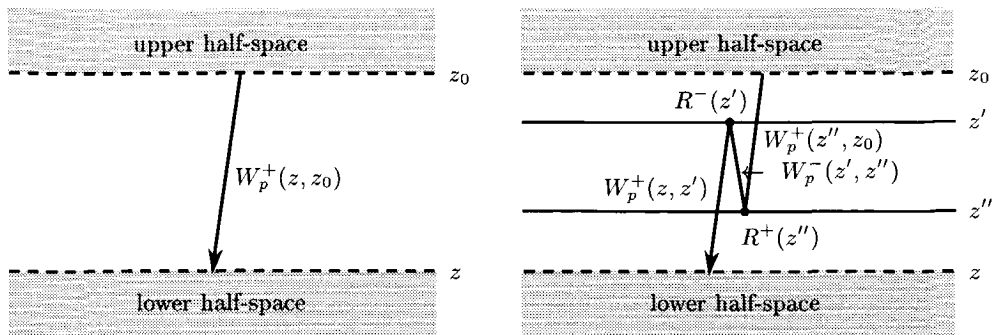


Fig. 2.1 A graphical representation of the different terms describing the Bremmer series expansion of $W_g^+(z, z_0)$ as given in Equation (2.5).

Another way to describe the effect of the multiples on the transmission response, is the Rytov approximation. This approximation is more accurate than the corresponding Bremmer series expansion for the calculation of transmission responses (Beydoun and Tarantola, 1988). Unlike the Bremmer expansion, the terms in the Rytov expansion cannot be attributed to multiples of a specific order. A further discussion of the Rytov expansion is beyond the scope of this description.

A full waveform synthetic seismogram describes the full response of the medium. It is commonly considered as a correct method, but it was never really proven that the representation of the earth by small layers is correct. The full waveform method is resource intensive. The velocity dispersion effects of fine-layering can also be described using a stratigraphic filter. Several studies were published on this topic. For most of these studies assumptions on the statistical stationarity of the medium parameters were made. The results after these assumptions will give a description in an average sense, which will become accurate after a long wave path has been travelled through the medium.

2.4 Stationary medium parameters: stratigraphic filter

The best-known formula in the field of the stratigraphic filter is the one O'Doherty and Anstey published in 1971. This formula is initially derived using a heuristic approach, and was later substantiated and expanded by a number of theoretical studies using both statistical (Banik et al., 1985a,b; Shapiro and Zien, 1993; Sams and Williamson, 1994) and deterministic (Kennett, 1974; Resnick et al., 1986; Bur-

ridge et al., 1988) approaches.

The O'Doherty-Anstey formula describes the effect of short-period multiple scattering on the phase velocity. The effect of multiple scattering caused by fine layering can be described as a filter applied to the wavelet, the so-called stratigraphic filter a :

$$w'(t) = a(t) * w_0(t), \quad (2.8)$$

with $w_0(t)$ the original wavelet, $w'(t)$ the wavelet after travelling through the medium, and $*$ denoting a convolution. In a similar way, the generalized propagation operator W_g^+ can be written as:

$$W_g^+(z, z_0) = W_p^+(z, z_0)A(\omega), \quad (2.9)$$

as a function of the propagation operators discussed in Section 2.3, and with $A(\omega)$ the Fourier transform of $a(t)$. Note that $a(t)$ is a causal function, describing the delay of W_g^+ relative to W_p^+ .

O'Doherty and Anstey (1971) found that the filter is related to the power spectrum R of the reflection coefficient time series. More specifically, they only discussed the complementary nature of $\ln|A(\omega)|$ and $R(\omega)$:

$$|A(\omega)| \sim e^{-t_p R(\omega)}, \quad (2.10)$$

without stating the quantitative relationship. $|A(\omega)|$ is the amplitude spectrum of the filter, ω the angular frequency, t_p the time traveled by the primary, and $R(\omega)$ the power spectrum of the reflection coefficient series.

Banik et al. (1985a) gave a more explicit formulation of the filter $A(\omega)$ based on a stochastic formulation. Several assumptions were made in the derivation, such as stationarity of the statistics of the material properties with time, and small contrasts. The filter $A(\omega)$ was found to become:

$$A(\omega) = e^{-j\omega F(\omega)t_p} = e^{\omega \Im[F(\omega)]t_p} e^{-j\omega \Re[F(\omega)]t_p}, \quad (2.11)$$

Where $F(\omega)$ is the Fourier transform of a causal function $f(t)$. The first factor on the right-hand side in Equation (2.11) is purely a frequency-dependent apparent attenuation, which can be described using the quality factor $Q(\omega)$:

$$\Im[F(\omega)] = -\frac{1}{2Q(\omega)}. \quad (2.12)$$

Note that the quality factor $Q(\omega)$ may depend upon frequency. The second factor on the right-hand side in Equation (2.11) describes an additional time delay $\delta t(\omega)$

caused by the short-period multiples:

$$\Re[F(\omega)] = \frac{\delta t(\omega)}{t_p}, \quad (2.13)$$

which also depends upon frequency.

$F(\omega)$ was found to be depending upon the spectrum of reflection coefficients $R(\omega)$, or alternatively, on the spectrum of the impedance fluctuations $M(\omega)$ (Banik et al., 1985a):

$$\Im[F(\omega)] = -\frac{R(\omega)}{\omega} = -\frac{1}{2} \omega M(2\omega), \quad (2.14)$$

and

$$\Re[F(\omega)] = \frac{1}{\pi} \text{f} \int_{-\infty}^{+\infty} \frac{\Im[F(\omega')]}{\omega' - \omega} d\omega', \quad (2.15)$$

with f denoting the Cauchy principal value of the integral, in which an infinitesimal small area around ω (a singular point of the integrand) is excluded from the integral. Note that $\Im[F(\omega)]$ depends on the impedance fluctuations $M(2\omega)$. This is due to the additional two-way traveltime of the multiples between pairs of reflectors. Note also that $F(\omega)$ is an analytic function, with $\Im[F(\omega)]$ and $\Re[F(\omega)]$ forming a Hilbert pair; Equation (2.15) is the definition of the Hilbert transform, so $\Re[F(\omega)]$ and $\Im[F(\omega)]$ are related to each other in the following manner:

$$\Re[F(\omega)] = \mathcal{H}[\Im[F(\omega)]], \quad (2.16)$$

and

$$\Im[F(\omega)] = -\mathcal{H}[\Re[F(\omega)]], \quad (2.17)$$

with \mathcal{H} used to indicate the Hilbert transform. This relationship is also known as the Kramers-Kronig relationship which is a consequence of the requirement of causality of $f(t)$ (Aki and Richards, 1980; Dahlen and Tromp, 1998)³.

When looking at the ray theory limit (see Section 2.2.1), the stratigraphic filter $a(t)$ will have no effect on the seismic wavelet. In this limit the layering of the earth is much larger than the seismic wavelength ($\lambda \ll d$). This means that the impedance fluctuations $M(2\omega)$ as written in Equation (2.14) will not have contributions within

³In Appendix A the Kramers-Kronig relationship is derived for an anelastic medium. This is another model than the scattering described here, but the same type of relationship occurs due to the requirement of causality.

the frequency band of the seismic wavelet w_0 . This will lead to a time delay $\delta t(\omega)$ that will be equal to zero in the frequency band of the seismic wavelet. This is also what Sams and Williamson (1994) show for a medium with small contrasts and with a constant density. Sams and Williamson (1994) also describe that in the long wavelength limit ($\lambda \gg d$), the results agree with the ones from equivalent medium theory (Section 2.2.2).

The results described in this section are derived using a stochastic formulation, predicting the average dispersion over a long path. This method does not predict the local fluctuations, and non-stationary behaviour.

Since the goal set at the beginning of this chapter was to get a local velocity for time-to-depth conversion and as a background model for pre-stack inversion, we need to find a method that takes local fluctuations and non-stationarity into account. In the following we will discuss a method that returns the local first break velocities in an efficient way.

2.5 Laboratory experiments

In literature Marion et al. (1994); Rio et al. (1996), several physical transmission experiments (jointly performed at Stanford University and Elf Aquitaine) were described. Mukerji (1995) gives a good overview of the different measurements and of the interpretations. The physical experiments were performed on artificial samples, and in a setting similar to a conventional laboratory core-sample measurement. For all these experiments the first break arrival of the wave is used to determine a velocity. Following Dellinger and Vernik (1994), the velocities associated with the first break arrival in a core-sample measurement setting is close to the phase velocity c_ϕ .

In the first set of measurements Marion et al. (1994), periodic stationary media are used. In these measurements, the transition between long and short wavelength limit is investigated. A second set of measurements deals with a non-stationary medium Rio et al. (1996). Both sets of measurements will guide the development of an approximate but efficient method to get the phase velocity c_ϕ as will be described in Section 2.6.

2.5.1 Stationary media

Several physical experiments have been performed at the transition between long and short wavelength limit. Here we will discuss some of these experiments, and will focus on the transition between both regimes. Note that in these experiments the first break velocities are used.

Marion et al. (1994) performed laboratory experiments using a periodic stack of plastic and steel discs. The reflection coefficient between both materials is 0.87 (see material properties in Figure 2.2). Both types of discs have a thickness of approximately $\frac{1}{2}$ mm. “Thick” layers were created by putting many discs of one of the materials together. Honey was used to ensure good coupling between the discs. In this way, a number of samples could be made with a changing thickness of the repeated pattern d , and with changing volume percentages of plastic and steel. Transmission measurements were made at 50 and 500 kHz. The first break travel-times were picked, and the corresponding velocity was calculated. Figure 2.2 shows the results for all the samples composed of $\frac{1}{3}$ plastic by volume. The experimental results show two distinct regimes: on the left-hand side an almost constant high velocity where the short wavelength limit holds, and on the right-hand side a considerably lower effective velocity where the long wavelength limit holds. The transition

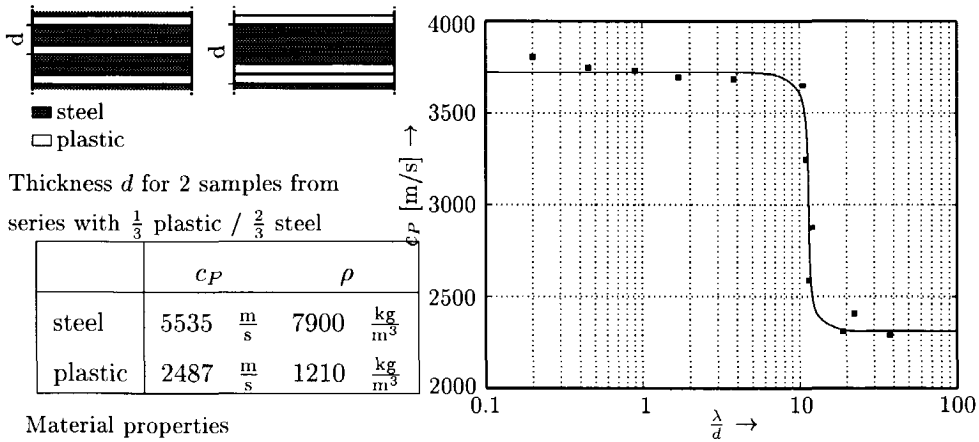


Fig. 2.2 Summary of experimental results of normal incidence propagation through stratified samples of plastic and steel layers at the transition from short to long wavelength behaviour. This figure summarizes all the measurements on samples composed of $\frac{1}{3}$ plastic and $\frac{2}{3}$ steel by volume. The seismic wavelength λ is normalized with the thickness of the repeated pattern (d) (see examples of d on the upper left). The velocity is defined as the ratio of the total length of the sample and the time needed for a P -wave to travel through it. The first breaks are picked. Note the logarithmic scale on the abscissa. The squares represent the measurements. The smooth curve only highlights the trend. The transition between both regimes is rather abruptly taking place at $\frac{\lambda}{d} = [10, 12]$. Modified after Marion et al. (1994).

between both regimes is rather abrupt (however, take note of the logarithmic scale along the abscissa). At $\frac{\lambda}{d} \approx 11$, the experimental results go from the one regime to the other. This transition value was experimentally found to be almost independent of the volume fractions of steel or plastic (Marion et al., 1994). The *amount* of velocity change is dependent of the composition, since both Equation (2.1) and (2.4) show a different dependence with the parameters of the medium. In this case, with a large contrast between material properties, the velocity change is large.

Melia and Carlson (1984) performed a similar experiment using a glass / epoxy system. The reflection coefficient between these materials is 0.66. The experiments were not as detailed as in Marion et al. (1994), since the sampling along $\frac{\lambda}{d}$ was much coarser. The transition was found to take place somewhere around $\frac{\lambda}{d} = 10 \pm 5$. The measurements might indicate that the transition is a little less abrupt than in Marion et al. (1994), and there is also a slight indication of a dependence of the transition on the volume fraction of both components. Both indications must be handled with care though, due to the coarse sampling along the $\frac{\lambda}{d}$ direction.

Marion et al. (1994) also performed numerical modeling experiments to investigate the influence of different material properties. Three material pairs were used, with reflection coefficients between both materials of respectively 0.20, 0.66 and 0.87. The results are not fully conclusive, due to the few data points around the transition, but an indication of a transition at lower $\frac{\lambda}{d}$ -values for materials with lower reflection coefficients was found. For instance for the three couples of materials, the transition zone for increasing reflection coefficients was respectively situated around $\frac{\lambda}{d} \approx 4, 6.5$ and 7.5 . This last value in contrast to the $\frac{\lambda}{d} \approx 11$ as found in the physical experiments. The difference was noticed by Marion et al. (1994) but not explained.

The different studies on the transition between ray theory and equivalent medium theory for periodical stratified media all give similar results. The transition seems to be happening over a relatively small $\frac{\lambda}{d}$ interval. The material properties, more specific the reflection coefficient between both materials, influence the position of the transition point.

2.5.2 Non-stationary media

Rio et al. (1996) performed similar experiments in non-stationary media. A stack of discs was incrementally built from scratch. Plastic and steel discs were used. Individual discs were approximately 0.5 mm thick. After each disc was added, a transmission measurement was made. The material for the next disc to be added was randomly chosen by tossing a fair coin. This resulted in the end in a stack of 140

discs with irregular layer thicknesses⁴ (left-hand side of Figure 2.3). The thicknesses varied between 1 and 10 discs (0.5 - 5 mm). By coincidence, zones with thick layers and zones with thin layers were present. The used signal had a wavelength of about 6 mm ($f_{\text{peak}} = 400$ kHz) when the stack was still small, attaining 24 mm ($f_{\text{peak}} = 100$ kHz) after passing through the full stack (Rio et al., 1996).

If we investigate the measurements (right-hand side of Figure 2.3), we notice that for the first 45 layers, the measurements are following the predictions from ray theory closely. In this part of the stack we also observe relatively thick layers. Only one layer of 1 disc is present, the other layers are between 3 and 10 discs thick. The divergence between measurements and ray theory coincides with the onset of a zone with relatively thin layers. The thickness of the layers in this zone is between 1 and 2 discs. The increment in propagation times (related to the slope of the curve) for this zone is very similar to the increment in the prediction from effective medium theory. In the zone between layers 65 and 107 the increment in propagation time is equal to the increment for ray theory. This again is a zone with relatively thick layers. These observations on increments of propagation times are confirmed for two zones at the bottom of the stack, respectively a zone with fine layers (discs 107-116), and a zone with thick layers (discs 117-140). Note that each time at the beginning of a “thick” plastic layer, a sharp rise in propagation time can be noticed. This is in fact a thin layering effect. Steel buffers are used between the sample and the transducers, so the first few plastic disks that will eventually make part of the “thick” layer, act first as “thin” layers.

In the next section we discuss a fast (but approximate) method that will give a simple first order approximation of the first break velocity.

2.6 Composite ray and effective media theory

We observed in the last section that neither effective medium theory nor ray theory is predicting the measured propagation times for the first break well (except for the first part). The increments of the propagation time follow ray theory closely in zones with thick layers, and follow effective medium theory in zones with thin layers. The transition between both theories seems to take place around a thickness of 2 (= 1 mm, at the beginning of the sample) to 3 discs (= 1.5 mm, at the end of the sample). Relative to the dominant wavelength, this becomes $\frac{\lambda}{d} = 6$ to 16.

⁴A layer is called a series of discs of the same material. The influence of the coupling material, honey, between the discs is ignored in this. The volume fraction of honey was estimated at 0.8 %.

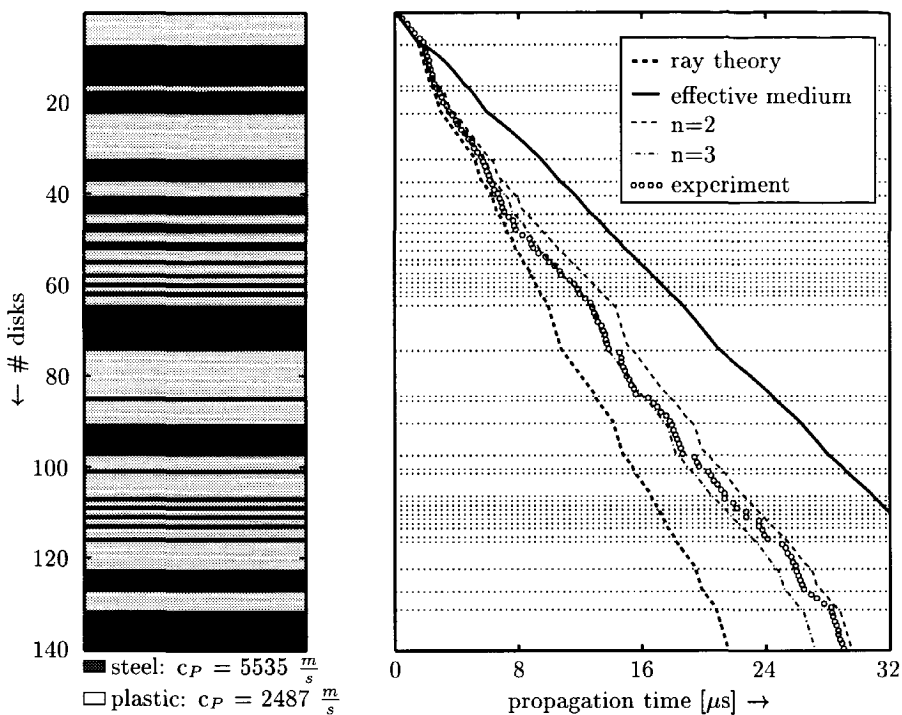


Fig. 2.3 Experimental results for a transmission measurement on a non-periodic layered medium. The medium consists of 140 layers of steel and plastic. On the left-hand side, the final stack of 140 layers is given. The stack was built up from top to bottom. On the right-hand side the results for the incremental transmission measurements are shown. The first break traveltimes were picked. The measurement started with only one disc between the transducers, and was repeated every time a new disc was added. The measured transmission times are indicated by the circles (\circ). The measurements lie in between the ray theory and the effective media theory results. See page 25 for an explanation for the other lines. Modified after Rio et al. (1996).

This range corresponds well with the transition observed for the experimental results on periodic samples (see Figure 2.2 on page 21), where a transition between ray theory and effective medium theory is situated around $\frac{\lambda}{d} \approx 11$. Although this transition is dependent on the contrast between the materials. For a more realistic situation with a reflectivity of 0.10 to 0.20, the transition can be estimated at around

$\frac{\lambda}{d} \approx 4$ to 7 (see section 2.5 for a discussion).

Sams and Williamson (1994) and Rio et al. (1996) proposed a composite method:

1. windowed effective medium theory,
2. ray theory.

What is this composite method actually doing ? Let us look at two extreme situations: a medium with only fine scale variability, and a medium with only long scale variability.

If we only have fine scale variability in the medium ($\lambda \gg d$), the running averaging in the first step will yield a slowly varying effective medium. This is in accordance with Folstad and Schoenberg (1992). Depending on the stationarity of the fine scale variability, this might even be a constant effective medium.

On the other hand, if there is only long scale variability in the medium, the first step will have almost no effect. Only the ray theory part will have an effect. Ray theory was already valid on the original material in the first place.

In essence, the first step regularizes the small scale variability in such a way that ray theory may be applied without a problem afterwards.

If this composite method is applied to the experiment described in Figure 2.3 on page 24, the experimental traveltimes are closely matched (Rio et al., 1996). The dashed thin line on Figure 2.3 is the result for a fixed “box-car” window of 2 discs⁵, the dash-dot thin line for a window of 3 discs long. We note that the experimental results are closely bounded by both results. We also note that at the beginning of the stack, the experimental results agree better with the results for the 2 disc window; near the end of the stack, the experiment is more closely followed by the results from the 3 disc window. This is probably caused by the longer wavelength of the pulse when travelling through the stack. Actually, a changing window should be used, relative to the wavelength of the pulse at that location.

Rio et al. (1996) evaluated the composite method for a number of synthetic random layered media. Each random medium had a different stochastic model describing the medium. Poisson, Gaussian and fractal media were studied. For all three models, a good agreement with the first break picks from a full waveform solution was found.

⁵A “box-car” window has everywhere a value of zero, except for $[z_0 - \frac{\sigma_z}{2}, z_0 + \frac{\sigma_z}{2}]$, where its value is $\frac{1}{\sigma_z}$. It is L_1 normed. This type of window is also known as the Haar wavelet. Strictly speaking it is not a wavelet because it has a DC-component.

2.6.1 Choice of window function

Following Herrmann (1997), the regularity of a window function is an important factor in the choice of these functions. Regular window functions are desired. The regularity is expressed as C^N . A window function $\psi(t)$ is C^N regular, when:

$$\begin{aligned} \forall n < N, n \in \mathbb{N}, \forall t \in \mathbb{R}, \forall \epsilon > 0, \exists \delta > 0 : \left| \frac{d^n \psi(t)}{dt^n} - \frac{d^n \psi(t + \delta)}{dt^n} \right| < \epsilon, \text{ and} \\ \forall n \geq N, n \in \mathbb{N}, \exists t \in \mathbb{R}, \exists \epsilon > 0, \forall \delta > 0 : \left| \frac{d^n \psi(t)}{dt^n} - \frac{d^n \psi(t + \delta)}{dt^n} \right| > \epsilon. \end{aligned} \quad (2.18)$$

These conditions mean that for a C^N regular window function $\psi(t)$, all derivatives $\frac{d^n \psi(t)}{dt^n}$ with $n < N$ are continuous over the whole time-range, while the ones with $n \geq N$ are not.

The three window functions discussed above, are drawn in Figure 2.4. Their first and second derivatives are given as well. It is clear that the first window function, the “box-car”, is C^0 continuous. The second window function, half a period of the cosine function, is C^1 continuous. The last one, the Gaussian window function, is C^∞ . This means that all its derivatives are continuous.

Following Herrmann (1997), the Gaussian window function is preferred for its C^∞ regularity. This one will be used as window function. The Gaussian function used is L_1 -normed, and is defined as:

$$\psi(t) = \frac{1}{\sigma_t} e^{-\pi(t/\sigma_t)^2}, \quad (2.19)$$

σ_t being the scale factor in time. This is the definition of the Gaussian function in the time domain. The Gaussian function can also be defined in the depth domain:

$$\psi(z) = \frac{1}{\sigma_z} e^{-\pi(z/\sigma_z)^2}, \quad (2.20)$$

with σ_z the scale factor in depth.

2.6.2 Regularized velocity at a certain scale

The scale dependent velocity can now be calculated. When the seismic wavelength λ_z in depth is known, the scale σ_z at which the medium needs to be averaged using effective medium theory is defined as:

$$\sigma_z \approx \frac{\lambda_z}{5}. \quad (2.21)$$

This value is taken with reference to the observations from the physical experiments in Section 2.5.

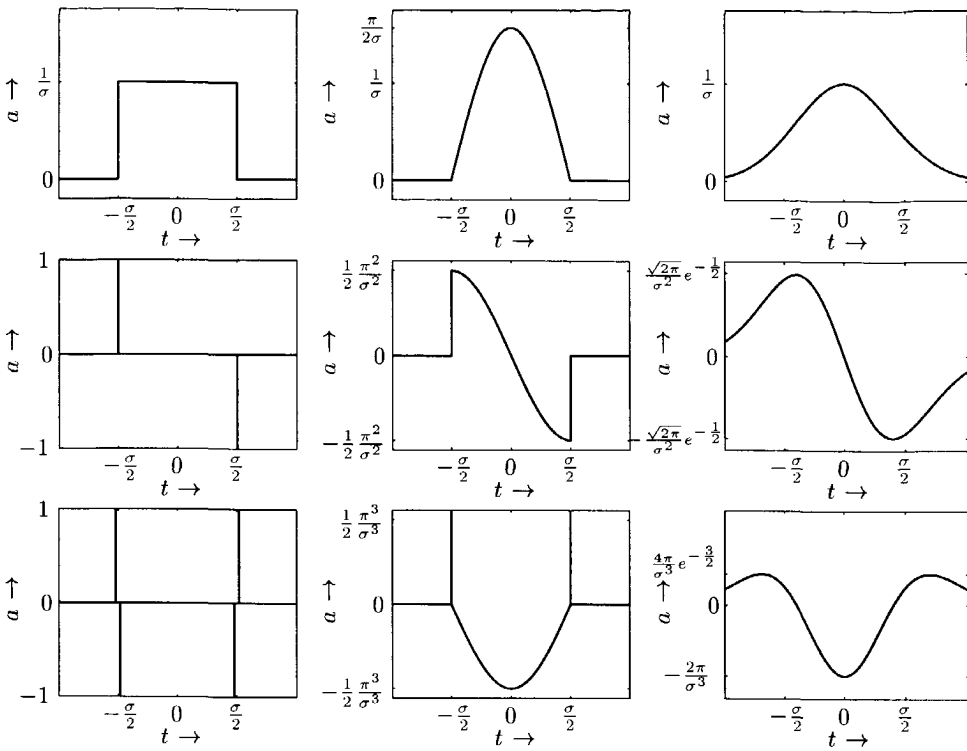


Fig. 2.4 Three window functions (top row), and their first (second row) and second derivative (bottom row). The “box-car” on the left-hand side, half a period of a cosine function in the middle, and the Gaussian-function on the right.

The well-log velocity c_P is subsequently regularized to the corresponding scale σ_z using the following formula:

$$\check{\kappa}(\sigma_z, z) = \frac{1}{\sigma_z} \int_{-\infty}^{+\infty} \kappa(z') e^{-\pi \left(\frac{z'-z}{\sigma_z} \right)^2} dz' = \frac{1}{\sigma_z} \int_{-\infty}^{+\infty} \frac{1}{\rho(z') c_P^2(z')} e^{-\pi \left(\frac{z'-z}{\sigma_z} \right)^2} dz'. \quad (2.22)$$

This is an equivalent medium theory averaging, as discussed in Section 2.2.2. Equation (2.22) represents the smoothing of compressibility $f(z) = \kappa(z)$:

$$\check{f}(\sigma_z, z) = \frac{1}{\sigma_z} \int_{-\infty}^{+\infty} f(z') \psi \left(\frac{z'-z}{\sigma_z} \right) dz', \quad (2.23)$$

using the original Gaussian function:

$$\psi(z) = e^{-\pi z^2}, \quad (2.24)$$

as smoothing function. Note that this type of scale-dependent smoothing is related to the continuous Gaussian wavelet transform (Mallat, 1999). The smoothing function used here, the Gaussian function in Equation (2.24), is however not a wavelet since it has a mean unequal zero. The *P*-wave velocity smoothed to scale σ_z is subsequently calculated from $\check{\kappa}(\sigma_z, z)$ in the following way:

$$\check{c}_P(\sigma_z, z) = \sqrt{\frac{1}{\check{\kappa}(\sigma_z, z) \check{\rho}(\sigma_z, z)}}, \quad (2.25)$$

with $\check{\rho}$ the smoothing of ρ as defined by Equation (2.23). Note that the accent on \check{c}_P differs from those on the other smoothed properties. This is because \check{c}_P is not directly calculated using Equation (2.23), but instead was derived from the smoothed properties $\check{\kappa}$ and $\check{\rho}$.

When we apply this regularization to the Saga well-log (see Appendix B for a geological description), we get the results as presented in Figure 2.5. We can easily see the smoothing effect for increasing scale σ_z . This is however not the only effect. Equation (2.22) shows an equivalent medium theory type of averaging, since it averages the compressibility $\kappa = \frac{1}{\rho c_P^2}$. The effect of this can best be seen by comparing the traveltimes calculated from $\check{c}_P(\sigma_z, z)$ and the one calculated from the original well-log velocity $c_P(z)$. The difference between both traveltimes is also called the drift. A one-way traveltime Δt between two depths z_1 and z_2 can be calculated using:

$$\Delta t(z_1, z_2) = \int_{z_1}^{z_2} \frac{1}{f(z')} dz', \quad (2.26)$$

for any type of velocity. When we use $f(z) = c_P(z)$, the ray theory Δt is calculated. When using $f(z) = \check{c}_P(\sigma_z, z)$, a $\check{\Delta}t(\sigma_z, z_1, z_2)$ at a certain scale σ_z is calculated.

Figure 2.6 shows the drift between the traveltimes calculated from the original well-log velocity c_P and those from $\check{c}_P(\sigma_z, z)$, i.e. $\check{\Delta}t(\sigma_z, z_1, z_2) - \Delta t(z_1, z_2)$. The relative difference in traveltimes is in the order of 1 %, since $\Delta t = 196$ ms for this interval. The drift originates from the averaging of compressibility $\kappa(z)$ in Equation (2.22) and the subsequent calculation of the *P*-wave velocity \check{c}_P in Equation (2.25).

This drift as calculated using the approximate method was checked using numerical modelling. A normal incidence plane wave Vertical Seismic Profile (VSP)

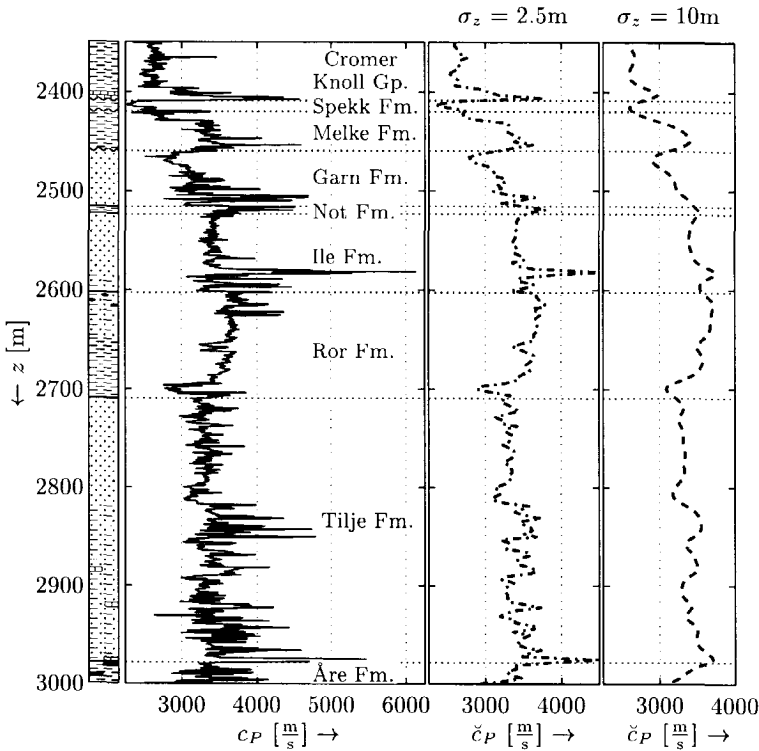


Fig. 2.5 Result for the regularizing of the P-wave velocity of the Saga well-log using Equation (2.25), using the original P-wave well-log c_P and the density well-log ρ . On the left-hand side the original P-wave well-log c_P , on the right-hand side \check{c}_P for $\sigma_z = 2.5$ and 10 m. A detailed geological description of the well-log can be found in Appendix B.

was modelled for the same piece of well-log, using an acoustic, flux-normalized reflectivity method (Kennett, 1983). Figure 2.7 shows the result when convolved with a Ricker wavelet⁶ with a dominant frequency f_{dom} of 100 Hz. The drift was calculated for the peak of the envelope, i.e. the drift associated with the group velocity c_g . Ricker wavelets with dominant wavelength $\lambda_t = \frac{1}{f_{\text{dom}}}$ that correspond to the scales σ_z in Figure 2.6 were used. This means that $\lambda_t = \frac{\lambda_z}{c_P}$ and from Equation (2.21) it follows that $\lambda_z = 5 \sigma_z$. A constant, average velocity over the interval of $3250 \frac{\text{m}}{\text{s}}$

⁶A Ricker-wavelet is defined as: $f(t) = (1 - 2(\pi f_0 t)^2) \cdot e^{-(\pi f_0 t)^2} \approx \cos(2\pi f_0 t) \cdot e^{-(\pi f_0 t)^2}$, with f_0 the peak frequency. The mean frequency (weighted by the amplitude spectrum) is given by $f_{\text{mean}} = \frac{2}{\sqrt{\pi}} f_0$ (Sheriff, 1991), and the dominant frequency by $f_{\text{dom}} = \frac{\pi}{\sqrt{6}} f_0$.

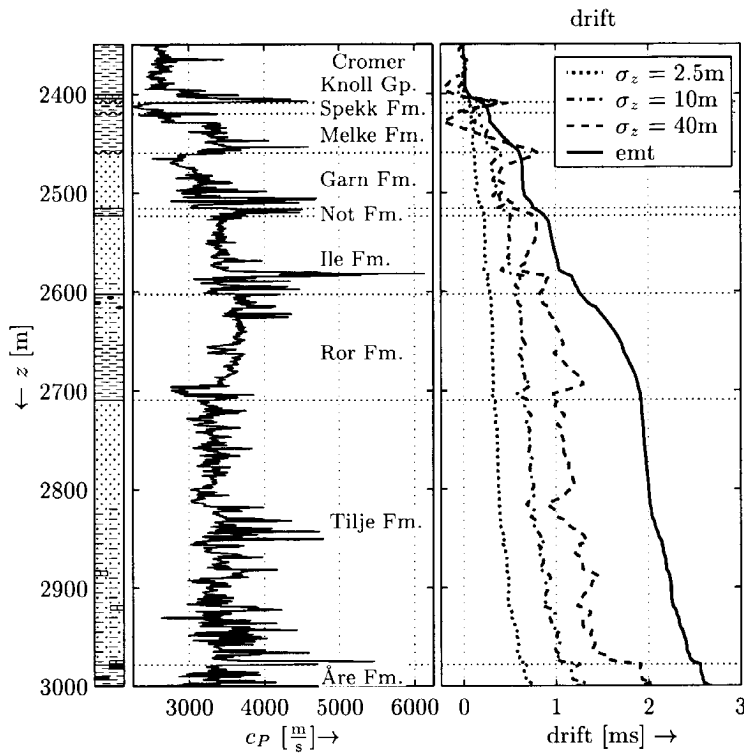


Fig. 2.6 Drift calculated for different scales. The drift is the difference between the one-way traveltime calculated from the original c_P (i.e. the traveltime of the primary, given by ray theory) and the one-way traveltime calculated from $\check{c}_P(\sigma_z, z)$. The top of the interval shown ($z = 2350\text{m}$) is taken as a reference. Note that the drift is steadily increasing with depth z , and that the effect is larger for larger scales σ_z . The result when applying equivalent medium averaging (“emt”) is also shown. This can approximately be considered as the result for $\sigma_z \rightarrow \infty$. As a reference, the primary traveltime for the interval shown is 196 ms. The drift is in the order of 1 % of the primary traveltime.

was used in the calculation of λ_t . Figure 2.8 gives the resulting drifts for the three values of λ_t . The drift is fluctuating a lot due to interference effects of the reflected waves. By applying running averaging with a window length that is proportional to the dominant wavelength of the Ricker wavelet used, the trend in the drift data can be emphasized. When comparing Figures 2.6 and 2.8, it appears that the drifts calculated using the approximate composite method compare well with the drifts

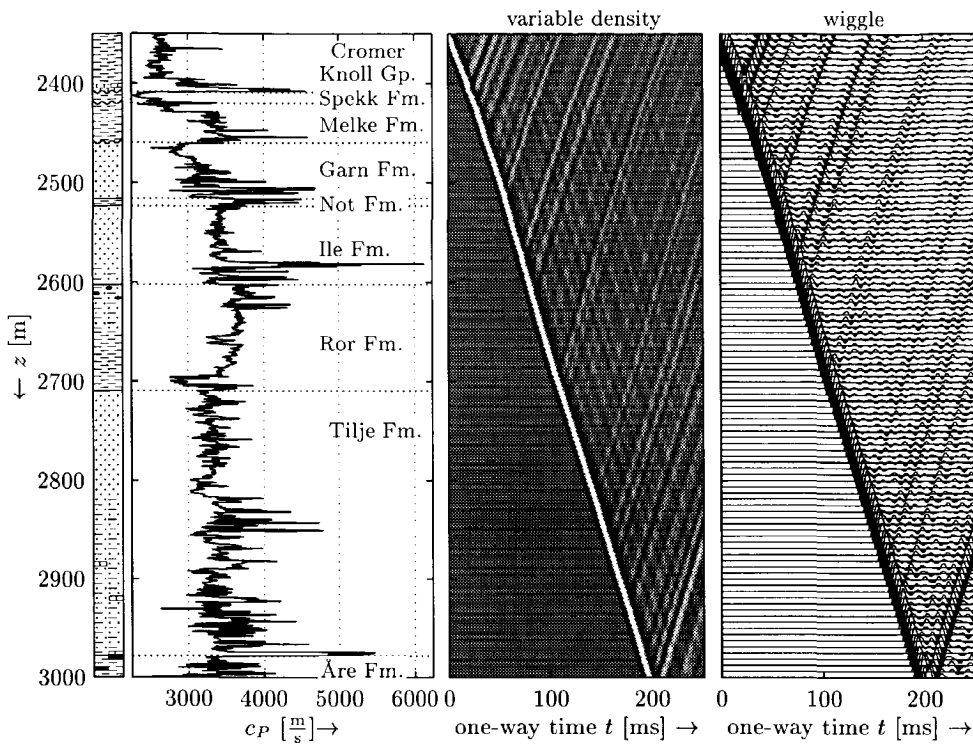


Fig. 2.7 Synthetic Vertical Seismic Profile (VSP) for part of the Saga well-log. A 100 Hz Ricker wavelet was applied for display. The Base Cretaceous Unconformity ($z = 2410$ m), with the overlying limestone layer at the base of Cromer Knoll Group, is a clear multiple generator. The same VSP-data is plotted as variable density and wiggle plot.

calculated from the numerical modelling results. The results for the numerical modelling compare very well with the results from the approximate method; both the value of the resulting drifts are in the same order of magnitude, and also the places where a sudden increase occurs tend to align for both drift curves. Only the results for the highest frequencies (or finest scales), are different: the drift found from the numerical modelling results are in the order of about 40 % of the value of the drift found from the approximate method. An explanation might be found in the extremely high frequency of 260 Hz of the wavelet used.

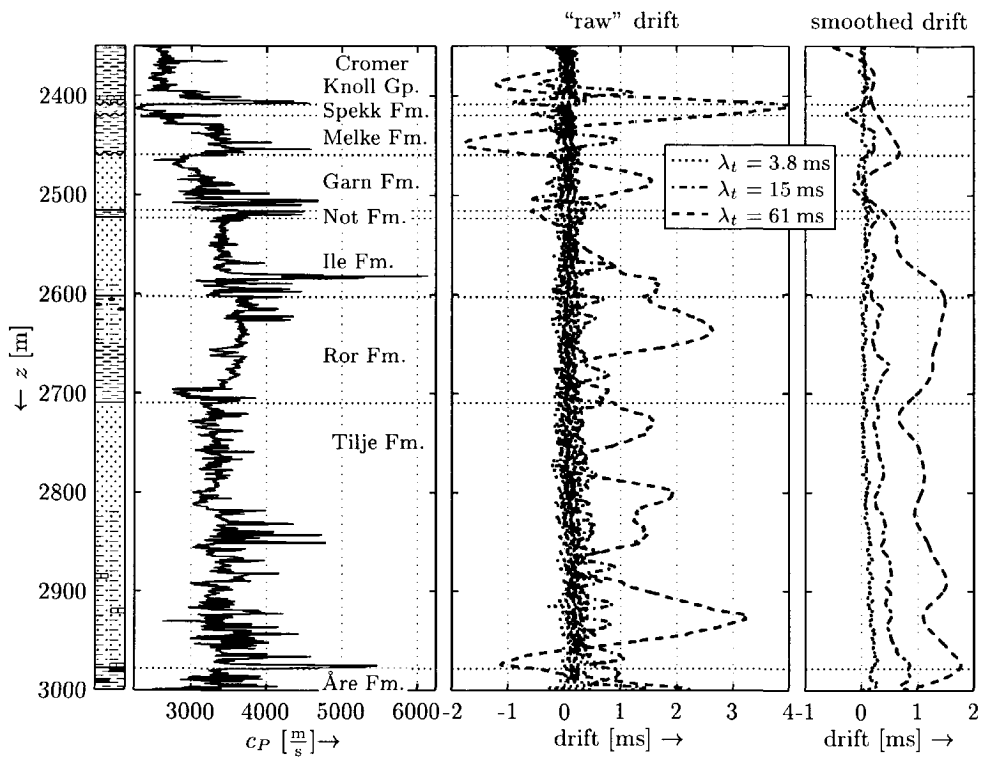


Fig. 2.8 Drift calculated for the Saga data set using numerical modelling. Ricker wavelets with dominant frequencies 260 Hz, 67 Hz and 16 Hz were used (resp. λ_t of 3.8 ms, 15 ms and 61 ms). The middle panel is the “raw” drift as picked for the maximum of the envelope. Due to the interference with reflections, the “raw” drift is fluctuating a lot. The right panel is a smoothed version of the “raw” drift. A clear trend can be seen, comparable to the trend observed from the approximate method (Figure 2.6). Also the locations with a sharp increase in the drift match.

2.6.3 Characterizing events

The regularized P -wave velocity \check{c}_P was only evaluated for two scales σ_z in Figure 2.5. Figure 2.9, middle panel, evaluates \check{c}_P for a range of scales σ_z . Note that a local velocity $\check{c}_P(\sigma_z, z_0)$ is clearly scale-dependent. This dependency can be

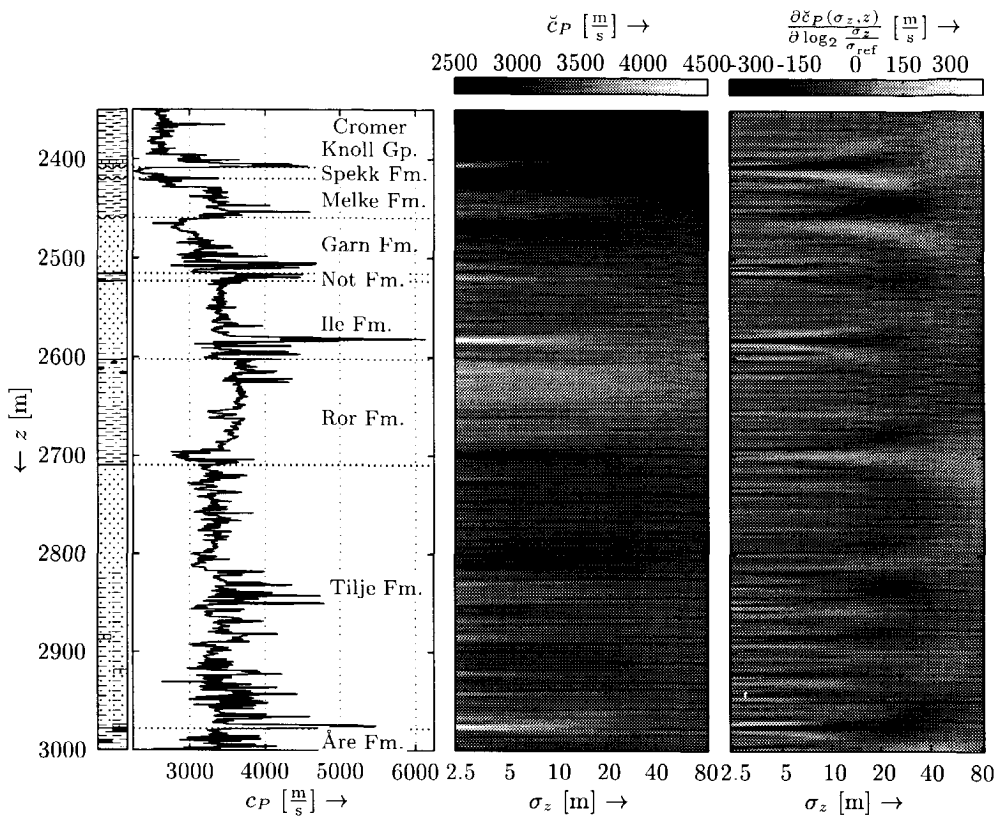


Fig. 2.9 The regularized velocities and their scale dependencies. On the left-hand side the original well-log. In the middle, the upscaled velocity using running effective medium averaging $\check{c}_P(\sigma_z, z)$ for a scale-range $\sigma_z = [2.5 \text{ m}, 80 \text{ m}]$. This corresponds (using $\frac{\lambda_z}{\sigma_z} = 5$) to wavelengths of approximately $\lambda_z = [12.5 \text{ m}, 400 \text{ m}]$. On the right-hand side the scale dependence of $\check{c}_P(\sigma_z, z)$. It is defined as the amount of change of $\check{c}_P(\sigma_z, z)$ for a doubling of the scale σ_z . The grayscale goes from -400 to +400 m/s, but a minimum of -750 m/s was found at location $z = 2976 \text{ m}$. This originates from a thin bed of limestone at the base of the Ile Formation.

quantified using:

$$\frac{\partial \check{c}_P(\sigma_z, z_0)}{\partial \log_2 \left(\frac{\sigma_z}{\sigma_{\text{ref}}} \right)}, \quad (2.27)$$

with σ_{ref} an arbitrary reference scale. Equation (2.27) signifies the change in velocity $\check{c}_P(\sigma_z, z)$ when the scale σ_z would be doubled. The result for this evaluation is shown in Figure 2.9 on the right-hand side. At the smaller scales, the scale dependency can be locally very high. But also at $\sigma_z = [5 \text{ m}, 10 \text{ m}]$, scales corresponding to common seismic wavelengths $\lambda_z = [25 \text{ m}, 50 \text{ m}]$, the velocities are still very dependent on scale.

As said previously, Equation (2.22) describes a smoothing of compressibility κ . The smoothing kernel used for this is the Gaussian function. In continuous Gaussian wavelet transforms, a derivative of the Gaussian function are used. Normally a wavelet is chosen with a sufficient number of vanishing moments. A wavelet ψ has p vanishing moments if (Mallat, 1999):

$$\int_{-\infty}^{+\infty} t^k \psi(t) dt = 0, \forall k : k \in \mathbb{N} \text{ and } 0 \leq k < p. \quad (2.28)$$

In other words, this means that a wavelet ψ with p vanishing moments is orthogonal to a polynomial of degree $p - 1$.

The continuous wavelet transform is normally performed using a wavelet with at least one vanishing moment. This makes it orthogonal to the average value of the function being analysed. As a consequence, the analysis results obtained through Equation (2.23) will be on average zero when using a wavelet with at least one vanishing moment. The locally largest diversions from zero are the so-called modulus maxima points, carrying the essential information in a signal. This essential information can be related to discontinuities and edges in the signal at the smallest scale (Mallat, 1999). Modulus maxima points are defined as the points (σ_{z_0}, z_0) where $|\check{f}(\sigma_{z_0}, z)|$ is locally maximum at $z = z_0$. The connection of the points (σ_{z_0}, z_0) for different scales σ_{z_0} leads to modulus maxima lines. These modulus maxima lines will detect the location of singularities where they converge at fine scales (Mallat, 1999).

In Equation (2.22), a Gaussian function is used as smoothing function. This function has no vanishing moments. This means that it is not orthogonal to the local average value, and that the results from Equation (2.22) in general will have a mean unequal zero, as can be seen clearly in Figures 2.5 and 2.9. The most interesting locations in this resulting signal will be those where the signal deviates most from its local average value. These locations are the points where the signal is locally extreme. The local extrema locations are the locations (σ_{z_0}, z_0) where:

$$\frac{\partial \check{f}(\sigma_{z_0}, z)}{\partial z} \bigg|_{z_0} = 0. \quad (2.29)$$

Extrema lines are defined as any connected curve in the (σ_z, z) -plane along which all

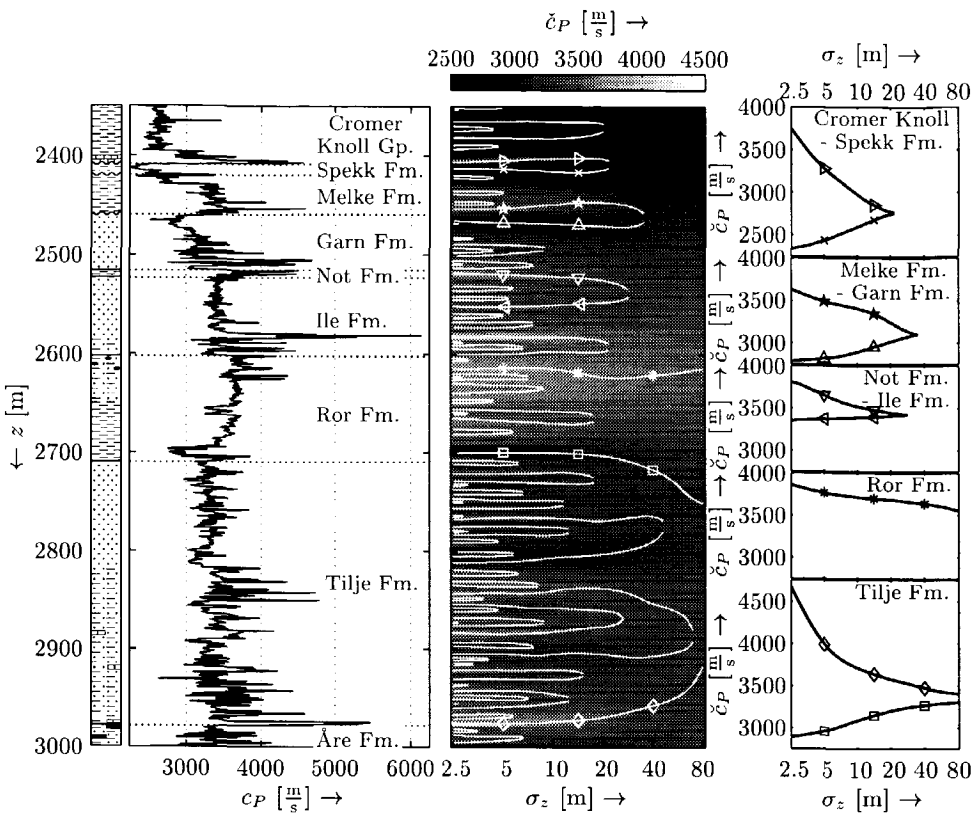


Fig. 2.10 The regularized velocities $\check{c}_P(\sigma_z, z)$ at different scales, and the extrema lines (middle panel). These lines indicate the interesting points in $\check{c}_P(\sigma_z, z)$. For some selected extrema lines (indicated by symbols in the middle panel) the values of $\check{c}_P(\sigma_z, z)$ along the extrema line are plotted (panels on the right-hand side). Note for instance in the top panel, the evolution of the extrema lines originating from the limestone at the base of Cromer Knoll Gp. and from the Spekk Formation and touching and disappearing at $\sigma_z \approx 20$ m. Note that the lines originating at the top of the Ror Fm. and the top and base of the Tilje Fm. are the only three to remain present over the entire scale range here analysed. It is also obvious that the regularized velocities still show a large evolution within the seismic scale range, i.e. $\sigma_z = [5 \text{ m}, 10 \text{ m}]$, corresponding to a seismic wavelength of $\lambda_z = [25 \text{ m}, 50 \text{ m}]$. This is for instance the case at the top of the reservoir interval, i.e. at the interface between Melke Fm. and Garn Fm. At $(\sigma_{z0}, z_0) = (2.5 \text{ m}, 2976 \text{ m})$ the scale dependency is largest: $\frac{\partial \check{c}_P(\sigma_z, z)}{\partial \log_2 \frac{\sigma_z}{\sigma_{ref}}} \Big|_{z_0} = -750 \frac{\text{m}}{\text{s}}$. This extrema line is depicted on the lower plot on the right-hand side.

points are extrema locations. These are related to the wavelet transform modulus maxima lines as discussed above. For the modulus maxima locations an additional condition, $|\tilde{f}(\sigma_{z_0}, z)|$ being a strict local maximum along the z -direction, must hold.

Using the extrema lines on the Saga well-log, the most interesting points in the signal can be followed along the scale axis (white lines in the middle panel of Figure 2.10). With increasing scale σ_z , the number of events decreases. Local maxima and minima tend to vanish in pairs at a certain scale. At the coarsest scale, $\sigma_z = 80$ m, only three events remain present. In this way a natural hierarchy in the events can be established (Vermeer, 1992). Starting from the coarsest scale, the events at that scale give the coarsest subdivision, or branches in the partitioning tree. While going to finer scales, every time an event appears, one branch of the hierarchy-tree will be subdivided in three branches. The points at which new events start can also be seen as bifurcation points.

2.7 Catch-22 problem

Until now, we have only discussed transmission data in this chapter. From this point on we will discuss reflection data. The results from the transmission type of data will be used further.

We found in the previous section that the regularized velocity is dependent upon the scale at which it is observed. This scale σ_z is related to the local wavelength of the seismic wave. More exactly, it is related to the wavelength in depth, λ_z , of the seismic wave:

$$\sigma_z = \frac{\lambda_z}{5}. \quad (2.30)$$

In reality we don't measure the seismic wave in depth, we measure the wave at the surface in time. What can be analysed directly on the seismic wave, is the seismic wavelength λ_t in time. The link between both domains (time and depth) is in fact the scale dependent regularized velocity:

$$\lambda_z(z) = \lambda_t(\check{t}(\sigma_z, z)) \quad \check{c}_P(\sigma_z, z) = \lambda_t(\check{t}(\frac{\lambda_z}{5}, z)) \quad \check{c}_P(\frac{\lambda_z}{5}, z), \quad (2.31)$$

with

$$\check{t}(\sigma_z, z) = 2 \int_0^z \frac{1}{\check{c}_P(\sigma_z, z')} dz', \quad (2.32)$$

the time-to-depth or depth-to-time relationship at a certain scale σ_z , and with $\check{c}_P(\sigma_z, z)$ the regularized velocity in time. From Equation (2.31) is it clear that a typical “catch-22 problem” (Heller, 1961; Herrmann, 1997; Dessim, 1997) arises:

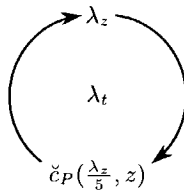


Fig. 2.11 Catch-22 situation with mutual dependent λ_z and $\check{c}_P(\frac{\lambda_z}{5}, z)$. λ_t is measured on the seismic trace. A combination of λ_z and $\check{c}_P(\frac{\lambda_z}{5}, z)$ needs to be found in order to match the observed $\lambda_t = \frac{\lambda_z}{\check{c}_P(\frac{\lambda_z}{5}, z)}$.

the regularized velocity $\check{c}_P(\sigma_z, z)$ being the link between the wavelength in time λ_t and the wavelength in depth λ_z is dependent upon the scale in itself (Figure 2.11).

2.8 Solution: iterative procedure

The “catch-22 problem” as described in previous section, is handled using an iterative procedure. The procedure will be explained in two stages.

2.8.1 Simplest case: constant wavelength in time λ_t

Let’s first take a simple case, by considering that the objective is to obtain a constant wavelength in time λ_t . The goal is to find the combination of λ_z and $\check{c}_P(\sigma_z, z)$ in order to attain the following equality:

$$\lambda_t = \frac{\lambda_z}{\check{c}_P(\sigma_z, z)}, \text{ with } \sigma_z = \frac{\lambda_z}{5}. \quad (2.33)$$

We use an iterative procedure, and start by assuming an initial scale in depth $\sigma_z^{(1)}$. For the i^{th} iteration, the scale is updated using the velocity evaluated at the scale obtained from the $(i-1)^{\text{th}}$ iteration:

$$\sigma_z^{(i)}(z) = \frac{\lambda_t}{5} \check{c}_P(\sigma_z^{(i-1)}(z), z). \quad (2.34)$$

Because we assumed in this simple case that the wavelength in time λ_t was constant, no iterative time-to-depth conversion needs to be done for the transformation of $\lambda_t(t)$ to $\lambda_t(z)$.

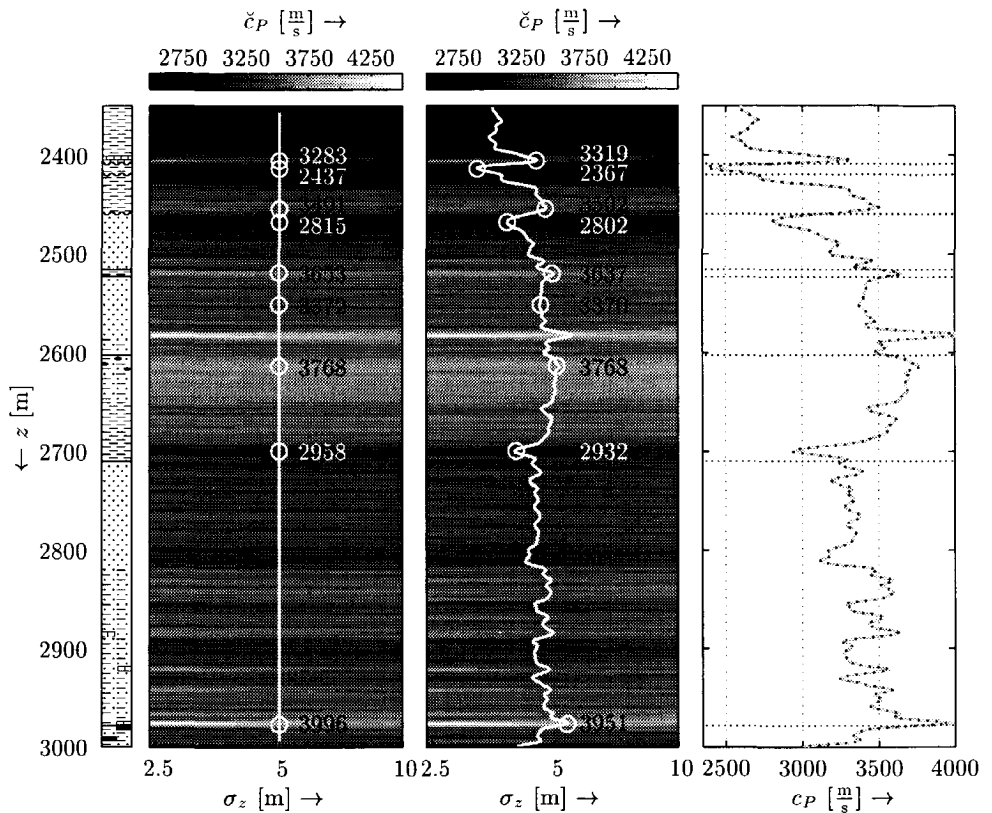


Fig. 2.12 The results of the iterative procedure for a desired wavelength in time λ_t of 6.67 ms, or a dominant frequency f_{dom} of 150 Hz. To the left the initial scale $\sigma_z^{(1)}(z) = 5$ m plotted on top of $\check{c}_P(\sigma_z, z)$ (in grey scale). For a few locations (corresponding to the extrema lines in Figure 2.10) the value of $\check{c}_P(\sigma_z^{(1)}, z)$ is printed. In the middle panel the final result $\sigma_z^{(3)}(z)$ (after 3 iterations) is plotted. Again the velocities $\check{c}_P(\sigma_z^{(3)}, z)$ at the locations corresponding to the same extrema lines are indicated. On the right-hand side, $\check{c}_P(\sigma_z^{(1)}, z)$ in grey line, and $\check{c}_P(\sigma_z^{(3)}, z)$ in dotted line are plotted. Note that the final selection of scales, $\sigma_z^{(3)}(z)$, and the corresponding velocity $\check{c}_P(\sigma_z^{(3)}, z)$ match in order to result in a constant $\lambda_t = 6.67$ ms.

Figure 2.12 shows the results after 3 iterations for a part of the Saga data set. The desired λ_t is 6.67 ms, equivalent to a dominant frequency f_{dom} of 150 Hz. Even for these high frequencies, with the associated high scale dependencies of the

velocities $\check{c}_P(\sigma_z(z), z)$, the iterative scheme converges after 3 iterations. A constant initial scale in depth $\sigma_z^{(1)}$ was chosen at 5 m. The final velocities are slightly different from the initial ones. At the locations with the highest scale dependency and at the same time a large difference from the initial scale (e.g. at $z = 2415$ m), relative differences between initial and final $\check{c}_P(\sigma_z, z)$ of up to 3 % could be observed.

The convergence of the iteration scheme was always observed, and tests so far showed no dependence of the final convergence result on the choice of the initial scale.

2.8.2 Non-constant wavelength in time $\lambda_t(t)$

Due to attenuation phenomena such as anelasticity, the wavelength of a seismic wavelet is changing with depth. Until this stage, the material properties were considered to be elastic. Only the effect of scattering was studied. In reality, both phenomena play a role. In this section, a data-driven approach is presented, to account approximately for the effect of attenuation. Often an approximately constant quality factor Q is observed in materials. As discussed in Appendix A, section A.3.5, this leads to an attenuation coefficient $\alpha(\omega)$ which is almost linear dependent on frequency ω (see Equation (A.50)). This means that the high frequencies in a signal get attenuated much faster than the low frequencies. This leads to a decrease of the bandwidth through time, or an increase of the dominant wavelength $\lambda_t(t)$ through time.

A similar iteration scheme as in Equation (2.34) is used for a non-constant wavelength $\lambda_t(t)$, only the depth-to-time conversion is updated in every iteration step. The scheme becomes:

$$\sigma_z^{(i)}(z) = \frac{\lambda_t(\check{\Delta}t^{(i-1)}(z))}{5} \check{c}_P(\sigma_z^{(i-1)}(z), z), \quad (2.35)$$

with:

$$\check{\Delta}t^{(i-1)}(z) = 2 \int_0^z \frac{1}{\check{c}_P(\sigma_z^{(i-1)}(z'), z')} dz', \quad (2.36)$$

the depth-to-time conversion.

The convergence of this version of the iteration scheme was also always observed.

In next section this procedure will be applied on the Saga-well.

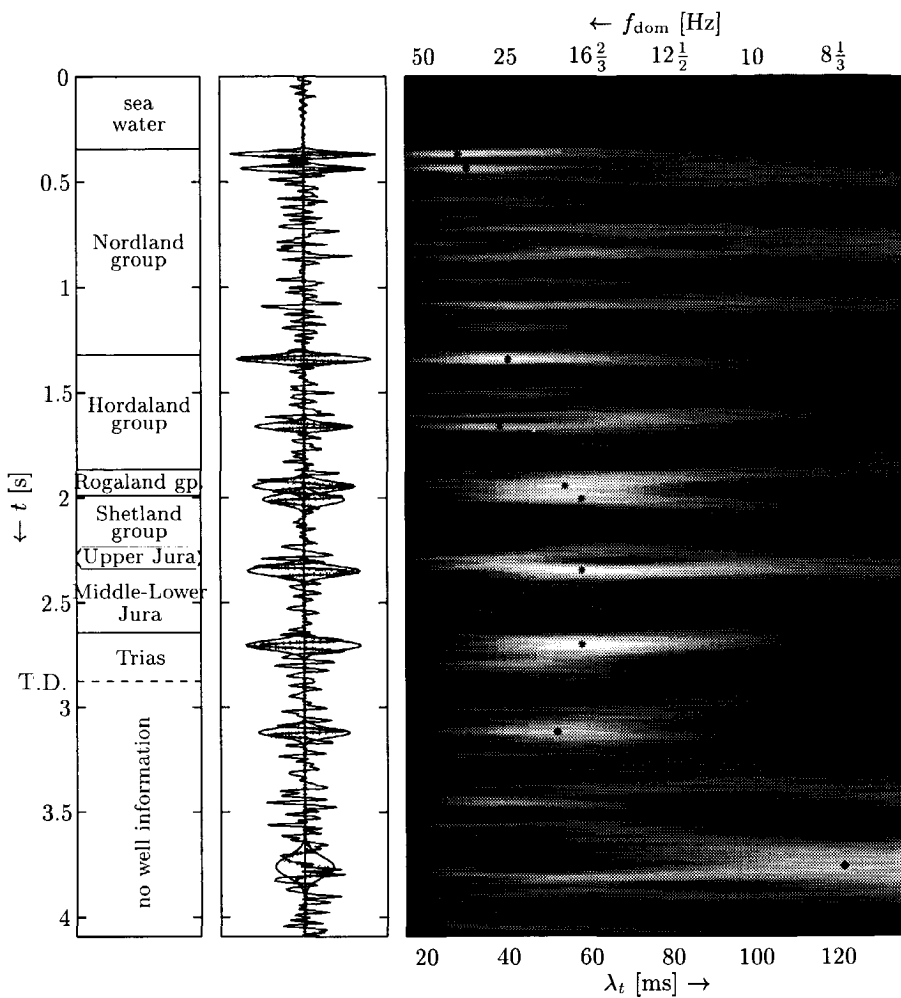


Fig. 2.13 The dominant wavelength λ_t for the seismic trace at the Saga-well. Matching pursuit is used (Mallat, 1999) (see on page 91 in Chapter 4 for a description). The middle panel shows the seismic trace. The panel on the left-hand side is $|\varsigma(\tau, \lambda_t)|$ for the original seismic trace. Iteratively, the best matching wavelet is selected (indicated by “*”). The residue after subtracting the wavelet from the seismic trace is used for calculating a new $|\varsigma(\tau, \lambda_t)|$, from which the next best matching wavelet is selected. This procedure was iterated until 10 wavelets were extracted. A clear evolution can be seen in the dominant wavelength: for the sea floor reflection is $\lambda_t = 28$ ms ($f_{\text{dom}} = 35.7$ Hz), around the Middle Jurassic reservoir is $\lambda_t = 58$ ms ($f_{\text{dom}} = 17.2$ Hz). “T.D.” indicates the total depth of the Saga-well.

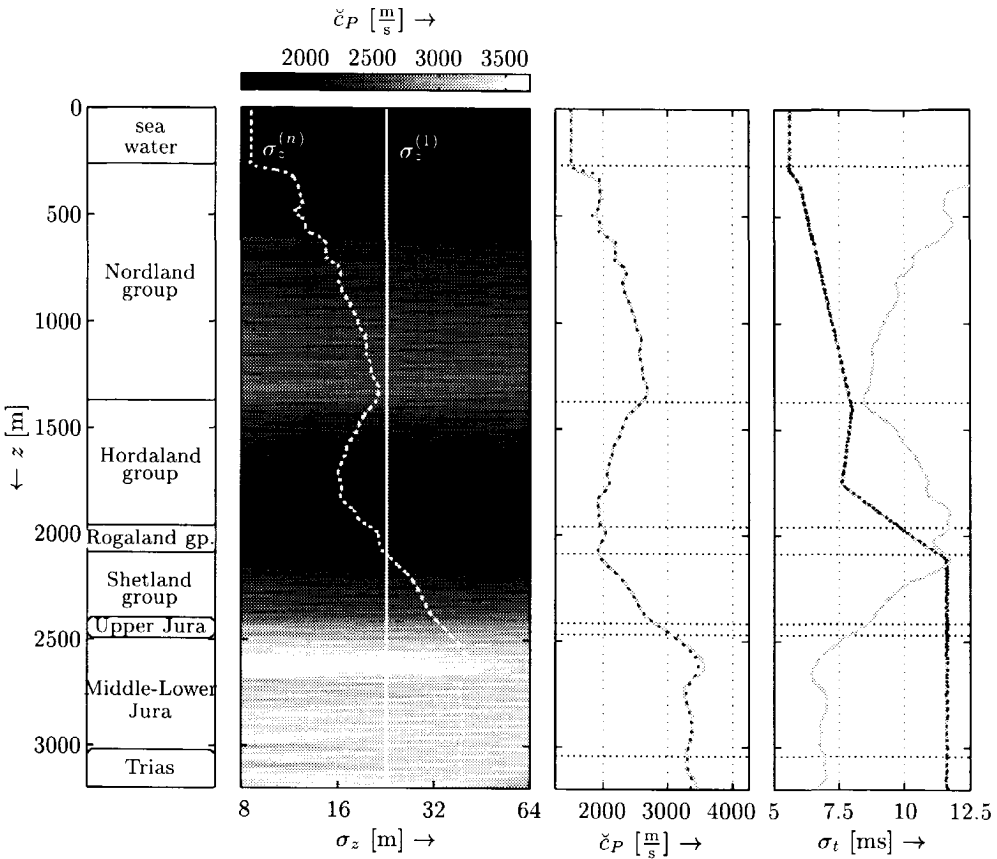


Fig. 2.14 Iteration results for the Saga-well. A constant scale $\sigma_z^{(1)}$ of $16\sqrt{2}$ m was used as starting point. On the second panel counted from the left-hand side, the final selection $\sigma_z^{(n)}$ and $\sigma_z^{(1)}$ are plotted on top of the regularized velocity $\check{c}_P(\sigma_z, z)$ (in grey scale). The third panel shows $\check{c}_P(\sigma_z^{(1)}, z)$ (in grey full line) and $\check{c}_P(\sigma_z^{(n)}, z)$ (in black dashed line). The panel on the right-hand side shows that the desired scale $\frac{\lambda_t}{5}$ and the obtained scale $\sigma_t = \frac{\sigma_z^{(n)}}{\check{c}_P(\sigma_z^{(n)}, z)}$ (in black dashed line) match. Initially there was a large mismatch between the desired scale and the scale obtained from the first iteration (in grey line). λ_t was obtained from the seismic trace, see Figure 2.13.

2.9 Application on the Saga-well

In this section, the procedure as described in previous section will be applied on the Saga-well. The time-dependent dominant wavelength $\lambda_t(t)$ is analysed using a

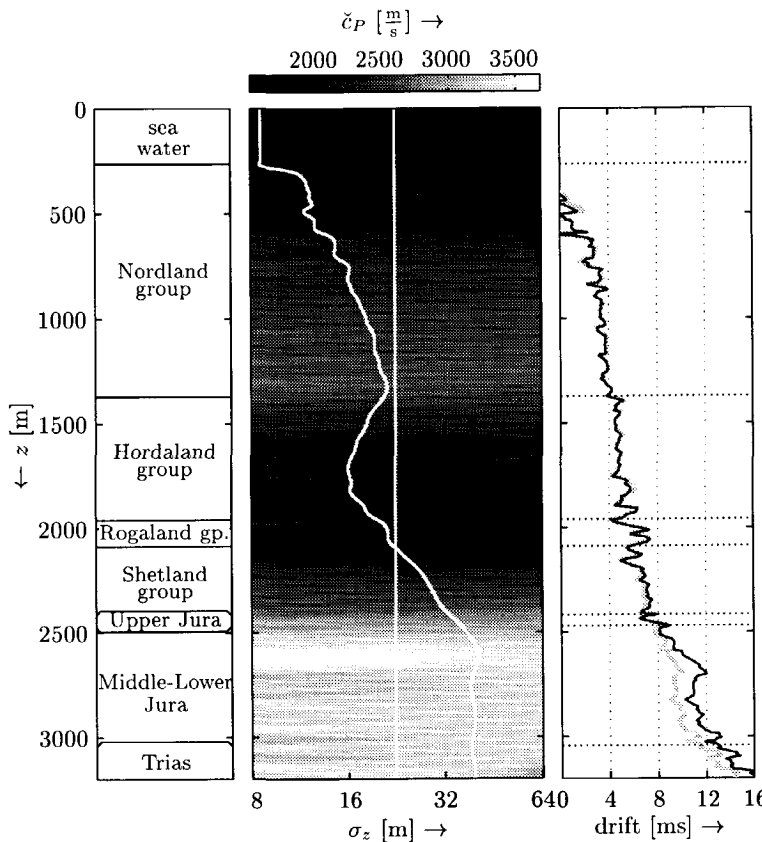


Fig. 2.15 Drift calculated using the first (grey line in right-hand panel) and the final iteration result (black line). Note the large increase around the Fangst Group interval (the reservoir here). On the reservoir interval is the drift increase about 4 ms, or a relative increase of 2 % in traveltime.

matching pursuit method⁷, but also other time-frequency methods could have been used. Another option is to predict the wavelength from an estimate of the quality factor Q for the geological layers.

Figure 2.13 shows the analysis on a seismic trace after Automatic Gain Control (AGC) was applied (AGC-window = 0.5 s). The seismic trace is a stacked result after prestack migration and is located at the Saga-well. The angle-dependent reflectivity

⁷The matching pursuit method will be extensively used in Chapter 4. A full description of the method is given in section 4.3.2 on page 91.

was imaged using the bifocal version of Common Focus Point (CFP) migration as discussed by Berkhou (1997a,b) and van Wijngaarden (1998). The prestack imaging result is subsequently filtered using the Zoeppritz-driven Linear Filtering (ZLF) method as discussed by van Wijngaarden (1998), and finally stacked.

The matching pursuit analysis is performed iteratively to find the 10 best matching atoms. After a best matching atom is found, this atom is subtracted from the signal, and the residue is used for the next iteration. The dominant wavelength $\lambda_t(t)$ derived from the 10 matched atoms is used as a point measurement of the local dominant wavelength λ_t of the seismic signal. For intermediate positions, the 10 local measurements are interpolated.

The result of the iteration for the Saga-well in Figure 2.14 shows that the correct combination of scale σ_z and regularized velocity $\check{c}_P(\sigma_z, z)$ is found in order to obtain the desired $\sigma_t = \frac{\lambda_t}{5}$. Starting from an average initial scale $\sigma_z^{(1)} = 16\sqrt{2}$, it is clear that a large initial mismatch is observed between the desired $\frac{\lambda_t}{5}$, with λ_t analysed on the seismic trace, and $\frac{\sigma_z^{(1)}(z)}{\check{c}_P(\sigma_z^{(1)}(z), z)}$. After 10 iterations, the combination of $\sigma_z^{(n)}(z)$ and $\check{c}_P(\sigma_z^{(n)}(z), z)$ matches the desired $\frac{\lambda_t}{5}$ perfectly⁸. The number of iterations needed is depending on the logarithmic sampling interval $\Delta \ln \frac{\sigma_z}{\sigma_{\text{ref}}}$. Here a very detailed logarithmic sampling interval of $\Delta \ln \frac{\sigma_z}{\sigma_{\text{ref}}} = \frac{1}{80}$ was used. Coarser sampling intervals can reduce the number of iterations to 5 or 6 at the expense of some increased inaccuracy.

Figure 2.15 also presents the drift as calculated for the final iteration result, and compares this with the result at the start of the iteration. An increase in the drift is observed around the reservoir interval.

⁸With a perfect match a difference of less than one sampling interval $\Delta \ln \frac{\sigma_z}{\sigma_{\text{ref}}}$ in the scale direction between $\frac{\sigma_z^{(n)}(z)}{\check{c}_P(\sigma_z^{(n)}(z), z)}$ and $\frac{\lambda_t}{5}$ is meant. The sampling in the scale direction is equidistant in $\log \frac{\sigma_z}{\sigma_{\text{ref}}}$.

2.10 Conclusions

In this chapter a first order correction has been proposed for the effect of fine layering on the propagation of P -waves perpendicular to a 1-D layered medium. Laboratory measurements of first break arrivals from literature were reviewed. From these laboratory measurements, it was found that mainly the fluctuations of the earth properties on scales smaller than one fifth of the dominant wavelength were responsible for the delays. This led to the construction of a simple first order correction on the velocities as published by Sams and Williamson (1994) and Rio et al. (1996). The corrected velocities are found by applying equivalent medium theory type of moving averaging with a window of approximately one fifth of the dominant wavelength. This results in a regularized velocity at a defined scale. Studying this result more closely showed an important dependency of the regularized velocity on the scale it was regularized to. Also traveltimes calculated using these regularized velocities were found to be dependent upon the scale.

A method was designed to regularize the velocities to a scale in accordance to the seismic data. A first step is to analyse the wavelength of the seismic trace in time using a matching pursuit approach. Velocities on the contrary are measured using a well-log in depth. The link between depth and time is the regularized, scale-dependent velocity. An iterative scheme was constructed to derive the mutual dependent scale in depth and the regularized velocity at that scale that together match the desired scale in time. The results for this procedure were checked with numerical modelling experiments. The drift (i.e. the time delay relative to ray theory) calculated from the resulting regularized velocities match well with the modelling results, both in trend as in the numerical values of the effective velocity. Only for very high frequencies a disagreement was observed.

When the medium properties are stationary and only fluctuating at a scale smaller than one fifth of the wavelength, the velocities resulting from this procedure will be equal to the equivalent medium averaged velocity.

The results from this procedure can help in resolving the mismatch often observed in tieing well-logs to the seismic data. Often traveltime discrepancies in the order of a few percents (occasionally up to five to ten percent) are encountered. When using the regularized velocity as described in this chapter, this discrepancy can largely be reduced. Applications that can benefit from this method can be found in seismic modelling and in the inversion of seismic data to acoustic impedance.

The procedure as described here is extended to wave propagation under oblique angles in the following chapter.

Chapter 3

P-wave propagation at an oblique angle

*Anisotropy can have a very important influence on the results of amplitude versus offset analysis. It also affects seismic imaging. Currently the anisotropy parameters are calculated over specific intervals assuming that the medium is stationary¹. Often it is however observed that the medium is non-stationary. When that happens, the anisotropy parameters need to be evaluated with the reference to scale, since their value will become scale dependent. In this chapter a method is proposed to calculate scale dependent anisotropy parameters. Subsequently, these parameters are used to derive a scale dependent *P*-wave velocity at oblique angles for a Vertical Transversely Isotropic medium.*

3.1 Introduction

In the previous chapter, the propagation of *P*-waves perpendicular to the layering of a 1-D layered medium was discussed. In this chapter, the extension to *P*-wave propagation at an oblique angle with 1-D layering is discussed.

First a theoretical description is given. *P*-wave propagation under an oblique angle through a transversely isotropic medium can be described in different ways. In this chapter, the behaviour of a transversely isotropic medium will initially be described starting from Hooke's law assuming a linear elastic medium. Alternatively a description is given using Thomsen anisotropy parameters. The description is made

¹The stationarity meant here is a stationarity of the medium (i.e. earth) properties in depth.

for the general case of an arbitrarily strong anisotropy, and is subsequently simplified for the case of weak anisotropy at a specific scale. Afterwards the Thomsen parameters are evaluated at different scales, and the scale dependency is investigated. Finally the iterative method as developed in Chapter 2 for normal incidence propagation is extended to oblique angles. In this method, the scale dependent Thomsen parameters will be used in the construction of an anisotropic velocity.

The results from this method can be used in different ways. The anisotropic velocities can be used for time-to-depth or depth-to-time conversion of pre-stack data in sophisticated inversion methods or in well-tying. The anisotropic velocities can also be used as a background velocity model for the p -to- α conversion² during pre-stack inversion.

3.2 Theory of elasticity

In general, a linear elastic material³ is defined as a material in which every component of stress σ_{ij} is linearly dependent on every component of strain ϵ_{kl} . This is also known as Hooke's law. For each of the three orthogonal directions, three stress components exist: two shear and one normal stress component (see Figure 3.1). In the same way, nine components exist for the strains (see Figure 3.2 for a brief description of the types of strains). Hooke's law can then be described using nine equations, one for each of the stresses. Each stress is linearly dependent on the nine components of strain. This can be written in the following form⁴ (Aki and Richards, 1980):

$$\sigma_{ij} = \sum_{k=1}^3 \sum_{l=1}^3 c_{ijkl} \epsilon_{kl}, \quad i, j = x, y, z, \quad (3.1)$$

leading to 81 stiffness coefficients c_{ijkl} . As a consequence, the stiffness coefficients c_{ijkl} can also be considered as:

$$c_{ijkl} = \frac{\partial \sigma_{ij}}{\partial \epsilon_{kl}}, \quad i, j, k, l = x, y, z. \quad (3.2)$$

However not all coefficients are independent. Because of the symmetry of stress ($\sigma_{ij} = \sigma_{ji}$), only six of the equations in Equation (3.1) are independent. Because

² p is the ray-parameter and α the angle of incidence of the plane wave at the boundary where the inversion is taking place.

³In Appendix A, anelastic media are described. The combined description of anisotropy and anelasticity is beyond the scope of this thesis and still subject of current research.

⁴Note that $k, l = 1, 2, 3$ in Equation (3.1) stands for $k, l = x, y, z$ respectively.

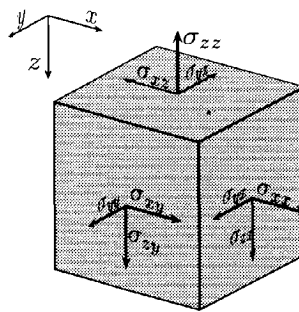


Fig. 3.1 Stresses acting on an infinitesimal block in a solid medium. Note that σ_{ij} with $i = j$ are normal stresses, and that σ_{ij} , with $i \neq j$, are shear stresses. The last subscript j indicates the plane σ_{ij} is acting on, the first subscript i indicates the direction.

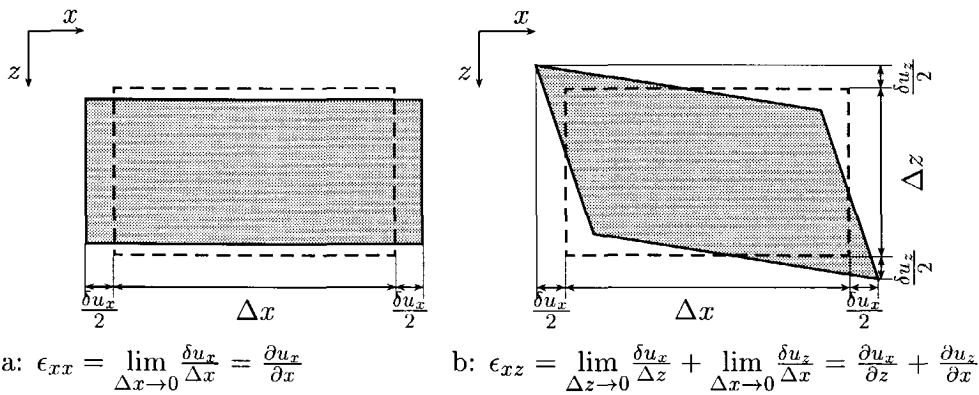


Fig. 3.2 Infinitesimal block after two different types of deformation: (a) tensile strain, ϵ_{xx} , and (b) shear strain, ϵ_{xz} . The initial form of the block is given in dashed line. u_x and u_z are the components of displacement.

of the symmetry of strain ($\epsilon_{ij} = \epsilon_{ji}$), only six terms on the right-hand side of Equation (3.1) are independent. This means that the following relationship exists between the 81 elastic moduli:

$$c_{ijkl} = c_{jikl} = c_{ijlk} = c_{jilk}, \quad (3.3)$$

resulting in 36 independent constants (Mavko et al., 1998). An additional require-

| ij or kl | xx | yy | zz | $zy=yz$ | $zx=xz$ | $xy=yx$ |
|---------------------|------|------|------|---------|---------|---------|
| α or β | 1 | 2 | 3 | 4 | 5 | 6 |

Table 3.1 Recipe for the conversion of subscripts for the elastic constants c_{ijkl} to the Voigt notation $c_{\alpha\beta}$, and for the conversion of stresses σ_{ij} and strains ϵ_{kl} to σ_α and ϵ_β respectively. Note that Equation (3.8) includes a factor 2 in the conversion between the shear stresses: $2\epsilon_{kl} = \epsilon_\beta$, $\beta = 4, 5, 6$.

ment comes when considering the elastic energy density function E , which can be defined in terms of the strain components ϵ_{ij} , such that the stresses σ_{ij} are (Aki and Richards, 1980):

$$\sigma_{ij} = \frac{\partial E}{\partial \epsilon_{ij}}. \quad (3.4)$$

Combined with Hooke's law (Equations (3.1) and (3.2)) this leads to the following condition (Aki and Richards, 1980; Dahlen and Tromp, 1998):

$$c_{ijkl} = c_{kl} \epsilon_{ij}, \quad (3.5)$$

which is a consequence of the equality of the mixed partial derivatives in E :

$$\frac{\partial^2 E}{\partial \epsilon_{kl} \partial \epsilon_{ij}} = \frac{\partial^2 E}{\partial \epsilon_{ij} \partial \epsilon_{kl}}. \quad (3.6)$$

This type of relationship is often encountered in thermodynamics and is known as a Maxwell relation (Dahlen and Tromp, 1998). Equation (3.5) further reduces the number of independent constants to 21. This is the maximum number of elastic constants that a linear medium can have. Materials with a triclinic symmetry are an example of the lowest form of symmetry, thus requiring the full 21 constants (Mavko et al., 1998). Due to the dependencies between the elastic constants, the elasticity can be represented more compactly without loss of generality with a change of indices. The so-called Voigt notation can be used. Table 3.1 gives the recipe for the conversion of the subscripts. Hooke's law as given in Equation (3.1), can be written in the following way using the Voigt notation:

$$\vec{\sigma} = \mathbf{c} \vec{\epsilon}, \quad (3.7)$$

with:

$$\mathbf{c} = \begin{bmatrix} c_{11} & c_{12} & c_{13} & c_{14} & c_{15} & c_{16} \\ c_{12} & c_{22} & c_{23} & c_{24} & c_{25} & c_{26} \\ c_{13} & c_{23} & c_{33} & c_{34} & c_{35} & c_{36} \\ c_{14} & c_{24} & c_{34} & c_{44} & c_{45} & c_{46} \\ c_{15} & c_{25} & c_{35} & c_{45} & c_{55} & c_{56} \\ c_{16} & c_{26} & c_{36} & c_{46} & c_{56} & c_{66} \end{bmatrix}, \quad \vec{\sigma} = \begin{bmatrix} \sigma_{xx} \\ \sigma_{yy} \\ \sigma_{zz} \\ \sigma_{yz} \\ \sigma_{xz} \\ \sigma_{xy} \end{bmatrix} = \begin{bmatrix} \sigma_1 \\ \sigma_2 \\ \sigma_3 \\ \sigma_4 \\ \sigma_5 \\ \sigma_6 \end{bmatrix} \quad \text{and} \quad \vec{\epsilon} = \begin{bmatrix} \epsilon_{xx} \\ \epsilon_{yy} \\ \epsilon_{zz} \\ 2\epsilon_{yz} \\ 2\epsilon_{xz} \\ 2\epsilon_{xy} \end{bmatrix} = \begin{bmatrix} \epsilon_1 \\ \epsilon_2 \\ \epsilon_3 \\ \epsilon_4 \\ \epsilon_5 \\ \epsilon_6 \end{bmatrix}. \quad (3.8)$$

Here \mathbf{c} is called the elastic modulus matrix, which is symmetric and in the most general case is characterized by 21 independent elastic constants. Note the factor 2 for the shear strains, ϵ_β , $\beta = 4, 5, 6$, in $\vec{\epsilon}$. This factor is a consequence of the symmetry of strain. This choice of $\vec{\epsilon}$ will simplify some of the derivations that follow.

Additional conditions imposed by symmetry considerations can greatly reduce this number of independent constants. An isotropic linear elastic material (having the maximum symmetry) is completely characterized using two independent constants c_{11} and c_{44} . The elastic modulus \mathbf{c} becomes:

$$\mathbf{c} = \begin{bmatrix} c_{11} & c_{12} & c_{12} & 0 & 0 & 0 \\ c_{12} & c_{11} & c_{12} & 0 & 0 & 0 \\ c_{12} & c_{12} & c_{11} & 0 & 0 & 0 \\ 0 & 0 & 0 & c_{44} & 0 & 0 \\ 0 & 0 & 0 & 0 & c_{44} & 0 \\ 0 & 0 & 0 & 0 & 0 & c_{44} \end{bmatrix}, \quad \text{with } c_{12} = c_{11} - 2c_{44}. \quad (3.9)$$

The elastic constants can also be written in this isotropic case in terms of the Lamé parameters λ and μ :

$$c_{11} = \lambda + 2\mu, \quad (3.10)$$

$$c_{12} = \lambda, \quad (3.11)$$

$$c_{44} = \mu. \quad (3.12)$$

Another important case is a transverse isotropic medium. When taking the z -axis as the symmetry axis (Vertical Transversely Isotropic, VTI), the elastic modulus matrix becomes:

$$\mathbf{c} = \begin{bmatrix} c_{11} & c_{12} & c_{13} & 0 & 0 & 0 \\ c_{12} & c_{11} & c_{13} & 0 & 0 & 0 \\ c_{13} & c_{13} & c_{33} & 0 & 0 & 0 \\ 0 & 0 & 0 & c_{44} & 0 & 0 \\ 0 & 0 & 0 & 0 & c_{44} & 0 \\ 0 & 0 & 0 & 0 & 0 & c_{66} \end{bmatrix}, \quad \text{with } c_{12} = c_{11} - 2c_{66}, \quad (3.13)$$

and is fully described using 5 independent components. The strength of the anisotropy of the VTI medium is hidden in the constants in Equation (3.13). From comparison with Equation (3.9), it is easy to derive the conditions of isotropy: $c_{11} = c_{33}$, $c_{44} = c_{66}$, and $c_{13} = c_{12}$. This means it is easy to determine from the elastic coefficients $c_{\alpha\beta}$ if a specific material is anisotropic or not. The strength of anisotropy, and its effects on seismic wavefields are not easy to understand from this description. The most common measure of anisotropy used until the mid-1980's, was the contrast between vertical and horizontal velocities. As will be discussed in section 3.4, this measure is not very relevant for most of the conventional forms of exploration geophysics (Thomsen, 1986). In conventional surface reflection geophysics most often the near-vertical *P*-wave data is used.

3.3 Long wavelength limit: anisotropic equivalent medium

As was described in section 2.2.2, the effect of fine layering on the plane-wave propagation normal to the fine layering can be described using effective medium theory. This means that the effects of fine layering at a scale much smaller than the seismic wavelength, can be described by using a homogeneous replacement medium, the equivalent medium. This theory can be extended towards the propagation of waves under oblique angles. This generalisation will be described here.

Since long it is known that fine layering expresses itself on a larger scale as anisotropy (Postma, 1955; Backus, 1962; Berryman, 1979; Helbig, 1994). Even when individual layers are isotropic, the effect on seismic wave propagation at low frequencies is the same as when the layered medium is replaced by a homogeneous, transversely isotropic material. Not only fine layering can give rise to anisotropy. Crampin et al. (1984) have recognized three basic classes in the causes for seismic anisotropy. Aside from the long-wavelength anisotropy class (where the fine layering anisotropy belongs to), he has a class for inherent or intrinsic anisotropy and a class of crack-induced anisotropy. A solid belongs to the inherent / intrinsic anisotropy class when the medium is homogeneously and continuously anisotropic down to the smallest particle size. This class includes among others crystalline anisotropy (for instance made up by preferential oriented anisotropic minerals) and direct stress-induced anisotropy. The crack-induced anisotropy class is for otherwise isotropic solids containing a distribution of inclusions (such as cracks or pores) which have a preferred orientation.

Backus (1962) derived the elastic coefficients for the equivalent medium, con-

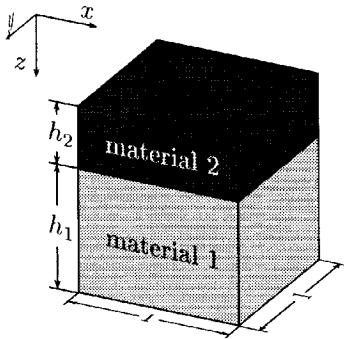


Fig. 3.3 A unit block virtually cut from the periodically layered medium. The medium is made up of two materials. The dimensions of the block are one length unit in the x and y -dimension, and one period of the layering ($h_1 + h_2$) in the z -direction.

sidering a representative block with unit cross section, extending in the z -direction over one period of a periodically layered medium (Figure 3.3). The appropriate boundary conditions must be applied, i.e. when the original medium was infinitely extended in the x - and/or y -dimensions, the strains along that dimension need to be set to zero. We follow here the description in Helbig (1994). We assume the fine layering consists only of two constituents, with thicknesses h_1 and h_2 respectively. This is not a necessary assumption, but made only to keep the derivation compact.

This derivation is done in the long-wavelength limit, i.e. we assume that the wavelength is much larger than $h_1 + h_2$. In fact, when the wavelength is sufficiently large, we can imagine that at any specific moment in time, it will become like a static loading. This is because towards this limit, the accelerations (and the resulting inertial forces) will become small. Due to the balance of forces, stresses acting on a common cross section must be constant through the block, regardless whether the block is considered consisting of fine layers or of the homogeneous replacement medium. This leads to the following conditions for the stresses acting on a plane perpendicular to the z -axis:

$$\sigma_3^{(1)} = \sigma_3^{(2)} = \sigma_{3e}, \quad (3.14)$$

$$\sigma_4^{(1)} = \sigma_4^{(2)} = \sigma_{4e}, \quad (3.15)$$

$$\sigma_5^{(1)} = \sigma_5^{(2)} = \sigma_{5e}, \quad (3.16)$$

with the superscripts (1) and (2) referring to the two materials, and the subscript “e”

to the equivalent medium. For the stresses acting on the planes perpendicular to the x - or y -direction, but only the ones pointing in the x - or y -direction, the equality of forces acting on the finely layered medium and those acting on the equivalent medium leads to the following equations:

$$h_1\sigma_1^{(1)} + h_2\sigma_1^{(2)} = (h_1 + h_2)\sigma_{1e}, \quad (3.17)$$

$$h_1\sigma_2^{(1)} + h_2\sigma_2^{(2)} = (h_1 + h_2)\sigma_{2e}, \quad (3.18)$$

$$h_1\sigma_6^{(1)} + h_2\sigma_6^{(2)} = (h_1 + h_2)\sigma_{6e}. \quad (3.19)$$

Continuity of displacements requires that all strains not involving a displacement or a derivative in the z -direction, must be constant:

$$\epsilon_1^{(1)} = \epsilon_1^{(2)} = \epsilon_{1e}, \quad (3.20)$$

$$\epsilon_2^{(1)} = \epsilon_2^{(2)} = \epsilon_{2e}, \quad (3.21)$$

$$\epsilon_6^{(1)} = \epsilon_6^{(2)} = \epsilon_{6e}. \quad (3.22)$$

For the displacements along the z -direction, the total displacement for the equivalent medium is equal to the sum of the displacements in the layers:

$$h_1\epsilon_3^{(1)} + h_2\epsilon_3^{(2)} = (h_1 + h_2)\epsilon_{3e}, \quad (3.23)$$

$$h_1\epsilon_4^{(1)} + h_2\epsilon_4^{(2)} = (h_1 + h_2)\epsilon_{4e}, \quad (3.24)$$

$$h_1\epsilon_5^{(1)} + h_2\epsilon_5^{(2)} = (h_1 + h_2)\epsilon_{5e}. \quad (3.25)$$

Bruggeman (1937) and Backus (1962) simplified the derivation drastically by expressing all the variable stress and strain components in terms of the components that were found to remain constant in this setting (see Equations (3.14) - (3.25)):

$$\begin{bmatrix} \sigma_1 \\ \sigma_2 \\ \sigma_3 \\ \epsilon_4 \\ \epsilon_5 \\ \sigma_6 \end{bmatrix} = \begin{bmatrix} c_{11} - \frac{c_{13}^2}{c_{33}} & c_{11} - 2c_{66} - \frac{c_{13}^2}{c_{33}} & \frac{c_{13}}{c_{33}} & 0 & 0 & 0 \\ c_{11} - 2c_{66} - \frac{c_{13}^2}{c_{33}} & c_{11} - \frac{c_{13}}{c_{33}} & \frac{c_{13}}{c_{33}} & 0 & 0 & 0 \\ -\frac{c_{13}}{c_{33}} & -\frac{c_{13}}{c_{33}} & \frac{1}{c_{33}} & 0 & 0 & 0 \\ 0 & 0 & 0 & \frac{1}{c_{44}} & 0 & 0 \\ 0 & 0 & 0 & 0 & \frac{1}{c_{44}} & 0 \\ 0 & 0 & 0 & 0 & 0 & c_{66} \end{bmatrix} \begin{bmatrix} \epsilon_1 \\ \epsilon_2 \\ \sigma_3 \\ \sigma_4 \\ \sigma_5 \\ \epsilon_6 \end{bmatrix}, \quad (3.26)$$

which is called the “pseudo-form” of Hooke’s law. This is fully equivalent with the conventional formulation of Hooke’s law for a VTI-medium (i.e. Equation (3.7), with the elastic modulus matrix from Equation (3.13)).

The elastic energy density function E as defined in Equation (3.4), can also be written as (Aki and Richards, 1980):

$$2E = \vec{\sigma}^T \vec{\epsilon} = \sum_{i=1}^6 \sigma_i \epsilon_i, \\ = \sigma_1 \epsilon_1 + \sigma_2 \epsilon_2 + \sigma_3 \epsilon_3 + \sigma_4 \epsilon_4 + \sigma_5 \epsilon_5 + \sigma_6 \epsilon_6, \quad (3.27)$$

which would read in the “conventional” notation (using σ_{ij} and ϵ_{kl}):

$$2E = \sigma_{xx} \epsilon_{xx} + \sigma_{yy} \epsilon_{yy} + \sigma_{zz} \epsilon_{zz} + 2\sigma_{yz} \epsilon_{yz} + 2\sigma_{xz} \epsilon_{xz} + 2\sigma_{xy} \epsilon_{xy}. \quad (3.28)$$

With the aid of Equation (3.26), E can be expressed in terms of the constant components, obtaining:

$$2E = \left(c_{11} - \frac{c_{13}^2}{c_{33}} \right) (\epsilon_1 + \epsilon_2)^2 + \frac{1}{c_{33}} \sigma_3^2 + \frac{1}{c_{44}} (\sigma_4^2 + \sigma_5^2) + c_{66} (\epsilon_6^2 - 4\epsilon_1 \epsilon_2). \quad (3.29)$$

The elastic energy density for the equivalent medium needs to be the same as the sum of the elastic energy density in the individual layers, and this for every possible value of the constant components. This means that the coefficients for each of the constant components in Equation (3.29) need to be averaged to obtain the equivalent medium component, i.e.:

$$c_{11e} - \frac{c_{13e}^2}{c_{33e}} = \left\langle c_{11} - \frac{c_{13}^2}{c_{33}} \right\rangle, \quad (3.30)$$

$$\frac{1}{c_{33e}} = \left\langle \frac{1}{c_{33}} \right\rangle, \quad (3.31)$$

$$\frac{1}{c_{44e}} = \left\langle \frac{1}{c_{44}} \right\rangle, \quad (3.32)$$

$$c_{66e} = \langle c_{66} \rangle, \quad (3.33)$$

with

$$\langle x \rangle = \frac{\sum_{i=1}^n h_i x_i}{\sum_{i=1}^n h_i}, \text{ with } n = 2, \quad (3.34)$$

the weighted average of property x . We use $n = 2$ since the layered medium is made of only two different materials. The weight is the thickness of the layer, h_i (see Figure 3.3). Note that this implies that the weights h_i are positive.

We saw that a VTI-medium is fully described by 5 independent components (Equation (3.13)). This means that we need a system of five independent equations to be able to derive the components for the equivalent medium. Equations (3.30) to (3.33) only make four relationships. Bruggeman (1937) suggested to use only a part

of the total energy density function E , by removing the elastic energy component related to σ_3 , the normal stress working perpendicular on the layering. This yields an additional relationship, i.e.:

$$\frac{c_{13e}}{c_{33e}} = \left\langle \frac{c_{13}}{c_{33}} \right\rangle. \quad (3.35)$$

Backus (1962) used an alternative method to derive the effective constants for a finely layered medium.

This system of equations can also be replaced by any set of five independent linear combinations, without that the results for the equivalent medium elastic constants will be altered. Backus (1962) suggested a set that is particularly useful:

$$S = \left\langle -\frac{1}{4} \left(c_{11} - \frac{c_{13}^2}{c_{33}} \right) + c_{66} \right\rangle, \quad (3.36)$$

$$T = \frac{1}{2} \left\langle 1 - \frac{c_{13}}{c_{33}} \right\rangle, \quad (3.37)$$

$$R = \left\langle \frac{1}{c_{33}} \right\rangle, \quad (3.38)$$

$$\frac{1}{L} = \left\langle \frac{1}{c_{44}} \right\rangle, \quad (3.39)$$

$$M = \langle c_{66} \rangle. \quad (3.40)$$

The equivalent medium elastic constants can in turn be calculated from these so-called Backus parameters as follows:

$$c_{11e} = \frac{(1 - 2T)^2}{R} + 4(M - S), \quad (3.41)$$

$$c_{13e} = \frac{1 - 2T}{R}, \quad (3.42)$$

$$c_{33e} = \frac{1}{R}, \quad (3.43)$$

$$c_{44e} = L, \quad (3.44)$$

$$c_{66e} = M. \quad (3.45)$$

These five components can be obtained from laboratory measurements. Five independent velocity measurements are needed. Commonly the following measurements are used: $c_P(0^\circ)$, $c_P(90^\circ)$, $c_P(45^\circ)$, $c_{SH}(90^\circ)$ and $c_{SH}(0^\circ)$ (Mavko et al.,

1998). The elastic constants can be derived from the measurements using:

$$c_{11e} = \rho c_P^2(90^\circ), \quad (3.46)$$

$$c_{12e} = c_{11e} - 2\rho c_{SH}^2(90^\circ), \quad (3.47)$$

$$c_{33e} = \rho c_P^2(0^\circ), \quad (3.48)$$

$$c_{44e} = \rho c_{SH}^2(0^\circ), \quad (3.49)$$

$$c_{13e} = -c_{44e} +$$

$$\sqrt{4\rho^2 c_P^4(45^\circ) - 2\rho c_P^2(45^\circ)(c_{11e} + c_{33e} + 2c_{44e}) + (c_{11e} + c_{44e})(c_{33e} + c_{44e})}. \quad (3.50)$$

Note that this method only applies when the layering of the core plug is fine compared to the wavelength of the ultrasonic measurement.

3.3.1 Special case: isotropic individual layers

In the special case when the fine layering is made up of isotropic materials, the reason for the specific choice of the Backus parameters (Equations (3.36) - (3.40)) becomes clear: they lead to a formulation in quantities that can directly be observed in well logs Folstad and Schoenberg (1992):

$$S = \rho_e \frac{c_{Se}^4}{c_{Pe}^2} = \left\langle \rho \frac{c_S^4}{c_P^2} \right\rangle = \left\langle \frac{\mu^2}{\lambda + 2\mu} \right\rangle, \quad (3.51)$$

$$T = \frac{c_{Se}^2}{c_{Pe}^2} = \left\langle \frac{c_S^2}{c_P^2} \right\rangle = \left\langle \frac{\mu}{\lambda + 2\mu} \right\rangle, \quad (3.52)$$

$$R = \frac{1}{\rho_e c_{Pe}^2} = \left\langle \frac{1}{\rho c_P^2} \right\rangle = \left\langle \frac{1}{\lambda + 2\mu} \right\rangle, \quad (3.53)$$

$$\frac{1}{L} = \frac{1}{\rho_e c_{Se}^2} = \left\langle \frac{1}{\rho c_S^2} \right\rangle = \left\langle \frac{1}{\mu} \right\rangle, \quad (3.54)$$

$$M = \rho_e c_{Se}^2 = \langle \rho c_S^2 \rangle = \langle \mu \rangle, \quad (3.55)$$

with λ and μ the Lamé parameters. It is clear that three well-log measurements (c_P , c_S and ρ) are needed to calculate the Backus parameters in this special case. Using Equations (3.41) to (3.45), the five elastic constants of the equivalent VTI medium can be derived. Note that the result from Equation (3.53) is in agreement with the derivation of the equivalent medium for normal incidence in Section 2.2.2.

Note as well that Equations (3.54) and (3.55) are respectively the harmonic and arithmetic average of ρc_S^2 , using the same (positive) weights. The following inequality exists between harmonic and arithmetic averages with positive weights

(Helbig, 1994):

$$\langle x \rangle \geq \frac{1}{\langle \frac{1}{x} \rangle} \xrightarrow{x = \rho c_s^2} c_{66e} \geq c_{44e}, \quad (3.56)$$

known as the “Cauchy-Schwartz-Kolmogorov inequality”. The equality sign holds only when $x_i = \rho_i c_{Si}^2 = x_0, \forall i$. As a consequence of this inequality, it is clear that a material with an anisotropy with $c_{44} \geq c_{66}$ cannot be due to fine layering with isotropic constituents (Helbig, 1994).

More inequalities exist between different parameters. Postma (1955) has shown that in a finely layered medium composed of two isotropic materials, the following inequality holds for an equivalent medium in the long-wavelength limit:

$$(c_{11e} - c_{44e})(c_{33e} - c_{44e}) - (c_{13e} + c_{44e})^2 \geq 0. \quad (3.57)$$

Berryman (1979) and Helbig (1979) have shown that this inequality holds for any horizontally stratified, homogeneous material whose constituents are isotropic. The proof is based on the same “Cauchy-Schwartz-Kolmogorov inequality” (see Berryman (1979) for a derivation).

Backus (1962) found a necessary and sufficient condition for a transversely isotropic material to be dynamically stable, i.e. no deformation $\vec{\epsilon}$ may cause a negative elastic energy density E . This means:

$$2E \geq 0, \forall \vec{\epsilon}. \quad (3.58)$$

Upon substitution of Equation (3.27) for E , this becomes:

$$\vec{\sigma}^T \vec{\epsilon} \geq 0, \forall \vec{\epsilon}, \quad (3.59)$$

and when substituting Equation (3.7) for $\vec{\sigma}^T$, it reads:

$$\vec{\epsilon}^T \mathbf{c}^T \vec{\epsilon} \geq 0, \forall \vec{\epsilon}. \quad (3.60)$$

Because \mathbf{c} is symmetric, its transpose, \mathbf{c}^T , is equal to \mathbf{c} , or:

$$\vec{\epsilon}^T \mathbf{c} \vec{\epsilon} \geq 0, \forall \vec{\epsilon}. \quad (3.61)$$

Equation (3.61) is nothing else than the definition of positive semi-definiteness of the elastic modulus matrix \mathbf{c} (Strang, 1988). There are several equivalent necessary and sufficient conditions for \mathbf{c} to be positive semi-definite. One of these conditions is that

all the principal submatrices⁵ have non-negative determinants (Strang, 1988). This results in the following necessary and sufficient conditions for the elastic constants $c_{\alpha\beta}$ of a dynamically stable transversely isotropic material:

$$c_{33e} \geq 0, \quad (3.62)$$

$$c_{44e} \geq 0, \quad (3.63)$$

$$c_{66e} \geq 0, \quad (3.64)$$

$$c_{12e} + c_{66e} \geq 0, \quad (3.65)$$

$$(c_{12e} + c_{66e})c_{33e} \geq c_{13e}^2. \quad (3.66)$$

From all the above conditions, some additional inequalities can be derived. Combining Equations (3.56) and (3.65) and the relationship $c_{12} = c_{11} - 2c_{66}$ leads to:

$$c_{11e} \geq c_{44e}, \quad (3.67)$$

and comparing Equations (3.57) and (3.67) leads to:

$$c_{33e} \geq c_{44e}. \quad (3.68)$$

3.3.2 Another special case: relationship between c_P and c_S

In the previous section, it was found that the equivalent medium parameters for fine layering due to isotropic layers could be calculated from the three well-log measurements: c_P , ρ and c_S . In reality, often c_S is lacking or its measurement is of bad quality.

Because the Poisson's ratio $\nu = \frac{\lambda}{2(\lambda+\mu)}$ is known to exhibit only small variations around $\frac{1}{3}$ for most of the homogeneous isotropic rocks found in nature, it is often assumed to be constant when c_S is lacking. In general, the Poisson's ratio ν is related to the Lamé parameters in the following way:

$$\mu = \frac{1-2\nu}{2\nu} \lambda, \quad (3.69)$$

Also the relationship between c_S and c_P can be written in the following way using the Poisson's ratio ν :

$$\frac{c_S}{c_P} = \sqrt{\frac{1-2\nu}{2(1-\nu)}}. \quad (3.70)$$

⁵Principal submatrices of a matrix \mathbf{c} are formed by deleting columns and rows together in \mathbf{c} , i.e. when the n -th row is removed, the n -th column is removed as well. Any number of rows and columns may be removed.

When assuming a constant Poisson's ratio, ν , a linear relationship $c_S = ac_P$ occurs. This linear dependence can in turn be used in Equations (3.51) to (3.55) to get the Backus parameters:

$$S = a^4 \langle \rho c_P^2 \rangle, \quad (3.71)$$

$$T = a^2, \quad (3.72)$$

$$R = \left\langle \frac{1}{\rho c_P^2} \right\rangle, \quad (3.73)$$

$$\frac{1}{L} = \frac{1}{a^2} \left\langle \frac{1}{\rho c_P^2} \right\rangle = \frac{R}{a^2}, \quad (3.74)$$

$$M = a^2 \langle \rho c_P^2 \rangle = \frac{S}{a^2}, \quad (3.75)$$

with

$$a = \frac{c_S}{c_P} = \sqrt{\frac{1-2\nu}{2(1-\nu)}}, \quad (3.76)$$

resulting in some dependencies between the elastic constants:

$$c_{33e} = \frac{1}{R}, \quad (3.77)$$

$$c_{66e} = M, \quad (3.78)$$

$$c_{11e} = (1-2a^2)^2 c_{33e} + 4(1-a^2) c_{66e}, \quad (3.79)$$

$$c_{13e} = (1-2a^2) c_{33e}, \quad (3.80)$$

$$c_{44e} = a^2 c_{33e}. \quad (3.81)$$

However, taking into account the argumentation of Thomsen (1990) against the use of the Poisson's ratio in geophysics, and his preference for relationships between c_P and c_S , we can take another route. In Mavko et al. (1998) some empirical relationships between c_P and c_S are presented. A well-known relationship is the so-called "mudrock line" as described by Castagna et al. (1985). This is derived specifically for sandstones and shales and is obtained from in-situ measurements. This relationship reads:

$$c_S = 0.8621 c_P - 1.1724, \quad (3.82)$$

with the velocities in $[\frac{\text{km}}{\text{s}}]$. Another relationship, also derived by Castagna et al. (1993), is a relationship specific for limestones. This reads:

$$c_S = -0.05508 c_P^2 + 1.0168 c_P - 1.0305, \quad (3.83)$$

with again all velocities in $[\frac{\text{km}}{\text{s}}]$.

Using this kind of relationships, often slightly adjusted to fit field or region specific data better, the missing c_S -log can be derived from the c_P -log and a lithological log (to find the areas with the appropriate lithology). Note that this is more than assuming a simple relationship between c_P and c_S , since the relationship used is adjusted for the specific lithology at that location. Afterwards a procedure can be followed as described in Section 3.3.1.

3.4 Thomsen anisotropic parameters

In 1986, Thomsen introduced the so-called Thomsen anisotropic parameters γ , δ and ϵ . These describe the most important aspects of anisotropy. Together with the “isotropic” quantities, the vertical P - and S -wave velocities $c_P(0^\circ)$ and $c_S(0^\circ)$, they describe the VTI-medium. The five independent elastic coefficients from Equation (3.13) can be replaced by the Thomsen parameters in the following way (Thomsen, 1986):

$$\alpha = \sqrt{\frac{c_{33}}{\rho}}, \quad (3.84)$$

$$\beta = \sqrt{\frac{c_{44}}{\rho}}, \quad (3.85)$$

$$\gamma = \frac{c_{66} - c_{44}}{2c_{44}}, \quad (3.86)$$

$$\delta = \frac{(c_{13} + c_{44})^2 - (c_{33} - c_{44})^2}{2c_{33}(c_{33} - c_{44})}, \quad (3.87)$$

$$\epsilon = \frac{c_{11} - c_{33}}{2c_{33}}, \quad (3.88)$$

with ρ the density, α the vertical P -wave velocity $c_P(0^\circ)$, and β the vertical S -wave velocity $c_S(0^\circ)$. The definition of the Thomsen parameters in Equations (3.84) to (3.88) is valid for the general case of arbitrarily strong anisotropy. Note that the subscripts “e” are removed from the elastic constants, because these formulas are valid for any type of VTI-medium, not restricted to an equivalent medium caused by fine layering.

Because the three parameters γ , δ and ϵ go to zero for isotropic media, they are called the anisotropy parameters. In addition the anisotropy parameters are also dimensionless. Therefore they are convenient to characterize the strength of anisotropy (Thomsen, 1986). The parameter ϵ is close to the relative difference between the horizontal and vertical P -wave velocities. This is what often simplistically is used as the “ P -wave anisotropy”. The parameter γ has the same meaning for SH -waves.

The parameter δ is responsible for the near-vertical *P*-wave velocity variations. It is this last parameter that is most important in describing the influence of anisotropy on common reflection data (Thomsen, 1986; Tsvankin, 1996).

Another advantage of the Thomsen notation is that the condition for elliptical anisotropy is very easy: $\epsilon = \delta$. In this case, the *P*-wave slowness surface and the wavefront are elliptical. Note that for transversely isotropic media caused by thin layering of isotropic layers, the inequality $\epsilon > \delta$ holds (Tsvankin, 1996; Berryman, 1979). This inequality can be proven using the inequalities between the elastic modulus constants for this type of material as given in Equations (3.56) - (3.57) and (3.62) - (3.68). For the same type of material, using Equations (3.56) and (3.63) leads to $\gamma > 0$ (Berryman et al., 1997).

Note that for a medium with a constant Poisson's ratio ν (equivalent to a linear relationship $c_S = a c_P$, see section 3.3.2) the Thomsen parameters become:

$$\gamma = \frac{1}{2a^2} (MR - a^2), \quad (3.89)$$

$$\delta = 0, \quad (3.90)$$

$$\epsilon = 2(1 - a^2)(MR - a^2), \quad (3.91)$$

where R and M are defined by Equations (3.73) and (3.75). It is clear that the following dependency exists between ϵ and γ for a medium with a constant Poisson's ratio:

$$\epsilon = 4a^2(1 - a^2)\gamma. \quad (3.92)$$

α and β are also dependent in the following manner:

$$\beta = a\alpha. \quad (3.93)$$

In this study, the focus is on the *P*-wave responses. Only four of the five coefficients are of importance (α , β , δ and ϵ). The γ coefficient only plays a role for *SH*-waves.

3.5 *P*-wave velocities assuming weak anisotropy

Thomsen (1986) described the effects of anisotropy assuming weak anisotropy ($|\epsilon| \ll 1$, $|\delta| \ll 1$, $|\gamma| \ll 1$). Here, the derivation of Tsvankin (1996) is mainly followed.

Unlike Thomsen (1986), Tsvankin (1996) formulates the *P*-wave phase velocity without making an assumption on the strength of the anisotropy. Weak anisotropy (as derived by Thomsen (1986)) is then considered as a special case of the general formulation.

In general, the *P*-wave phase velocity c_ϕ in a VTI medium can be written as a function of the elastic coefficients $c_{\alpha\beta}$ in the following way (White, 1983; Tsvankin, 1996):

$$2\rho c_\phi^2(\theta) = (c_{11} + c_{44}) \sin^2 \theta + (c_{33} + c_{44}) \cos^2 \theta + ((c_{11} - c_{44}) \sin^2 \theta - (c_{33} - c_{44}) \cos^2 \theta)^2 + 4(c_{13} + c_{44})^2 \sin^2 \theta \cos^2 \theta)^{1/2}, \quad (3.94)$$

where θ is the phase angle measured from the symmetry axis. When dividing both sides of Equation (3.94) by the squared *P*-wave velocity perpendicular on the layering, $\alpha^2 = c_P^2(0^\circ)$, and substituting the anisotropic coefficients ϵ and δ as defined in Equations (3.88) and (3.87), we get (Tsvankin, 1996):

$$\frac{c_\phi^2(\theta)}{\alpha^2} = 1 + \epsilon \sin^2 \theta - \frac{f}{2} + \frac{f}{2} \sqrt{1 + \frac{4 \sin^2 \theta}{f} (2\delta \cos^2 \theta - \epsilon \cos 2\theta) + \frac{4\epsilon^2 \sin^4 \theta}{f^2}}, \quad (3.95)$$

where

$$f = 1 - \frac{\beta^2}{\alpha^2} = 1 - \frac{c_{44}}{c_{33}}, \quad (3.96)$$

is the only term containing the *S*-wave vertical velocity β . This equation can be simplified by separating the dependency on the “nonelliptical” term ($\epsilon - \delta$):

$$\frac{c_\phi^2(\theta)}{\alpha^2} = 1 + \epsilon \sin^2 \theta - \frac{f}{2} + \frac{f}{2} \sqrt{\left(1 + \frac{2\epsilon \sin^2 \theta}{f}\right)^2 - \frac{2(\epsilon - \delta) \sin^2 2\theta}{f}}. \quad (3.97)$$

Clearly, for elliptical anisotropy ($\epsilon = \delta$), Equation (3.97) becomes:

$$\frac{c_\phi^2(\theta)}{\alpha^2} = 1 + 2\delta \sin^2 \theta = 1 + 2\epsilon \sin^2 \theta. \quad (3.98)$$

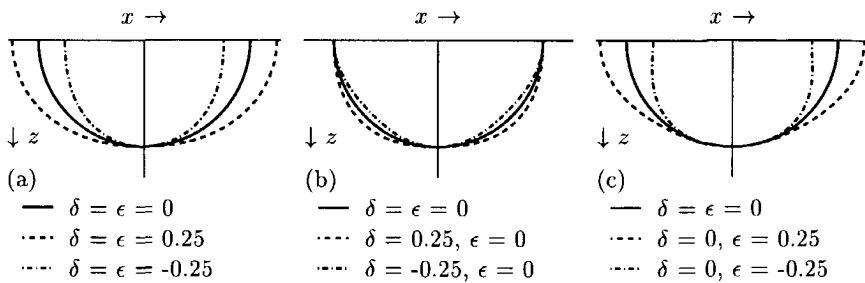


Fig. 3.4 Some wavefronts⁸ for different values of the Thomsen anisotropy parameters δ and ϵ . (a) elliptical anisotropy, (b) near-vertical effect of δ , and (c) large-angle effects of ϵ .

We can expand the radical in Equation (3.97) in a Taylor expansion, and when we assume weak anisotropy ($|\delta| \ll 1$ and $|\epsilon| \ll 1$), terms quadratic in δ and ϵ can be dropped. When doing this, Equation (3.97) becomes:

$$\frac{c_\phi^2(\theta)}{\alpha^2} = 1 + 2\delta \sin^2 \theta + 2(\epsilon - \delta) \sin^4 \theta. \quad (3.99)$$

Taking the square root and linearizing further in δ and ϵ , this leads to:

$$c_\phi(\theta) = \alpha(1 + \delta \sin^2 \theta \cos^2 \theta + \epsilon \sin^4 \theta), \quad (3.100)$$

the weak-anisotropy approximation as derived by Thomsen (1986). From this equation, it is easy to understand the physical meaning of the two anisotropy parameters δ and ϵ . It is clear from both Equation (3.100) and the wavefronts drawn in Figure 3.4 that the parameter δ is more important than ϵ in describing the near-vertical effects of anisotropy. On the other hand, ϵ is the important factor describing the deviation from α towards the large angles.

The group velocity c_g (responsible for energy propagation) can be derived from the phase velocity c_ϕ as follows (Berryman, 1979):

$$c_g = c_\phi \sqrt{1 + \left(\frac{1}{c_\phi} \frac{dc_\phi}{d\theta} \right)^2}. \quad (3.101)$$

⁸The wavefronts are drawn by evaluating the phase velocity c_ϕ at the group angle ψ . As will be explained on the facing page, this is the same as the group velocity c_g when weak anisotropy is assumed.

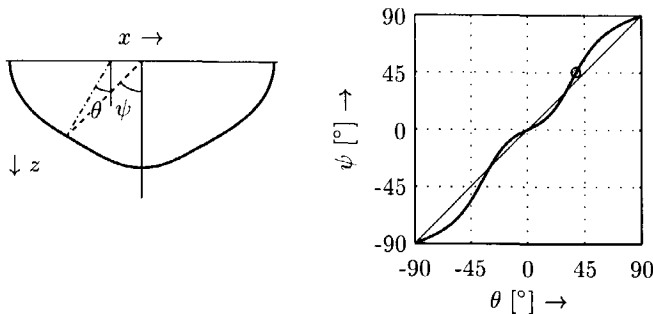


Fig. 3.5 Difference between phase angle θ and group angle ψ for an anisotropic medium ($\delta = -0.25$ and $\epsilon = 0.25$). On the left-hand side, a graphical explanation of the two different angles θ and ψ . On the right-hand side, $\psi(\theta)$ for this specific medium. $\theta = 38.3^\circ$ corresponds to $\psi = 45^\circ$ as indicated on both plots as an example.

The derivative $dc_\phi/d\theta$, linearized in δ and ϵ , can be calculated using Equation (3.100). This results in:

$$\frac{dc_\phi}{d\theta} = \alpha \sin 2\theta (\delta \cos 2\theta + 2\epsilon \sin^2 \theta). \quad (3.102)$$

The series expansion of Equation (3.101) is:

$$c_g = c_\phi \left(1 + \frac{1}{2} \left(\frac{1}{c_\phi} \frac{dc_\phi}{d\theta} \right)^2 + \dots \right). \quad (3.103)$$

Linearizing in δ and ϵ , Equation (3.103) will clearly reduce to $c_g \approx c_\phi$. This means that in the weak anisotropy approximation the group velocity c_g coincides with the phase velocity c_ϕ at the same angle.

We saw that in the weak anisotropy approximation the group velocity c_g and phase velocity c_ϕ are (after linearization in δ and ϵ) approximately the same. However, group velocity should not be evaluated at the phase angle θ , but instead at the group angle ψ . Since the wavefront is non-spherical, the phase angle θ (also called the wavefront-normal angle) is different from the group angle ψ . The group angle ψ is the ray angle from the source point to the wavefront (Figure 3.5). Berryman (1979) relates the group angle ψ to the phase angle θ in the following way:

$$\tan \psi = \frac{\tan \theta + \frac{1}{c_\phi} \frac{dc_\phi}{d\theta}}{1 - \frac{\tan \theta}{c_\phi} \frac{dc_\phi}{d\theta}}. \quad (3.104)$$

When linearizing in δ and ϵ (under the assumption of weak anisotropy), this simplifies to (Thomsen, 1986; Tsvankin, 1996):

$$\tan \psi = \tan \theta [1 + 2\delta + 4(\epsilon - \delta) \sin^2 \theta]. \quad (3.105)$$

It is clear that ψ and θ are different, even with elliptical anisotropy ($\delta = \epsilon$). Note that in the symmetry direction and in the isotropy plane ($\theta = 0^\circ$ and $\theta = 90^\circ$), the phase c_ϕ and group velocities c_g and the angles θ and ψ all coincide.

Note that this is all in the long wavelength or equivalent medium limit. In the next section, we will extend the method described in Chapter 2 towards anisotropic media. Similar as in section 2.6 was done for normal incidence, the small scale variability will be regularized towards a certain scale in depth σ_z . Afterwards a proper combination of scale in depth σ_z and velocity at that scale $\check{c}_P(\sigma_z, z)$ will be iteratively searched for in order to attain the desired scale in time σ_t .

3.6 Thomsen anisotropic parameters at a certain scale

Using the three well-log measurements c_P , c_S and ρ , and assuming isotropic individual layers, the Equations (3.51) to (3.55) can be used to calculate the Backus parameters. Similar to what we have done in Chapter 2, the Backus parameters will be regularized to a certain scale σ_z using a smoothing procedure. The general definition in Equation (2.23) on page 27 is repeated here for convenience:

$$\check{f}(\sigma_z, z) = \frac{1}{\sigma_z} \int_{-\infty}^{+\infty} f(z') e^{-\pi \left(\frac{z'-z}{\sigma_z} \right)^2} dz'. \quad (3.106)$$

As shown in section 3.3, the Backus parameters are the ones that need to be averaged. This leads to:

$$\check{S}(\sigma_z, z) = \frac{1}{\sigma_z} \int_{-\infty}^{+\infty} \rho(z') \frac{c_S^4(z')}{c_P^2(z')} e^{-\pi \left(\frac{z'-z}{\sigma_z} \right)^2} dz', \quad (3.107)$$

$$\check{T}(\sigma_z, z) = \frac{1}{\sigma_z} \int_{-\infty}^{+\infty} \frac{c_S^2(z')}{c_P^2(z')} e^{-\pi \left(\frac{z'-z}{\sigma_z} \right)^2} dz', \quad (3.108)$$

$$\check{R}(\sigma_z, z) = \frac{1}{\sigma_z} \int_{-\infty}^{+\infty} \frac{1}{\rho(z') c_P^2(z')} e^{-\pi \left(\frac{z'-z}{\sigma_z} \right)^2} dz', \quad (3.109)$$

$$\check{L}^{-1}(\sigma_z, z) = \frac{1}{\sigma_z} \int_{-\infty}^{+\infty} \frac{1}{\rho(z') c_S^2(z')} e^{-\pi \left(\frac{z'-z}{\sigma_z} \right)^2} dz', \quad (3.110)$$

$$\check{M}(\sigma_z, z) = \frac{1}{\sigma_z} \int_{-\infty}^{+\infty} \rho(z') c_S^2(z') e^{-\pi \left(\frac{z'-z}{\sigma_z} \right)^2} dz'. \quad (3.111)$$

Note that the accents on the averaged Backus parameters, Equations (3.107) - (3.111), scale are different than the ones used in the definition of the smoothing transformation in Equation (3.106). If we take \check{S} as an example: \check{S} is not the smoothing of $S = \langle \rho c_S^4/c_P^2 \rangle$, but instead \check{S} is the smoothing of $\rho c_S^4/c_P^2$.

These Backus parameters calculated on a certain scale are in turn used in analogy to Equations (3.41) - (3.45) to calculate the elastic parameters at that scale:

$$\check{c}_{11}(\sigma_z, z) = \frac{(1 - 2\check{T})^2}{\check{R}} + 4(\check{M} - \check{S}), \quad (3.112)$$

$$\check{c}_{13}(\sigma_z, z) = \frac{1 - 2\check{T}}{\check{R}}, \quad (3.113)$$

$$\check{c}_{33}(\sigma_z, z) = \frac{1}{\check{R}}, \quad (3.114)$$

$$\check{c}_{44}(\sigma_z, z) = \check{L}, \quad (3.115)$$

$$\check{c}_{66}(\sigma_z, z) = \check{M}. \quad (3.116)$$

These elastic constants can be used to calculate the Thomsen parameters in analogy with Equations (3.84) - (3.88). The Thomsen parameters can be calculated on a certain scale σ_z using:

$$\check{\alpha}(\sigma_z, z) = \sqrt{\frac{\check{c}_{33}}{\check{\rho}}}, \quad (3.117)$$

$$\check{\beta}(\sigma_z, z) = \sqrt{\frac{\check{c}_{44}}{\check{\rho}}}, \quad (3.118)$$

$$\check{\gamma}(\sigma_z, z) = \frac{\check{c}_{66} - \check{c}_{44}}{2\check{c}_{44}}, \quad (3.119)$$

$$\check{\delta}(\sigma_z, z) = \frac{(\check{c}_{13} + \check{c}_{44})^2 - (\check{c}_{33} - \check{c}_{44})^2}{2\check{c}_{33}(\check{c}_{33} - \check{c}_{44})}, \quad (3.120)$$

$$\check{\epsilon}(\sigma_z, z) = \frac{\check{c}_{11} - \check{c}_{33}}{2\check{c}_{33}}. \quad (3.121)$$

Figures 3.6 to 3.8 present the scaling results for the Thomsen parameters as calculated for the Saga data set (see Appendix B for a description⁹). All the parameters are clearly scale dependent. The velocities $\check{\alpha}$ ($= \check{c}_P(0^\circ)$) and $\check{\beta}$ ($= \check{c}_S(0^\circ)$)

⁹Note that c_S was calculated from c_P using the “mudrock” line (Equation (3.82)) in the sandstone and shale intervals and Equation (3.83) for the limestone layers.

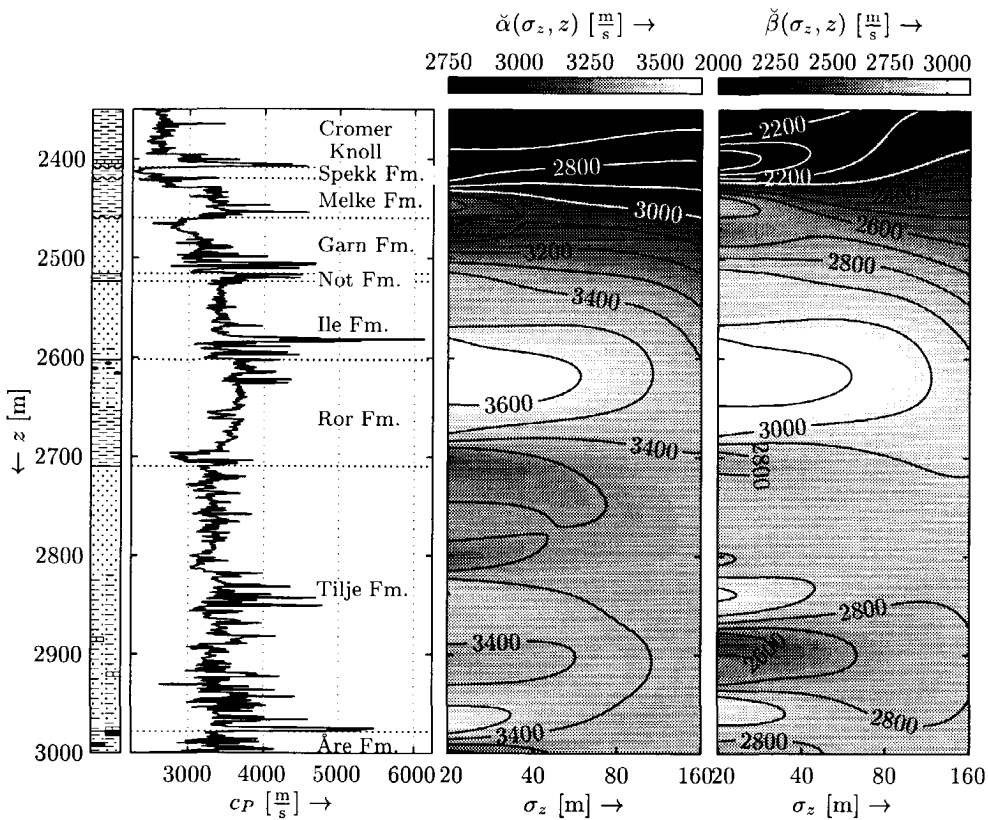


Fig. 3.6 The Thomsen parameters $\check{\alpha}$ and $\check{\beta}$ for a range of scales σ_z for the Saga data set. $\check{\alpha}$ is the scaled P-wave velocity perpendicular to the layering. This is equal to \check{c}_P as defined in Section 2.6. Figure 2.5 on page 29, shows the same results as $\check{\alpha}$, only for a partly different scale range σ_z . $\check{\beta}$ is the S-wave velocity perpendicular to the layering. There is clearly a scale dependency for both $\check{\alpha}$ and $\check{\beta}$. The contour lines drawn in the two panels on the right-hand side should not be mistaken for extrema lines.

show a similar scale behaviour (Figure 3.6). The similarity is expected, since a linear relationship (the so-called “mudrock line” as described in section 3.3.2) was used to construct c_S from c_P in the shale and sandstone intervals. The differences between $\check{\alpha}$ and $\check{\beta}$ are situated around the limestone layers, since at these locations another relationship between c_P and c_S exists (see section 3.3.2).

The anisotropic parameters $\check{\gamma}$, $\check{\delta}$ and $\check{\epsilon}$ (Figures 3.7 and 3.8) clearly honor the

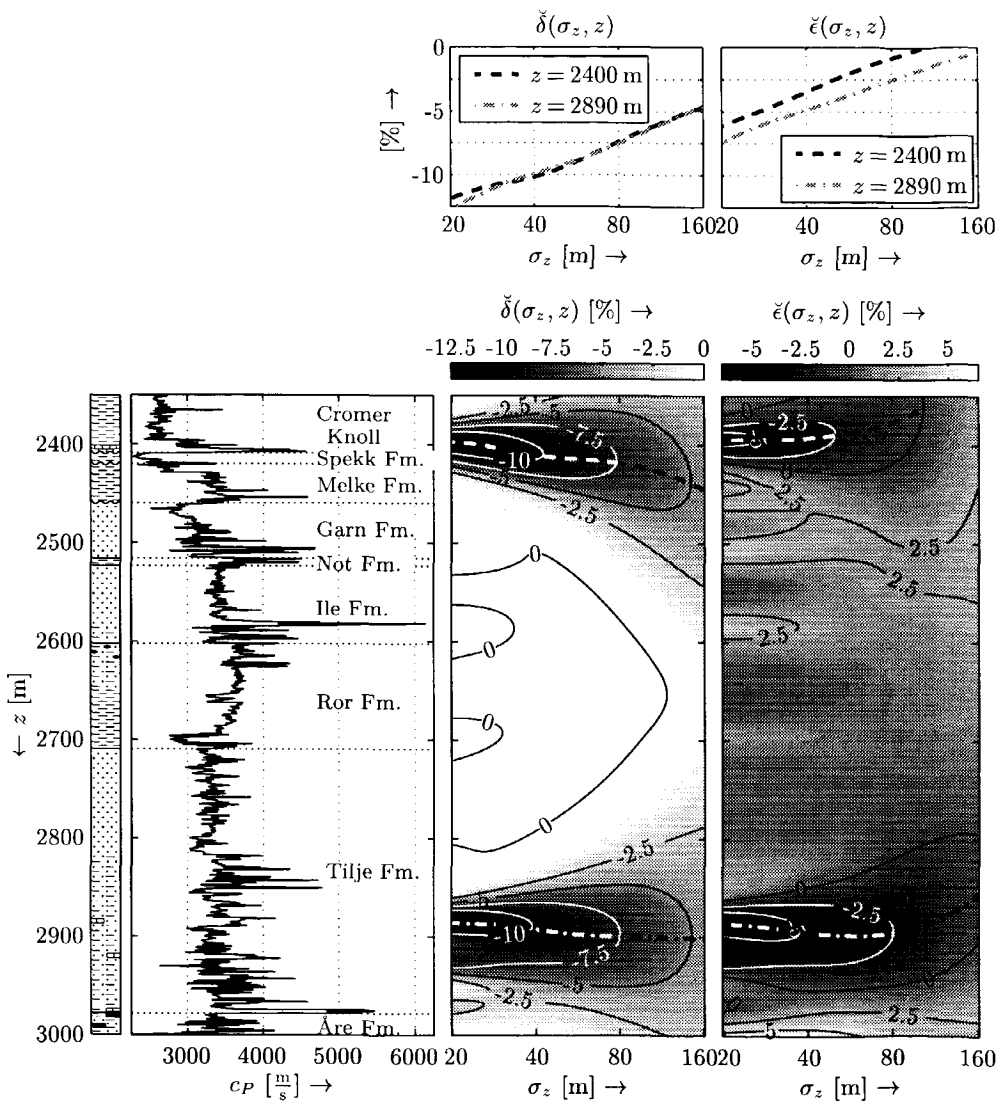


Fig. 3.7 The Thomsen parameter $\check{\delta}$ and $\check{\epsilon}$ for a range of scales σ_z for the Saga data set (with contour lines added). The inequality $\check{\epsilon} > \check{\delta}$ holds as expected. $|\check{\delta}|$ and $|\check{\epsilon}|$ are largest around a limestone layer at the base of the Cromer Knoll Group ($z = [2395 \text{ m}, 2408 \text{ m}]$) and some limestone layers in the Tilje formation (e.g. at $z = [2881 \text{ m}, 2890 \text{ m}]$). For these two events, the values of $\check{\delta}$ and $\check{\epsilon}$ along the modulus maxima lines (see page 34 for a definition) are plotted in the top part of the figure. The scale dependency is clearly more than a second order effect. In the area “far” away from the limestone layers ($z = [2450 \text{ m}, 2850 \text{ m}]$), $\check{\delta}$ is almost zero due to the linear relationship between c_P and c_S (see Equation (3.90)).

assumption of weak anisotropy: the maximum absolute value for any of these parameters in the interval studied is less than 12.5 %. It is also clear that $\epsilon > \delta$ and $\gamma > 0$, as expected for fine layering of anisotropic layers. Note that the Thomsen parameters are clearly scale dependent. Typical values for the scale dependency are around 2.5 % for a doubling of the scale σ_z . This scale dependency is more than just a second order effect; the scale dependency is of the order of the value of the anisotropy parameters in itself.

The Thomsen parameters were also calculated for well A from the Mobil AVO data set. In this well, a high quality c_s log is available. Appendix C gives a brief description of this well. Figure 3.9 shows the results only for the anisotropic parameters important for P -wave propagation, i.e. δ and ϵ . In areas with a good linear correlation between c_P and c_S , the value for δ remains small. For areas with a discrepancy between c_P and c_S , δ shows a clearly higher value. At these locations, δ is also clearly scale dependent. ϵ on the other hand is more or less scale invariant.

Because of the observed scale dependency of the anisotropic parameters, it is worthwhile to extend the iterative search method as described in section 2.8. The method in section 2.8 was developed for normal incidence waves. In next section, the procedure will be extended to waves traveling under oblique angles with the 1-D layering.

3.7 Extended catch-22 problem

In section 2.5.2, some measurements were described for normal wave propagation in a non-stationary medium. From this experiment, we derived an estimate for the transition point between ray theory and equivalent medium theory. This was used to construct a composite method, where the small scale variability is first regularized using a moving averaging technique based on equivalent medium theory, and afterwards ray theory could be applied. The transition point used was σ_z , and was calculated from the seismic wavelength λ_z in the following way:

$$\sigma_z = \frac{\lambda_z}{5}. \quad (3.122)$$

There are no similar laboratory measurements (as were used in the normal incidence case) for establishing the transition point for waves traveling under oblique angles. It is known that the resolution of a plane wave is decreasing with increasing incidence angle. The relationship between both is (Wapenaar et al., 1999, and see

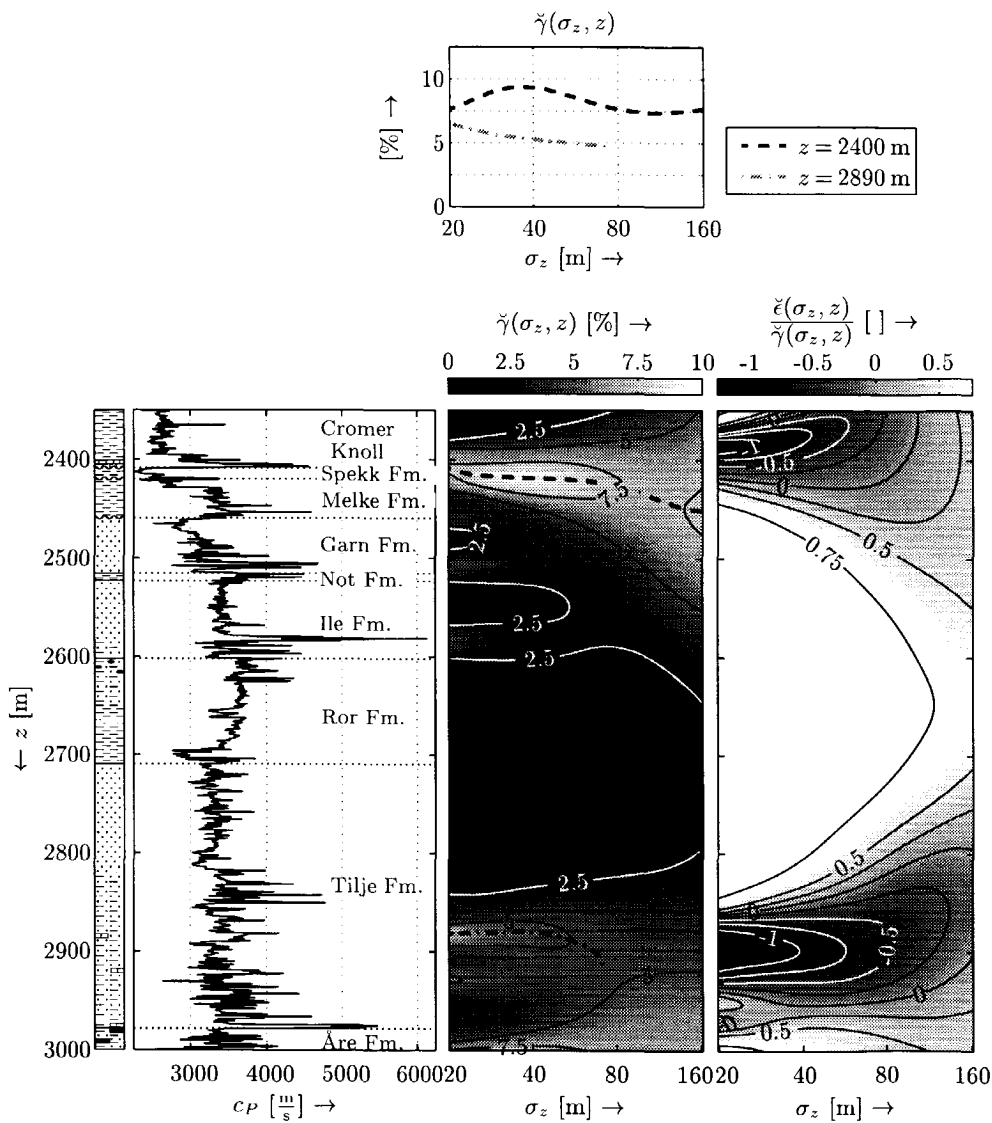


Fig. 3.8 Thomsen parameter $\check{\gamma}$ for the Saga data set. On the right-hand side the ratio between $\check{\epsilon}$ and $\check{\gamma}$. In the area “far” away from the limestone layers ($z = [2450 \text{ m}, 2850 \text{ m}]$), the ratio between $\check{\epsilon}$ and $\check{\gamma}$ is close to 0.76, which is as predicted from Equation (3.92) using the parameters for the “mudrock” line (Equation (3.82)). Note that this area with a constant ratio between $\check{\epsilon}$ and $\check{\gamma}$ is approximately the same area where $\check{\delta}$ is close to zero (see Figure 3.7). In the top part of the figure, the values along the modulus maxima lines for the same events as in Figure 3.7 are plotted.

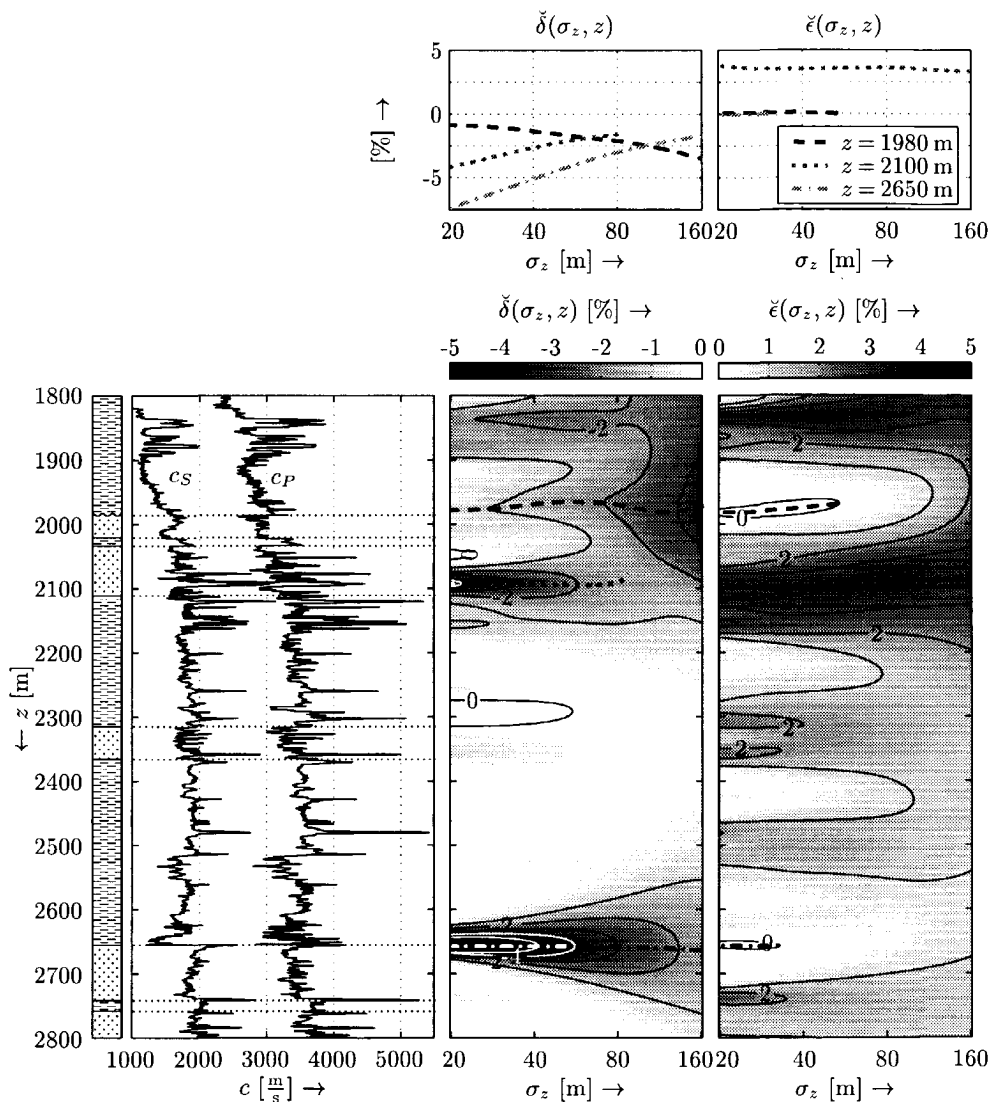


Fig. 3.9 The Thomsen parameters $\check{\delta}$ and $\check{\epsilon}$ for well A of the Mobil AVO data set (see Appendix C for a description). This well has oil and gas bearing sandstones. All well logs were measured (c_P , c_S and ρ). Anisotropy has the same order of magnitude as for the Saga data set. For a relatively large interval, $z = [2150 \text{ m}, 2600 \text{ m}]$, $\check{\delta}$ is almost zero. In this interval, c_P and c_S have a high correlation coefficient of 0.94. There are two locations where $|\check{\delta}|$ shows higher values: around $z = 2100 \text{ m}$, and at about $z = 2650 \text{ m}$. At these locations, the correlation between c_P and c_S is resp. -0.05 and 0.11. $\check{\epsilon}$ shows almost no scale dependency.

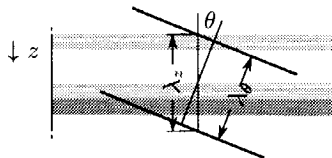


Fig. 3.10 Relationship between the wavelength measured perpendicular on the plane wave λ_θ , and the corresponding vertical wavelength λ_z .

Figure 3.10):

$$\lambda_z = \frac{\lambda_\theta}{\cos \theta}, \quad (3.123)$$

with θ the angle between the normal on the plane wave and the vertical, λ_θ the wavelength measured in depth perpendicular on the plane wave, and λ_z the corresponding vertical wavelength. Combining Equations (3.122) and (3.123) results in:

$$\sigma_z = \frac{\lambda_\theta}{5 \cos \theta}. \quad (3.124)$$

When we want to calculate the velocity at a certain scale for a plane wave with a given ray parameter p , again a catch-22 problem occurs as described in section 2.7 for the normal incidence case. In that section the problem was described of converting the measured seismic wavelength, λ_t , to a wavelength in depth, λ_z . To accomplish this, the unknown scale dependent velocity \check{c}_P is needed:

$$\lambda_z = \lambda_t(\check{t}(\sigma_z, z)) \check{c}_P(\sigma_z, z) = \lambda_t(\check{t}(\sigma_z, z)) \check{c}_P\left(\frac{\lambda_z}{5}, z\right). \quad (3.125)$$

Note that the wavelength in depth, λ_z , appears on both sides of the equation.

In the case of a plane wave travelling under oblique angles, an extra complication occurs. Normally we start from a desired ray parameter p . The angle θ the plane is traveling, is a function of the given ray parameter p , and the unknown velocity \check{c}_P at a certain scale, namely:

$$\check{\theta} = \arcsin(p \check{c}_P). \quad (3.126)$$

This makes that the phase angle $\check{\theta}$ is also scale dependent. Assuming weak anisotropy for simplicity, the velocity \check{c}_P can be calculated (in analogy with Equation (3.100))

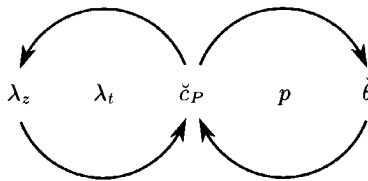


Fig. 3.11 A double catch-22 problem. On the one side the mutual dependence between λ_z and \check{c}_P . On the other side the mutual dependence of $\check{\theta}$ with \check{c}_P .

by:

$$\check{c}_P(\check{\theta}) = \check{\alpha}(1 + \check{\delta} \sin^2 \check{\theta} \cos^2 \check{\theta} + \check{\epsilon} \sin^4 \check{\theta}). \quad (3.127)$$

It is clear that we have an extended catch-22 problem here (Figure 3.11). On the one side the catch-22 problem as we had before in section 2.7. Only this time it is a little more complicated because the phase angle $\check{\theta}$ is found in Equation (3.124). On the other side, a second catch-22 problem occurs between the group angle $\check{\psi}$ and \check{c}_P .

3.8 Solution: extension of iterative method

The extended “catch-22 problem” as described in previous section, is only an extension of the one we had for the normal incidence case (section 2.8). It will be tackled in a similar way as the single “catch-22 problem” in section 2.8: using an iterative method.

First we start with the simplest case: when we want to obtain a constant wavelength in time λ_t . The goal is then to find a combination of λ_z , $\check{\theta}$ and \check{c}_P to attain the following equality:

$$\lambda_t = \frac{\lambda_z \cos \check{\theta}}{\check{c}_P(\check{\theta}, \sigma_z, z)}, \quad (3.128)$$

with σ_z from Equation (3.124), $\check{\theta}$ from Equation (3.126) and \check{c}_P from Equation (3.127).

An iterative procedure is used. For a given rayparameter p , the procedure starts by assuming an initial scale in depth $\sigma_z^{(1)}$ and an initial phase angle $\theta^{(1)} =$

$\arcsin \left[p \check{c}_P(0, \sigma_z^{(1)}, z) \right]$. For the i^{th} iteration, the scale is updated using the scale obtained from the $(i-1)^{\text{th}}$ iteration:

$$\sigma_z^{(i)}(z) = \frac{1}{5} \frac{\lambda_t}{\cos \check{\theta}^{(i-1)}} \check{c}_P(\check{\theta}^{(i-1)}, \sigma_z^{(i-1)}, z), \quad (3.129)$$

with the velocity $\check{c}_P(\check{\theta}^{(i-1)}, \sigma_z^{(i-1)}, z)$:

$$\check{c}_P(\check{\theta}^{(i-1)}, \sigma_z^{(i-1)}, z) = \check{\alpha}^{(i-1)} \left[1 + \check{\delta}^{(i-1)} \sin^2 \check{\theta}^{(i-1)} \cos^2 \check{\theta}^{(i-1)} + \check{\epsilon}^{(i-1)} \sin^4 \check{\theta}^{(i-1)} \right], \quad (3.130)$$

with $\check{\alpha}^{(i-1)}$ short for $\check{\alpha}(\sigma_z^{(i-1)}, z)$, and similarly for the other Thomsen parameters δ and ϵ , and with $\check{\theta}^{(i-1)}$ short for $\check{\theta}^{(i-1)}(\sigma_z^{(i-1)}, z)$. The phase angle θ is also updated:

$$\check{\theta}^{(i)}(z) = \arcsin \left[p \check{c}_P \left(\check{\theta}^{(i-1)}, \sigma_z^{(i-1)}, z \right) \right]. \quad (3.131)$$

When the wavelength in time λ_t is constant, no iterative time-to-depth transformation $z^{(i)}(t)$ needs to be used for the transformation of $\lambda_t(t)$ to $\lambda_t(z)$. When the wavelength in time λ_t is not constant, the time-to-depth conversion needs to be updated after every iteration step, using the latest $\check{c}_P(\check{\theta}^{(i-1)}, \sigma_z^{(i-1)}, z)$.

The convergence of the iteration scheme was always observed, and tests so far showed no dependence of the final convergence result on the choice of the initial scale. Even close to critical angle the procedure was stable. Probably the fact that $\sigma_z^{(i)}(z) \rightarrow \infty$ at critical angle is beneficial in this respect.

3.9 Application on the Saga-well

The iterative procedure described in previous section is applied to the Saga data-set. Using the analysed wavelength $\lambda_t(t)$ for the Saga data-set (Figure 2.13 on page 40), the iterative procedure can be started. The Thomsen anisotropic parameters at a certain scale as calculated in section 3.6 are used as an input.

Figure 3.12 shows the results around the reservoir zone in the Saga-well. It is clear that the velocities are changing with dip. For instance around the transition from Ile to Ror Formation (at $z = 2602$ m), the velocity is clearly changing from $3500 \frac{\text{m}}{\text{s}}$ to $3300 \frac{\text{m}}{\text{s}}$. These changes in velocity are partly caused by the effect of anisotropy, and partly due to the scale dependency of the parameters. In Figure 3.13 the effect of both factors is investigated. The results from the method here described are compared with the results when the Thomsen parameters are calculated over a

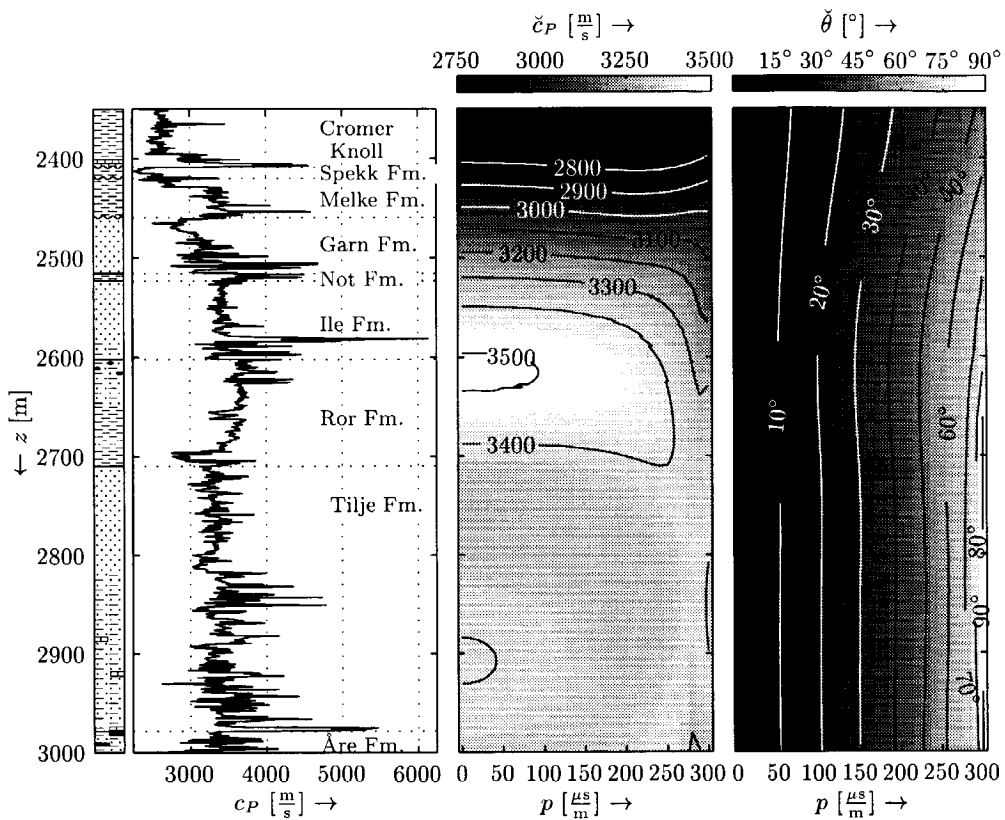


Fig. 3.12 A detailed look on the reservoir zone. Velocity is clearly changing with ray-parameter p .

fixed interval (not scale dependent). The intervals are taken as Upper Jurassic ($z = [2408 \text{ m}, 2460 \text{ m}]$), Mid Jurassic ($z = [2460 \text{ m}, 2710 \text{ m}]$) and Lower Jurassic ($z = [2710 \text{ m}, 2978 \text{ m}]$). A comparison shows large differences between the velocities calculated using the Thomsen parameters obtained for the respective interval and the Thomsen parameters obtained using the method proposed here. This difference is also related to the important scale dependency of the Thomsen parameters as discussed in section 3.6. The Thomsen parameters calculated over an interval can be considered as being calculated on a large scale, almost the long wavelength limit or effective medium theory, as discussed for the P -wave velocity normal to the layering (section 2.2.2).

The results for the Saga-well were also validated using numerical modelling.

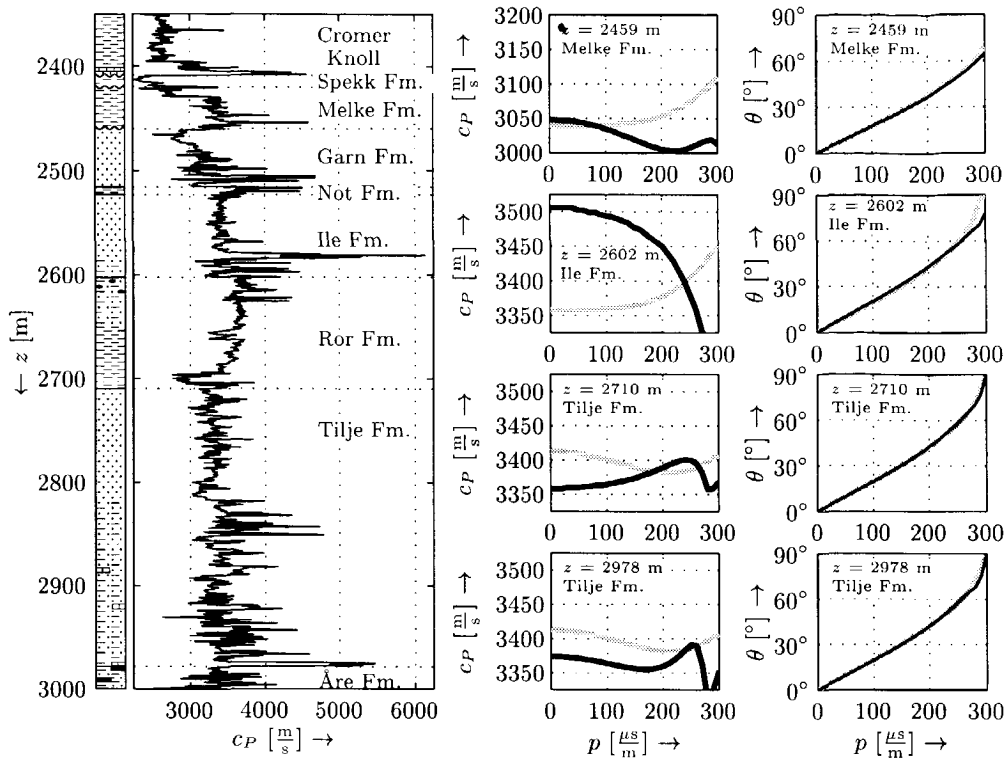


Fig. 3.13 A comparison between using equivalent average properties calculated over a fixed interval (results are in grey line) and scaling averaged properties (in black line). The first is the conventional way, the second is the method described here. For four locations, the results for the anisotropic velocities are compared. Note the additional effect of the scale dependence of the anisotropic parameters. These are in the same order of magnitude as the effect of anisotropy. Also the corresponding angles θ are drawn for the four locations. There is a deviation between both angles, which is most obvious near critical angle. These differences may have an important effect in inversion (see text).

A plane wave Vertical Seismic Profile (VSP) was modelled in this piece of well-log, using an acoustic, flux-normalized reflectivity method for oblique propagation (Kennett, 1983). The results were subsequently convolved using a Ricker wavelet with a dominant frequency f_{dom} of 17.2 Hz, as observed from the seismic trace at the reservoir interval. Subsequently, the drift was calculated for the peak of the envelope, i.e. the drift associated with the group velocity c_g . Because the “raw”

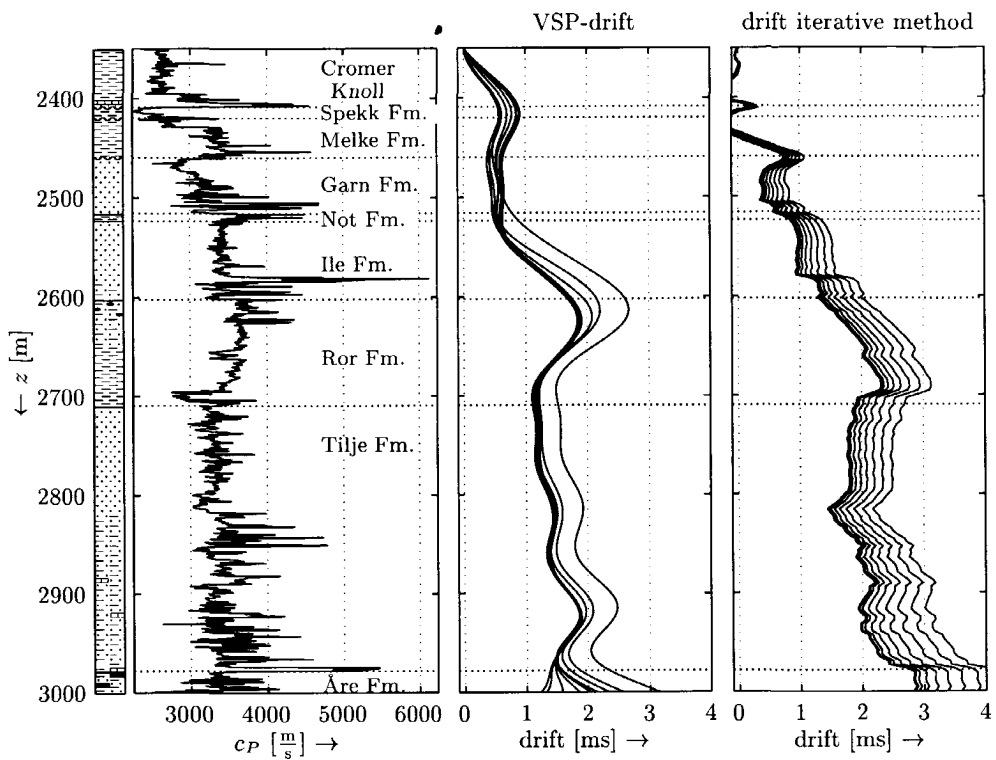


Fig. 3.14 A comparison of the drift calculated from the iterative procedure (right-hand side) and from numerical modelling (in the middle). The synthetic plane wave Vertical Seismic Profile (VSP) was modelled using an acoustic, flux-normalized reflectivity method. The peak of the envelope was picked, and the associated drift was calculated. Subsequently the result was smoothed. The results are presented for ray parameter values $p = 0, 20, \dots, 160 \frac{\mu s}{m}$. Results for both methods compare favourable.

drift obtained from the VSP is heavily fluctuating due to interference effects with reflected wavelets, a smoothing needed to be performed in order to be able to highlight the trends. Figure 3.14 compares the results for this smoothed VSP-drift with the drift obtained from the iterative method. The comparison is done below critical angle ($p < 162.6 \frac{\mu s}{m}$). The drift for both methods compare well. The points of sudden increase are at about the same position, and the increase of drift with increasing angles is also of the same magnitude. Only the drift calculated from the approximate method are about 25 % higher than the (smoothed) results for the numerical modelling.

3.10 Influence of background velocity on inversion results

A study from van Wijngaarden (1998) on the same well-log shows that the background velocity is an important factor in the inversion. Relative small differences in this velocity can have a large effect on the inversion results. Figure 3.15 shows the Reflection Coefficient (RC) gather derived using the bifocal imaging approach (van Wijngaarden, 1998). A RC gather contains the rayparameter p dependent reflectivity, which is related to the angle dependent reflection information. The link between angle and rayparameter p is the background velocity: $\bar{\alpha} = \arcsin(\bar{c}_P \times p)$.

The amplitude versus rayparameter p information contained in the RC gather can be used to estimate the contrast parameters. The type of velocity used as background velocity plays an important role. Table 3.2 shows the results for the contrast parameters when the anisotropic velocity calculated as an equivalent average is used. These results can be compared with the results when the scaling averaged velocity is used. There are clearly differences. The differences observed for the acoustic impedance contrast $\frac{\Delta Z}{Z}$ is almost zero, which is expected because the impedance contrast is not depending on \bar{c}_P . This is also in agreement with the results from van Wijngaarden (1998). The other two contrasts, P -velocity c_P and shear modulus μ , are both clearly dependent on the background velocity \bar{c}_P .

| depth | equivalent averaged velocity | | | scaling averaged velocity | | |
|--------|------------------------------|--------------------------------|--------------------------------|---------------------------|--------------------------------|--------------------------------|
| | $\frac{\Delta Z}{Z}$ | $\frac{\Delta c_P}{\bar{c}_P}$ | $\frac{\Delta \mu}{\bar{\mu}}$ | $\frac{\Delta Z}{Z}$ | $\frac{\Delta c_P}{\bar{c}_P}$ | $\frac{\Delta \mu}{\bar{\mu}}$ |
| 2459 m | 0.0276 | 0.2464 | 0.0614 | 0.0278 | 0.2869 | 0.0803 |
| 2602 m | -0.0280 | 0.2792 | 0.1545 | -0.0279 | 0.2881 | 0.1588 |
| 2710 m | -0.0409 | -0.1179 | -0.1006 | -0.0409 | -0.1194 | -0.1016 |
| 2978 m | -0.0075 | 0.1683 | 0.0993 | -0.0075 | 0.1739 | 0.1016 |

Table 3.2 Difference in contrast parameters when using the conventional background velocity and the scaling velocity. Note that the inversion results are only meant to indicate the influence of the background velocity.

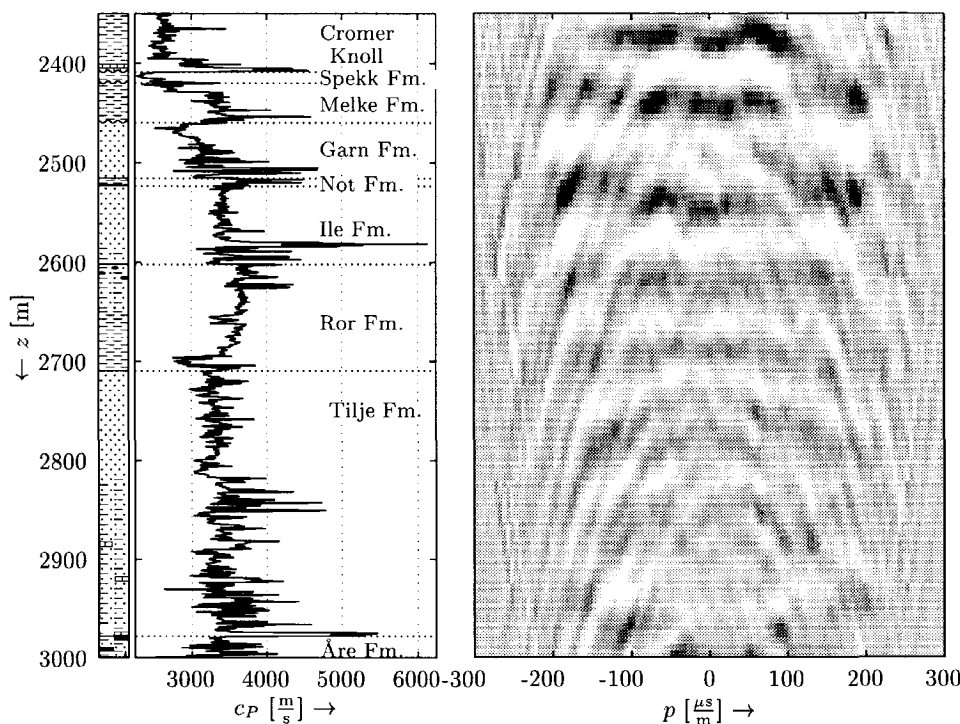


Fig. 3.15 A reflection coefficient (RC) gather derived using the bifocal imaging method (van Wijngaarden, 1998).

3.11 Conclusions

In this chapter the iterative method as developed in Chapter 2 has been extended to plane waves travelling under oblique angles. The anisotropy caused by fine layering on P -wave propagation under oblique angles is described. The Thomsen anisotropy parameters were discussed. It was found that for non-stationary media the Thomsen parameters become scale dependent. A variation of the Thomsen parameters across the scales in the order of 100 % was found. Due to this fact, the iterative procedure as established in Chapter 2 was extended to include propagation under oblique angles. The result of this iterative procedure is regularized anisotropic velocity at a defined scale for plane waves travelling under oblique angles. This regularized velocity is a first order correction for the effect of non-stationary fine layering on the propagation of P -waves. The results of this procedure were compared with numerical modelling results, and the comparison was favourable.

The results may be used as a background model in a pre-stack inversion method. Due to the non-linear effect of the background model on the inversion result, a large difference is found between the inversion results based on a conventional equivalent average velocity and the regularized velocity as found using the method described in this chapter.



Chapter 4

Characterizing local wavelet shapes using Gabor-atoms

A methodology to extract local wavelet attributes from 3D migrated data-volumes for reservoir geophysical and engineering applications is presented. The method is based on characterizing the local wavelet shape by fitting Gabor-atoms. First, the method is checked on typical synthetic petrophysical log-signatures. Afterwards, the results are confirmed on real data examples. The method described here is more flexible than taking plain seiscrops and uses more than just the amplitude information. Unlike most other types of attributes, a priori information is used by assuming a range of wavelet shapes and wavelengths. Whenever these assumptions on wavelet shapes and wavelengths hold, this method is less sensitive to noise than the well-known instantaneous or response attributes. In some cases the method is able to differentiate between different facies types on the basis of the attributes.

4.1 Introduction

In Herrmann (1997); Dessim (1997) the characterization of the seismic response of asymmetrical acoustic impedance singularities was described. Asymmetrical log-shapes are also of key importance in the geological interpretation of well-log data. Log-shapes are commonly compared with schematical signatures that are representative for specific sediments. From a seismic modelling study, it was noticed that these asymmetrical log-shapes have a direct influence on the shape of the seismic wavelet. In this chapter a robust methodology is developed to determine the type of geological structure through the phase attribute extracted from seismic data. Afterwards the method is tested on two 3-D data-sets with increasing complexity.

4.2 Geological sequences at layer scale

4.2.1 Petrophysical interpretation at layer scale

In Chapter 2, the existence and importance of heterogeneities at different scales were discussed. Detailed knowledge of the heterogeneities at layer scale becomes more important at the reservoir management stage¹. Knowledge of spatial distribution and connectivity of e.g. channels are important throughout the full reservoir life, but the importance increases even more at this stage.

At the layer scale (a scale with a thickness between 5 and 50 meter, see Figure 1.2 and Table 1.1 on page 6), different geological entities can be subdivided by their depositional environment (e.g. river channel, levee, marsh, crevasse splay, mouth bar, etc.). These subdivisions are called facies. Each facies has its own characteristic internal evolution of the energy of deposition and type of lower and upper boundary. This signature is often very well captured by the gamma-ray log (Emery and Myers, 1996). A higher gamma-ray log reading indicates a higher amount of fine minerals (e.g. clay). A clean, coarse grained (i.e. clay poor) sandstone very often shows a small gamma-ray log reading.

The internal evolution within a facies can be a fining upward² or a coarsening upward³ sequence (Figure 4.1 after Emery and Myers, 1996). The former is typical for channel fills, where a new river channel is incised into earlier sediments, only allowing coarse material to settle. After this high energetic regime, the channel breaks through its natural levees. Once that happens, the flow through the channel is lowered considerably, lowering the energy in the system. Depending on the situation, a considerable amount of gradually finer material can be deposited, resulting in a bell shape. In other situations the old river bed is directly filled with clay particles, the so-called clay plug, resulting in an abrupt transition. The resulting log shape has then typically a blocky shape. A blocky shape may also occur due to erosion; the top part of a bell shape may be removed, leaving a blocky shape.

The latter (coarsening upward sequences) are typical for offlap deposits. These are systems that prograde into a low energy environment. The lowermost sediments reflect a low energetic depositional environment and progressively higher energetic sediments are deposited as the facies moves further into the low energetic environ-

¹Terminology for the stages in reservoir life is taken from Richardson and Sneider (1992).

²A fining upward sequence is also sometimes called a dirtying upward sequence. This is because a fining upward sequence may start as a coarse-grained (“clean”) sandstone at the bottom of the layer and evolves towards a sandstone containing more clays (“dirt”) or a sandy clay in the top part.

³Also known as a cleaning upward sequence.

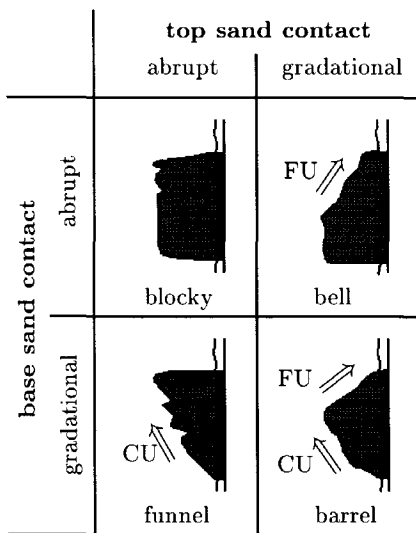


Fig. 4.1 Overview of some typical gamma-ray log-shapes at layer scale.

ment. Typical examples are fluviomarine fans. The river delta progressively builds out into the marine (low energetic) system. These settings typically result in funnel shape logs. A barrel shape log is often a composite deposit of a bell-type over a funnel-type sequence.

4.2.2 From gamma-ray log signatures to acoustic impedance trends

Natural radioactivity is not very important nor useful for seismic applications. However, sedimentary interpretations are heavily based on the gamma-ray log. It is also often observed that an inverted seismic trace comes close to the gamma-ray log. The most important property governing the normal incidence reflection is the acoustic impedance Z . It is related to the normal incidence P -wave reflection coefficient and is derived by multiplying density ρ and P -wave velocity c_P . Although the relationship between acoustic impedance and gamma radioactivity is not straightforward, often an average monotonic function is observed. Both density ρ and P -wave velocity c_P seem to be influenced by the average particle size.

However, in theory, a changing particle size does not influence density ρ . If only the size of the particles changes, the porosity (and the bulk density) should remain constant. However, the sorting of the particles, the particle shape and the mineral-

ogy often does not remain constant with changing particle size. Often it is observed that in lower energetic environments (hence smaller particle size), the sorting of the grains will be poorer. Due to filling up the pores in between the larger grains with small grains, the porosity ϕ will decrease and the bulk density ρ will increase⁴. Also particle shapes change often from spherical-like for the coarse particles to flake-like for fine particles such as clay minerals. The flake-like and relative soft clay particles often can be packed much denser than the spherical-like coarse particles, also leading to a lower porosity ϕ for shales. Diagenetic processes like cementation and alterations can also play a role. All these effects often will cause an increasing density with decreasing particle size: i.e. shales will often show higher densities than sandstones. Mavko et al. (1998) also reports average densities for different lithologies. For sandstones and shales these are respectively $\rho = 2.37 \frac{\text{g}}{\text{cm}^3}$, and $\rho = 2.55 \frac{\text{g}}{\text{cm}^3}$.

In theory, the relationship between a changing particle size and P -wave velocity c_P is not very clear either. There are some models for specific lithologies or rock types, but a relationship that includes several different rock types is more difficult to find. In general, the P -wave velocity is dependent on density ρ , bulk compression modulus K and on the shear modulus μ :

$$c_P = \sqrt{\frac{K + \frac{4}{3}\mu}{\rho}}. \quad (4.1)$$

We have already discussed the influence of particle size on density ρ in the previous paragraph. Empirically a strong relationship is reported between bulk density ρ and P -wave velocity c_P (see for a good overview Mavko et al., 1998). A well known empirical relationship between c_P and ρ is Gardner's relationship, which reads (Gardner et al., 1974):

$$\rho = 1.741 \sqrt[4]{c_P}, \quad (4.2)$$

or

$$c_P = 0.1088 \rho^4, \quad (4.3)$$

with density ρ measured in $[\frac{\text{g}}{\text{cm}^3}]$ and c_P in $[\frac{\text{km}}{\text{s}}]$. The relationship in Equation (4.2) is an average relationship for many rock types, but lithology-specific versions exist as well (Castagna et al., 1993). A comparison between Equation (4.3) and Equation (4.1), suggests a strong dependency between K and ρ : $K \sim \rho^9$ (and from there to particle size, see previous paragraph). This strong relationship is also supported from the so-called contact models, where the effective elastic properties of granular

⁴The relationship between the bulk density ρ and porosity ϕ is $\rho = \rho_m(1 - \phi) + \phi\rho_f$, with ρ_m is the average density of the matrix (grains) and ρ_f is the density of the pore fluid.

materials are described. For instance the uncemented sand model⁵ as described in Mavko et al. (1998), suggests a sharp decrease in bulk compression modulus K with increasing porosity ϕ (or decreasing density ρ). Cementation or diagenetic alteration of the particles for instance can change K drastically (Avseth et al., 1998). Diagenesis in itself is often highly unpredictable and sometimes cannot be attributed to a specific facies type or particle sizes. All the above suggests that the P -wave velocity c_P will have the same trend as density ρ^4 , i.e. a smaller velocity for the coarse sands relative to the finer sediments such as fine sandstone and shales.

Although the relationship between acoustic impedance Z and gamma radioactivity as discussed above is not straightforward, often an average monotonic relationship between both properties is observed. This relationship however cannot be applied over long log sections, because the effect of an increasing hydrostatic pressure with depth will also play a role. An increasing hydrostatic pressure will have an effect on both density ρ and compression modulus K . On relative small depth intervals (for instance 50 to 100 meter), the influence of this trend can often be neglected. As a consequence, the asymmetry of the signatures as described in Figure 4.1 remains present (Emery and Myers, 1996). Figure 4.2 shows the example of well A of the Mobil data set. The signatures are preserved. In this well, clean sands have on average a lower acoustic impedance Z than the surrounding shale intervals.

Often a sand-shale cross-over depth is observed. This means that at a certain depth, the acoustic impedance of sand becomes higher than that of shale. This comes from the different effect of compaction profile of shales and sandstones with depth. Shales are often heavily compacted in the shallow subsurface, after which the compaction rate decreases with depth (Avseth, 2000). Sandstones on the other hand are progressively mechanically compacted with depth. At a depth of 2500 to 3000 meter, chemical compaction starts to become dominant. Due to pressure solution and quartz cementation, the compaction is suddenly increased, leading to a noticeably increase in acoustic impedance Z (Avseth, 2000). Using cross plotting of acoustic impedance versus depth for shales and sandstones, the acoustic impedance contrasts between shales and sandstones can be investigated at an early stage of a study. When the acoustic impedance of the coarser grained material (i.e. sandstone) is higher than that of the finer grained material (i.e. shales), the same asymmetry as in Figure 4.1 would be observed, only the polarity would change.

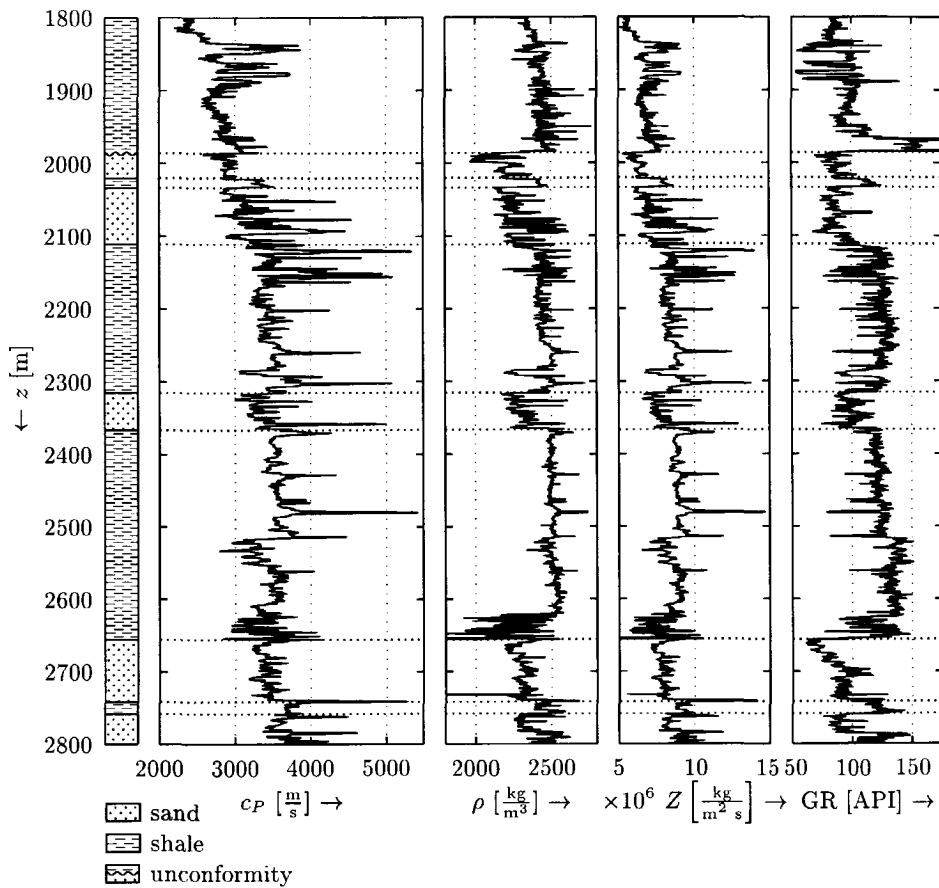


Fig. 4.2 Well A of the Mobil data set (see Appendix C for a description): the gamma-ray log trends observed in the sandstone intervals are also visible in the acoustic impedance Z . The acoustic impedance Z for the sandstone layers is lower than for the shale intervals. Note the general trend (especially in the shale intervals) of increasing acoustic impedance Z with depth z , the so-called compaction trend.

4.2.3 Seismic modelling for the typical sequences

The acoustic impedance expressions for the four types of sequences described in the previous section (Figure 4.1) are synthesized. The assumption is made that

⁵The uncemented sand model is a heuristic combination between Hertz-Mindlin contact theory and the Hashin-Strikman lower bound, and provides accurate estimates in sands where cement is deposited in the interstitial pore space (Mavko et al., 1998).

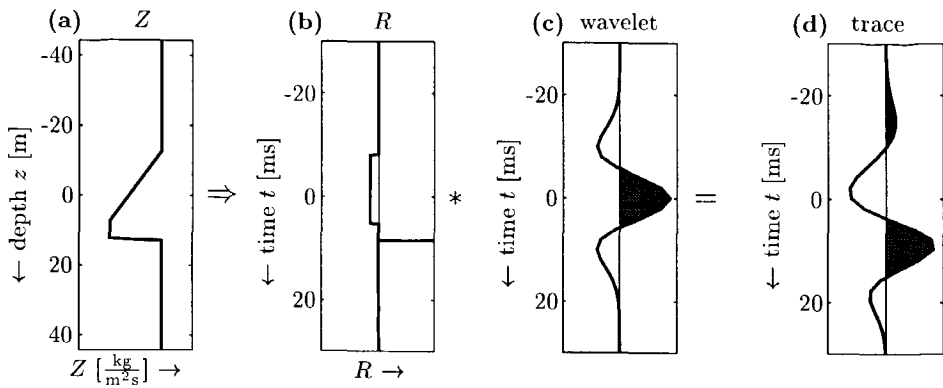


Fig. 4.3 The construction of the normal-incidence seismic response. Example for the Dirtying-up trend (bell). (a) acoustic impedance Z (layer thickness is 25 meter) (b) schematized reflectivity response in TWT (c) 40 Hz Ricker-wavelet (d) seismic response as a convolution of the layer-code response (b) with the Ricker-wavelet (c).

the acoustic impedance for porous sands is lower than that for shales, as also done in Emery and Myers (1996). A thickness of 25 meter (corresponding to approximately 18 ms two-way travel time (TWT)) was assumed for the sequences. The effect of thickness variations will be discussed in section 4.3.3.

Using a layer-code algorithm, and a convolution with a Ricker-wavelet, a seismic trace is constructed (Figure 4.3). The peak frequency f_o of the Ricker-wavelet is chosen at 40 Hz⁶. On the right-hand side of each sub-figure of Figure 4.4, the seismic response is presented. Note that (aside from an eventual small travel time effect) only the polarity of the seismic trace would change when porous sandstone would exhibit a higher acoustic impedance than shale.

Although the resolution of the seismic measurement is too small to resolve the internal detail of the sequence, the shape of the resulting wavelet is noticeably different (Figure 4.4).

⁶A Ricker-wavelet is defined as: $f(t) = (1 - 2(\pi f_o t)^2).e^{-(\pi f_o t)^2} \approx \cos(2\pi f_o t).e^{-(\pi f_o t)^2}$, with f_o the peak frequency. The mean frequency (weighted by the amplitude spectrum) $f_{\text{mean}} = \frac{2}{\sqrt{\pi}} f_o$ (Sheriff, 1991). Following Barnes (1991), f_{mean} for isolated wavelets is also equal to the response frequency (see section 4.3.1).

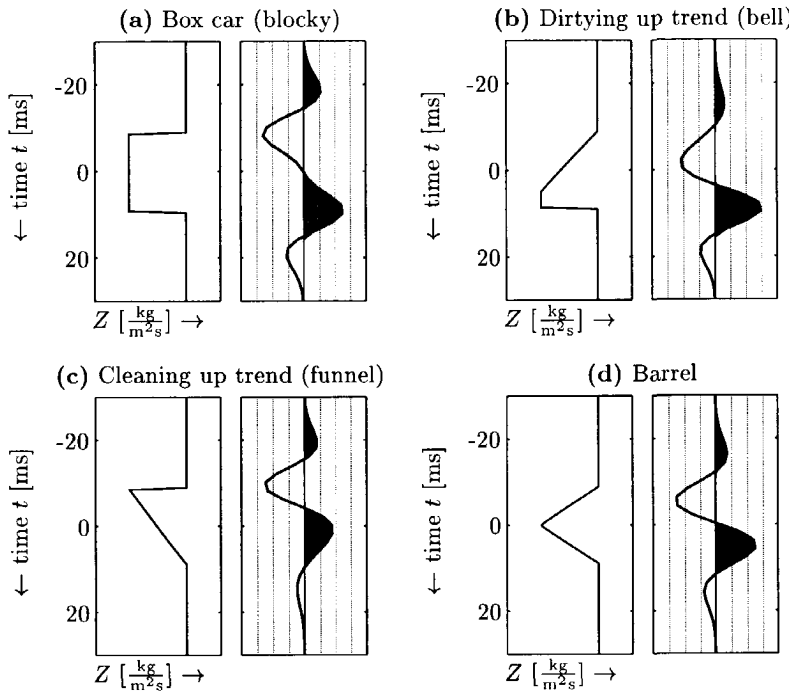


Fig. 4.4 Normal-incidence seismic response of the four typical sequences using the methodology described in Figure 4.3. On the left-hand side of each of the four sub-plots, the acoustic impedance profile is given (in TWT to compare better with the seismic traces). On the right-hand side the seismic response is presented. Porous sand is assumed to have a lower acoustic impedance than shale.

4.3 Analysis of the seismic measurement

4.3.1 Instantaneous and response attributes

The difference in shapes for the different wavelets from Figure 4.4 can best be characterized using phase. In Figure 4.6 the effect of a phase-shift is depicted.

Instantaneous attributes (e.g. instantaneous phase) have already been used extensively in exploration seismology (Neidell and Taner, 1971; Taner et al., 1979; Taner and Sheriff, 1977; Robertson and Nogami, 1984). These attributes are available in common interpretation systems (Geoquest, 1999). They were found to be very helpful in highlighting subtle changes, e.g. related to tuning effects.

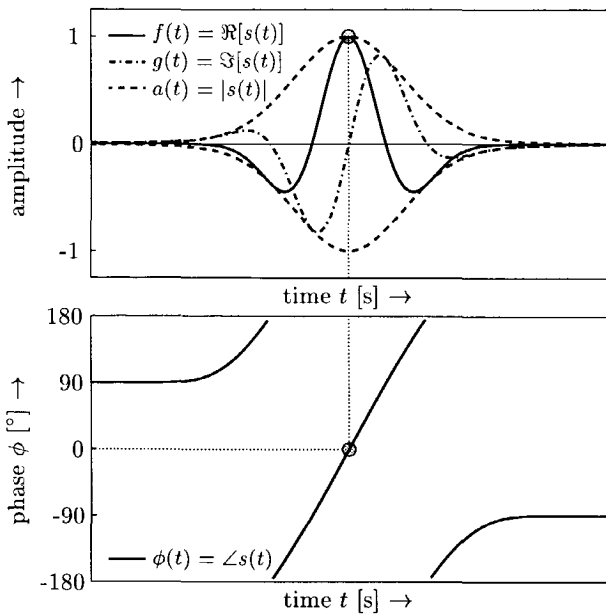


Fig. 4.5 The instantaneous phase (below) calculated for the Ricker-wavelet. The phase is changing as a function of time. By extracting the response attributes at the peak of the envelope, a unique attribute is assigned to the event. In this case, the response phase is 0° for the Ricker-wavelet, and -90° for its quadrature $g(t)$ (not shown).

The instantaneous attributes for a real, non-periodic function $f(t)$ can be expressed using the concept of the analytic trace (Gabor, 1946) (Figure 4.5). An analytic trace $s(t)$ is a complex function that can be constructed as:

$$s(t) = f(t) + jg(t) = a(t)e^{j\phi(t)}, \quad (4.4)$$

with $f(t)$ the function in itself, and

$$g(t) = \frac{1}{\pi} \int_{-\infty}^{+\infty} \frac{f(t')dt'}{t' - t} = \frac{1}{\pi} \lim_{\epsilon \rightarrow 0} \left[\int_{-\infty}^{t-\epsilon} \frac{f(t')dt'}{t' - t} + \int_{t+\epsilon}^{+\infty} \frac{f(t')dt'}{t' - t} \right] \quad (4.5)$$

the quadrature of $f(t)$, calculated using the Hilbert transform (Bracewell, 2000). The symbol f denotes the Cauchy principal value at discontinuities (Weisstein, 2000), and is expanded in the last part of Equation (4.5). The Hilbert transform as defined in Equation (4.5) can also be considered as:

$$g(t) = \frac{-1}{\pi t} * f(t), \quad (4.6)$$

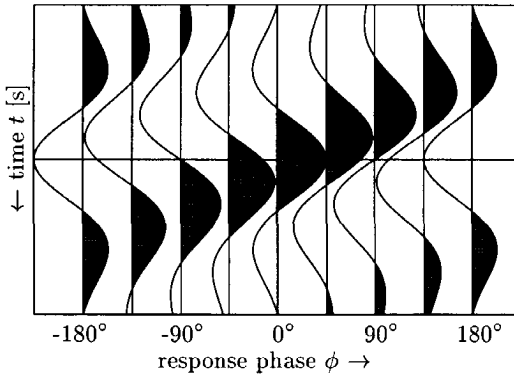


Fig. 4.6 Real part of an analytic Gabor-atom as a function of the response phase. All have the same Gaussian basis function, the same scale σ , the same modulus and the same modulation $\xi = 1$. Only the response phase ϕ ranges from -180° to 180° .

the convolution of $f(t)$ with $\frac{-1}{\pi t}$ (Bracewell, 2000). The Fourier transform of $\frac{-1}{\pi t}$ is $j \operatorname{sgn} \omega$, which is equal to $+j$ for positive frequencies ω , and $-j$ for negative frequencies ω . This means that $g(t)$ has the same amplitude spectrum as $f(t)$, with its phase spectrum being $\pm 90^\circ$ shifted relative to the one for $f(t)$.

From Equation (4.4) it is clear that

$$f(t) = \Re[s(t)] = a(t) \cos \phi(t), \quad (4.7)$$

$$g(t) = \Im[s(t)] = a(t) \sin \phi(t), \quad (4.8)$$

where $a(t)$ is the instantaneous amplitude (or envelope) and $\phi(t)$ the instantaneous phase. They can be calculated from the analytic trace using:

$$a^2(t) = f^2(t) + g^2(t) = s(t)s^*(t) \quad (4.9)$$

$$\tan \phi(t) = \frac{g(t)}{f(t)} = \frac{1}{j} \frac{|s(t) - s^*(t)|}{|s(t) + s^*(t)|}. \quad (4.10)$$

Instantaneous frequency $f_{\text{inst}}(t)$ is defined using:

$$f_{\text{inst}}(t) = \frac{1}{2\pi} \frac{d\phi(t)}{dt}. \quad (4.11)$$

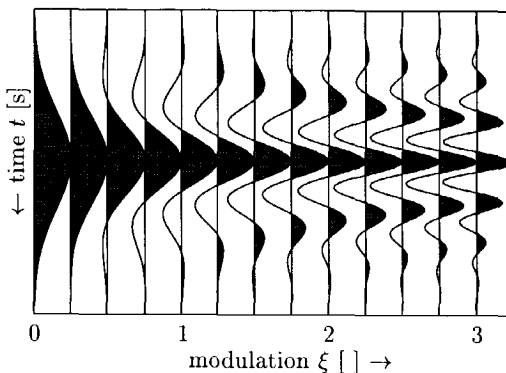


Fig. 4.7 Influence of modulation on the real part of a Gabor-atom. All atoms have the same Gaussian basis function, the same scale σ , and the same modulus. Only the frequency modulation ξ ranges from 0 (= basis-function) to 3.

A disadvantage of the instantaneous attributes in general is their sensitivity to noise, and the fact that even for an isolated event the attributes change as a function of time (Figure 4.5). By selecting the attributes at the maximum of the envelope, a unique value can be assigned to the seismic event. This type of attributes is known under a number of names, such as principal, characteristic, response (Bodine, 1986) or wavelet attributes (Taner, 1998). The frequency attribute computed in this way for an isolated wavelet, is for instance equal to the mean frequency calculated from the Fourier-spectrum (Bodine, 1986; Barnes, 1991; Grace, 1981; Steeghs, 1997). This extraction of instantaneous attributes at the peak of the envelope will result in attributes that are most representative for the local event, but still based on very localized information. This makes this method more vulnerable for noise as will be shown in section 4.3.4. The use of a priori information, in the form of a common seismic wavelet shape and an expected frequency range will lower the influence of noise.

4.3.2 Deriving amplitude, phase and scale using Matching Pursuit

In the case of a seismic trace, where events are not isolated and noise is present, the user can provide extra information in the form of a frequency range and an expected approximate wavelet shape. In this way, the analysis can be based on a certain window (\sim scale σ) of the trace instead of instantaneous (sample by sample). The matching pursuit approach (Mallat and Zhang, 1993), based on the continuous

wavelet transform⁷, has this feature that a priori information can be included in the form of a wavelet shape and a frequency range. In that approach a set of basis functions is generated by scaling, translating, and modulating a single window function $\psi(t)$:

$$\psi_{(\sigma, \xi, \tau)}(t) = \frac{1}{\sqrt{\sigma}} \psi\left(\frac{t - \tau}{\sigma}\right) e^{j2\pi\xi\left(\frac{t - \tau}{\sigma}\right)}, \quad (4.12)$$

where σ is the scale (the width of the atom), τ is the translation (or the timing of the atom), ξ is the frequency modulation (see Figure 4.7) (Chakraborty and Okaya, 1995; Mallat and Zhang, 1993). Note that Equation (4.12) describes a complex, analytic function. A wide set of basis functions can be chosen depending on the circumstances (see Herrmann (1997) for a discussion). Here the Gaussian-function is chosen as basis function, resulting in:

$$\psi_{(\sigma, \xi, \tau)}(t) = \frac{\sqrt{2}}{\sqrt{\sigma}} e^{-\pi\left(\frac{t - \tau}{\sigma}\right)^2} e^{j2\pi\xi\left(\frac{t - \tau}{\sigma}\right)}, \quad (4.13)$$

the so-called Gabor-atoms⁸. Mallat and Zhang (1993) described the excellent time-frequency resolution of these atoms⁹.

The frequency modulation ξ is chosen to be 1 (because the shape of the real-part of the atom resembles the often observed Ricker-wavelet (Figure 4.5) (Ricker, 1953)), resulting in a complex atom as presented in Figures 4.8 and 4.9. These atoms constitute a set of functions $\psi_{(\sigma, \xi=1, \tau)}(t)$, with changing time-shift (τ) and scale (σ). The modulation ξ is fixed at 1.

Matching Pursuit is performed by projecting these atoms onto the trace $s(t)$:

$$\varsigma(\tau, \sigma) = \langle s(t), \psi_{(\sigma, \xi=1, \tau)}(t) \rangle, \quad (4.14)$$

with

$$\langle f, g \rangle = \int_{-\infty}^{+\infty} f(t) \bar{g}(t) dt, \quad (4.15)$$

⁷Note that not all the real parts of Gabor-atoms are wavelets. Only for $\xi \geq 2$ one of the admissibility conditions ($\int_{-\infty}^{+\infty} \Re(\psi_{(\sigma, \xi, \tau)}(t)) dt = 0$) is met (Chakraborty and Okaya, 1995; Morlet et al., 1982).

⁸Note that $\psi_{(\sigma, \xi, \tau)}(t)$ is L_2 -normalized, e.g. $\|\psi_{(\sigma, \xi, \tau)}(t)\| = \int_{-\infty}^{+\infty} |\psi_{(\sigma, \xi, \tau)}(t)|^2 dt = 1$. This explains the unusual $\sqrt{2}$ constant in Equation (4.13).

⁹These atoms show the best joint localization in time and frequency, honoring the lower bound for Heisenberg's uncertainty relationship (Morlet et al., 1982; Bodine, 1986). This relationship is also known as the uncertainty principle of sampling theory, and says that there is a trade-off between localization in the time domain and localization in the spectral (frequency) domain.

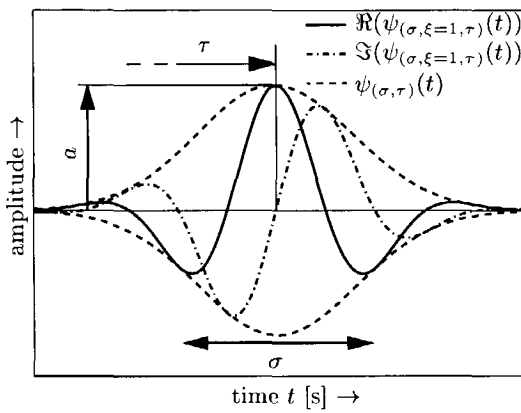


Fig. 4.8 The Gabor-atom $\psi_{(\sigma, \xi=1, \tau)}(t)$ used in the matching pursuit analysis. The envelope is the Gaussian function. The real and imaginary part of the complex function are presented. The real part is a windowed cos-function, the imaginary part being a windowed sin-function.

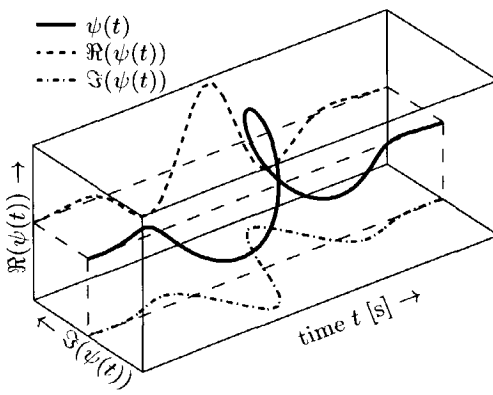


Fig. 4.9 A 3D presentation of the complex Gabor-atom. In solid line the complex trace, in dashed line the real part, and in dash-dot line the imaginary part is presented.

the inner product of f and g , and $\bar{g}(t)$ the complex conjugate of $g(t)$ (Mallat and Zhang, 1993). Because of the following property of the Gabor-atoms:

$$\bar{\psi}_{(\sigma, \xi, \tau=0)}(t) = \psi_{(\sigma, \xi, \tau=0)}(-t), \quad (4.16)$$

is Equation (4.14) equivalent to:

$$\varsigma(t, \sigma) = \psi_{(\sigma, \xi=1, \tau=0)}(t) * s(t), \quad (4.17)$$

with

$$\{f * g\}(t) = \int_{-\infty}^{+\infty} g(t') f(t - t') dt', \quad (4.18)$$

the convolution of f and g . Equation (4.17) has the advantage over Equation (4.14) that τ is eliminated as running variable. The variable t in $\varsigma(t, \sigma)$ (Equation (4.17)) is equivalent to the time shift τ from Equation (4.14). The variable t of a convolution result signifies a relative time shift, τ , between both functions used in the convolution.

The best match is found where $|\varsigma(\tau, \sigma)| = a(\tau, \sigma)$ is maximized as a function of time-shift and scale (Mallat and Zhang, 1993) (Figure 4.10(b)):

$$\begin{aligned} |\varsigma(\tau_{\text{opt}}, \sigma_{\text{opt}})| &\geq |\varsigma(\tau, \sigma)|, \\ \forall(\tau, \sigma) \ni \tau_{\text{min}} \leq \tau &\leq \tau_{\text{max}} \wedge \sigma_{\text{min}} \leq \sigma \leq \sigma_{\text{max}}. \end{aligned} \quad (4.19)$$

This analysis is done on a time-window $[\tau_{\text{min}}, \tau_{\text{max}}]$ which contains the seismic event of interest, and for a specified scale range $[\sigma_{\text{min}}, \sigma_{\text{max}}]$ (Figure 4.10(b)). The attributes resulting from the matching pursuit are equal to the parameters for the best fitting Gabor-atom:

$$\begin{cases} \text{timing :} & \tau_{\text{opt}} \\ \text{scale :} & \sigma_{\text{opt}} \\ \text{phase :} & \phi_{\text{opt}} = \arctan \left(\frac{\Im(\varsigma(\tau_{\text{opt}}, \sigma_{\text{opt}}))}{\Re(\varsigma(\tau_{\text{opt}}, \sigma_{\text{opt}}))} \right) \\ \text{amplitude :} & a_{\text{opt}} = |\varsigma(\tau_{\text{opt}}, \sigma_{\text{opt}})|. \end{cases} \quad (4.20)$$

Note that $\varsigma(\tau, \sigma_{\text{opt}})$ is an analytic trace, and that ϕ_{opt} and a_{opt} are respectively the response phase and amplitude at location τ_{opt} . The response frequency f of $\varsigma(\tau, \sigma_{\text{opt}})$ is equal to:

$$f = \frac{1}{\sigma_{\text{opt}}}. \quad (4.21)$$

Equation (4.19) was described as giving the best match, and that can be explained when we decompose the signal $s(t)$ into:

$$s(t) = a_{\text{opt}} \Re(\psi_{(\sigma_{\text{opt}}, \xi=1, \tau_{\text{opt}}, \phi_{\text{opt}})}(t)) + r(t), \quad (4.22)$$

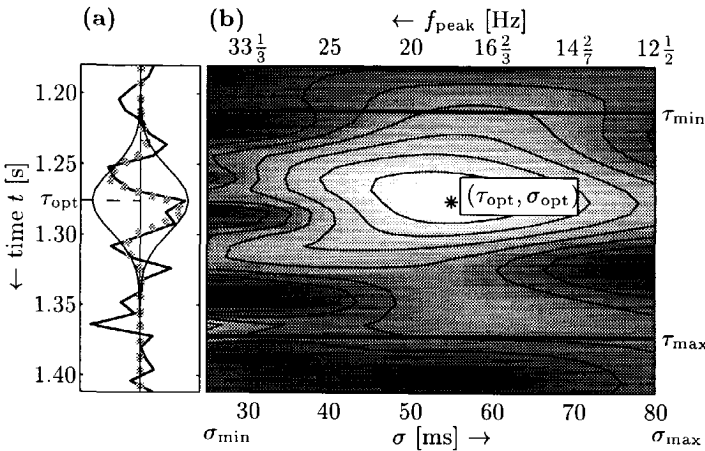


Fig. 4.10 Example of the matching pursuit using a Gabor-atom. (a) the original trace and the matched atom in dashed line. The envelope of the matched wavelet is also presented in thin line. (b) $|s(\tau, \sigma)|$ plotted in a shade of grey (dark is low and white is high) and as contour lines. $|s(\tau_{\text{opt}}, \sigma_{\text{opt}})|$ is indicated by an asterisk (*). The corresponding peak frequencies (f_{peak}) of the atoms are plotted along the top of the figure.

with the first component on the right-hand side being the best matching atom and $r(t)$ the residue, and

$$\psi_{(\sigma, \xi, \tau, \phi)}(t) = \psi_{(\sigma, \xi, \tau)}(t) e^{j\phi}. \quad (4.23)$$

Due to the normalization of $\psi_{(\sigma, \xi, \tau)}(t)$ and to the fact that $r(t)$ is orthogonal to $\psi_{(\sigma, \xi, \tau)}(t)$, Equation (4.19) is equivalent to minimizing $\|r(t)\|$ for $t \in [\tau_{\min}, \tau_{\max}]$ (Mallat and Zhang, 1993). The best matching atom is plotted on Figure 4.10(a). This atom will have the same attributes as given by Equation (4.20)¹⁰.

In this chapter we stopped after one atom was fitted, but the method can be used to iteratively match additional atoms to $r(t)$. After subtracting the fitted atom from the seismic trace, a new atom is matched to the residual. Figure 4.11 shows an example of iteratively matching atoms. The five strongest events are successfully extracted, leaving a small residue $r_5(t)$. The residue $r_5(t)$, still shows some clear events that can be extracted with Gabor atoms. A few more iterations will reduce the residue even further. When the set of atoms that is used in the match-

¹⁰Response frequency is equal to peak and mean frequency, due to the specific shape of the Gabor atoms.

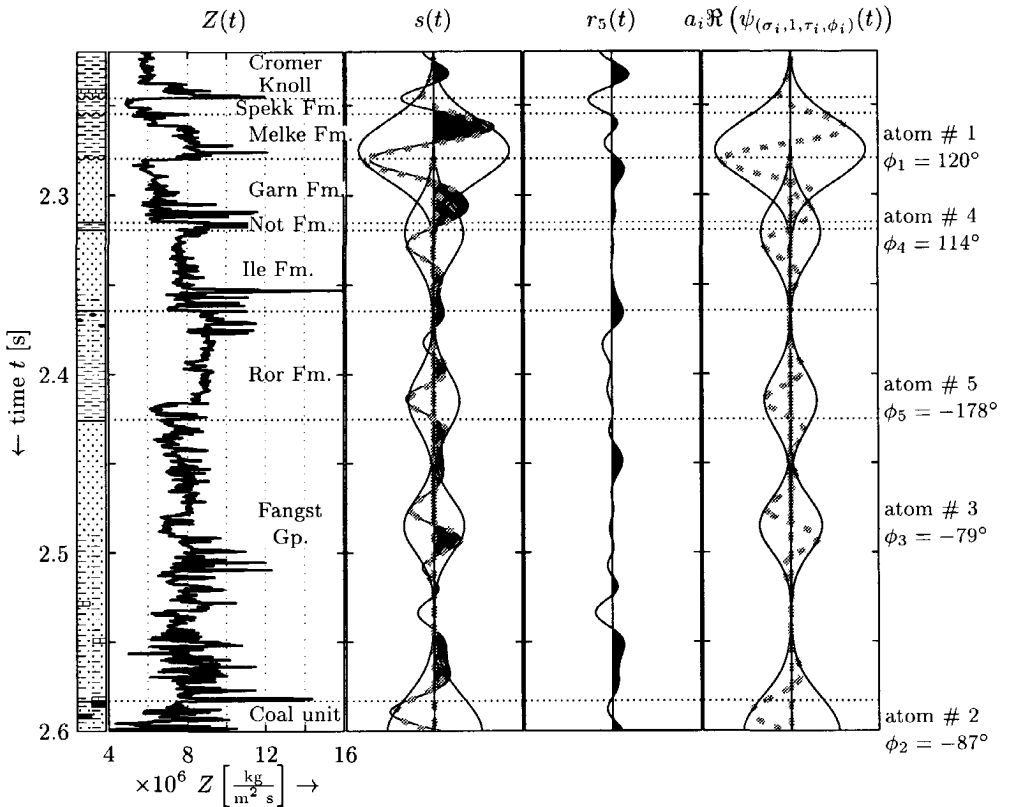


Fig. 4.11 Example of iteratively matching atoms on a synthetic seismic trace $s(t)$ calculated from the acoustic impedance $Z(t)$ for the Saga well-log (see Appendix B for a brief description). A 25 Hz Ricker wavelet was used. The residual energy after five iterations, $\|r_5(t)\|$, is 11 % relative to the energy originally in the seismic trace $\|s(t)\|$ in the interval shown.

ing pursuit is complete (i.e. spanning the total space to which $s(t)$ belongs), the residue $\|r_n(t)\|$ will become arbitrary small, i.e. $\lim_{n \rightarrow \infty} \|r_n(t)\| = 0$. In the method described here, the set of atoms was deliberately restricted. This means that the subset of atoms used here is not complete, i.e. the residue will not exactly go to zero.

From the example discussed in Figure 4.10, we note that the high frequency (noisy) part of the trace is ignored. Only the global shape of an event within the allowed time-range is fitted using a family of atoms that are expected in seismics. This is in fact a data-adaptive high-cut filter. Due to the non-local character, the analysis using the matching pursuit approach is very stable. The analysis is per-

formed using atoms within a certain range of lengths (the scale range), thus lowering the effects of noise. Moreover the *event* that matches the family of Gabor-atoms best within the time-window is selected, so no additional picking has to be performed.

4.3.3 Characterization of typical sequences using phase

The matching pursuit methodology presented in the previous section is applied to characterize the seismic expression of the typical sequences found in section 4.2.3. A summary of the analysis results for the four sequences from Figure 4.4 is presented in Figure 4.12. These results are for a specific ratio between dominant wavelength

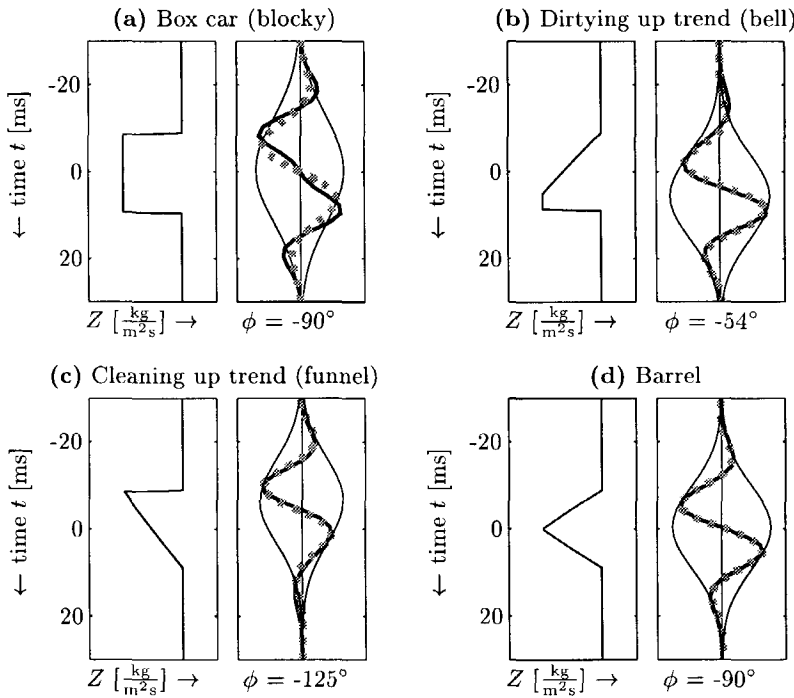


Fig. 4.12 The results of the matching pursuit analysis of the typical sequences. For each of the four sub-plots, the matched atom (dashed gray line) and the envelope (thin line) are plotted on top of the seismic trace. Additionally the phase (ϕ) of the best-matched atom is plotted below each seismic trace. A layer thickness d of 25 meter and a dominant wavelength λ_{dom} of 35 meter is used.

and layer thickness. In this case, the layer thickness is 25 meter, and the dominant wavelength of the wavelet is 35 meter.

When the ratio between layer thickness and dominant wavelength is changed, the phase attribute will change as well. This phenomenon of constructive and destructive interference of wavelets originating from two closely spaced reflectors is called the tuning effect (Widess, 1973; Neidell and Poggiagliomi, 1977; Neidell, 1981; Sheriff, 1991). The classical tuning curve indicates the change in maximum ampli-

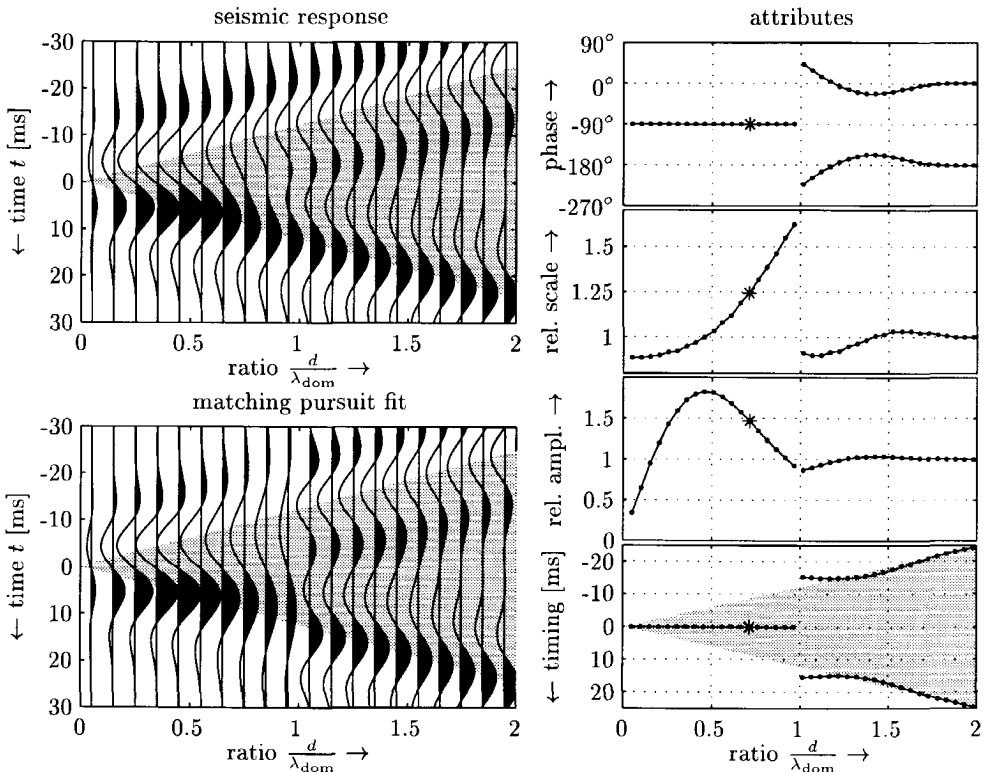


Fig. 4.13 The effect of a changing ratio between layer thickness d and dominant wavelength λ_{dom} for the block-type sequence. For layer thicknesses d smaller than the dominant wavelength λ_{dom} , only one event is fitted using matching pursuit. The phase attribute ϕ for this event is equal to -90° . For layer thicknesses d higher than the dominant wavelength λ_{dom} , two separate events are fitted. The phase attribute for these two events are around 0° and -180° .

tude of the seismic response for a wedge with constant material properties, i.e. a block-type sequence with changing thickness. Using the tuning curve, the layer thickness can be calculated from the observed seismic amplitude. Figure 4.13 shows the attributes extracted on such a wedge. The amplitude attribute is the tuning curve. Note that there are two distinct regimes in Figure 4.13. When the layer thickness d is smaller than the dominant wavelength of the seismic wave λ_{dom} only

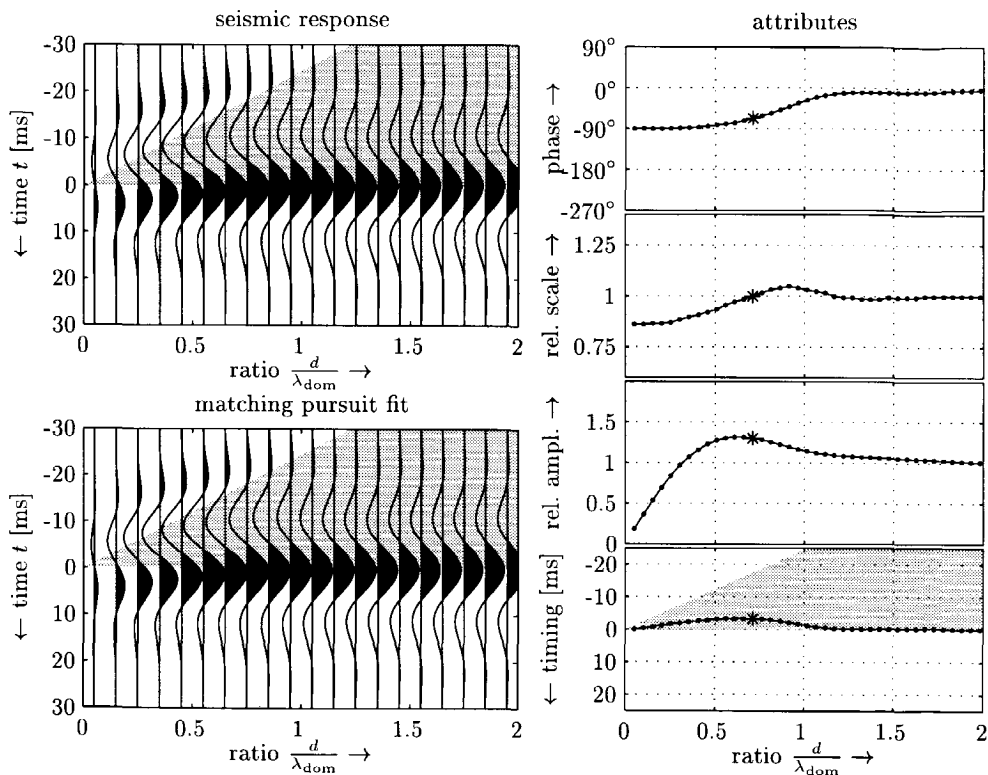


Fig. 4.14 The effect of a changing ratio between layer thickness d and dominant wavelength λ_{dom} for the bell-type sequence. The phase attribute changes from -90° to 0° , but remains in the fourth quadrant. This means that although the phase attribute is changing, it is still possible to discriminate the type of sequence in the range $\frac{d}{\lambda_{\text{dom}}} = [0.5, 1.25]$. For layers thinner than half the dominant wavelength, the phase attribute is close to -90° . For layers thicker than 1.25 times the dominant wavelength, the phase attribute is close to 0° . Note that the seismic response mainly comes from the abrupt base contact of the “thick” layer.

one event is fitted. This event has a constant phase attribute ϕ of -90° . When the layer thickness d becomes larger than the dominant wavelength λ_{dom} , two events are fitted. The phase attribute ϕ for these two events fluctuates around 0° and -180° .

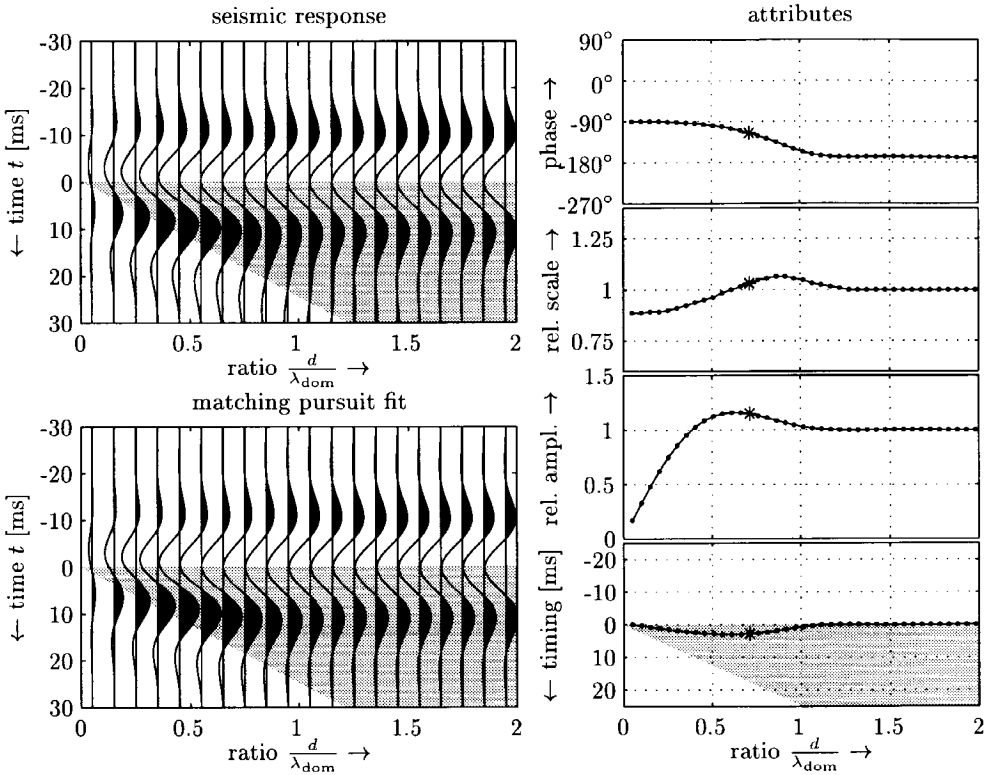


Fig. 4.15 The effect of a changing ratio between layer thickness d and dominant wavelength λ_{dom} for the funnel-type sequence. The phase attribute changes from -90° to -180° , but remains in the third quadrant. This means that although the phase attribute is changing, it is still possible to discriminate the type of sequence in the range $\frac{d}{\lambda_{\text{dom}}} = [0.5, 1.25]$. For layers thinner than half the dominant wavelength, the phase attribute is close to -90° . For layers thicker than 1.25 times the dominant wavelength, the phase attribute is close to -180° . The seismic response for “thick” layers is dominated by the abrupt contact at the top of the funnel-type sequence; the effect of the gradational base contact is only a slight asymmetry in the wavelet, i.e. the phase attribute ϕ is slightly different from -180° .

With increasing thickness of the layer, the seismic response of the abrupt transitions at base and top of the layer become individual, non-interfering reflections.

Figure 4.14 shows the tuning effects for a bell-type sequence. The phase attribute clearly varies continuously from -90° (when the layer thickness is small compared to the dominant wavelength of the wavelet) to 0° (when the layer thickness is large compared to the dominant wavelength). When the layer thickness is small compared to the dominant wavelength, the results are the same as for the block-type sequence. However, at layer thicknesses d between 0.5 and 1.25 times the dominant wavelength λ_{dom} , the phase attribute ϕ is distinctly different from that of the block-type sequence. When the layer thickness is large compared to the dominant frequency, the seismic response is dominated by the abrupt transition at the base of the bell-type of sequence. This means that the seismic response in this extreme is comparable to the response of a step-function.

Figure 4.15 shows the tuning effects for a funnel-type sequence. The phase attribute clearly varies continuously from -90° (when the layer thickness is small compared to the dominant wavelength of the wavelet) to -180° (when the layer thickness is large compared to the dominant wavelength). When the layer thickness is small compared to the dominant wavelength, the results are the same as for the block-type sequence. However, at layer thicknesses d between 0.5 and 1.25 times

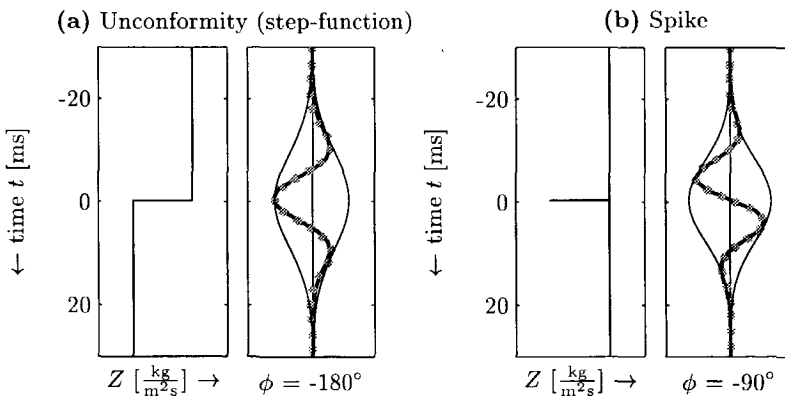


Fig. 4.16 The response for two additional log-shapes. These complement the typical sequences as presented in Figure 4.12. The seismic response for a step-function is the original seismic wavelet ($\phi = 0^\circ$ or -180°). The seismic response for a spike in acoustic impedance is a differentiation of the original seismic wavelet ($\phi = \pm 90^\circ$).

the dominant wavelength λ_{dom} , the phase attribute ϕ is distinctly different from that of the block-type sequence. When the layer thickness is large compared to the dominant frequency, the seismic response is dominated by the abrupt transition at the top of the funnel-type of sequence. This means that the seismic response in this extreme is comparable to the response of a step-function.

From the analysis of the effect of a changing layer thickness, we note that the effect of a very thin layer is comparable for all sequence-types. Also when the layer is very thick compared to the seismic wavelength, a similar response can be seen for all sequence types, i.e. the seismic response is similar to the response for a step-function. Two sequences, the step-function and the “spike”, are analysed additionally in Figure 4.16. They complement the four typical sequences as described previously. The “spike” can be considered as any type of sequence embedded between half-spaces with equal properties, where the layer thickness is very small compared to the seismic wavelength. The step-function represents unconformity type of boundaries, where the material properties are distinctly different over a considerable distance on both sides of the boundary, i.e. the wavelength is small compared to the layer thickness.

Phase appears to be a good attribute for characterizing the type of sequence at the layer scale (Figure 4.17). The symmetrical acoustic impedance profiles like blocky-, bell- and “spike”-type sequences, show a phase of almost 90° (or -90° for the complement, see section 4.2.2). The noticeable asymmetric acoustic impedance profiles, like funnel- and bell-type sequence, give a significant deviation from 90° . The amount of deviation is a function of the layer thickness (relative to the seismic wavelength) and the actual log-shape. The funnel-type of sequence (cleaning-up trend) shows a negative deviation, the bell-type (dirtying-up trend) a positive deviation. The step-function results in a phase of 0° or 180° .

These numerical values are only valid for sequences embedded in two layers with equal seismic properties, and when the seismic wavelet is close to zero-phase. When one of these sequences is not embedded between two layers with the same properties, this can be seen as the superposition of the step-function with the sequence, as will be explained in the next section. When the properties of the layers above and below show little regional variation (for instance deep marine shales), the phase-attribute will still be useful as a relative discriminator. The actual value will however be changed by the influence of the step-function. When the seismic wavelet is not properly zero-phased, all the phases will be shifted. The method will still be useful in a relative way or after correction when the actual phase of the seismic wavelet is known.

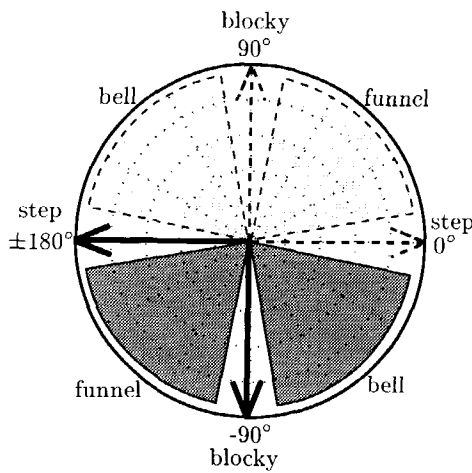


Fig. 4.17 The extracted phases for the different log-shapes plotted in a rose-diagram. The complements are plotted as well (dashed) because of the polarity-change when the porous sandstone would show a higher acoustic impedance than shale. Blocky- and barrel-type sequences have a phase of $\approx -90^\circ$, funnel-type has a negative deviation from -90° , bell-type a positive. The step-function has a phase around $\pm 180^\circ$. The “spike” is similar to the blocky- and barrel-type of sequences.

4.3.4 Influence of noise: comparison with response phase

As already said earlier, the attributes obtained from the matching pursuit method resemble the so-called response attributes (Taner et al., 1979). Using the analytic trace various types of attributes like instantaneous phase and instantaneous frequency can be elegantly calculated on each time-sample (often after interpolating the seismic trace). So-called response attributes are derived by extracting the instantaneous attributes at the maximum of the envelope (see section 4.3.1 for an example). This is indeed very similar to this method. The main difference with the matching pursuit method, is that in the latter a wavelet shape and a scale range are assumed. Hereby a more global shape is extracted. The response attributes are more detailed, but as a draw-back, they are more sensitive for noise. In Figure 4.18, the sensitivity of both methods for white noise is compared. A bell-shape sequence with a thickness of 25 meter was used. For each Signal-to-Noise ratio (S/N), one hundred experiments were performed. For each experiment the phase was calculated twice: once using the matching pursuit method and once using the response attributes. From the one hundred measurements the mean value and the standard deviation were calculated. Note that the response phase tends towards $\phi = 0^\circ$ for

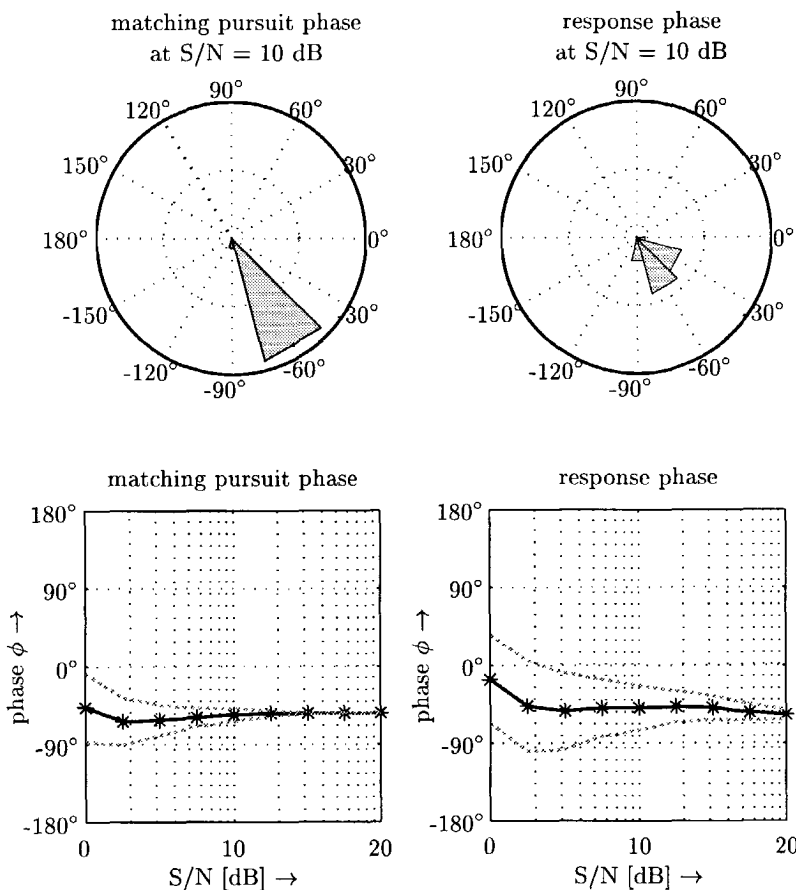


Fig. 4.18 A comparison of the influence of white noise on the phase obtained from the matching pursuit method and the response phase. The bell-sequence was used ($\phi = -54^\circ$). On the lower plots, the mean phase (full line) and the standard deviation (dotted lines) are plotted in function of the Signal-to-Noise ratio (S/N). Note that an increasing S/N means a lower noise level. The matching pursuit method is better both with respect to bias as with respect to the standard deviation of the phase distribution. For instance at a Signal-to-Noise ratio (S/N) of 10 dB (i.e. energy of the signal is ten times higher than that of the added white noise) is the bias for the matching pursuit method $\Delta\phi = 2.1^\circ$, and for the response phase it is $\Delta\phi = 7.7^\circ$. The standard deviation is resp. $\sigma = 7.5^\circ$ and $\sigma = 26^\circ$.

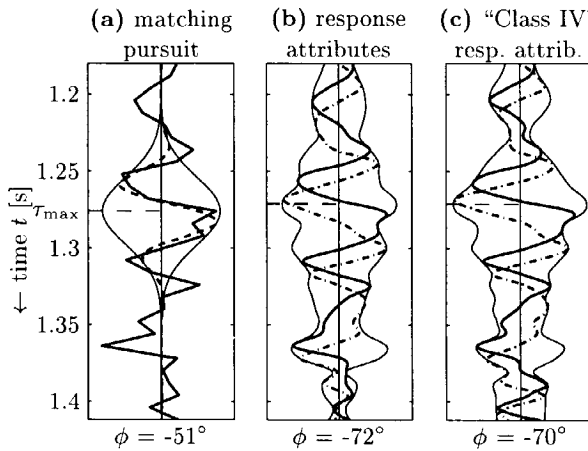


Fig. 4.19 Comparison between phase extracted using (a) matching pursuit, (b) response attributes and (c) areal averaged “Class IV” response attributes. (a) the original trace (solid line), with the matched atom superimposed (dashed line). The envelope (thin line) indicates the support/scale of this atom. (b) analytic trace (real part in solid line, imaginary part in dash-dot line), with its envelope (thin line) as calculated with the SRCAAttrib software (Rock Solid Images, 1997). This includes standard a band-pass filter prior to the Hilbert transform. Response attributes are extracted at each peak in the envelope. (c) Areal averaged seismic trace using the default dipscan parameters (averaging over 7 lateral positions). The Response attributes are extracted from this averaged trace are called the “Class IV” attributes. The phases (ϕ) extracted using all three techniques are different, because the scale of investigation is different.

high noise levels, a feature already described by White (1991).

From the results in Figure 4.18, it is clear that the matching pursuit method is more robust in the presence of white noise. In order to get the same accuracy, the response phase allows between 6 and 9 dB less noise compared to the matching pursuit method. Or conversely, even with a 4 to 8 times increased noise energy level, the matching pursuit method is equally accurate than the response phase calculation on the trace with the normal noise level. This difference comes from the wavelet shape that is assumed in the matching pursuit method, i.e. the family of atoms are fitted over a certain time window. This means that the effect of the white noise is “averaged” along the time direction.

Also in the calculation of response attributes, a method was found to diminish the effect of random noise; the software of Seismic Research Corporation has the option for calculating the attributes after weighted summation of neighboring traces along the direction of maximum semblance (“Class IV” attributes in Taner, 1998). In fact, the main difference is then the direction of “averaging”; the matching pursuit approach averages along the time direction by fitting a larger atom, the “Class IV” response attributes average along the reflector. To reach the same accuracy as the matching pursuit method, an average over 16 up to 64 traces has to be made. However, as a draw-back, the subtle sedimentary features one wants to extract from the seismic data will become blurred as well. The matching pursuit approach discussed above does not have this draw-back.

Both the matching pursuit method and the calculation of response attributes are similar in costs towards a high number of samples N . Following Mallat (1999), matching pursuit costs in the order $O(N \log_2 N)$ calculations. On the other hand, the calculation of the analytic trace uses the Fast Fourier Transform (FFT). The calculation of a FFT is also of the order $O(N \log_2 N)$. However, for the relatively small number of samples used here, matching pursuit is more expensive than the calculation of the analytic trace. Depending on the required accuracy, the difference is in the order of a factor 10 to 30.

4.3.5 The effect of pore fill

The effect of substitution of the pore fill on the different attributes, can easily be investigated. Figure 4.20 shows a simple example of a bell-type sequence with different pore fill. The substitution of the pore fluid was done using the well-known Gassmann equation (Gassmann, 1951; Castagna et al., 1993). The amplitude attribute shows a large effect on the substitution of the pore liquids. The effect on the other attributes is rather moderate.

4.3.6 Application to a synthetic seismic trace

How good the method will work, depends on how well a particular layer or event is present in the seismic trace as a distinct seismic response, not altered by the interference from other events above or below. Figure 4.21 explains the results for the events analysed in the synthetic trace generated from the Saga-well. Five atoms were fitted to the seismic data. We will now explain the values for the phase attributes.

First the strongest event will be discussed. It is annotated as “atom # 1”, and it encompasses the Melke and Spekk Formations. From the extracted phase

attribute, it should correspond with a bell-shape, i.e. a dirtying upward trend. This corresponds well with the geological description of the Melke Formation, as being a period characterized by a regional transgression (see Appendix B). Also the acoustic impedance around that location shows a bell shape, combined with a (relative to the strength of the bell-shape) minor step function.

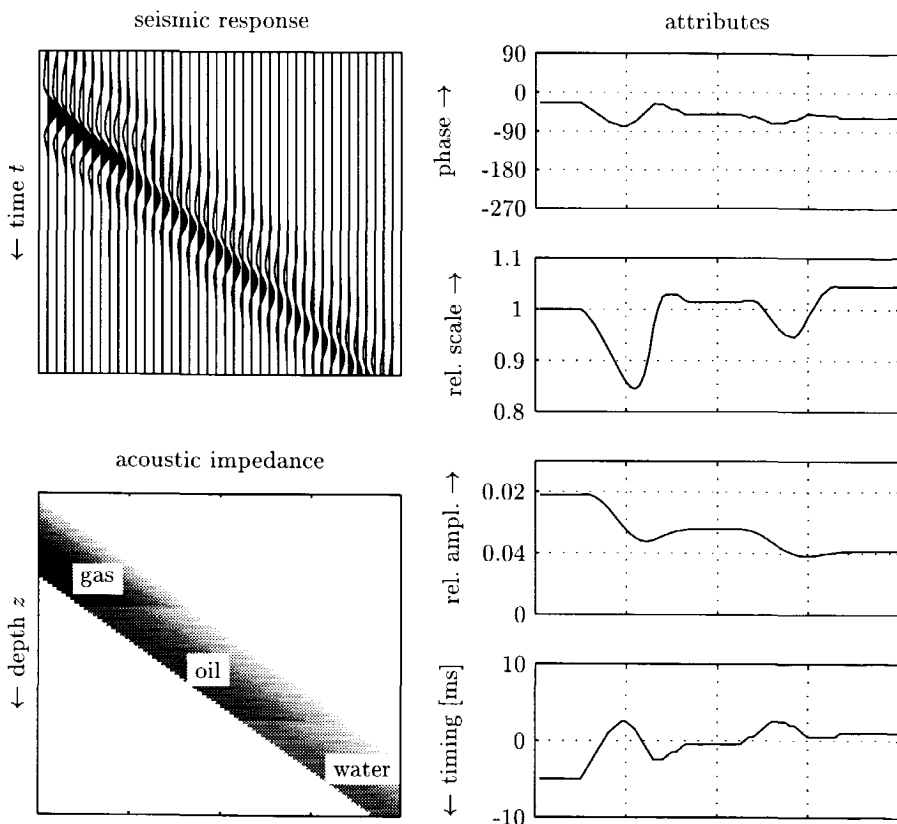


Fig. 4.20 The effect of a changing pore fill on the attributes extracted with the matching pursuit method. The amplitude changes most. Especially for the gas filled sand, the amplitudes are much higher than in the water or oil filled case. In the transition zones, where two the sand interval is filled with two different fluida, all attributes show some respons. In general are the responses for all attributes (except amplitude) only minor.

Another example is the event characterized at the bottom of the Ror Formation (fifth atom). From the extracted phase attribute, it should correspond to a step-function. This corresponds well with the sudden change in lithology from the marine sandstones in the top of the Lower Jurassic Sandstone unit, to the claystones and mudstones in the Ror Formation.

The third event, in the Tilje Formation, is more difficult to explain. From the phase attribute extracted, one would conclude a bell-type of sequence. It seems that two different effects play a role: the effect of a relatively small step function superimposed on a funnel type of sequence. This makes that the phase of the funnel

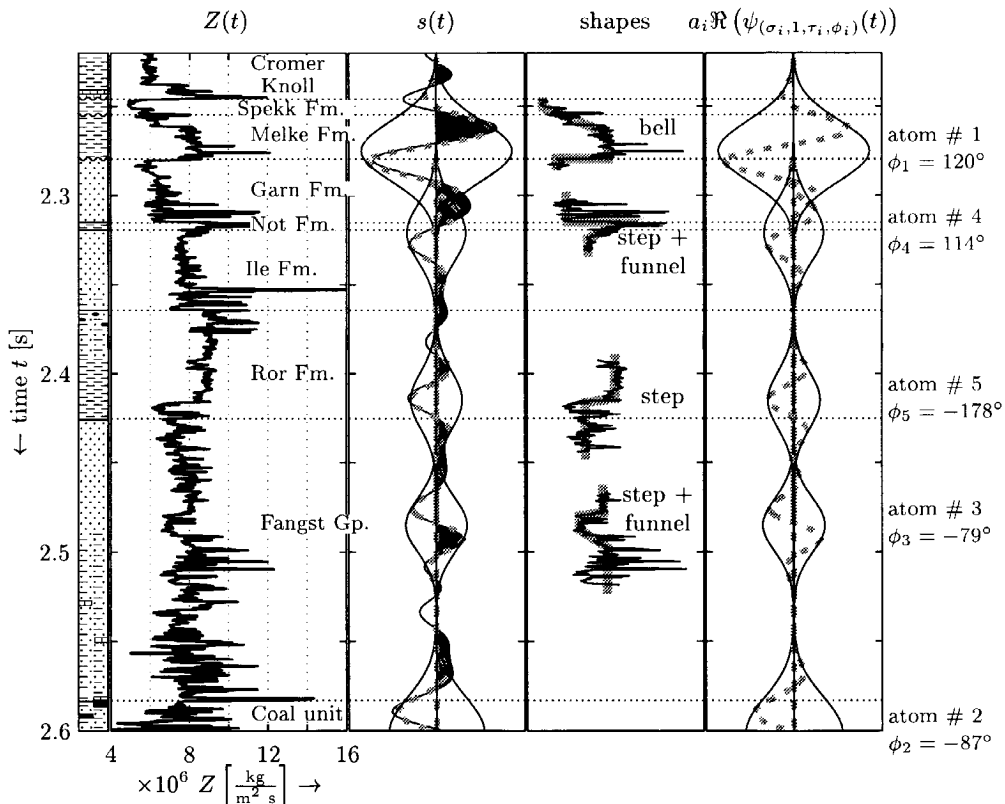


Fig. 4.21 Explanation of the phase-results for the different events analysed in the Saga-well. The shapes in the acoustic impedance Z at the location where the atoms are extracted, are schematically drawn.

(e.g. $\phi \approx -125^\circ$), is partly counteracted by the effect of the step function ($\phi = 0^\circ$). The combined effect results in a phase of $\phi = -79^\circ$.

For the fourth event (around Not Formation), the correct extraction of the local phase seems to be hampered by the extraction of the first atom. One of the small side-lobes of the first atom, alters the peak at $t = 2.3$ s this atom is using. Because this fourth event is much smaller than the first one, even a small discrepancy between the actual wavelet (i.e. a Ricker wavelet), and the Gabor atom, leads to the erroneous extraction of atoms in its direct vicinity.

It is clear from this synthetic example, that the explanation often has to be found in a combined effect of several superimposed types of sequences. When the acoustical properties of the layers above and below the sedimentary unit of interest are relatively constant on a regional scale, changes in the sedimentary unit will still be unambiguously detectable using the phase attribute. The appropriate phase values for the different types of sequences however will be different depending on the specific properties of the layers below and above.

In more complex situations, where interference effects of superimposed sequences are important, catalogues of possible permutations in the sedimentological sequence for the local sedimentological environment can be studied. This can be done deterministically (e.g. Mijnssen (1991) gives some examples for the deltaic environment) or it can be done statistically using simulated wells based on geological knowledge of the local sedimentological environment (de Groot, 1995; de Groot et al., 1996).

In the next section, the described methodology will be evaluated on a rather shallow 3-D data-set from the Gulf of Mexico, and on a much deeper 3-D data-set from Northern Europe.

4.4 Application to 3-D migrated data-sets

The method described in previous section is well suited to work quantitatively in situations where relatively thick sands are inbedded in laterally invariant shales. Additionally, the sedimentary package should show a low net-to-gross ratio, such that the seismic response from the facies is not interfering with other seismic responses. In the first example, originating from the Gulf of Mexico, both conditions are fulfilled.

In a second example (Northern Europe), the first condition is not fulfilled. In these conditions, the quantitative use of this method is not possible, but still

qualitative results can be obtained.

4.4.1 Description of the first data-set: Gulf of Mexico

The described methodology is applied on a 3-D migrated data-set (courtesy of GECO-Prakla¹¹) on the continental shelf in the Gulf of Mexico. The data originates from the South Marsh Island area, of the coast of Louisiana, west of the current delta of the Mississippi river.

The original data had an in-line and a cross-line spacing of 12.5 m and 25 m, respectively. The sampling interval in time was 4 ms. A down-sampled version was provided with spacings of respectively 25 m, 50 m and 8 ms. A total of 126 time-slices were available ranging from 0.5 to 1.5 s. The areal extent is 14.5 km by 22 km.

The sedimentary layers imaged in the seismic cube are Pleistocene in age. In the Pliocene and Pleistocene the main depocenter of the Mississippi river system was migrating basinwards and westwards (Hunt and Burgess, 1995). The sedimentary features in the area are paralic (deposited at or near sea level, for instance a delta system (Haskell et al., 1995)) and submarine slumps (Nissen et al., 1995). Other important features in the data are salt and wrench fault tectonic features and some subtle synclines. Away from the disturbed zone caused by the salt diapire, the sediments were only mildly influenced by tectonics.

The current Mississippi delta is considered to be representative for the delta in the Pleistocene age. A radar image acquired during NASA's Mission to Planet Earth programme (Figure 4.22) shows the present-day active Mississippi delta front (NASA, 1995). Some important structures can be seen on the image. The main distributary channel (denoted with C on Figure 4.22) has a width of 1.4 km. A whole hierarchy of smaller distributary channels exists, down to a width of 80 meter. On Figure 4.22 also the natural levees (L) are indicated. Under extreme flooding, the river can break through its levees, creating a crevasse splay, a type of fan (F) deposited in mud flats/marsh land. A marsh island can be seen on the image (the S-shape feature on the image at the mouth of the almost horizontal channel in the lower-right corner). No clear distributary mouth bar is however visible. The Gulf of Mexico (or the open sea) is situated at the right and the bottom part.

The Mississippi delta-system deposits its sediments on the continental shelf, draping it over the edge onto the continental slope (a passive margin) (Press and

¹¹Amoco Production Company and Dr. Walter Rietveld specifically are acknowledged for making the data available.

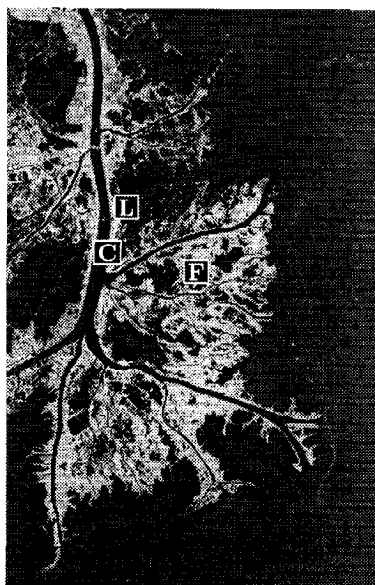


Fig. 4.22 Spaceborne Imaging Radar-C/X-Band Synthetic Aperture Radar picture of the present Mississippi-delta. The area shown is approximately 63 km by 43 km. Some geological facies are indicated: **C** distributary channel, **L** natural levee, **F** crevasse splay (a type of fan).

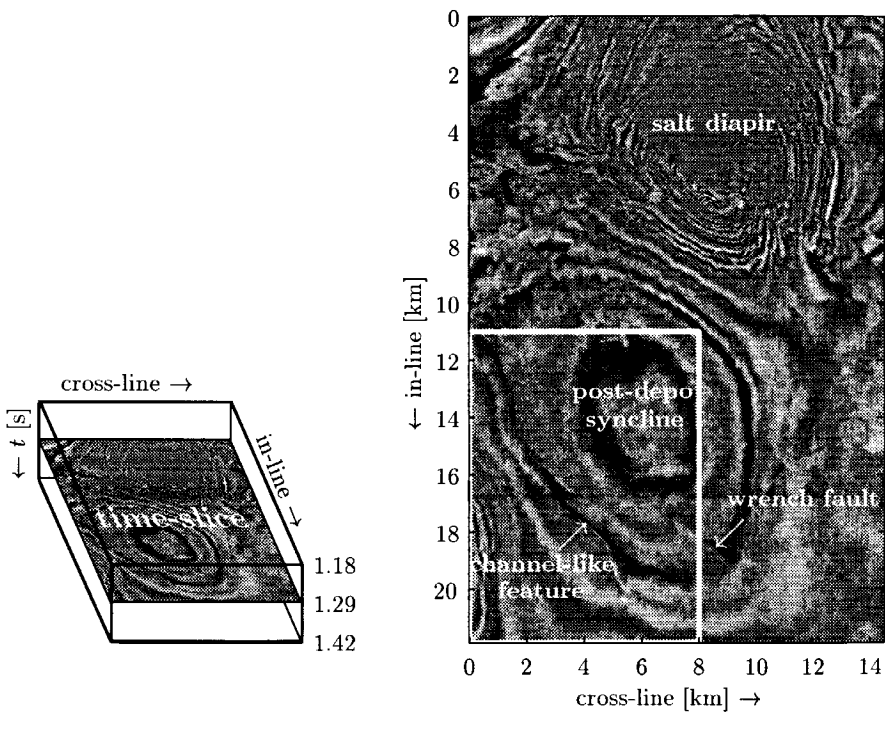
Siever, 1985; Hunt and Burgess, 1995). Due to subsea currents, at some locations along the slope, sub-marine fans / canyons exist, partly eroded in the shelf. Sediments on the slope can be triggered to generate a turbidite. These currents may gully the slope and excavate new sub-marine canyons. The slope can also become unstable without additional sedimentary loading, thus forming slumps.

This data-set was used in a variety of characterization studies. Dessing (1997) used it for 3-D wavelet-based image analysis, Steeghs (1997) used it for the evaluation of time-frequency analysis tools based on the Wigner distribution. A more extensive data-set (a larger areal coverage) has been studied using coherence cube technology¹² (Bahorich and Farmer, 1995; Haskell et al., 1995; Nissen et al., 1995; Gersztenkorn and Marfurt, 1996; Gersztenkorn et al., 1996; Marfurt et al., 1998). In section 4.6, the results from the different techniques will be compared. The sub-set we have used is located on the left third of Figure 6 in Bahorich and Farmer (1995).

¹²Coherence cube is a trademark of Coherence Technology Company.

4.4.2 Characterization of a delta front system

A time slab between 1.180 and 1.412 s (30 time-samples) was selected from the 3-D data-set. Figure 4.23 presents the configuration of the selected time-slab. Some features on the time-slice in the middle of the slab, namely $t = 1.292$ s, are indicated as well. The analysis results from the indicated region will be presented. The Gabor-atoms were fitted on the inner 20 time samples, using five outer samples on top and bottom to avoid edge effects. A scale-range σ from 32 to 80 ms was used.



(a) Configuration of selected time-slab.

(b) Time-slice at $t = 1.292$ s.

Fig. 4.23 Configuration of the selected time-slab. Approximately the middle time-slice at $t = 1.292$ s is also given as reference. The analysis results for the indicated rectangle are shown in Figure 4.24. On the time slice two types of fractures are visible: some associated with the salt diapir, and a wrench fault system going through the upper-right corner of the rectangle. Another channel-like feature can be seen on the diagonal of the rectangle. Data courtesy of GECO-Prakla.

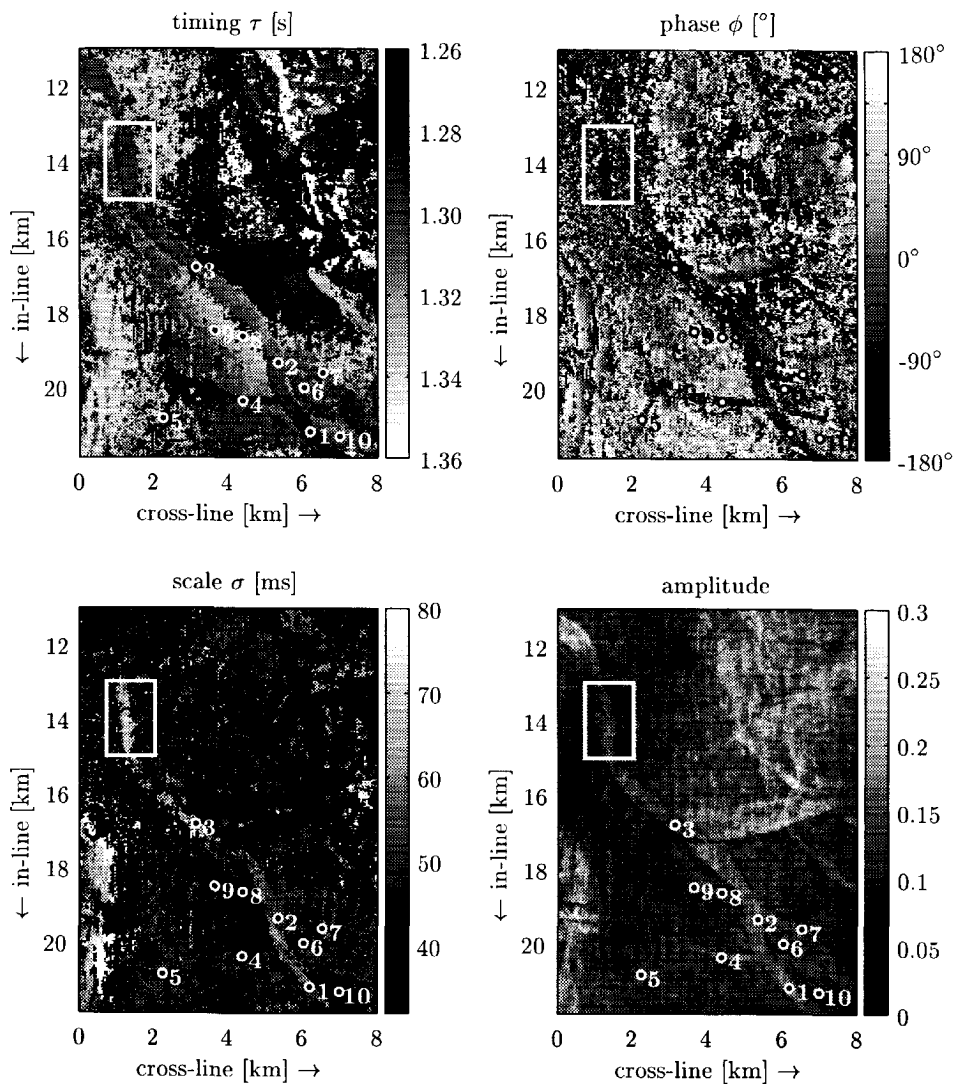


Fig. 4.24 The parameters τ , ϕ , σ and amplitude for the best-fitted Gabor-atom in the time window [1.180 s, 1.412 s]. This analysis is performed trace-by-trace in the time direction, and the resulting parameters are plotted in map view. For each in-line/cross-line position, the analysis result for the trace in the time window is plotted. The numbers [1-3] indicate a 500 m wide channel-like feature, [4] a fault, [5] a small distributary channel (100 - 200 m wide), [6, 7] a point bar and [8-10] marsh or possibly levee. At each location the fit is shown in Figure 4.26. The box indicates the location for the zoom on Figure 4.29.

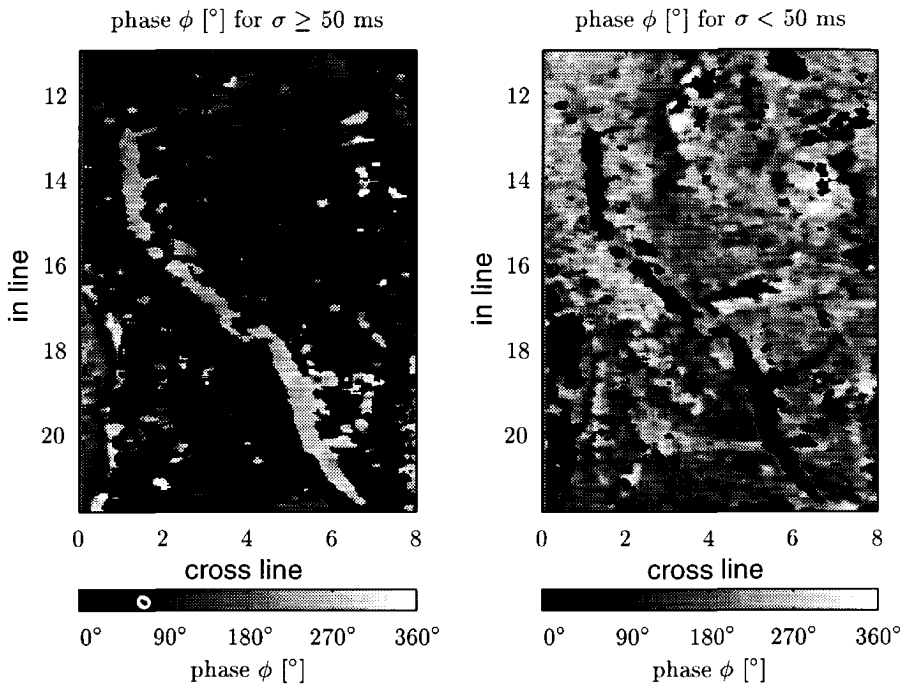


Fig. 4.25 The phase information from Figure 4.24 filtered and subdivided between locations with a scale σ larger or smaller than 50 ms. The phase attribute was also L1/L2-filtered¹⁵. The colorbar differs from the one used for Figure 4.24 and $\phi = [-180^\circ, 0^\circ]$ is mapped to $\phi = [180^\circ, 360^\circ]$.

Figure 4.10 visualizes the chosen parameters τ and σ . The analysis results for this time slab are given in Figures 4.24 to 4.30.

Figure 4.24 shows the results of the matching pursuit analysis using Gabor-atoms. The analysis was performed trace-by-trace, and the four resulting parameters are plotted in map view (Figure 4.24). The fitting follows consistent geological features as can be seen from the timing τ . A channel-like feature [1-3] is consistently picked, even though the fit is independently done from trace to trace. A second feature indicated by [6, 7] is also consistently picked. The method seems to be very well suited in finding geological events, and can be used for tracking purposes. The

¹⁵ A L1/L2 filter works in two steps. In a first step, the values in the neighbouring locations are taken and ordered in size. A percentage of the highest and of the lowest values are eliminated. In a second step, the average of the remaining values is calculated.

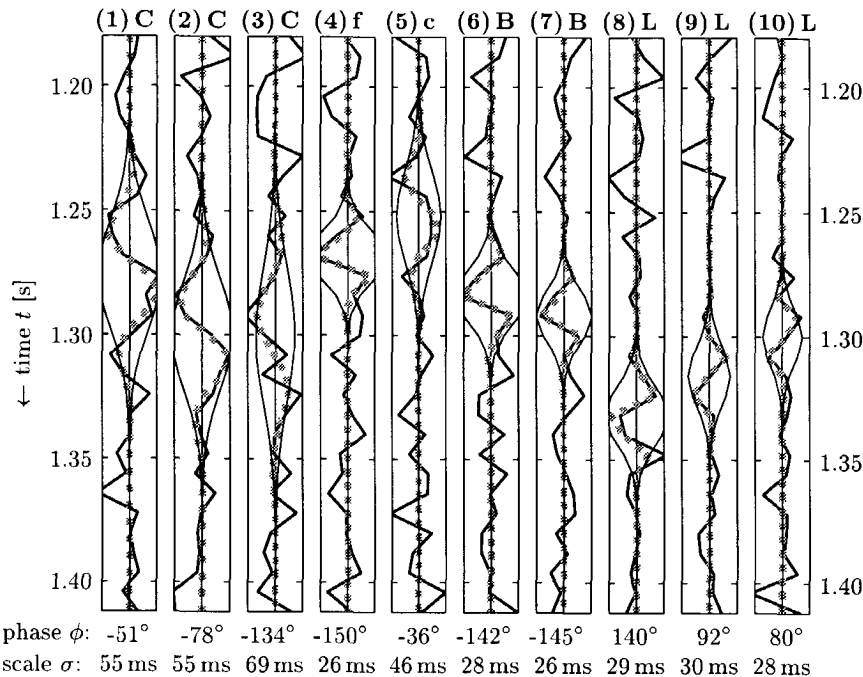


Fig. 4.26 The traces and the analysis results for the 10 locations indicated on Figure 4.24. The type of facies is indicated above the trace. The first three traces are taken from the channel-like feature (C). Trace 4 is on a fault (f) and trace 5 on a small channel (c). Traces 6 and 7 are from a point bar (B). The last three are from levee or marsh (L). The original trace is drawn in a thick solid line, the fitted atom in a thick dashed line, the envelope in thin solid line. Note that the fits are often very well, and are not much influenced by some high frequency features. This feature makes this method less vulnerable in the presence of noise. Under each trace the phase ϕ and the scale σ of the fitted Gabor-atom is indicated. Note that the phase ϕ for the channel is around -90° , that of the point bar around -45° and for the levee around $+100^\circ$.

amplitude from the Gabor-atom shows that the channel contrasts well with the marine clays in which it is inbedded (Watkins et al., 1987), as already could be seen from the unprocessed seismic time slice (Figure 4.23). Some acquisition footprint effects can be noted as streaks along the in-line direction. Note that the amplitude derived from the Gabor-atoms is always positive in sign. The scale σ of the picked events shows that the main channel-like feature [1-3] has a thickness of up to 80 ms,

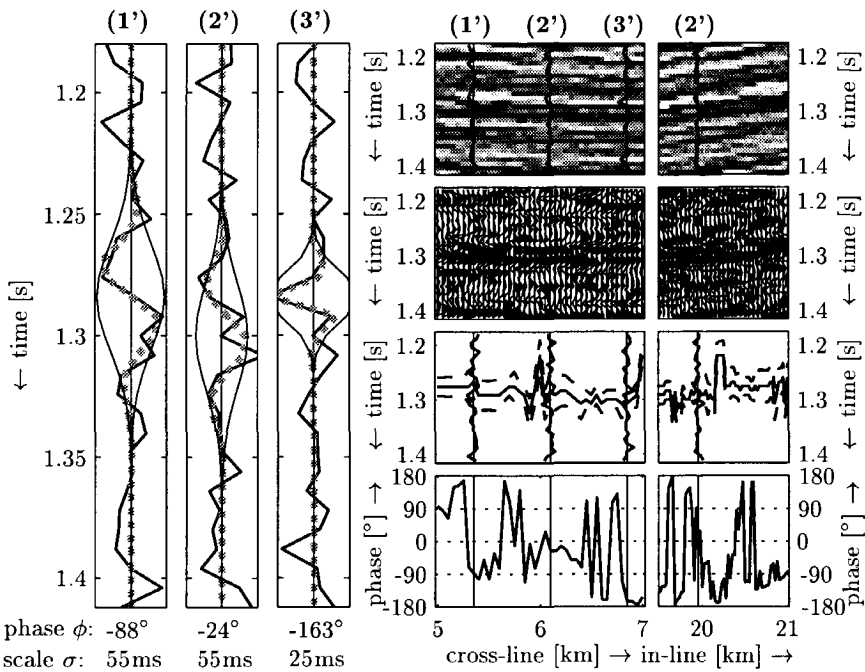


Fig. 4.27 Seismic cross-section along in-line = 19.95 km, compared with the matching pursuit results. On the left-hand side, for three traces the fitted Gabor-atom (in dashed line) with its phase and scale attributes (below the plot). On the right-hand side a cross section along the locations. The two upper plots give the seismic data in greyscale and wiggle plot. Note the typical “frying pan” pattern, composed out of the channel sand and the point bar to the right of it. Note also a small fault at in-line = 20.5 km. The third plot gives the location (τ , solid line) and the width of the fitted atom ($\tau \pm \frac{\sigma}{2}$, dashed lines). Note the shape and the thickness of the channel section. The figure at the bottom gives the extracted phase information (ϕ) along the line. Figure 4.28 gives a schematic cross section at cross-line = [5 km, 6.25 km].

considerable higher than the other events found. Haskell et al. (1995, 1998) found that the channel-like features did not migrate much laterally, explaining the thick sand bodies. The channels follow mainly the regional dip and show a low sinuosity. There are a few locations however, where the channel crosses an active fault. Under the influence of the fault, the channel was forced to migrate laterally and a point

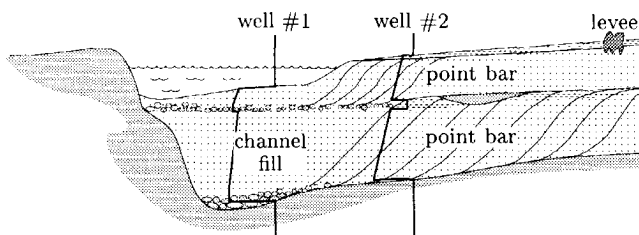


Fig. 4.28 A schematic cross-section through the point bar as found in Figure 4.27. Two typical gamma-ray logs are drawn schematically at two locations. It is clear that the log shape of well #1, through the channel fill, can be classified as a blocky shape. The phase attribute of $\phi \approx -90^\circ$ is in agreement with this. The log shape of well #2, through the point bar, has a typical bell-shape. This is in agreement with a phase attribute of $\phi \approx -150^\circ$. Note that the channel is sand-filled (well information described in Haskell et al. (1998)). This is particular, since commonly the channel part is filled with clays, the so-called clay plug. This figure is modified after Haskell et al. (1998).

bar is developed Haskell et al. (1998). Locations [6,7] indicate such a point bar. Locations [6,7] show a somewhat higher σ than its surrounding, although not so extreme as the channel. The phase information ϕ shows the distributary channels, and the point bar (see Figure 4.25 for a more detailed and filtered version of the phase attribute).

Figure 4.26 shows the fitted Gabor-atoms at the locations 1 to 10 on Figure 4.24. A cross-section perpendicular to the channel at the location of the point bar is made in Figure 4.27. The channel and the point bar seem to be well fitted. Their seismic expression resembles a “frying pan”. Note also the differences in phase ϕ for the different sedimentary facies types. Figure 4.28 shows a schematic cross-section through the point bar. Also two typical well-log profiles (as found in Haskell et al. (1998)) are schematized. The well-logs indicate that the channel part is filled with sand. This is uncommon in these settings. Commonly the channel part of the ox-bow is filled with soft clays after avulsion has occurred, the so-called clay plug. In section 4.5 the phase results from this example will be discussed in more detail. Some internal structures can also be seen in the analysis results (attributes) for the main distributary channel. The main part of the channel has a phase around -90° . Figures 4.29 and 4.30 show some internal structures in the main distributary channel. These structures may be interpreted as tidal flats or possibly parts of a small point bar. The patterns found in Figure 4.29 might confirm this.

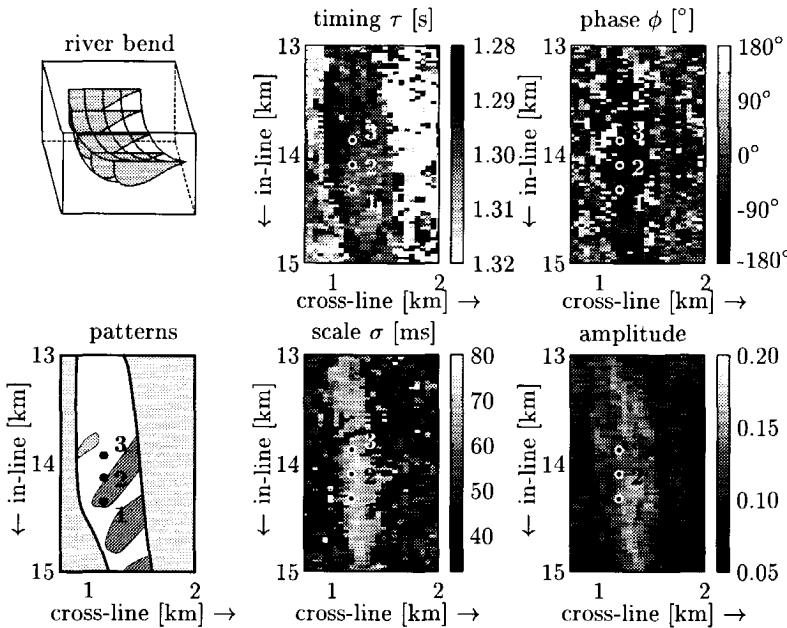


Fig. 4.29 A zoom on a part of the main distributary channel (rectangle on Figure 4.24). Some subtle changes can be seen on the Matching Pursuit results (on the right-hand side), indicating some internal structures. An interpretation of the structures is sketched on the left-hand side. Note also that the scale attribute indicates a larger thickness on the left-hand side of the channel, due to a right turn bend just below the part analyzed here. For the locations [1-3] the traces with analysis results are plotted in Figure 4.30. The phase information is sensitive to very subtle changes.

The main channel-feature as investigated in this section is too thick to be a normal distributary channel. The width of the distributary channel is here approximately 650 meter. On average the scale attribute ranges from 60 to 70 ms. In depth this would be approximately $\Delta s = [75 \text{ m}, 105 \text{ m}]$. The resulting width to thickness ratio $W/T = [6, 9]$ is however low for non-migrating distributary channel-fills when compared to the typical range of $W/T = [15, 60]$ mentioned by Weber (1986). Wider distributary channel-fills ($W > 500$) even tend to have a W/T larger than 40. A normal thickness for a channel this wide would be between 3 en 15 meter. Also the fact that the channel bed is sand-filled is exceptional. A possible explanation might

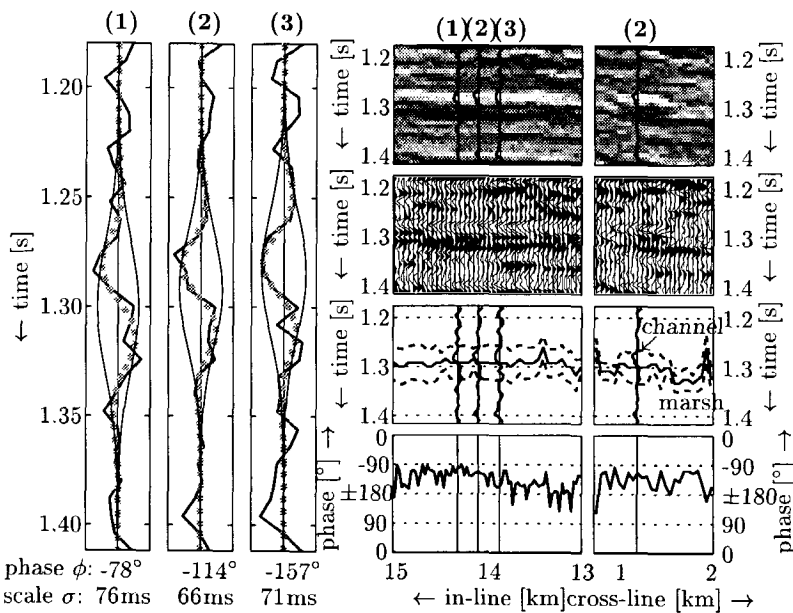
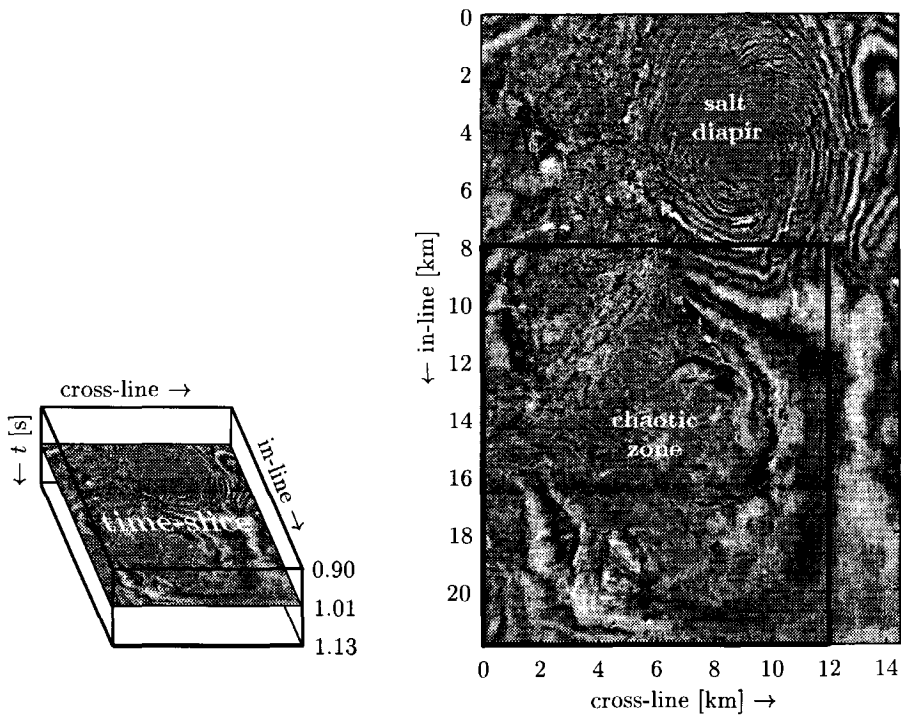


Fig. 4.30 The analysis results for the locations [1-3] on Figure 4.29 on the left-hand side. The original trace (solid line) with the matched Gabor-atom (thick dashed line) are given. The scale and phase attributes for these fits are given below the plots. In the middle a cross-section along the axis of the channel, through the three locations is given (cross-line = 1.2 km, in-line = [13 km, 15 km], $t = [1.18 \text{ s}, 1.412 \text{ s}]$). The 2 upper plots are a greyscale and a wiggle plot of the seismic data. The third plot gives the location (τ , full line) and the width of the fitted atom ($\tau \pm \frac{\sigma}{2}$, dashed lines). The last plot gives the phase attribute (ϕ) along the line. Note also the very subtle but consistent changes in this attribute, causing the patterns seen on Figure 4.29. On the right-hand side a cross-section perpendicular to the axis of the channel and through location 2 is made (in-line = 14.1 km, cross-line = [0.75 km, 2 km]). The section of the channel can be seen.

be that the channel is part of a incised valley system (see for an example in Posamentier (2000)). This occurs when the relative sea level drops considerably, and the channel incises into the shelf. Due to the incision of the channels in stiff and difficult erodible marine clays (Watkins et al., 1987), the channel is more or less canalized. Only where the channel is forced by an active fault, lateral migration occurs.

4.4.3 Characterisation of a sub-marine fan system

A time slab between 0.900 and 1.132 s was selected from the 3-D data-set. Figure 4.31(a) shows the configuration of the selected time slab, Figure 4.31(b) shows the time-slice in the middle of the slab, namely at $t = 1.012$ s. In the right-upper corner we find again the salt diapir with associated emplacement fractures. The feature we want to analyze is the lobate, chaotic structure inside the rectangle on Figure 4.31(b). Nissen et al. (1995); Haskell et al. (1995, 1998) analyzed the same



(a) Configuration of selected time-slab.

(b) Time-slice at $t = 1.012$ s.

Fig. 4.31 Time slice at $t = 1.012$ s. The analysis results for the indicated rectangle are shown in Figure 4.34. In the middle of the rectangle a lobate, reversed ♣-shaped area with rather chaotic seismic events is present. This area is identified as a sub-marine canyon with slump blocks (Nissen et al., 1995). The shelf edge is located outside the data-volume to the north, the head is around in-line = 19 km. Data courtesy of GECO-Prakla.

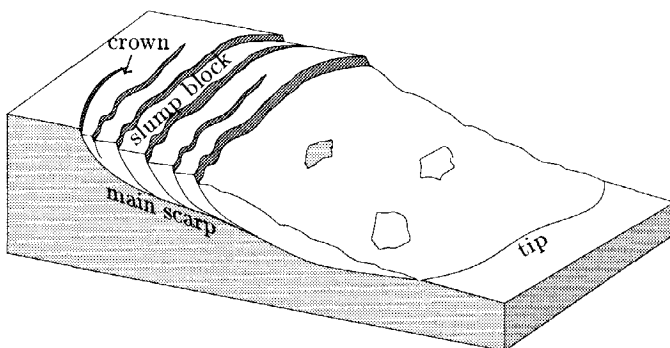


Fig. 4.32 A schematic cross-section through a slump feature.

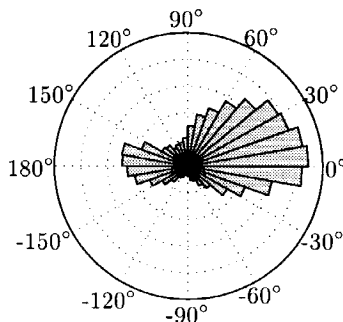


Fig. 4.33 Angle histogram for the phase attribute for a subset including only clearly detected lobes as shown in Figure 4.34 (in-line = [16 km, 20 km] and cross-line = [3 km, 7 km]). The histogram shows two clear peaks, at $\phi \approx 180^\circ$ and $\phi \approx 0^\circ$. The one at $\phi \approx 0^\circ$ is most pronounced. This agrees well with the interpretation of the erosive basis of the submarine canyon as being a step-function.

data-set (supplemented with 5 wells) using the *coherence cube-technology*, and found an approximately 350 meter thick Late Pleistocene sediment package, extending from approximately 750 to 1100 m below sea level. In two-way time (TWT) this corresponds to 800 - 1100 ms¹⁶. It is interpreted as the head of a submarine canyon, eroded at the shelf edge (Haskell et al., 1998). Some chunky structures were found,

¹⁶The strongest and most interesting reflectors in this package are situated at the bottom of the Pleistocene package, explaining the selection (between 0.900 and 1.132 s) of the seismic data to be analysed.

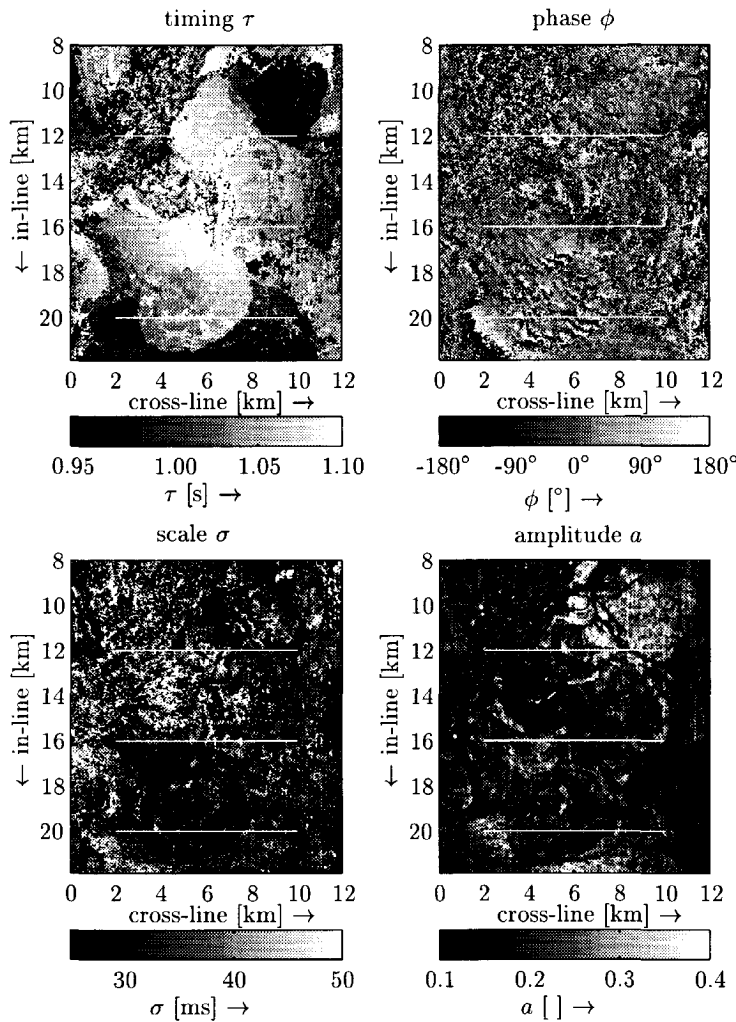


Fig. 4.34 The analysis results for the region with the sub-marine fan system. The timing results (τ) display several lobby events on different time-levels. The noisy zone around coordinate (cross-line = 4 km, in-line = 14 km) is caused by the feature running out of the time window. Some smaller structures are visible, but also some noise is present. The phase attribute (ϕ) is rather scattered, but with a preference for $\phi = 0^\circ$ (Figure 4.33). The observed scattering of the values of ϕ is partly due to the predominant small scales observed ($\sigma = [24 \text{ ms}, 32 \text{ ms}]$, equal to 3 - 4 samples). This makes the phase attribute ϕ more susceptible to noise. The amplitude and timing attributes show a surprising detail. The picked event is mainly the basis of the sub-marine canyon and the scarps for the different slumps.

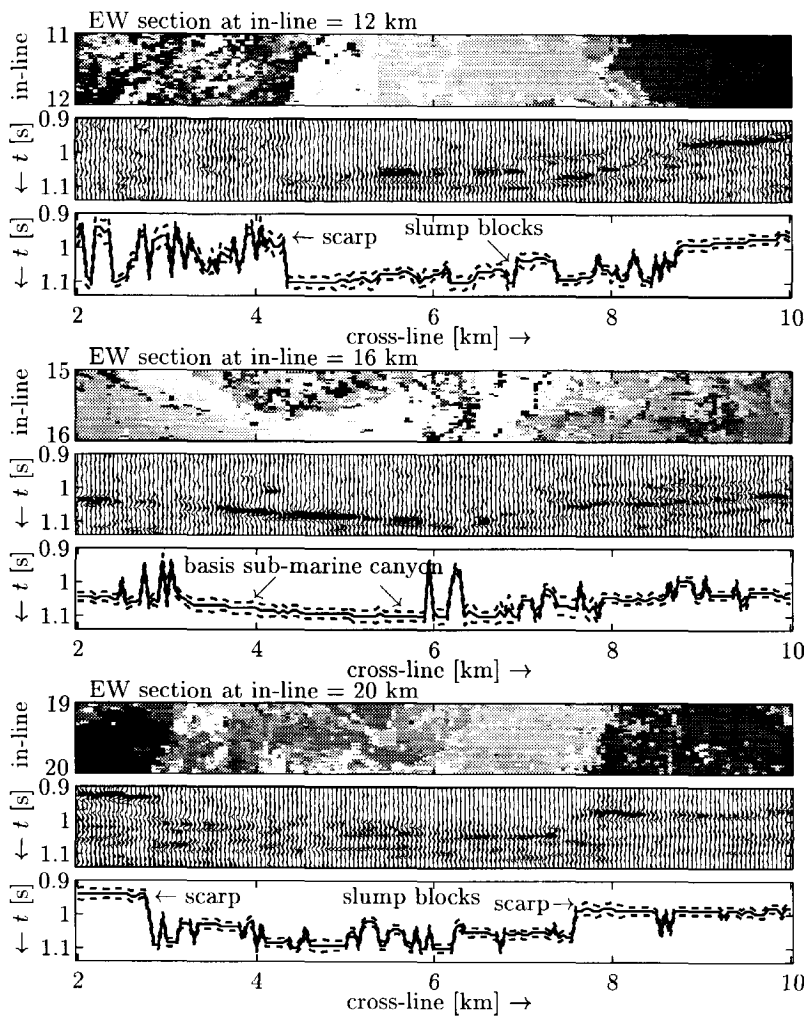


Fig. 4.35 The seismic cross-section at the three in-line positions indicated on Figure 4.34. For each cross-section a part of the timing-map on Figure 4.34 is reproduced for reference. Secondly the seismic data is reproduced on the given location. Thirdly the location of the fitted event is drawn: τ (the middle of the event) is indicated in solid line, the top and bottom $\tau \pm \frac{\sigma}{2}$ are given in dashed line. Step-like features can be noticed, especially on in-line = 20 km. The outer ones are the slump scarps (arrows). The smaller inner ones are evidence for slump-blocks. The picks are independent from trace to trace, but are nevertheless very consistent. The main event picked is interpreted as the basis of the sub-marine canyon.

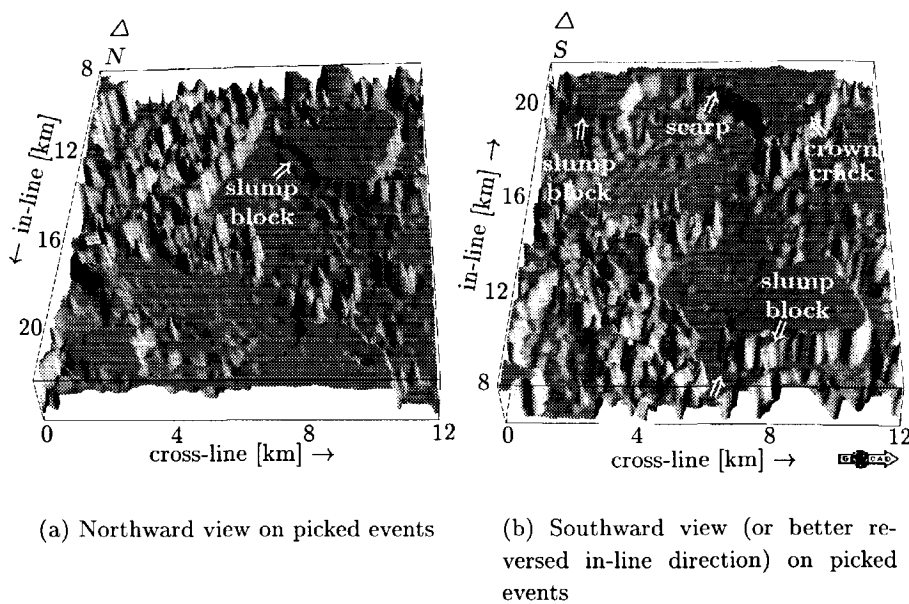


Fig. 4.36 View on the top of the picked events after L_1/L_2 filtering and down-sampling (to 100 by 100 m). A surface was constructed in gOcad. The height is the time of the top ($\tau - \frac{\sigma}{2}$) of the picked event. The general blocky structure can be easily studied. Notice the step-like small blocks (indicated by arrows) at the edge of some of the large blocks.

interpreted as intact slump blocks (Figure 4.32). In the region of in-line = 16 - 20 km, the head is situated. Around this head some arculate rotational fractures can be seen, interpreted as “crown cracks” (Haskell et al., 1998; Coleman, 1982).

The time-slab was analysed using the matching pursuit method described in section 4.3.2. The results within the frame indicated on Figure 4.31 are given in Figure 4.34. The results are in general noisier than the results obtained for the delta front system in the last section, but that is no surprise as the depositional system in this environment is much chaotic. The timing results clearly show lobate structures. The amount of detail that can be seen is surprisingly good. The phases are more scattered than in the previous chapter. Because of the abrupt nature of the lower contact of the slumps with the underlaying sediments, a step-function type of event can be expected. In the histogram for the phase-attribute shown in Figure 4.33, clearly two peaks can be seen at $\phi = 0^\circ$ and $\phi = 180^\circ$, with the first peak being much more pronounced.

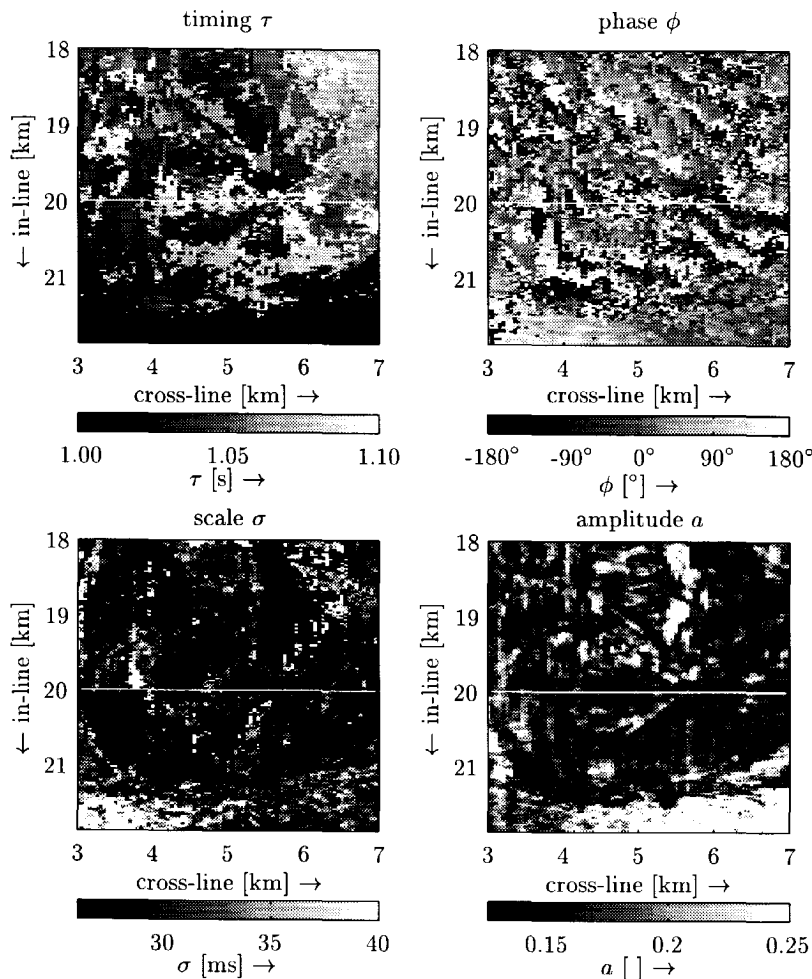


Fig. 4.37 A zoom on the central lower part of Figure 4.34. Note the detailed features on the timing and the amplitude data. The features almost look like a frozen liquid with little chunky particles (slump blocks) in it.

For three in-line cross-sections the results are compared with the seismic data (Figure 4.35). The scarps can be easily seen. Some blocky features can be seen, possibly slump blocks. In some areas consistent features were extracted that can hardly be seen in the original data. As explained in section 4.3.2, only the best fit is selected in the time-window. When several competing features are present in

the time window, this can cause problems. Nothing however obstructs the fitting of more than one event (Chakraborty and Okaya, 1995, and Figure 4.11). Two views on the top of the picked structures are given in Figure 4.36. The several blocky features are clearly visible and interpretable on a graphical workstation. Very small blocks in the order of 200 by 800 meter can be studied. Figure 4.37 shows a zoom on the data. Note the very small features in the timing and the amplitude data.

4.4.4 Description and results for the second data-set: Northern Europe

Because the first data-set was very shallow ($t = [0.5 \text{ s}, 1.5 \text{ s}]$), another dataset was studied to validate the potential of the method. Saga Petroleum generously offered a 3D data-set originating somewhere from Northern Europe. The total area of the survey is 1600 km^2 . The subset we received is $17.4 \text{ km} \times 40 \text{ km}$. The sampling in both in-line and cross-line direction is 18.75 meter. The sampling in the time-direction is 4 ms. The data comes from an area with a water depth of approximately 1400 meter. The zone of interest is at more than three seconds two-way traveltime. It contains a distributary channel system, approximately 15 km wide running in the

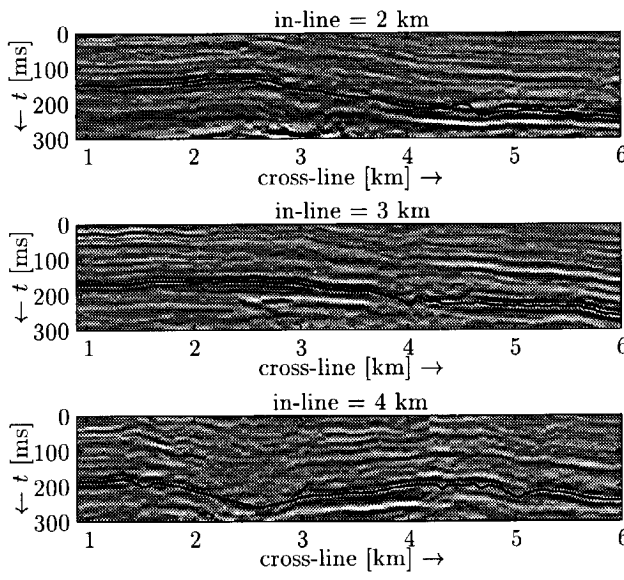


Fig. 4.38 Some cross-sections through the data-volume. The interpreted horizon used for the matching pursuit is indicated. Note that the time-axis was shifted.

cross-line direction. The horizons at this location seem to be influenced by later tectonics. Saga provided us with four interpreted horizons throughout this channel system.

One of the interpreted horizons was selected. Every other trace in the in-line

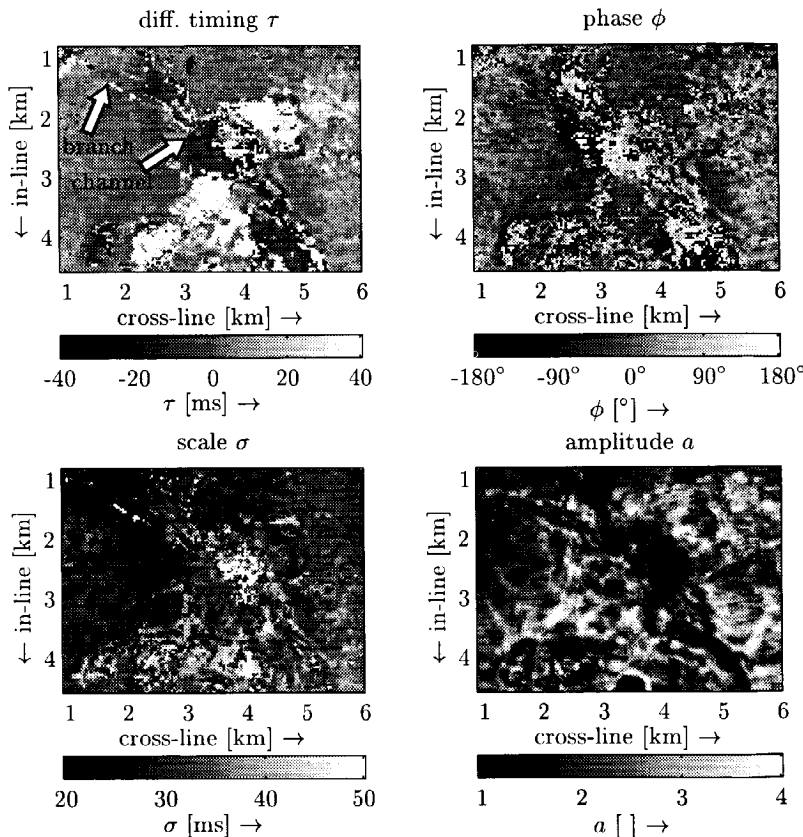


Fig. 4.39 Analysis results for the Northern Europe data-set. A 1 km-wide channel belt running diagonally just below the interpreted horizon is detected (arrow). At some places individual, 200 meter wide, channels can be seen. The interpretation is made not so much on the scale information, but more on the combination of phase, amplitude and timing. Note that not the absolute timing is shown due to the overprint from the later tectonics, but only the differential timing (relative to the interpreted horizon).

and the cross-line direction was used, resulting in a sampling interval of 37.5 meter. Due to tectonics, the window on which the matching pursuit procedure was done was chosen relative to an interpreted horizon. A time slab of 50 samples (200 ms) was chosen, around one of the interpreted horizons. A scale-range of $\sigma = [16 \text{ ms}, 60 \text{ ms}]$ was used. The results (Figure 4.39) show a 1 km wide channel system, running diagonally. Some smaller (200 meter wide) channels and branches were also detected. Channels are characterized by low amplitudes (unlike the Gulf of Mexico example).

Although this data-set is much deeper and severely influenced by tectonics, the results still are very good. Some artifacts in the picking of the events were noticed due to difficulties on the interpretation of the boundaries. Because a time-window relative to an interpreted horizon was used, this may generate artifacts when the interpretations are not consistent.

4.5 Geological classification by means of wavelet shape attributes

The matching pursuit results worked well in detecting different geological events. The analysis results for the delta front and the sub-marine fan system seemed to show distinct ranges for the different properties of the fitted Gabor-atom.

Because of the fact that in the delta front example different geological features were present, this dataset was used to study the possibility to relate the attribute values directly to the geological features. Moreover, the results from the synthetic examples from section 4.3.3, can be checked with examples from real data.

The results for the real data are selected from the Gulf of Mexico data set,

| Facies | in-line range | cross-line range |
|---------------------|--------------------|------------------|
| Incised valley fill | 19.1 km - 19.8 km | 5.0 km - 5.5 km |
| Levee / marsh | 18.5 km - 20.0 km | 3.8 km - 4.8 km |
| Point bar | 19.5 km - 20.25 km | 6.0 km - 6.9 km |

Table 4.1 The selections used for the generation of the histograms in Figures 4.40 and 4.41. Note that these selections do not enclose the total area of a specific facies type. Due to the noisy character of the point bar results, only the locations where the timing $\tau \in [1.292s, 1.308s]$ were selected for the generation of the point bar histograms.

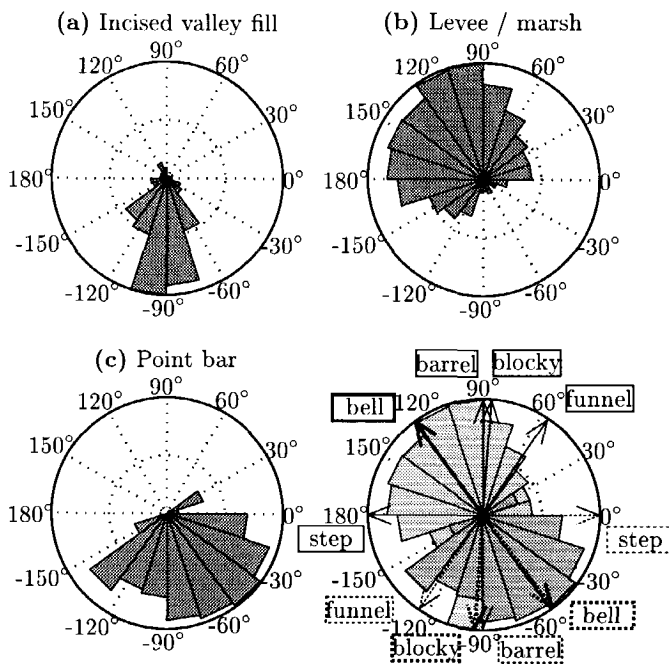


Fig. 4.40 Phase attribute (ϕ) extracted from the optimal Gabor-atom for different facies types. Distinct distributions of the phase attribute for each facies seems to exist. On the right bottom figure, the distributions of the three facies types are compared with the synthetic results from Figure 4.17.

the delta front system (section 4.4.2). The actual areas selected for each facies are given in Table 4.1. In Figures 4.40 and 4.41, the histograms for the shape attributes (phase ϕ , scale σ and amplitude a) from the matching pursuit analysis are shown. Each of them characterizes a distinct aspect of the wavelet-shape. Especially the phase attribute seems promising for the characterization of geological structures. Comparing with the modeling results (section 4.3.3), a good agreement was found. The incised valley fill was classified as a blocky type of sequence. The levee/marsh is classified as a bell-type sequences but with an opposite polarity. The point bar is found to be a bell-type of sequence which is in agreement with Haskell et al. (1998) (see also Figure 4.28). Some precautions have to be taken when using these results. The synthetic modeling was done by studying the typical log-shapes in isolation and embedded between two layers with the same acoustical properties. Problems may arise when different sequences are stacked on top of each other. A seismic wavelet hardly ever carries information about one sequence only. Problems may also arise when the layers above and below have different acoustical properties. As was shown

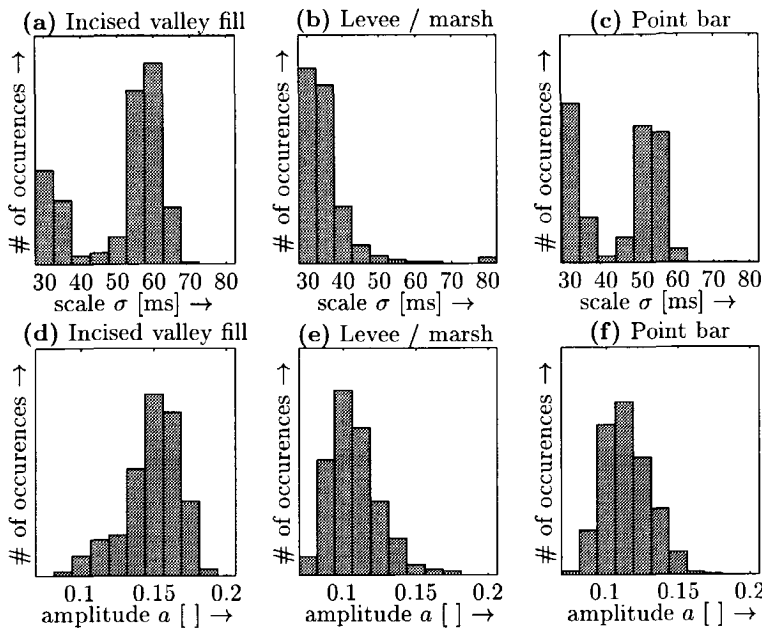


Fig. 4.41 The histograms for scale σ (a-c) and amplitude (d-f) for the fitted Gabor-atoms. The incised valley fill exhibits a relatively large scale and high amplitude.

with a synthetic example in section 4.3.6, a difference in acoustical properties in the layer above and below the sedimentary layer under study would cause the phase attribute to be shifted.

In the results shown here, most likely almost no difference in acoustical properties between the layers above and below was present. The delta front system studied here was deposited in marine shales. Marine shales are often found to show very little change in their acoustical properties. In addition, the Mississippi was starved at the time the studied sediments were deposited. This means that only relatively little coarse material (e.g. sand) was transported and deposited by the Mississippi river in that period, leading to a low occurrence of sandstone units in the sediment package. In comparison, marine clays are very abundant, leading to a high degree of spatially isolated sandbodies.

Although the phase attribute already showed a good separation between the different facies types, the attributes scale σ and amplitude show an additional separation for the different facies types (Figure 4.41). Combining the three attributes

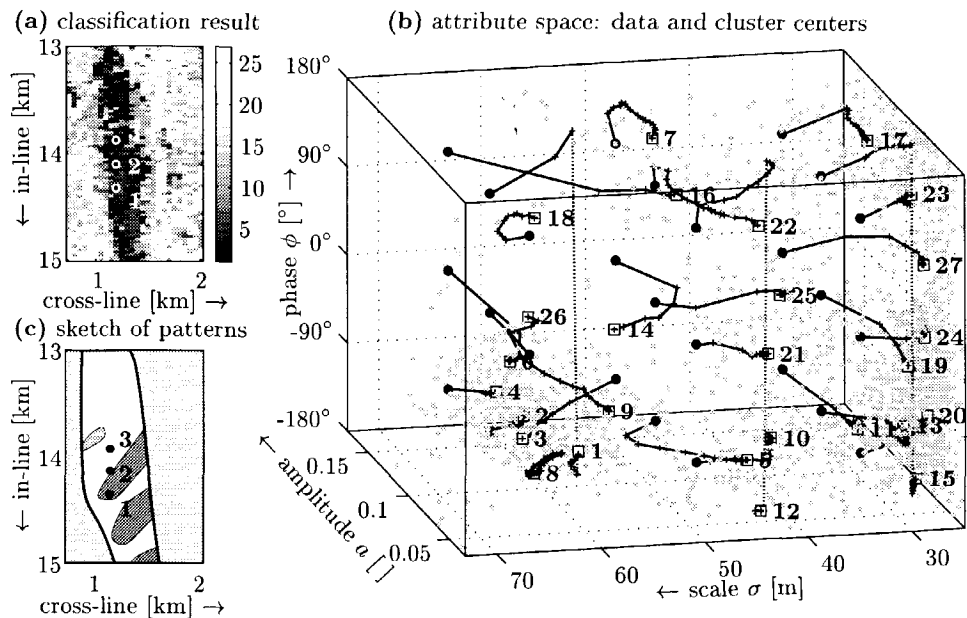


Fig. 4.42 *K*-means clustering results for the same area as in Figure 4.29. The method was adapted to take the circular phase axis into account. (a) Resulting classification (resulting class number is plotted in gray-scale). The locations [1-3] indicate the traces plotted in Figure 4.30. (b) Attribute space: data (*) and clustering results. Starting from 27 equidistant locations (●), the cluster centers move via intermediate (+) locations to the final locations (□). Numbering at the final location corresponds with the class numbers in (a). The numbering is increasing with distance of the cluster centers to the center of the data cloud for the main incised valley fill (bottom left). Note that the majority of the data points in the $\sigma = 24$ ms plane are points coming from outside the channel. (c) A sketch of the patterns found in (a).

related to the wavelet shape, gives an even better separation in attribute space (Figure 4.42). Using a clustering technique, the data is grouped on the basis of closeness in three-dimensional attribute space. Other classification methods such as the unsupervised techniques from the neural network domain can be used as well (de Groot, 1995).

4.6 Comparison with other techniques

The first data-set (Gulf of Mexico) has been used in multiple characterization studies. Different methods were tested on the same data-set. The different methods we know of are:

- coherence cube technology (Bahorich and Farmer, 1995)
- eigenstructure-algorithm (Gersztenkorn and Marfurt, 1996)
- wavelet-based edge detection (Dessing, 1997)
- local Radon-Wigner-algorithm (Steeghs, 1997)
- matching pursuit method (this chapter)

A discussion of the results on the basis of the publications can be made. First let us briefly discuss the different techniques.

The coherence cube technology (Bahorich and Farmer, 1995) was first tested on the Gulf of Mexico data-set. The algorithm looks for changes in adjacent traces by calculating in a time-window the coherency between a trace with its neighbors. At the beginning only two neighboring traces (three traces in total) were used, now this number can be higher. The results on the Gulf of Mexico data-set show very good results on the extraction of faults, but the results on the channels is not so good. Moreover, as a relative method, it is not straightforward to make the connection with the material properties (e.g. facies type).

Gersztenkorn and Marfurt (1996) compute the eigenstructure of the covariant matrix of neighboring traces in a given time-interval. This method is related to the coherence cube technology, and looks also at changes between traces. The results are slightly better than those of the coherence cube, but again the method has problems in detecting channels.

The wavelet-based edge detection (Dessing, 1997), is also looking for changes in the seismic volume. It uses a very straightforward method by combining 1-D edge detection measurements at an appropriate scale in the three axis directions. This method is mainly sensitive to changes in amplitudes, and is therefore in this data-set, where the channels have a high impedance contrast with the surrounding marine shales, very powerful.

Steeghs (1997) uses the local Wigner-Radon algorithm to calculate local power spectra of the seismic signal. In this way, he is not only extracting the local mean

| relative methods | absolute methods |
|------------------------------|------------------------------|
| coherence cube technology | |
| eigenstructure method | matching pursuit method |
| wavelet-based edge detection | |
| | local Radon-Wigner algorithm |

Table 4.2 Global classification of the different characterization techniques applied to the Gulf of Mexico data-set.

frequency (= instantaneous frequency) but also the higher moments¹⁷. These results are absolute measures of attributes of the trace, and not like in the previous methods, a measure of difference between traces (e.g. relative attributes). However, in his thesis Steeghs (1997) is using these results to extract local dip-information, what after all is again a relative measure. His results show a successful extraction of faults, but seems not so successful in finding channels. This might be because they only give a very subtle dip-change.

The matching pursuit approach (this chapter) is a typical absolute measure. The method also assumes a wavelet shape and a frequency range. This is a priori information, making this approach more robust. The combined inspection of the four attributes gave the opportunity to extract and classify geological bodies. The method is not particularly suited to detect faults. For fault detection, methods looking for changes in the horizontal direction are more suited. However, the results for the sub-marine fan indicated that the matching pursuit method was able to locate the main faults, like the scarps. This is probably similar to what one can expect from automatically tracked events on a modern interpretation package. Especially with the option (existing in some of the packages) to track using the envelope of the signal. An automatic tracker might have problems due to the discontinuous events.

A first basic difference between these five methods is the type of attributes they extract: the results for the first three methods are based on *differences* between traces (Table 6.1). These methods extract relative attributes, differences from one trace to another. This type of attribute is very powerful in looking at lateral changes. So when the predominant interest is to look for lateral changes in some character of the seismic data, these attributes are very powerful. The last method on the contrary, extracts absolute attributes, e.g. it extracts characteristics at one trace at the

¹⁷This makes that the local Wigner-Radon algorithm extracts more detailed information from the seismic signal. For that reason, it might however be more sensitive to noise and be more difficult for interpretation.

time. This makes it more suitable for building a link towards underlying material properties (e.g. geology). The fourth method, the local Radon-Wigner-algorithm, is in principle an absolute method. By using the raw results to construct a dip-map makes it again a relative method.

4.7 Discussion and conclusions

The attributes derived from the optimal fitted Gabor-atom form an independent set of parameters; each of the attributes characterizes another aspect of the local wavelet. The amplitude is only related to the strength of the wavelet, the phase ϕ to its shape, and the scale σ to its length. A study on some synthetic examples showed that the shape (or phase) of the seismic wavelet might be indicative for the type of sequence. Sequences as dirtying-up (bell-shape) and cleaning-up (funnel-type) produce asymmetrical seismic traces. A matching pursuit approach with Gabor-atoms was chosen to characterize real data. A time window has to be selected. Depending on the geology, this time-window can be constant over the whole volume, or it can be relative to an interpreted horizon. The methodology proved to be very stable in the presence of noise, due to the fitting over a certain length of the trace. Compared with the response phase as calculated from the analytic trace, the phase attribute derived from the matching pursuit method allows 6 to 9 dB extra noise.

Application of the methodology on a 3-D data-set from the Gulf of Mexico proved its ability to extract consistent geological features. Even in the complicated case of deep-marine slump structures, it was able to unravel very small details. Application on a second and deeper data-set from Northern Europe proved that the method can also be applied on deeper and structural more complex data. The quality of the interpreted horizons is very important in this case. The phase information extracted for different geological facies types seems to give distinct distributions, especially in combination with the other attributes. The phase information seems to be highly sensitive for subtle changes in the shape of the wavelet.

The described method analyses the data trace-by-trace, independently. The attributes are absolute and can therefore be used for the characterization of the local facies. Other methods (like coherence cube technology, and 3-D wavelet-based image analysis) are relative, e.g. they look at relative changes between traces. Relative methods are very well suited for the analysis of edges and changes in structures, not for the characterization of the structures. The main difference with the related response attributes are that a priori information in the form of an expected wavelet shape and a frequency range are used. This makes the matching pursuit method less sensitive to noise.

Chapter 5

Conclusions

Two main topics were discussed in this thesis:

- the effect of non-stationary small layering on the propagation of P -waves, i.e. the effect on the W -operators,
- characterisation of layer scale sequences using seismic attributes extracted using a matching pursuit approach, i.e. attributes of the bandlimited R^+ operator.

Effect on the W -operators:

From a review of numerical and laboratory experiments found in the literature, a first-order correction on P -wave velocities derived from well-logs has been proposed to compensate for fine layering effects. The methods available currently, make stringent assumptions on the stationarity of the layering. The proposed method, however, uses an equivalent medium type of moving averaging with a window length of approximately one fifth of the dominant wavelength of the seismic wave. Therefore, no assumptions on the stationarity of the medium parameters are made. The procedure results in an “effective velocity” at a specified scale. The “effective velocity” is slightly lower than the P -wave velocities from the well-log. It has been shown that in this way the delay effects (also called drift), originating from multiples generated by fine layering, are accounted for. An important observation made is that the “effective velocities” show a significant dependency for the scale. This observation was also confirmed with numerical modelling experiments. Because of the scale dependency of the “effective velocity”, an iterative procedure has been designed to calculate the “effective velocities” on a scale in accordance with the seismic data. A first step is to analyse the dominant wavelength of the seismic trace in time. The well-log velocities are always measured in depth. The link between depth and seismic time is the scale-dependent effective velocity. An iterative procedure has been constructed

to derive the mutual dependent scale in depth and the “effective velocity” at that scale that together match the desired seismic scale in time.

The proposed method for the estimation of scale-dependent effective velocities was also extended to plane P -wave propagation under oblique angles. In a similar way as for normal incidence wave propagation, the effective Thomsen anisotropy parameters have been estimated. A variation of the effective Thomsen parameters across the scales in the order of 100 % was found. This means that Thomsen parameters without a reference to scale have limited meaning.

The effective velocities as found from this method, may be used in well-tieing and as background velocities in pre-stack inversion. The effective velocities can also be used in the migration process. The effective velocities might be experimentally verified using the velocity model as inverted from the data-derived migration operators, using the CFP method.

Attributes of the bandlimited R^+ operator:

The second main topic described in this thesis is the characterisation of local wavelet shape using Gabor-atoms. Due to the bandlimited nature of the R^+ operator, bandlimited basic functions, such as the Gabor-atoms, are well suited for characterisation purposes. Asymmetrical sequences at layer scale are very important in the geological interpretation of well-log measurements. From a study of synthetic traces, it was found that asymmetrical sequences also produce asymmetric seismic responses. Using a matching pursuit approach with a restricted set of Gabor-atoms, this asymmetry in the seismic response was characterised. The proposed method proved to be very stable in the presence of noise. Compared with the response phase (as often used in seismic characterisation), the phase attribute derived with the matching pursuit method allows an extra 6 to 9 dB of noise.

An application on a 3-D data-set from the Gulf of Mexico proved that consistent geological features were extracted. In a deltaic environment, different facies types could be distinguished with the aid of the matching pursuit method. Also in the complicated case of deep-marine slump features, very small details were unraveled. The proposed method analyses the data trace-by-trace, independently. This means that the attributes are absolute. Relative methods (such as coherence cube technology), look at changes between traces. Relative methods are very well suited for the analysis of edges and changes in structures, while an absolute method can be used for the characterization of the local facies.

Appendix A

Anelastic media

In the main thesis, the layer properties were consider to be elastic. The effect of scattering was described. In this appendix, anelastic media are discussed. Some of the theory, such as the Kramers-Kronig relationship, is similar for both anelastic media as for scattering media.

A.1 Introduction

When the velocity is frequency dependent, the medium is said to be dispersive. First the case of a harmonic plane wave in a non-dispersive medium is discussed. Afterwards the properties of a dispersive medium are discussed. A part of the description is based on Dahlen and Tromp (1998).

A.2 Constant phase velocity: no dispersion

A harmonic plane wave travelling along the z -direction in a homogeneous material may be defined as:

$$f(z, t) = a e^{j(\omega t - kz)}, \quad (\text{A.1})$$

with z the depth coordinate, $k = \frac{\omega}{c_\phi}$ the wavenumber, ω the circular frequency, c_ϕ the phase velocity and a the amplitude.

Waves are often not harmonic, this means they are containing different frequency components. In this case the propagating wave can be described using the

inverse Fourier transformation:

$$f(z, t) = \frac{1}{2\pi} \int_{-\infty}^{+\infty} F(0, \omega) e^{j[\omega t - kz]} d\omega, \quad (\text{A.2})$$

with

$$F(0, \omega) = \int_{-\infty}^{+\infty} f(0, t) e^{-j\omega t} dt, \quad (\text{A.3})$$

the forward Fourier transformation of the wave at $z = 0$. $F(0, \omega)$ can be seen as a generalisation of the amplitude factor a for the monochromatic plane wave as described in Equation (A.1). $F(0, \omega)$ is a frequency dependent amplitude factor, but because it may be a complex function, it may also add a phase-shift.

When velocity $c_\phi = \omega/k$ is independent of frequency, the medium is called non-dispersive. A wave will retain its shape exactly, as all its frequency components will travel coherently with the same velocity c_ϕ . The wave will be delayed in time as it travels further in the perfectly elastic homogeneous material. This can be shown by rewriting Equation (A.2) in the following way:

$$f(z, t) = \frac{1}{2\pi} \int_{-\infty}^{+\infty} F(0, \omega) e^{j\omega t} e^{-j\omega \frac{z}{c_\phi}} d\omega, \quad (\text{A.4})$$

where $f(z, t)|_{z=0}$ can be recognized. By applying the time-delay property of the Fourier transform, Equation (A.4) becomes:

$$f(z, t) = f\left(0, t - \frac{z}{c_\phi}\right). \quad (\text{A.5})$$

This is nothing else than the wave at depth is zero $f(0, t)$, delayed with $t_0 = \frac{z}{c_\phi}$. The wavenumber in a non-dispersive medium is equal to $k = \frac{\omega}{c_\phi}$, and is linear in ω .

A.3 Non-constant phase velocity: dispersion

When phase velocity $c_\phi(\omega)$ is frequency dependent, the wave becomes dispersive, i.e. the shape of the wave becomes distorted while traveling through the medium. Dispersion is always associated with attenuation. Both aspects can nicely be described

using a complex wavenumber $k(\omega)$ (Aki and Richards, 1980)¹:

$$k(\omega) = \frac{\omega}{c_\phi(\omega)} - j\alpha(\omega), \quad (\text{A.6})$$

with $c_\phi(\omega)$ the phase velocity and $\alpha(\omega)$ an attenuation factor. Upon insertion of Equation (A.6), Equation (A.2) becomes:

$$\begin{aligned} f(z, t) &= \frac{1}{2\pi} \int_{-\infty}^{+\infty} F(0, \omega) e^{j[\omega t - (\frac{\omega}{c_\phi(\omega)} - j\alpha(\omega))z]} d\omega \\ &= \frac{1}{2\pi} \int_{-\infty}^{+\infty} F(0, \omega) e^{-\alpha(\omega)z} e^{j[\omega t - \frac{\omega}{c_\phi(\omega)}z]} d\omega. \end{aligned} \quad (\text{A.7})$$

The attenuation factor $\alpha(\omega)$ clearly describes an exponential decay with z of the amplitude of a specific frequency component ω .

A.3.1 Constitutive relationships

Not every complex wavenumber $k(\omega)$ is physically possible. From energy considerations it follows for instance that $\alpha(\omega) > 0$, as will be discussed later. Also a strict relationship exists between $\alpha(\omega)$ and $c_\phi(\omega)$, based on the so-called Kramers-Kronig relationship. The discussion will start from the constitutive relationships governing an anelastic material.

In Chapter 3, Hooke's law was described in general as:

$$\vec{\sigma} = \mathbf{c} \vec{\epsilon}, \quad (\text{A.8})$$

describing the stress - strain relationship in a linear elastic material. Stress $\vec{\sigma}$ depends upon the local instantaneous strain $\vec{\epsilon}$, a dependency fully described by the elastic modulus matrix \mathbf{c} . In a linear anelastic material, stress $\vec{\sigma}(t)$ is assumed to depend linearly upon the entire past history of strain $\vec{\epsilon}(t)$, i.e.

$$\vec{\sigma}(t) = \int_{-\infty}^t \mathbf{m}(t-t') \vec{\epsilon}(t') dt', \quad (\text{A.9})$$

with $\mathbf{m}(t)$ the anelastic modulus matrix. The lower limit of integration $-\infty$ reflects the dependence upon the entire past, and the upper limit t ensures that there is no dependence upon the deformation in the future, i.e. it ensures causality (Dahlen and

¹In Aki and Richards (1980) another sign-convention for the Fourier-transformation is used. Associated, the sign of the imaginary part of the complex wavenumber $k(\omega)$ is different as well: $k(\omega) = \frac{\omega}{c_\phi(\omega)} + j\alpha(\omega)$.

Tromp, 1998). Equation (A.9), can also be rewritten as:

$$\vec{\sigma}(t) = \int_{-\infty}^{+\infty} \mathbf{m}(t-t') \vec{\epsilon}(t') dt', \text{ with } \mathbf{m}(t) = \mathbf{0}, \forall t < 0, \quad (\text{A.10})$$

or using the convolution notation:

$$\vec{\sigma}(t) = \mathbf{m}(t) * \vec{\epsilon}(t). \quad (\text{A.11})$$

From a substitution of a unit step function for one of the strain components ϵ_β of $\vec{\epsilon}(t)$ in Equation (A.10), it is clear that $m_{\alpha\beta}(t)$ is the time derivative of the stress relaxation function $n_{\alpha\beta}(t)$ for σ_α (Kjartansson, 1979; Dahlen and Tromp, 1998), i.e. $m_{\alpha\beta}(t) = \dot{n}_{\alpha\beta}(t)$. The stress relaxation functions $\mathbf{n}(t)$ for an anelastic material decrease monotonically from their unrelaxed value \mathbf{n}^u at $t = 0$ to the relaxed value \mathbf{n}^r at $t \rightarrow \infty$ (Dahlen and Tromp, 1998), i.e.:

$$0 < n_{\alpha\beta}^r \leq n_{\alpha\beta}^u < \infty, \text{ if } n_{\alpha\beta} \neq 0, \forall t. \quad (\text{A.12})$$

The constitutive relationship for an anelastic material can also be written as the inverse of Equation (A.11), i.e.

$$\vec{\epsilon}(t) = \mathbf{s}(t) * \vec{\sigma}(t), \quad (\text{A.13})$$

with $\mathbf{s}(t)$ the anelastic compliance matrix. It is clear when combining Equations (A.11) and (A.13) that the components of $\mathbf{m}(t)$ and $\mathbf{s}(t)$ must satisfy the following condition:

$$\sum_{\beta=1}^6 m_{\alpha\beta}(t) * s_{\beta\gamma}(t) = \delta_{\alpha\gamma} \delta(t), \quad (\text{A.14})$$

with $\delta(t)$ the Dirac delta function. This means that $s_{\alpha\beta}(t)$ and $m_{\beta\alpha}(t)$ are each others inverse. Note that $s_{\alpha\beta}(t)$ is the time derivative of the creep function $u_{\alpha\beta}(t)$, i.e. the strain ϵ_α that results from a unit step function in stress σ_β (Kjartansson, 1979; Dahlen and Tromp, 1998).

Equation (A.10) states the condition of causality on $\mathbf{m}(t)$. Alternatively, it is also possible to require causality for $\mathbf{s}(t)$. There is still some debate whether causality should be required for both $s_{\alpha\beta}(t)$ and $m_{\beta\alpha}(t)$, or just for one of these two functions.

A.3.2 Harmonic stimulation

Until now, only the transient response to a non-periodic stimulus was considered. The response for a harmonic variation can be described using $\nu = \omega + j\gamma$, a

complex angular frequency² (Dahlen and Tromp, 1998):

$$\vec{\sigma}(t) = \Re \left[\vec{\Sigma}(\nu) e^{j\nu t} \right], \quad (\text{A.15})$$

$$\vec{\epsilon}(t) = \Re \left[\vec{E}(\nu) e^{j\nu t} \right]. \quad (\text{A.16})$$

Because of linearity, $\vec{\Sigma}(\nu)$ and $\vec{E}(\nu)$ are related through:

$$\vec{\Sigma}(\nu) = \mathbf{M}(\nu) \vec{E}(\nu), \quad (\text{A.17})$$

where

$$\mathbf{M}(\nu) = \int_{-\infty}^{+\infty} \mathbf{m}(t) e^{-j\nu t} dt, \text{ with } m_{\alpha\beta}(t) = 0, \forall t < 0, \quad (\text{A.18})$$

which is only defined for $\Im(\nu) = \gamma \leq 0$. Alternatively, $\mathbf{M}(\nu)$ can also be described in function of the stress relaxation function $\mathbf{n}(t)$:

$$\mathbf{M}(\nu) = j\nu \int_{-\infty}^{+\infty} \mathbf{n}(t) e^{-j\nu t} dt, \text{ with } n_{\alpha\beta}(t) = 0, \forall t < 0. \quad (\text{A.19})$$

The components of the complex modulus matrix $\mathbf{M}(\nu)$ are analytic functions, satisfying³ (Dahlen and Tromp, 1998):

$$\mathbf{M}(-\nu^*) = \mathbf{M}^*(\nu), \quad (\text{A.20})$$

in the lower half of the complex frequency plane $\Im(\nu) = \gamma \leq 0$. At very low frequencies, stress and strain are related by the real-valued relaxed moduli:

$$\lim_{|\nu| \rightarrow 0} \mathbf{M}(\nu) = \mathbf{M}^r, \quad (\text{A.21})$$

with the r from relaxed, and conversely at very high frequencies, stress and strain are related by the real-valued unrelaxed moduli \mathbf{M}^u :

$$\lim_{|\nu| \rightarrow \infty} \mathbf{M}(\nu) = \mathbf{M}^u. \quad (\text{A.22})$$

Since there is a non-zero response in the unrelaxed situation, and there is a finite response in the relaxed situation, the relaxed and unrelaxed moduli (for the components $M_{\alpha\beta}$ that are not zero for symmetry reasons, see section 3.2) honour the following relationship:

$$0 < M_{\alpha\beta}^r \leq M_{\alpha\beta}^u < \infty. \quad (\text{A.23})$$

Materials honouring Equation (A.23) are called anelastic. The more general viscoelastic materials may have $\mathbf{M}^r = 0$ or $\mathbf{M}^u \rightarrow \infty$ (Dahlen and Tromp, 1998).

²A real angular frequency will be denoted by ω , a complex frequency by ν .

³The symbol * denotes the complex conjugate, e.g. $\nu^* = \omega - j\gamma$.

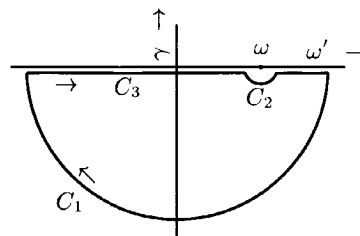


Fig. A.1 Integration contour C used for the Cauchy's theorem in Equation (A.25). The integration goes clock-wise along the contour C .

A.3.3 Cauchy's integral theorem and Kramers-Kronig relations

The causal nature of a function $g(t)$ in the time domain gives rise to an important relationship between the real and imaginary part of $G(\nu)$ in the frequency domain⁴. When a complex function $G(\nu)$ is complex differentiable in a region R , i.e. $G(\nu)$ is analytic (Titchmarsh, 1964), and its partial derivatives are continuous throughout the same region, Cauchy's integral theorem states that:

$$\oint_C G(\nu) \, d\nu = 0, \quad (\text{A.24})$$

for any closed contour C completely contained in R (Titchmarsh, 1964). A specific choice of the integration path C and function $G(\nu)$ will lead to the Kramers-Kronig relations between the real and imaginary components of $\mathbf{M}(\omega)$. Later this relationship will be transformed to a relationship between dispersion $c_\phi(\omega)$ and attenuation $\alpha(\omega)$. First the integration path C that will be used is investigated. A complex function $G(\nu)$, with the following properties:

1. $G(\nu)$ is analytic in the lower half frequency plane, $\Im(\nu) = \gamma \leq 0$,
2. $\lim_{|\nu| \rightarrow \infty} G(\nu) = 0$

is assumed. Because of the first property, the Cauchy integral theorem holds for any closed contour in the lower half frequency plane. Figure A.1 shows the specific choice for the contour C that was made (Dahlen and Tromp, 1998). The contour

⁴This statement is only valid for functions not containing a distribution at $t = 0$. In Equations (A.31) and (A.32) the effect of a δ -function is already taken into account by the factor \mathbf{M}^α . These equations are not valid for other types of distributions at $t = 0$.

integral for C can be written as:

$$\lim_{|\nu| \rightarrow \infty} \int_{C_1} \frac{G(\nu)}{\nu - \omega} d\nu + \lim_{\epsilon \rightarrow 0} \int_{C_2} \frac{G(\nu)}{\nu - \omega} d\nu + \lim_{\epsilon \rightarrow 0} \left(\int_{-\infty}^{-\epsilon} + \int_{\epsilon}^{\infty} \right) \frac{G(\omega')}{\omega' - \omega} d\omega' = 0 \quad (\text{A.25})$$

with ω an arbitrary real valued frequency, ω' a dummy integration variable and the different parts of the contour as shown in Figure A.1.

The contribution from C_1 (the large semi-circular arc) will vanish because the function vanishes sufficiently fast for $|\nu| \rightarrow \infty$ due to the second property:

$$\lim_{|\nu| \rightarrow \infty} \int_{C_1} \frac{G(\nu)}{\nu - \omega} d\nu = \pi \lim_{|\nu| \rightarrow \infty} G(\nu) = 0. \quad (\text{A.26})$$

The contribution from part C_2 , the small arc with radius ϵ around point ω , can be rewritten by using a transformation to a local polar coordinate system with origin in ω . This is done by substituting $\nu = \omega + \epsilon e^{j\theta}$ (Dahlen and Tromp, 1998):

$$\lim_{\epsilon \rightarrow 0} \int_{C_2} \frac{G(\nu)}{\nu - \omega} d\nu = \lim_{\epsilon \rightarrow 0} j \int_{\pi}^0 G(\omega + \epsilon e^{j\theta}) d\theta = -j \pi G(\omega). \quad (\text{A.27})$$

Part C_3 of the contour goes along the real frequency axis. A small region around ω is excluded from the integral. This is because ω is a singular point for function $\frac{G(\nu)}{\nu - \omega}$, i.e. the function fails to be analytic. Using the Cauchy principal value, designated by the symbol \mathcal{P} , the contribution from C_3 to the integral becomes:

$$\lim_{\epsilon \rightarrow 0} \left(\int_{-\infty}^{-\epsilon} + \int_{\epsilon}^{\infty} \right) \frac{G(\omega')}{\omega' - \omega} d\omega' = \mathcal{P} \int_{-\infty}^{+\infty} \frac{G(\omega')}{\omega' - \omega} d\omega'. \quad (\text{A.28})$$

Substituting the results from Equations (A.26) - (A.28) into Equation (A.25), leads to the following relationship for $G(\omega)$ along the real frequency axis:

$$G(\omega) = \frac{1}{j\pi} \mathcal{P} \int_{-\infty}^{+\infty} \frac{G(\omega')}{\omega' - \omega} d\omega'. \quad (\text{A.29})$$

For anelastic materials, $\mathbf{M}(\nu) - \mathbf{M}^u$ will honour the conditions as set forward for $G(\nu)$ (see Equations (A.20) and (A.23)). For convenience the complex modulus along the real frequency axis, $\mathbf{M}(\omega)$ will be decomposed in its real and imaginary parts:

$$\mathbf{M}(\omega) = \mathbf{M}_1(\omega) + j\mathbf{M}_2(\omega). \quad (\text{A.30})$$

When substituting $G(\omega) = \mathbf{M}(\omega) - \mathbf{M}^u$ in Equation (A.29) and equating real and imaginary parts, the following relations are obtained (Dahlen and Tromp, 1998):

$$\mathbf{M}_1(\omega) - \mathbf{M}^u = \frac{1}{\pi} \int_{-\infty}^{+\infty} \frac{\mathbf{M}_2(\omega')}{\omega' - \omega} d\omega', \quad (\text{A.31})$$

and

$$\mathbf{M}_2(\omega) = -\frac{1}{\pi} \int_{-\infty}^{+\infty} \frac{\mathbf{M}_1(\omega') - \mathbf{M}^u}{\omega' - \omega} d\omega', \quad (\text{A.32})$$

the so-called Kramers-Kronig relations. When using \mathcal{H} for the Hilbert transform (Bracewell, 2000), Equations (A.31) and (A.32) can be written as:

$$\mathbf{M}_1(\omega) - \mathbf{M}^u = \mathcal{H}[\mathbf{M}_2(\omega)], \quad (\text{A.33})$$

and

$$\mathbf{M}_2(\omega) = -\mathcal{H}[\mathbf{M}_1(\omega) - \mathbf{M}^u], \quad (\text{A.34})$$

relating real and imaginary parts of $\mathbf{M}(\omega) - \mathbf{M}^u$ as Hilbert transforms of each other, i.e. they are a Hilbert transform pair. Note that when one of the two sides is known over the whole frequency range ω , the other side of the pair can be calculated using the Hilbert transform.

Phase velocity $c_\phi(\omega)$ and attenuation coefficient $\alpha(\omega)$ for a specific type of wave in a specific direction, can be calculated in function of the modulus $M_{\alpha\beta}$. When we take for instance the component governing the P -wave propagation along the z -axis, M_{33} in the Voigt notation, or M in short, P -wave velocity c_ϕ and attenuation coefficient $\alpha(\omega)$ can be related to $M = M_1 + jM_2$ using the dispersion relationship for acoustic wave propagation (O'Donnell et al., 1981):

$$k^2 = \frac{\omega^2 \rho}{M(\omega)}. \quad (\text{A.35})$$

To satisfy the dispersion relationship, the wavenumber $k(\omega)$ needs to be complex. We make the following identification:

$$k(\omega) = \frac{\omega}{c_\phi(\omega)} - j\alpha(\omega), \quad (\text{A.36})$$

with $c_\phi(\omega)$ the phase velocity, and $\alpha(\omega)$ the attenuation coefficient (see Equation (A.7)). Modulus M can be related to the phase velocity and attenuation coefficient by:

$$\frac{\omega^2}{c_\phi^2(\omega)} - \alpha^2(\omega) - j\frac{2\omega\alpha(\omega)}{c_\phi(\omega)} = \frac{\omega^2 \rho}{M_1(\omega) + jM_2(\omega)} = \omega^2 \rho \frac{M_1(\omega) - jM_2(\omega)}{|M(\omega)|^2}, \quad (\text{A.37})$$

with $|M(\omega)|^2 = M_1^2(\omega) + M_2^2(\omega)$. When equating real and imaginary parts, Equation (A.37) leads to:

$$\left[\frac{\omega^2}{c_\phi^2(\omega)} - \alpha^2(\omega) \right] = \omega^2 \rho \frac{M_1(\omega)}{|M(\omega)|^2}, \quad (\text{A.38})$$

and

$$\frac{2\omega\alpha(\omega)}{c_\phi(\omega)} = \omega^2 \rho \frac{M_2(\omega)}{|M(\omega)|^2}. \quad (\text{A.39})$$

Usually, attenuation is small, so the magnitude of the imaginary parts of the wavenumber k and of modulus M are much less than the magnitude of the real part, i.e. $|\alpha(\omega)c_\phi(\omega)/\omega| \ll 1$, and $|M_2(\omega)| \ll |M_1(\omega)|$, $\forall \omega$. This leads to the following relationships for c_ϕ and α as function of M :

$$c_\phi(\omega) = \sqrt{\frac{M_1(\omega)}{\rho}}, \quad (\text{A.40})$$

and

$$\alpha(\omega) = \frac{\omega}{2c_\phi(\omega)} \frac{M_2(\omega)}{M_1(\omega)}. \quad (\text{A.41})$$

A.3.4 Quality factor Q and energy dissipation

As mentioned previously, aside from causality, there is another fundamental property the wavenumber $k(\omega)$ has to obey, i.e. a dispersive medium must dissipate energy. This means that the work done against the internal friction needs to be positive.

Let's consider a harmonic stimulation at real frequency $\omega > 0$. The stress $\sigma(t) = \Re[\sigma(\omega)e^{j\omega t}]$ and the strain $\epsilon(t) = \Re[\epsilon(\omega)e^{j\omega t}]$ follow an elliptical hysteresis loop (Figure A.2). The work done during one cycle in a unit volume, against internal friction is equal to the area within the hysteresis loop (Dahlen and Tromp, 1998):

$$\oint \dot{E} dt = \oint \sigma \dot{\epsilon} dt = \pi M_2(\omega) |\epsilon(\omega)|^2. \quad (\text{A.42})$$

This means that the imaginary modulus $M_2(\omega)$ is proportional to the rate of energy dissipation. The dissipated energy appears as heat in the material. Energy dissipation should always be positive in order to comply with the laws of physics. This means that the imaginary part of the modulus M should always be positive, i.e. $M_2(\omega) > 0$.

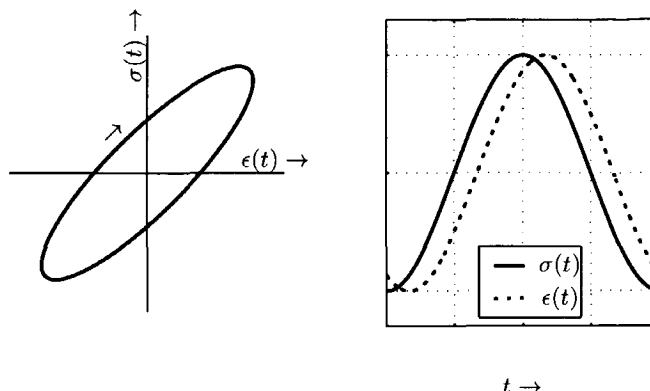


Fig. A.2 The stress-strain hysteresis loop, causing the dissipation of energy in a dispersive medium. On the right-hand side, a plot of the stress $\sigma(t)$ and strain $\epsilon(t)$. Note the phase lag ϕ between stress and strain. In this case $\phi = \pi/3$.

The quality factor Q is defined as (O'Connell and Budiansky, 1978):

$$Q(\omega) = \frac{M_1(\omega)}{M_2(\omega)}. \quad (\text{A.43})$$

It is clear when writing the complex modulus $M(\omega)$ in the form: $|M(\omega)| e^{j\phi(\omega)}$, that the angle $\phi(\omega) = \arctan(Q^{-1}(\omega))$ can also be interpreted as a phase lag between stress $\sigma(\omega)$ and strain $\epsilon(\omega)$ in a harmonic oscillation. The quantity $4\pi Q^{-1}(\omega)$ can also be interpreted as a fractional average energy dissipation per cycle. The Q -factor as defined in Equation (A.43) is related to the attenuation coefficient $\alpha(\omega)$ in the following manner (see Equation (A.41)):

$$Q(\omega) \approx \frac{\omega}{2\alpha(\omega)c_\phi(\omega)}, \quad (\text{A.44})$$

which is an approximated relationship, due to the large Q -approximation used in Equation (A.41)⁵. It is clear that the attenuation coefficient $\alpha(\omega)$ should always be positive for a dissipative medium or zero for a lossless medium.

A.3.5 Constant Q -behaviour

Several models exist for the description of the attenuation of waves. Kjartansson (1979) describes a constant Q model.

⁵Using another derivation of the Q -factor, this equation may become exact (e.g. in Aki and Richards (1980)). Note that Equations (A.43) and (A.44) are not identical.

Kjartansson (1979) proposes a complex modulus:

$$M(\omega) = M_0 \left(\frac{j\omega}{\omega_0} \right)^{2\eta} = M_0 \left| \frac{\omega}{\omega_0} \right|^{2\eta} e^{j\pi\eta \operatorname{sgn}(\omega)}, \quad (\text{A.45})$$

where $0 < \eta < \frac{1}{2}$, $M_0 = |M(\omega_0)| = \sqrt{M_1^2(\omega_0) + M_2^2(\omega_0)}$ and $\operatorname{sgn}(\omega)$ is the sign-function (also called signum):

$$\operatorname{sgn}(\omega) = \begin{cases} +1 & \text{if } \omega > 0, \\ 0 & \text{if } \omega = 0, \\ -1 & \text{if } \omega < 0. \end{cases} \quad (\text{A.46})$$

Note that $M(\omega)$ in Equation (A.45) can be seen as the Fourier transform of:

$$m(t) = \frac{M_0}{\omega_0} \frac{H(t)}{\Gamma(-2\eta)} \left(\frac{t}{t_0} \right)^{-(2\eta+1)}, \quad (\text{A.47})$$

with $H(t)$ the heavyside function, Γ the Γ -function and $t_0 = \frac{1}{\omega_0}$. Using the definition of Q from O'Connell and Budiansky (1978) as given in Equation (A.43), the Q -factor related to this complex modulus $M(\omega)$ is found to be strictly independent of frequency:

$$Q(\omega) = Q_0 \operatorname{sgn}(\omega), \text{ with } \frac{1}{Q_0} = \tan(\pi\eta), \quad (\text{A.48})$$

or

$$\eta = \frac{1}{\pi} \arctan \left(\frac{1}{Q_0} \right) \stackrel{Q_0 \gg 1}{\approx} \frac{1}{\pi Q_0}. \quad (\text{A.49})$$

Phase velocity $c_\phi(\omega)$ and attenuation coefficient $\alpha(\omega)$ are found to be respectively:

$$c_\phi(\omega) = c_0 \left| \frac{\omega}{\omega_0} \right|^\eta \stackrel{Q_0 \gg 1}{\approx} c_0 \left[1 + \frac{1}{\pi Q_0} \ln \left(\left| \frac{\omega}{\omega_0} \right| \right) \right], \quad (\text{A.50})$$

and

$$\alpha(\omega) \approx \frac{|\omega|}{2Q_0 c_\phi(\omega)}, \quad (\text{A.51})$$

with c_0 the phase velocity at some reference frequency ω_0 . Because $c_\phi(\omega)$ is slightly dependent on frequency, constant Q is not exactly the same as assuming that $\alpha(\omega)$ is strictly proportional to frequency ω (Kjartansson, 1979), as often erroneously assumed in literature.

Note that a material with a strictly constant quality factor Q is not anelastic, since it does not honour the anelastic constraints as given in Equation (A.23). This

can be seen in Equation (A.45): because $\eta > 0$, $\lim_{\omega \rightarrow \infty} |M(\omega)| \rightarrow \infty$. Instead a strict constant Q material is viscoelastic (Dahlen and Tromp, 1998). The prerequisites for the derivation of the Kramers-Kronig relationships, as described in previous section, are not honoured. Still, a material with a constant quality factor Q over the entire frequency range is causal⁶ (see Equation (A.47)). A possible objection might be that it is not physical, since $\lim_{\omega \rightarrow \infty} c_\phi(\omega) \rightarrow \infty$. However, Kjartansson (1979) states that there are fundamental physical limits to all continuum mechanics models (including the strict constant Q -model): “*no continuum model [...] can have any significance at wavelengths shorter than the molecular separation nor at periods longer than the age of the universe.*” So, even for the strict constant Q -model, upper and lower bounds can be defined for the modulus $M(\omega)$.

On the other hand, a strict constant Q -model with these “physical limits” to continuum mechanics is not so much different from the range of models that show a quasi-constant Q behaviour within some frequency band. This kind of models lead (within the frequency band) to the same logarithmic behaviour of the phase velocity c_ϕ as found for the strict constant Q model in Equation (A.50). The constant Q -model is only more convenient since, due to its simplicity, it allows to derive exact expressions for wave propagation and the formulation of scaling relationships.

Often a quasi-constant Q behaviour within the seismic frequency range is observed⁷. Sheriff (1991) reports that typical quality factors Q observed in rocks in the seismic frequency range are in the order of 50 to 300.

A.3.6 Phase and group velocity

Figure A.3 shows some snap-shots of a wave traveling in a highly dispersive medium with a constant Q -factor of 2 (which is very low). The wavelet starts as a symmetric Ricker-wavelet, and soon becomes distorted and asymmetric.

From Figure A.3, we can find velocities for different aspects of the travelling wave. One is the phase velocity. Sheriff (1991) defines it as: “*The velocity of any given phase (such as a trough) ...*”. This means that phase velocity is associated with the locations in the (z, t) -plane where the phase $\phi = (k_1 z - \omega t)$ is constant.

⁶Aki and Richards (1980) use a more strict definition of causality. Their definition of causality requires that the $f(z, t) = 0$ until an arrival time z/c_ϕ^∞ .

⁷Typically, the seismic frequency range is relatively narrow (2 to 120 Hz following Sheriff and Geldart, 1995). Laboratory measurements show that when a much broader frequency range is investigated, the quality factor Q appears to be strongly frequency dependent (Castagna et al., 1993). Murphy (1984) for instance reports important attenuation peaks between seismic and sonic log frequencies. Sonic log measurements are typically performed at frequencies around 10 kHz.

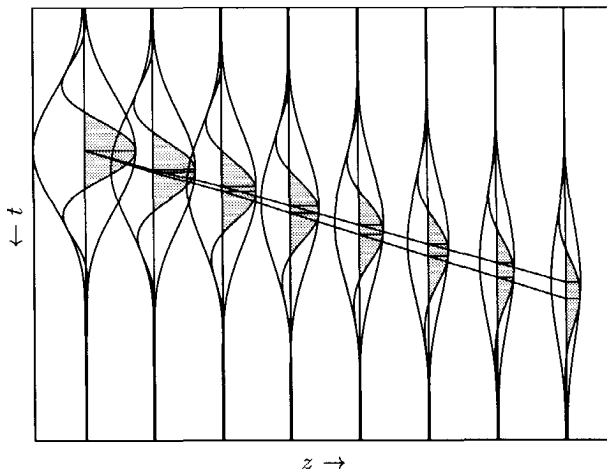


Fig. A.3 A VSP (Vertical Seismic Profile) type of display of a wave travelling in a highly dispersive medium. The medium is a constant Q -medium, with $Q_0 = 2$. The wave is recorded in time at several locations z in the medium. The left-most trace represents the recording at location $z = 0$ where it showed a symmetric Ricker-shape. Towards the right the wave is recorded for increasing distance z in the medium. Note that the wave stretches and becomes asymmetric due to the dispersion. The slope dz/dt of the different events indicate their resp. velocities. Group velocity c_g (associated with the peak of the envelope) is larger than the phase velocity c_ϕ (related to a peak): $c_g = 1.1732 c_\phi$.

Note that k_1 is the real part of k . The associated phase velocity c_ϕ is then:

$$c_\phi = \frac{dz}{dt} = \frac{\omega}{k_1}. \quad (\text{A.52})$$

This is the velocity associated with the trough in Figure A.3.

Equation (A.2) describes the wave at any location and time. In Figure A.3 we have taken a Ricker-wavelet at $z = 0$. This means $f(z, t)$ at $z = 0$ is:

$$f(0, t) = \left(1 - \frac{1}{2}(\omega_0 t)^2\right) e^{-\frac{1}{4}(\omega_0 t)^2}. \quad (\text{A.53})$$

This is the definition of a Ricker-wavelet with peak frequency $f_0 = \frac{\omega_0}{2\pi}$. The Fourier

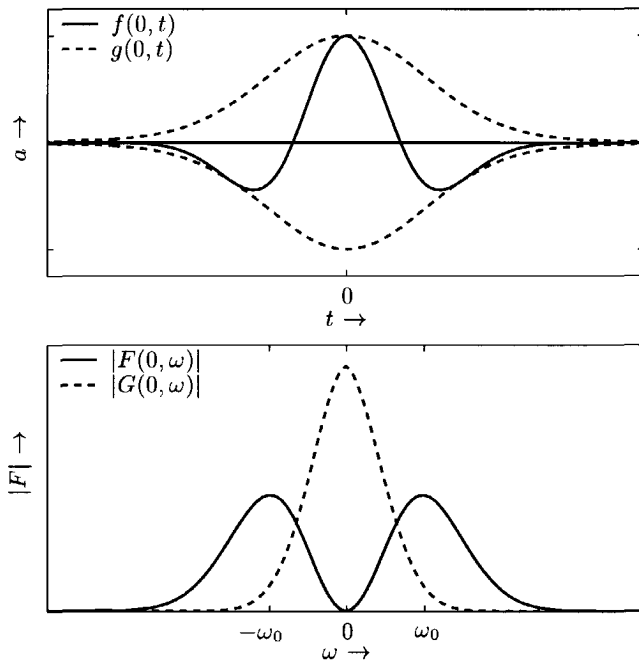


Fig. A.4 Ricker-wavelet $f(0, t)$ and its envelope $g(0, t)$ above, and below their amplitude spectra.

transformation of the Ricker-wavelet is, following Sheriff (1991), equal to:

$$F(0, \omega) = 4\sqrt{\pi} \frac{\omega^2}{\omega_0^3} e^{-\left(\frac{\omega}{\omega_0}\right)^2}, \quad (\text{A.54})$$

which is an even function in ω . Figure A.4 shows the Ricker-wavelet $f(0, t)$ and its amplitude spectrum $|F(0, \omega)|$.

Equation (A.53) can be approximated as:

$$f(0, t) \approx \cos(\omega_0 t) e^{-\frac{1}{4}(\omega_0 t)^2}. \quad (\text{A.55})$$

This can be considered as a modulated carrier signal $\cos(\omega_0 t)$, with the modulation:

$$g(t) = e^{-\frac{1}{4}(\omega_0 t)^2}. \quad (\text{A.56})$$

Because $g(t)$ is a Gaussian function, its Fourier transform:

$$G(\omega) = 2 \frac{\sqrt{\pi}}{\omega_0} e^{-\left(\frac{\omega}{\omega_0}\right)^2} \quad (\text{A.57})$$

is also Gaussian. The Fourier spectrum of the approximation in Equation (A.55) can easily be written as:

$$F(0, \omega) \approx \frac{1}{2} [G(-(\omega + \omega_0)) + G(\omega - \omega_0)]. \quad (\text{A.58})$$

$G(\omega - \omega_0)$ is a Gaussian function centered around ω_0 . $F(0, \omega)$ is real and symmetric, since $f(0, t)$ is symmetric and real (Oppenheim et al., 1997). Note that the inverse Fourier transform of $\frac{1}{2} [G(-(\omega + \omega_0)) + G(\omega - \omega_0)]$ can also be written as:

$$\begin{aligned} f(z, t) &= \frac{1}{2\pi} \int_{-\infty}^{+\infty} \frac{1}{2} [G(-(\omega + \omega_0)) + G(\omega - \omega_0)] e^{(j\omega[t - \frac{z}{c}])} d\omega \\ &= \frac{1}{2\pi} \Re \left[\int_0^{+\infty} [G(-(\omega + \omega_0)) + G(\omega - \omega_0)] e^{(j\omega[t - \frac{z}{c}])} d\omega \right] \quad (\text{A.59}) \\ &= \frac{1}{2\pi} \Re \left[\int_{-\infty}^{+\infty} G(\omega - \omega_0) e^{(j\omega[t - \frac{z}{c}])} d\omega \right]. \end{aligned}$$

$k(\omega)$ can be approximated using a Taylor series around ω_0 . If we are using only two terms in the expansion, we get:

$$k_1(\omega) \approx k_1(\omega_0) + k'_1(\omega_0)(\omega - \omega_0). \quad (\text{A.60})$$

Note that this represents the local approximation around ω_0 of $k(\omega)$.

The waveform of the propagating wave, $f(z, t)$, as described by Equation (A.2) is difficult to solve due to the frequency dependence of $c(\omega)$. When we use the approximations given in Equations (A.58) and (A.60), and the properties given in Equation (A.59), we can approximate Equation (A.2) by:

$$f(z, t) \approx \Re \left[\frac{1}{2\pi} \int_{-\infty}^{+\infty} G(\omega - \omega_0) e^{j(\omega t - [k_1(\omega_0) + k'_1(\omega_0)(\omega - \omega_0)]z)} d\omega \right], \quad (\text{A.61})$$

what can be written as:

$$f(z, t) \approx \frac{1}{2\pi} \Re \left[e^{j[\omega_0 t - k_1(\omega_0)z]} \int_{-\infty}^{+\infty} G(\omega - \omega_0) e^{j(\omega - \omega_0)[t - k'_1(\omega_0)z]} d\omega \right], \quad (\text{A.62})$$

or as:

$$f(z, t) \approx \cos[\omega_0 t - k_1(\omega_0)z] g[t - k'_1(\omega_0)z]. \quad (\text{A.63})$$

This indicates that the carrier signal (peaks and troughs) moves with the phase velocity $c_\phi = \frac{\omega}{k_1}|_{\omega_0}$, while the modulating envelope moves with the group velocity:

$$c_g = \frac{1}{k'_1(\omega_0)} = \frac{d\omega}{dk_1} \Big|_{\omega_0}. \quad (\text{A.64})$$

Note that Equation A.63 is not describing the changing wavelet shape, as seen in Figure A.3. This has to do with the approximations used in the derivation of this formula. The use of additional terms in the Taylor expansion of Equation A.60 will lead to the description of the changing wavelet shape.

The group velocity c_g can be expressed in the phase velocity c_ϕ in various equivalent ways (Mavko et al., 1998):

$$c_g = c_\phi + k_1 \frac{dc_\phi}{dk_1}, \quad (\text{A.65})$$

or

$$\frac{1}{c_g} = \frac{1}{c_\phi} - \frac{\omega}{c_\phi^2} \frac{dc_\phi}{d\omega}. \quad (\text{A.66})$$

These equations show clearly that the group velocity c_g is equal to the phase velocity c_ϕ whenever c_ϕ is frequency independent. When the phase velocity c_ϕ is frequency dependent, the medium is said to be dispersive. Dispersion is termed *normal* if $\frac{dc_\phi}{dk} < 0$ and *inverse* or *anomalous* if $\frac{dc_\phi}{dk} > 0$ (Mavko et al., 1998; Sheriff, 1991). As a rule, geometric dispersion (such as Rayleigh waves and waveguides), exhibits normal dispersion. On the other hand, intrinsic dissipation (such as viscoelasticity and small scale multiples) leads to anomalous or inverse dispersion (Mavko et al., 1998).

Appendix B

Geological description of Saga-well

In this thesis, the Saga-well is used in several examples. This appendix gives an overview of the geological description of the well-log.

B.1 Regional geological and structural setting

The well is situated on the Mid-Norwegian Møre-Lofoten Shelf, which is a passive continental margin lying between 62° and 70° N (Hagevang and Rønnevik, 1986). The Møre-Lofoten Shelf is separated in three areas: the narrow Møre Shelf in the south, the wide Nordland Shelf in the center, and the narrow Lofoten Shelf in the north. The development of the Møre-Lofoten continental margin is dominated by the post-Jurassic subsidence of the Møre and Vørings basins. The sedimentary Trøndelag Platform (the Southern part of the Møre-Lofoten Shelf) acted as a major, stable platform during the Cretaceous.

The Halten Terrace (where the well is located) forms a complex basin-and-range province in front of the southern part of the Trøndelag Platform, where it makes the transition towards the Møre basin (Hagevang and Rønnevik, 1986). The Halten Terrace was a part of a regional basin until Middle-Late Jurassic time. The main tectonic activity took place during the Middle to Late Jurassic Kimmerian tectonic phases (Ekern, 1987). Cretaceous deposits are mainly found in structurally enhanced areas created by differential subsidence. Almost continuous rapid subsidence and sedimentation took place from Late Cretaceous times onwards (Ekern, 1987).

Mesozoic sequences contain the reservoirs, source rocks and sealing rocks for all known Mid-Norwegian hydrocarbon accumulations (Fagerland, 1994). Between

1981 and 1991, 12 major discoveries were made on the Mid-Norway Shelf. Most of the discoveries were made on the Halten and Dønna Terrace, where the widest belt of mature Jurassic source rocks are found. Following a recent overview of Norwegian Petroleum Directorate (1999), a total of 114 wells were drilled on the Halten and Dønna Terrace, discovering approximately 1200 million Sm³ oil equivalent. An estimate of 26 % additional reserves still remains to be discovered in the area.

B.2 Well description

The well has been drilled offshore Mid-Norway, and proved a gas/condensate discovery in Garn Formation, the top-part of the Fangst Group (nomenclature is taken from Dalland et al. (1988)). The hydrocarbons are structurally trapped in a horst (Fagerland, 1994). The Gas Water Contact (GWC) is found at 2516.5 m, being in the Not Formation shale/silt section. In Figure B.1 an overview is given of the stratigraphic column around the reservoir zone in the well, together with the c_P and the ρ well-log readings. Diagenesis was found to be the single most important factor affecting reservoir quality (Bjørlykke et al., 1986).

In the following section, a lithostratigraphic summary is given of the different formations. This is also summarized in the core description as given on the left-hand side of Figure B.1. In 1988 the lithostratigraphic naming was changed, which should be taken into consideration when looking up the older references mentioned. Dalland et al. (1988) gives a good overview of the renaming. For the sake of completeness, the old names are also mentioned in the description.

B.2.1 Short lithologic description of the formations

Åre Formation The Late Triassic to Early Jurassic Åre Formation (previously known as the Hitra Formation) consists mainly of lower delta plain sandstones interbedded with carbonaceous shales which occasionally grades into fine laminae of coal (Fagerland, 1994; Ekern, 1987). These laminae are usually less than 1 meter in thickness, and can easily be determined by low c_P , low ρ and high resistivity readings. The Åre Formation is equivalent to the Statfjord Group and the lower part of the Dunlin Group in the North Sea (Hagevang and Rønnevik, 1986).

Tilje Formation The lower Jurassic Tilje Formation (previously known as the Aldra Formation) consists of sandstones with a grain size ranging from very fine to very coarse, and were deposited in a marine transgression. The grains are poorly sorted. The sediments are deposited in a deltaic, coastal lagoonal environment in the lower parts to shallow marine, bar-type deposits upwards in the sequence (Fagerland, 1994; Ekern, 1987). Most of the sandstones show a coarsening upward

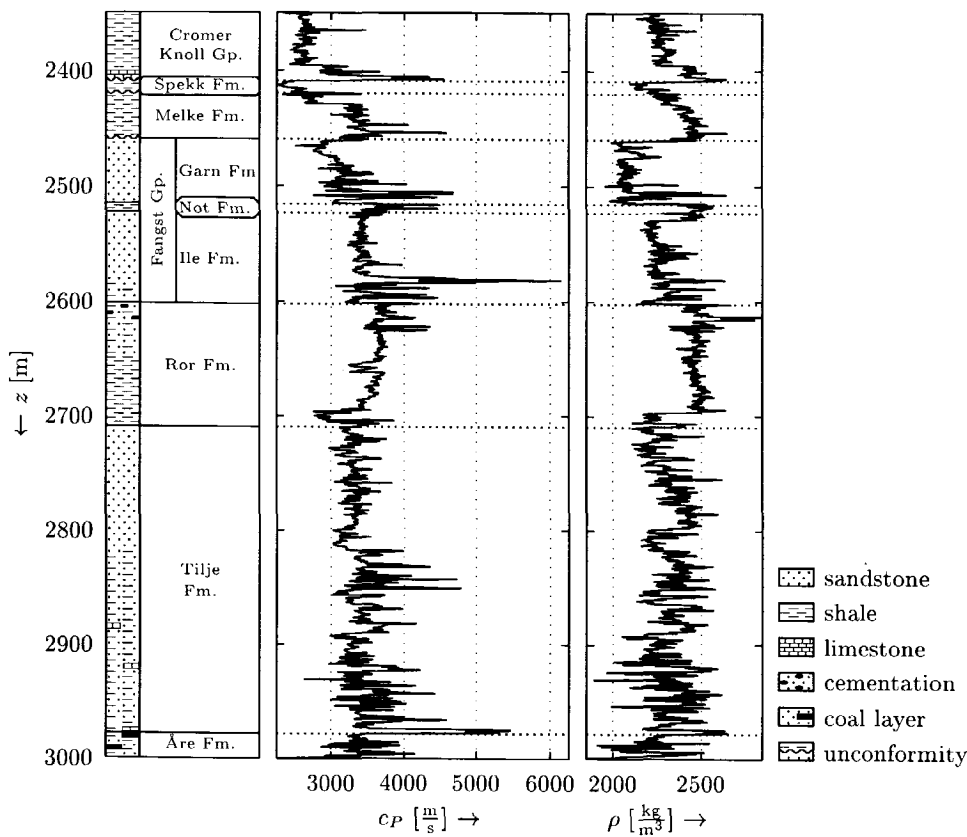


Fig. B.1 Geological description of a subset of the well-log used. To the left the core description, with the zonation and formation names. In the middle and the right the corresponding well-log measurements of c_P and ρ .

sequence. The uppermost part of the sequence are well-sorted marine sandstones with good reservoir characteristics.

Ror Formation The Ror Formation (previously known as the Leka Formation) represents offshore muds and sands deposited in an overall regressive phase. Predominantly claystones and siltstones were deposited (Ekern, 1987). This formation is developed as four or five cleaning upward sequences. The lower part of the cycles consists of claystones to siltstones, developing to fine-grained sandstone alternating with shale and siltstone in the upper parts. The topmost part is calcite cemented, with a fair amount of pyrite and glauconite.

Fangst Group The depositional environment of the Fangst Group is interpreted as marginal marine (Bjørlykke et al., 1986; Ekern, 1987). It is a massive regressive sandstone complex, also known as Tomma Formation. It is comparable with the Brent Group in the North Sea (Hagevang and Rønnevik, 1986). The top of the sequence is marked by a major unconformity, referred to as the middle Kimmerian unconformity. The thickness of this unit is greatly dependent on structural position on the Halten Terrace because of erosion.

This sandstone unit is divided into three parts, previously known as Tomma 1 to 3. The lower part (Ile Formation) is an alternation between a medium to coarse grain sandstone and a fine to medium grain sandstone, interlaminated with shales. It is interpreted as deposited in a tidally influenced coast-line environment. The sands have poor to good reservoir properties, depending on the degree of diagenesis. The middle part, Not Formation, is a 15 m thick firm sandy siltstone deposited during a transgressive phase. The upper part, called Garn Formation, consists of a fine to medium grained, moderately well sorted sandstone. The sediments were deposited during a major regression, in a high-energy, wave dominated shoreface environment. The sands have good to excellent reservoir properties.

Melke Formation The Melke Formation consists of a firm and silty claystone, deposited in an open marine shale setting (Fagerland, 1994). Traces of loose, very fine grained sandstone occur throughout the sequence. The formation is developed as an overall fining-upward sequence, representing the onset of a regional transgressive period (Hagevang and Rønnevik, 1986).

Spekk Formation The Spekk Formation is characterized by a high Uranium content, and is composed of a claystone/shale. It has a high organic content and is the considered the main source rock in this region. The Spekk Formation is an excellent, oil-prone source rock. The top of the Jurassic is marked by the late Kimmerian unconformity (Hagevang and Rønnevik, 1986), known as the regional Base Cretaceous Unconformity (see also Appendix C).

Cromer Knoll Group The upper part of the Lower Cretaceous consist of firm claystone with minor siltstone. The lowermost part consists of a soft marl, with a hard crystalline limestone at the base. The Cromer Knoll Group forms the main regional seal for all the Mid-Norway structures (Fagerland, 1994).

Appendix C

Geological description of well A from the Mobil AVO data set

Following the 64th SEG International Exposition and Annual Meeting in 1994 in Los Angeles, a workshop entitled “Comparison of seismic inversion methods on a single real data set” was held. For this workshop, a data set comprising a seismic line with two intersecting wells (wells A and B) was made public by Mobil. The results from the workshop are published in Keys and Foster (1998a). Due to acquisition problems, well B missed important parts of the cs log, making it less useful. Well A is selected for this study, since it contains a long record of high quality logs. In this appendix, a brief geological description is given for the data set.

C.1 Regional geological setting

The data set comes from the North Viking Graben in the North Sea (Keys and Foster, 1998b). The North Sea is an intracratonic basin with a complex history. The structural history has been studied extensively, and is described in great detail in Ziegler (1982). The north-north east trending Viking Graben formed as a result of a rifting phase in Late Permian to Triassic times. The Graben was a part of the Triassic rift system, that eventually led to the break-up of the Pangea mega-continent with the opening of the Central Atlantic Ocean at the onset of the Mid Jurassic time. This rifting phase is commonly referred to as the Mid Kimmerian tectonic phase. The Viking Graben remained active until the Late Kimmerian tectonic phase in Early Cretaceous times, when the onset of sea-floor spreading in the Central and North Atlantic and in the Western Neo-Thetys eventually caused a re-orientation of stresses. This caused a number of the Triassic and Jurassic grabens to

become inactive (Ziegler, 1982). The Early Cretaceous rifting phase was associated with a significant eustatic sea-level drop that is expressed by a regional regression in Western and Central Europe. This sea-level drop caused an extensive period of erosion, creating a significant regional unconformity at base Cretaceous (see also Appendix B). The inactive Viking Graben continued to undergo normal thermal subsidence from the Early Cretaceous onwards.

As a result, the structural framework of the reservoirs in the Viking Graben is one of tilted and subsequently eroded fault blocks.

C.2 Well description

The interval depicted in Figure C.1 contains a major unconformity at $z = 1986$ m, at base Cretaceous. Below the unconformity are the Jurassic syn-rift sediments located. These Jurassic age sediments form the primary target in the North Viking Graben. In the Jurassic times, an overall transgressive system governed the deposition. A few periods of regression have created coarse sediments, which form now the reservoir intervals. These Jurassic reservoirs range in depositional environments from fluvial to deltaic and shallow marine, and are embedded in deep water shales. The reservoirs are sometimes vertically stacked (Keys and Foster, 1998a). The gamma ray log clearly shows the coarsening upward sequences in the sandstone intervals.

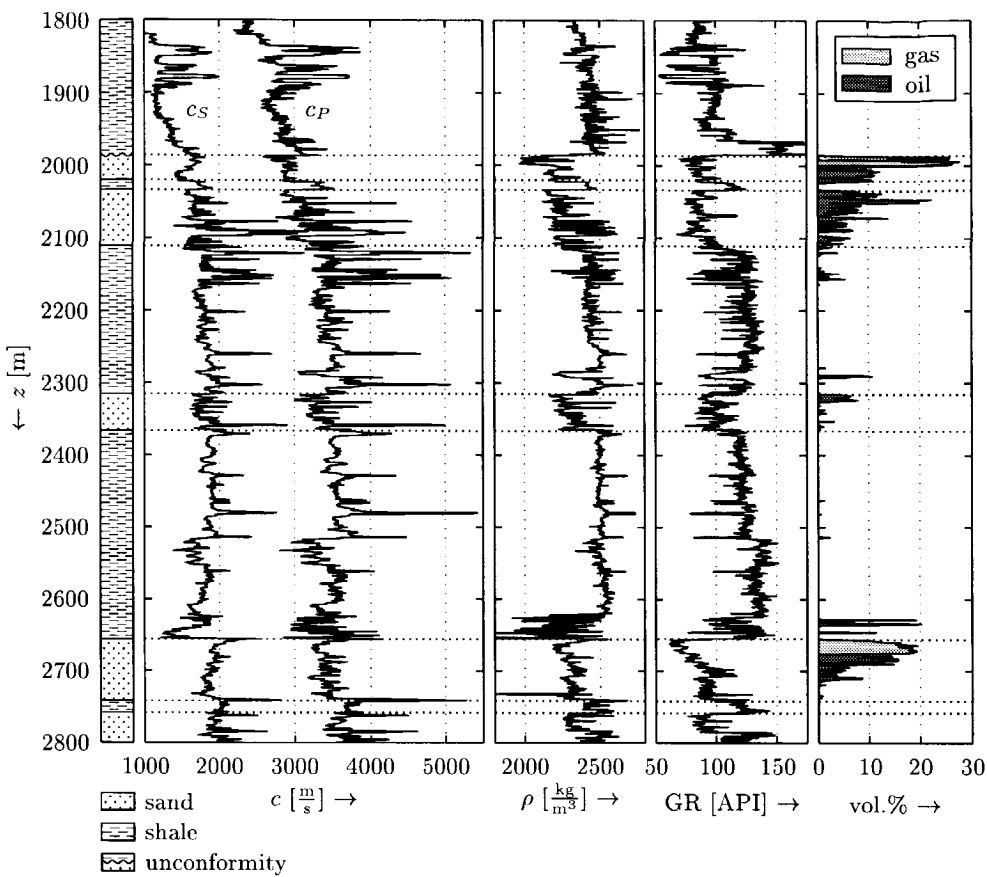


Fig. C.1 An overview of well A from the Mobil AVO data set. The most important logs are plotted: velocities c_P and c_S , density ρ , gamma ray log (GR) in API-units (American Petroleum Institute, API), and volume percentage of gas and oil. On the left-hand side, a lithology log is given, indicating the major shale and sandstone intervals. The GR-log was used to construct the lithology log. The GR-log measures natural radioactivity. This is an excellent lithology indicator: low values indicate a clean sandstone, high values normally indicate high clay content i.e. a shale. Note that some of the thinner sands that can be seen on the GR-log, are not included in the lithology log. It is clear that most of the sandstone layers in this interval are hydrocarbon bearing, often with a relatively thin gas cap.

Bibliography

Aki, K. and Richards, P. G. (1980). *Quantitative seismology, theory and methods: Volume 1*. W. H. Freeman & Co.

Allaby, A. and Allaby, M. (1999). *A dictionary of earth sciences*. Oxford Univ. Press, Inc. 2nd edition.

Avseth, P. Å. (2000). *Combining rock physics and sedimentology for seismic reservoir characterization in North Sea turbidite systems*. Ph.D. thesis, Stanford University.

Avseth, P. A., Dvorkin, J., Mavko, G., and Rykkje, J. (1998). Diagnosing high-porosity sands for reservoir characterization using sonic and seismic. In *68th Ann. Internat. Mtg., Soc. Expl. Geophys., Expanded Abstracts*, pages 1024–1027.

Backus, G. E. (1962). Long-wave elastic anisotropy produced by horizontal layering. *J. Geophys. Res.*, **67**(11), 4427–4440.

Bahorich, M. and Farmer, S. (1995). 3-D seismic discontinuity for faults and stratigraphic features: The coherence cube. *The Leading Edge*, **14**(10), 1053–1058.

Banik, N. C., Lerche, I., and Shuey, R. T. (1985a). Stratigraphic filtering part I: Derivation of the O'Doherty-Anstey formula. *Geophysics*, **50**(12), 2768–2774.

Banik, N. C., Lerche, I., Resnick, J., and Shuey, R. T. (1985b). Stratigraphic filtering part II: Model spectra. *Geophysics*, **50**(12), 2775–2783.

Barnes, A. E. (1991). Instantaneous frequency and amplitude at the envelope peak of a constant-phase wavelet. *Geophysics*, **56**(7), 1058–1060.

Berkhout, A. J. (1982). *Seismic migration: Imaging of acoustic energy by wave field extrapolation: Volume A: Theoretical aspects*, volume 14A of *Developments in Solid Earth Geophysics*. Elsevier Science Publ. Co. Inc., 2nd edition.

Berkhout, A. J. (1984a). *Seismic migration: Imaging of acoustic energy by wave field extrapolation: Volume B: Practical aspects*, volume 14B of *Developments in Solid Earth Geophysics*. Elsevier Science Publ. Co. Inc.

Berkhout, A. J. (1984b). *Seismic resolution. A quantitative analysis of the resolving power of acoustical echo techniques*. Geophysical Press.

Berkhout, A. J. (1989). Key issues in integrated seismic exploration. *First Break*, **7**(8), 323–334.

Berkhout, A. J. (1997a). Pushing the limits of seismic imaging, part I: Prestack migration in terms of double dynamic focusing. *Geophysics*, **62**(3), 937–953. Available from URL: <http://www.seg.org/publications/geoarchive/1997/may-jun/berkhout1.pdf>.

Berkhout, A. J. (1997b). Pushing the limits of seismic imaging, part II: Integration of prestack migration, velocity estimation, and AVO analysis. *Geophysics*, **62**(3), 954–969. Available from URL: <http://www.seg.org/publications/geoarchive/1997/may-jun/berkhout2.pdf>.

Berkhout, A. J. and Wapenaar, C. P. A. (1990a). Delphi: Delft philosophy on acoustic and elastic inversion. *The Leading Edge*, **9**(2), 30–33.

Berkhout, A. J. and Wapenaar, C. P. A. (1990b). Delphi: Delft philosophy on acoustic and elastic inversion, part 2. *The Leading Edge*, **9**(3), 53–59.

Berryman, J. G. (1979). Long-wave elastic anisotropy in transversely isotropic media. *Geophysics*, **44**(5), 896–917.

Berryman, J. G., Grechka, V., and Berge, P. A. (1997). Analysis of Thomsen parameters for finely layered VTI media. In *67th Ann. Internat. Mtg., Soc. Expl. Geophys., Expanded Abstracts*, pages 941–944.

Beydoun, W. B. and Tarantola, A. (1988). First Born and Rytov approximations: Modeling and inversion conditions in a canonical example. *J. Acoust. Soc. Am.*, **83**(3), 1045 – 1055.

Bjørlykke, K., Aagaard, P., Dypvik, H., Hastings, D. S., and Harper, A. S. (1986). Diagenesis and reservoir properties of Jurassic sandstones from the Haltenbanken area, offshore mid Norway. In A. M. Spencer, editor, *Habitat of hydrocarbons on the Norwegian continental shelf*, chapter 20, pages 275–286. Graham & Trotman Ltd.

Bodine, J. H. (1986). Waveform analysis with seismic attributes. *Oil and Gas J.*, **84**, 59–63.

Bracewell, R. N. (2000). *The Fourier transform and its applications*. McGraw-Hill Book Co., 3rd edition.

Bruggeman, D. A. G. (1937). Berechnung verschiedener physikalischer Konstanten von heterogenen Substanzen. Teil 3: Die elastischen Konstanten der quasi-isotropen Mischkörper aus isotropen Substanzen. *Annalen der Physik*, **5-29**, 160–178.

Burridge, R., Papanicolaou, G., and White, B. (1988). One-dimensional wave propagation in a highly discontinuous medium. *Wave Motion*, **10**(1), 19–44.

Castagna, J. P., Batzle, M. L., and Eastwood, R. L. (1985). Relationships between compressional-wave and shear-wave velocities in clastic silicate rocks. *Geophysics*, **50**(4), 571–581.

Castagna, J. P., Batzle, M. L., and Kan, T. K. (1993). Rock physics - the link between rock properties and AVO response. In J. P. Castagna and M. M. Backus, editors, *Offset-dependent reflectivity - Theory and practice of AVO analysis*, volume 8 of *Investigations in geophysics*, pages 135–171. Soc. Expl. Geophys.

Chakraborty, A. and Okaya, D. (1995). Frequency-time decomposition of seismic data using wavelet-based methods. *Geophysics*, **60**(6), 1906–1916. Available from URL: <http://seg.org/publications/geoarchive/1995/nov-dec/geo6006r1906.pdf>.

Coleman, J. M. (1982). *Deltaic sand bodies*. Am. Assn. Petr. Geol., 3rd edition.

Crampin, S., Chesnokov, E. M., and Hipkin, R. A. (1984). Seismic anisotropy - the state of the art: II. *Geophys. J. Roy. Astr. Soc.*, **76**, 1–16.

Dahlen, F. A. and Tromp, J. (1998). *Theoretical global seismology*. Princeton Univ. Press.

Dalland, A., Worsley, D., and Ofstad, K. (1988). *A lithostratigraphic scheme for the Mesozoic and Cenozoic succession offshore mid- and northern Norway*, volume 4 of *Bulletin*. Norwegian Petroleum Directorate.

de Groot, P. F. M. (1995). *Seismic reservoir characterisation employing factual and simulated wells*. Ph.D. thesis, Delft University of Technology.

de Groot, P. F. M., Bril, A. H., Floris, F. J. T., and Campbell, A. (1996). Monte carlo simulation of wells. *Geophysics*, **61**(3), 631–638.

Dellinger, J. and Vernik, L. (1994). Do traveltimes in pulse-transmission experiments yield anisotropic group or phase velocities? *Geophysics*, **59**(11), 1774–1779. Available from URL: <http://seg.org/publications/geoarchive/1994/nov/geo5911r1774.pdf>.

Dessing, F. J. (1997). *A wavelet transform approach to seismic processing*. Ph.D. thesis, Delft University of Technology.

Ekern, O. F. (1987). Midgard. In A. M. Spencer, editor, *Geology of the Norwegian oil and gas fields*, chapter 35, pages 403–410. Graham & Trotman Ltd.

Emery, D. and Myers, K., editors (1996). *Sequence stratigraphy*. Blackwell Scientific Publications, Inc.

Fagerland, N. (1994). Mid-Norway shelf. In H. Kulke, editor, *Regional petroleum geology of the world - part 1: Europe and Asia*, pages 113–119. Gebrüder Borntraeger.

Folstad, P. G. and Schoenberg, M. (1992). Low frequency propagation through fine layering. In *62nd Ann. Internat. Mtg., Soc. Expl. Geophys., Expanded Abstracts*, pages 1278–1281.

Gabor, D. (1946). Theory of communication. *J. Inst. Elect. Eng.*, **93**, 429–457.

Gardner, G. H. F., Gardner, L. W., and Gregory, A. R. (1974). Formation velocity

and density - The diagnostic basis for stratigraphic traps. *Geophysics*, **39**(6), 770–780.

Gassmann, F. (1951). Elastic waves through a packing of spheres. *Geophysics*, **16**(4), 673–685.

Geoquest (1999). *Geoframe seismic interpretation using Charisma - Course guide*.

Gersztenkorn, A. and Marfurt, K. J. (1996). Eigenstructure based coherence computations. In *66th Ann. Internat. Mtg., Soc. Expl. Geophys., Expanded Abstracts*, pages 328–331.

Gersztenkorn, A., Sharp, J. A., Sheet, R. M., and Marfurt, K. J. (1996). Delineation of wrench tectonic features using 3-D coherency - offshore Trinidad. In *66th Ann. Internat. Mtg., Soc. Expl. Geophys., Expanded Abstracts*, pages 344–347.

Grace, O. D. (1981). Instantaneous power spectra. *J. Acoust. Soc. Am.*, **69**(1), 191–198.

Hagevang, T. and Rønnevik, H. C. (1986). Basin development and hydrocarbon occurrences offshore Mid-Norway. In M. T. Halberty, editor, *Future petroleum provinces in the world*, volume 40 of *AAPG Memoir*, pages 599–613. Am. Assn. Petr. Geol.

Haskell, N. L., Nissen, S. E., Lopez, J. A., and Bahorich, M. S. (1995). 3-D seismic coherency and the imaging of sedimentological features. In *65th Ann. Internat. Mtg., Soc. Expl. Geophys., Expanded Abstracts*, pages 1532–1534.

Haskell, N. L., Nissen, S. E., Lopez, J. A., and Bahorich, M. S. (1998). 3-D seismic coherency and the imaging of sedimentological features. In F. M. Gradstein, K. O. Sandvik, and N. J. Milton, editors, *Sequence stratigraphy - concepts and applications*, NPF special publication 8, pages 197–214. Elsevier Science Publ. Co. Inc.

Helbig, K. (1979). Discussion on "The reflection, refraction and diffraction of waves in media with elliptical velocity dependence" (F.K. Levin). *Geophysics*, **44**(5), 987–990.

Helbig, K. (1994). *Foundations of anisotropy for exploration seismics*. Pergamon Press, Inc.

Heller, J. (1961). *Catch-22*. Simon & Schuster.

Herrmann, F. J. (1997). *A scaling medium representation, a discussion on well-logs, fractals and waves*. Ph.D. thesis, Delft University of Technology.

Hubral, P., Treitel, S., and Gutowski, P. R. (1980). A sum autoregressive formula for the reflection response. *Geophysics*, **45**(11), 1697–1705.

Hunt, Jr., J. L. and Burgess, G. (1995). *Depositional Styles from Miocene Through Pleistocene in the north central Gulf of Mexico: An Historical Reconstruction*.

Technical Report GP-9513, U.S. Minerals Management Service. Also published in: *Gulf Coast Assn. Geol. Soc. Trans.*, **45**, 275-284. Available from URL: <http://www.gomr.mms.gov/homepg/pubinfo/techcat/jess2.html>.

Hutton, J. (1788). Theory of the earth: or an investigation of the laws observable in the composition, dissolution, and restoration of land upon the globe. *Trans. Roy. Soc. Edinburgh*, **1**, 209-304.

Kennett, B. L. N. (1974). Reflections, rays and reverberations. *Bull. Seis. Soc. Am.*, **64**, 1685-1696.

Kennett, B. L. N. (1983). *Seismic wave propagation in stratified media*. Cambridge Univ. Press.

Keys, R. G. and Foster, D. J., editors (1998a). *Comparison of seismic inversion methods on a single real data set*, volume 4 of *Open File Publications*. Soc. Expl. Geophys.

Keys, R. G. and Foster, D. J. (1998b). A data set for evaluating and comparing seismic inversion methods. In R. G. Keys and D. J. Foster, editors, *Comparison of seismic inversion methods on a single real data set*, volume 4 of *Open File Publications*, chapter 1, pages 1-12. Soc. Expl. Geophys.

Kjartansson, E. (1979). Constant Q -wave propagation and attenuation. *J. Geophys. Res.*, **84**(B9), 4737-4748. Also reprinted in Z. Wang and A. Nur, editors, *Seismic and acoustic velocities in reservoir rocks - volume 2: theoretical and model studies*, volume 10 of *Geophysics reprint series*, pages 416-427. Soc. Expl. Geophys.

Levin, F. K. (1979). Seismic velocities in transversely isotropic media. *Geophysics*, **44**, 918-936.

Mallat, S. (1999). *A wavelet tour of signal processing*. Academic Press Inc., 2nd edition.

Mallat, S. and Zhang, Z. (1993). Matching pursuit with time frequency dictionaries. *IEEE Trans. Signal Process.*, **41**(12), 3397-3415.

Marfurt, K. J., Kirlin, R. L., Farmer, S. L., and Bahorich, M. S. (1998). 3-D seismic attributes using a semblance-based coherency algorithm. *Geophysics*, **63**(4), 1150-1165. Available from URL: <http://seg.org/publications/geoarchive/1998/jul-aug/marfurt.pdf>.

Marion, D., Mukerji, T., and Mavko, G. (1994). Scale effects on velocity dispersion: From ray to effective-medium theories in stratified media. *Geophysics*, **59**(10), 1613-1619. Available from URL: <http://seg.org/publications/geoarchive/1994/oct/geo5910r1613.pdf>.

Mavko, G., Mukerji, T., and Dvorkin, J. (1998). *The rock physics handbook; tools for seismic analysis of porous media*. Cambridge Univ. Press.

Melia, P. J. and Carlson, R. L. (1984). An experimental test of P-wave anisotropy

in stratified media. *Geophysics*, **49**(4), 374–378.

Mendel, J. M. (1978). Bremmer series decomposition of solutions to the lossless wave equation in layered media. *IEEE Trans. Geosc. Remote Sensing*, **GE-16**(2), 103–112.

Miall, A. D. (1999). *Principles of sedimentary basin analysis*. Springer-Verlag Berlin, 3rd edition.

Mijnssen, F. C. J. (1991). *Characterization of deltaic rocks for numerical reservoir simulation*. Ph.D. thesis, Delft University of Technology.

Morlet, J., Arens, G., Fourgeau, E., and Giard, D. (1982). Wave propagation and sampling theory. *Geophysics*, **47**(2), 203–236.

Mukerji, T. (1995). *Waves and scales in heterogeneous rocks*. Ph.D. thesis, Stanford University.

Murphy, III, W. F. (1984). Acoustic measures of partial gas saturation in tight sandstones. *J. Geophys. Res.*, **89**(B13), 11549–11559. Also reprinted in A. Nur and Z. Wang, editors, *Seismic and acoustic velocities in reservoir rocks - volume 1: experimental studies*, volume 10 of *Geophysics reprint series*, pages 259–269. Soc. Expl. Geophys.

NASA (1995). *Mississippi river delta, Louisiana*. Picture P-45759 made from space shuttle Endeavour on October 2, 1995. The picture was acquired by the Spaceborne Imaging Radar-C/X-Band Synthetic Aperture Radar (SIR-C/X-SAR). Available electronically from URL: <http://www.jpl.nasa.gov/radar/sircxsar/delta.html>.

Neidell, N. S. (1981). *Stratigraphic modeling and interpretation: geophysical principals and techniques*, volume 13 of *Education course note series*. Am. Ass. Petr. Geol.

Neidell, N. S. and Poggiagliomi, E. (1977). Stratigraphic modeling and interpretation - geophysical principals and techniques. In C. E. Payton, editor, *Seismic stratigraphy; applications to hydrocarbon exploration*, volume 26 of *Memoir*, pages 389–416. Am. Ass. Petr. Geol.

Neidell, N. S. and Taner, M. T. (1971). Semblance and other coherency measures for multichannel data. *Geophysics*, **36**(3), 482–497.

Nissen, S. E., Haskell, N. L., Lopez, J. A., Donlon, T. J., and Bahorich, M. S. (1995). 3-D seismic coherency techniques applied to the identification and delineation of slump features. In *65th Ann. Internat. Mtg., Soc. Expl. Geophys., Expanded Abstracts*, pages 1535–1536.

Norwegian Petroleum Directorate (1999). *The petroleum resources on the Norwegian continental shelf 1999*. Technical report, Norwegian Petroleum Directorate. Available from URL: <http://www.npd.no/engelsk/npetrres/petres99/>.

O'Connell, R. J. and Budiansky, B. (1978). Measures of dissipation in viscoelastic media. *Geophys. Res. Lett.*, **5**(1), 5–8.

O'Doherty, R. F. and Anstey, N. A. (1971). Reflections on amplitude. *Geophys. Prosps.*, **19**, 430–458.

O'Donnell, M., Jaynes, E. T., and Miller, J. G. (1981). Kramers-Kronig relationship between ultrasonic attenuation and phase velocity. *J. Acoust. Soc. Am.*, **69**(3), 696–701.

Oppenheim, A. V., Willsky, A. S., and Hamid, S. (1997). *Signal & systems*. Prentice-Hall, Inc., 2nd edition.

Payton, C. E., editor (1977). *Seismic stratigraphy - applications to hydrocarbon exploration*. Am. Assn. Petr. Geol.

Posamentier, H. (2000). 3-D sliced, diced and studied - an exercise in geomorphology. *AAPG Explorer*, **21**(8), 14–16.

Postma, G. W. (1955). Wave propagation in a stratified medium. *Geophysics*, **20**(4), 780–806.

Press, F. and Siever, R. (1985). *Earth*. W. H. Freeman & Co., 4th edition.

Press, F. and Siever, R. (1997). *Understanding earth*. W. H. Freeman & Co., 2nd edition.

Reading, H. G., editor (1996). *Sedimentary environments: process, facies and stratigraphy*. Blackwell Scientific Publications, Inc., 3rd edition.

Resnick, J. R., Lerche, I., and Shuey, R. T. (1986). Reflection, transmission and the generalized primary wave. *Geophys. J. Roy. Acoust. Soc.*, **87**, 349–377.

Richardson, F. G. and Sneider, R. M. (1992). Synergism in reservoir management. In R. E. Sheriff, editor, *Reservoir geophysics*, volume 7 of *Investigations in Geophysics*, pages 6–11. Soc. Expl. Geophys.

Ricker, N. (1953). The form and laws of propagation of seismic wavelets. *Geophysics*, **18**(1), 10–40.

Rio, P., Mukerji, T., Mavko, G., and Marion, D. (1996). Velocity dispersion and upscaling in a laboratory-simulated VSP. *Geophysics*, **61**(2), 584–593. Available from URL: <http://seg.org/publications/geoarchive/1996/mar-apr/geo6102r0584.pdf>.

Robertson, J. D. and Nogami, H. H. (1984). Complex seismic trace analysis of thin beds. *Geophysics*, **49**(4), 344–352.

Rock Solid Images (1997). *SRCAATTRIB (Version 2.1): Seismic trace attribute computation & display program - User's guide*.

Sams, M. S. and Williamson, P. R. (1994). Backus averaging, scattering and drift. *Geophys. Prosps.*, **42**(6), 541–564.

Shapiro, S. A. and Zien, H. (1993). The O'Doherty-Anstey formula and localization of seismic waves. *Geophysics*, **58**(5), 736–740. Available from URL: <http://seg.org/publications/geoarchive/1993/may/geo5805r0736.pdf>.

Sheriff, R. E. (1991). *Encyclopedic dictionary of exploration geophysics*, volume 1 of *Geophysical reference series*. Soc. Expl. Geophys., 3rd edition.

Sheriff, R. E. and Geldart, L. P. (1995). *Exploration seismology*. Cambridge Univ. Press, 2nd edition.

Steeghs, T. P. H. (1997). *Local power spectra and seismic interpretation*. Ph.D. thesis, Delft University of Technology.

Strang, G. (1988). *Linear algebra and its applications*. Harcourt Brace Jovanovich, Inc., 3rd edition.

Taner, M. T. (1998). *Attributes revisited*. Technical report, Rock Solid Images. Available from URL: http://www.rocksolidimages.com/sol/sol_pdf/atr8_revisit.html.

Taner, M. T. and Sheriff, R. E. (1977). Application of amplitude, frequency, and other attributes to stratigraphic and hydrocarbon determination. In C. E. Payton, editor, *Seismic stratigraphy - applications to hydrocarbon exploration*, pages 301–328. Am. Assn. Petr. Geol.

Taner, M. T., Koehler, F., and Sheriff, R. E. (1979). Complex seismic trace analysis. *Geophysics*, **44**(6), 1041–1063.

Thomsen, L. (1986). Weak elastic anisotropy. *Geophysics*, **51**(10), 1954–1966. Also reprinted in Z. Wang and A. Nur, editors, *Seismic and acoustic velocities in reservoir rocks - volume 2: theoretical and model studies*, volume 10 of *Geophysics reprint series*, pages 395–407. Soc. Expl. Geophys.

Thomsen, L. (1990). Poisson was not a geophysicist ! *The Leading Edge*, **9**(12), 27–29.

Titchmarsh, E. C. (1964). *The theory of functions*. Oxford Univ. Press, Inc., 2nd edition.

Tsvankin, I. (1996). P-wave signatures and notation for transversely isotropic media: An overview. *Geophysics*, **61**(2), 467–483. Available from URL: <http://seg.org/publications/geoarchive/1996/mar-apr/geo6102r0467.pdf>.

US Geological Survey (2000). Rock cycle. Available from URL: <http://wrgis.wr.usgs.gov/docs/parks/rxmin/rockcycle.pdf>.

Vail, P. R., Mitchum, Jr., R. M., Todd, R. G., Widmier, J. M., Thompson, III, S., Sangree, J. B., Bubb, J. N., and Hatlelid, W. G. (1977). Seismic stratigraphy and global changes of sea-level. In C. E. Payton, editor, *Seismic stratigraphy; applications to hydrocarbon exploration*, volume 26 of *Memoir*, pages 49–212. Am. Ass. Petr. Geol.

van Wijngaarden, A. J. (1998). *Imaging and characterization of angle-dependent seismic reflection data*. Ph.D. thesis, Delft University of Technology.

Vermeer, P. L. (1992). *The multiscale and wavelet transform with applications in well-log analysis*. Ph.D. thesis, Delft University of Technology.

Wapenaar, C. P. A. and Berkhouit, A. J. (1989). *Elastic wave field extrapolation: redatuming of single- and multi-component seismic data*, volume 2 of *Advances in exploration geophysics*. Elsevier Science Publ. Co. Inc.

Wapenaar, C. P. A., van Wijngaarden, A. J., van Geloven, W. J. F., and van der Leij, T. S. (1999). Apparent AVA effects of fine layering. *Geophysics*, **64**(6), 1939–1948. Available from URL: <http://seg.org/publications/geoarchive/1999/nov-dec/geo6406r1939.pdf>.

Watkins, J. S., Schneider, L., Hilterman, F., and Spencer, L. (1987). Interactive and conventional interpretation of seismic data from Eugene Island, South Marsh Island, and Green Canyon OCS area, offshore Louisiana. In *57th Ann. Internat. Mtg., Soc. Expl. Geophys., Expanded Abstracts*, page POS2.10.

Weber, K. J. (1986). How heterogeneity affects oil recovery. In L. W. Lake and H. B. Carroll, Jr., editors, *Reservoir characterization*, pages 487–544. Academic Press Inc.

Weisstein, E. W. (2000). *Eric Weisstein's world of mathematics*. Available from URL: <http://mathworld.wolfram.com/>.

White, J. E. (1983). *Underground sound: Application of sound waves*, volume 18 of *Methods in geochemistry and geophysics*. Elsevier Science Publ. Co., Inc.

White, R. E. (1991). Properties of instantaneous seismic attributes. *The Leading Edge*, **10**(7), 26–32.

Widess, M. B. (1973). How thin is a thin bed? *Geophysics*, **38**(6), 1176–1180.

Ziegler, P. A. (1982). *Geological atlas of western and central Europe*. Shell Internationale Petroleum Maatschappij, Den Haag.

Summary

Integration of seismic data with well-log data

Two main topics are addressed in this thesis. Firstly the effect of fine layering on seismic wave propagation is studied. A second topic is the use of the matching pursuit method to extract attributes for seismic interpretation. In the following the two topics will be discussed separately.

In seismic exploration, the information contained in well-log measurements is used to verify and calibrate at several stages during processing and interpretation. In order to be able to use the information contained in the well-log, the information in the well-log needs to be aligned with the seismic data. This process is called well-tieing, and includes the conversion of the well-log measurements from depth to the time domain. It is often observed that a discrepancy occurs between the traveltimes from the seismic measurement and the traveltimes computed from the P -wave velocity measurements in the well. Commonly this difference is in the order of a few percents, but can occasionally reach five up to ten percent. One of the most important reasons for this difference is the different frequency range at which the well-log and the seismic measurement are performed; well-log measurements are performed using acoustic signals with a much broader frequency spectrum, especially towards higher frequencies. Small scale layering will have a different effect at these different frequency ranges. From a review of literature, it was found that the ratio between the scale of the measurement and the scale of the small scale layering is an important factor. In Chapter 2 a first order correction is used to compensate for the effect of scale differences between measurements of P -wave propagation perpendicular to the layering. The method was first described by Sams and Williamson (1994) and

Rio et al. (1996), and consists of a moving averaging procedure with a window of approximately one fifth of the dominant wavelength of the seismic wave. The result is a velocity at a specified scale. This procedure was successfully verified with numerical modelling experiments. When the earth properties in depth are stationary, and the layer thicknesses are smaller than one fifth of the seismic wavelength, the result from this procedure is equal to an equivalent medium averaged velocity.

Using techniques similar to the wavelet transform, the effect of a change of the scale on the velocity was studied in detail, resulting in the observation that the scale-dependency of the velocity is important. Because the scale-dependent velocity establishes also the link between the well-log measurements made in depth and the seismic data in time, a catch 22 problem occurs. Because of this observation, an iterative procedure was developed to derive a mutual dependent scale in depth and velocity at that scale that together match the scale in time of the seismic.

In Chapter 3 the procedure is extended to P -wave propagation under oblique angles. A method is proposed to calculate the Thomsen anisotropy parameters (Thomsen, 1986) when the earth properties are non-stationary in depth. In these situations the Thomsen parameters become scale dependent. A variation of the Thomsen parameters across the scales in the order of 100 % was found. Due to this fact, the iterative procedure as established in Chapter 2 was extended to include propagation under oblique angles. The result of this iterative procedure is a regularized anisotropic velocity at a defined scale for plane waves travelling under oblique angles. This regularized velocity is a first order correction for the effect of non-stationary fine layering on the propagation of P -waves. The results obtained from this procedure were compared with numerical modelling results, and the comparison was favourable. The scale dependent velocities as described in Chapters 2 and 3 can be used for different purposes. The velocities can be used for the time-to-depth or depth-to-time conversion for well-tie, modelling and inversion purposes. Using the velocities derived with this method, will diminish the traveltime mismatch between seismic and well-log data. The anisotropic velocity results may be used as a background model in pre-stack inversion. Due to the non-linear effect the background velocity has on the inversion result, a large difference is found between the inversion results based on a conventional equivalent average velocity and the regularized velocity as found using the method described in this chapter.

The second topic deals with seismic interpretation and is described in Chapter 4 of this thesis. The need for more detailed interpretations in the reservoir management stage of the reservoir is increasing. A few of the driving forces for this increasing need are the increasing sedimentological complexity of the petroleum reservoirs under production, the increased use of advanced production methods (e.g. horizontal wells, gas and/or water injection) and the fact that a large number of the important fields in for instance the North Sea are at the end of the plateau stage

and about to decline in production. All these factors lead to an increased need for detailed interpretations at the scale of individual sandbodies or stacks of sandbodies. A method to derive robust attributes and relate those attributes in some favourable cases to the type of sandbody is discussed in this thesis (Chapter 4). By use of a matching pursuit approach and by making an assumption on the range of wavelet shapes and wavelengths, a robust extraction of seismic attributes from noisy seismic signals is made. Compared to the conventional response phase computed from the analytic trace, the phase extracted using the matching pursuit method allows 6 to 9 dB extra noise for the same accuracy.

In cases with a low net-to-gross ratio (low percentage of reservoir sands in a non-reservoir matrix), with relative thick sands (between 0.5 and 1.25 times the dominant wavelength of the seismic wave) and with a lateral invariant matrix (e.g. a marine shale) it is possible to relate the phase attribute to the type of sand sequence (coarsening or fining upward sequence). This information is directly useful for reservoir engineers to update their reservoir model and to optimize well-planning. The amplitude as extracted from the wavelet is also very sensitive for the pore fluids.

The matching pursuit method was applied on a 3-D data set from the Gulf of Mexico, and proved to be able to pick consistent geological features in a delta front environment. The phase attribute also allowed an interpretation of the type of sequence. In a more complicated example from Northern Europe, the results could only be used qualitatively.



Samenvatting

Integratie van seismische data en boorputmetingen*

In dit proefschrift worden twee onderwerpen behandeld. Een eerste onderwerp bestudeert het effect van fijngelaagdheid op de voortplanting van seismische golven. Het tweede onderwerp handelt over het gebruik van de “matching pursuit” methode om attributen goed bruikbaar voor seismische interpretatie te bepalen. In hetgeen volgt zal ieder van de twee onderwerpen afzonderlijk besproken worden.

In seismische exploratie wordt de informatie van boorgatmetingen op verschillende stappen tijdens het verwerken en interpreteren van de seismische gegevens gebruikt als controle en kalibratie. Om de informatie in de boorgatmetingen goed te kunnen gebruiken, is het nodig dat de boorgatmetingen netjes opgelijnd zijn met de seismische gegevens. Dit proces wordt het verbinden van de seismische gegevens met het boorgat genoemd (“well-tieing”). Dit proces houdt ook in dat de boorgatmetingen worden omgezet van het diepte naar het tijdsdomein. Hierbij wordt vaak opgemerkt dat er een verschil bestaat tussen de seismische looptijden bepaald uit de seismische gegevens, en de looptijden berekend uit de in het boorgat gemeten ultrasonen P -golfsnelheid. Vaak is dit verschil in de orde van enkele procenten, maar het verschil kan af en toe oplopen tot vijf á tien procent. Eén van de hoofdoorzaken van dit verschil is het verschil in frekwentie spektrum van de akoestische signalen waarmee de boorgatmeting en de seismische meting zijn uitgevoerd: boorgatmetingen worden uitgevoerd met akoestische signalen die een veel groter frekwentie spektrum omvatten vergeleken met de seismische signalen. Fijngelaagde media reageren anders op deze verschillende golven. Uit een overzicht van de literatuur, is het duidelijk dat de verhouding tussen de schaal van de meting en de schaal van de fijngelaagdheid een

*Dutch summary of *Integration of seismic data with well-log data*.

belangrijke factor is. In Hoofdstuk 2 wordt er een benaderende methode gebruikt om het effect van de fijngelaagdheid op de looptijden van seismische golven die loodrecht invallen op de gelaagdheid, te voorspellen. Deze methode is reeds beschreven door Sams and Williamson (1994) en Rio et al. (1996), en bestaat uit het bepalen van een lopend gemiddelde over een venster dat ongeveer één vijfde bedraagt van de dominante golflengte van de seismische golf. Het resultaat is een snelheid op een bepaalde schaal. De resultaten van deze methode zijn vergeleken met de resultaten uit numerieke modelleringsexperimenten, en waren hiermee in overeenkomst. Wanneer de fijngelaagdheid in de aarde diktes vertoont die kleiner zijn dan één vijfde van de seismische golflengte, en wanneer de eigenschappen van de aarde stationair zijn in de diepte richting, dan komen de resultaten van deze methode overeen met de snelheid berekend volgens de equivalente medium theorie.

Het effect van een verandering van de schaal op de voortplantingssnelheid is gedetailleerd bestudeerd. Hierbij werden technieken gebruikt die analoog zijn aan de wavelet transformatie. Hieruit volgde dat de schaal-afhankelijkheid van de snelheid belangrijk is. Omdat echter de schaal-afhankelijke snelheid ook de verbinding vormt tussen de boorgatmetingen in diepte en de seismische metingen in tijd, ontstaat er een “catch 22” probleem. Omwille van deze observatie, werd een iteratieve procedure ontworpen waarbij de wederzijds afhankelijke schaal in diepte en de snelheid op deze schaal samen worden gevonden, zodat ze gekombineerd de gewenste schaal in tijd opleveren.

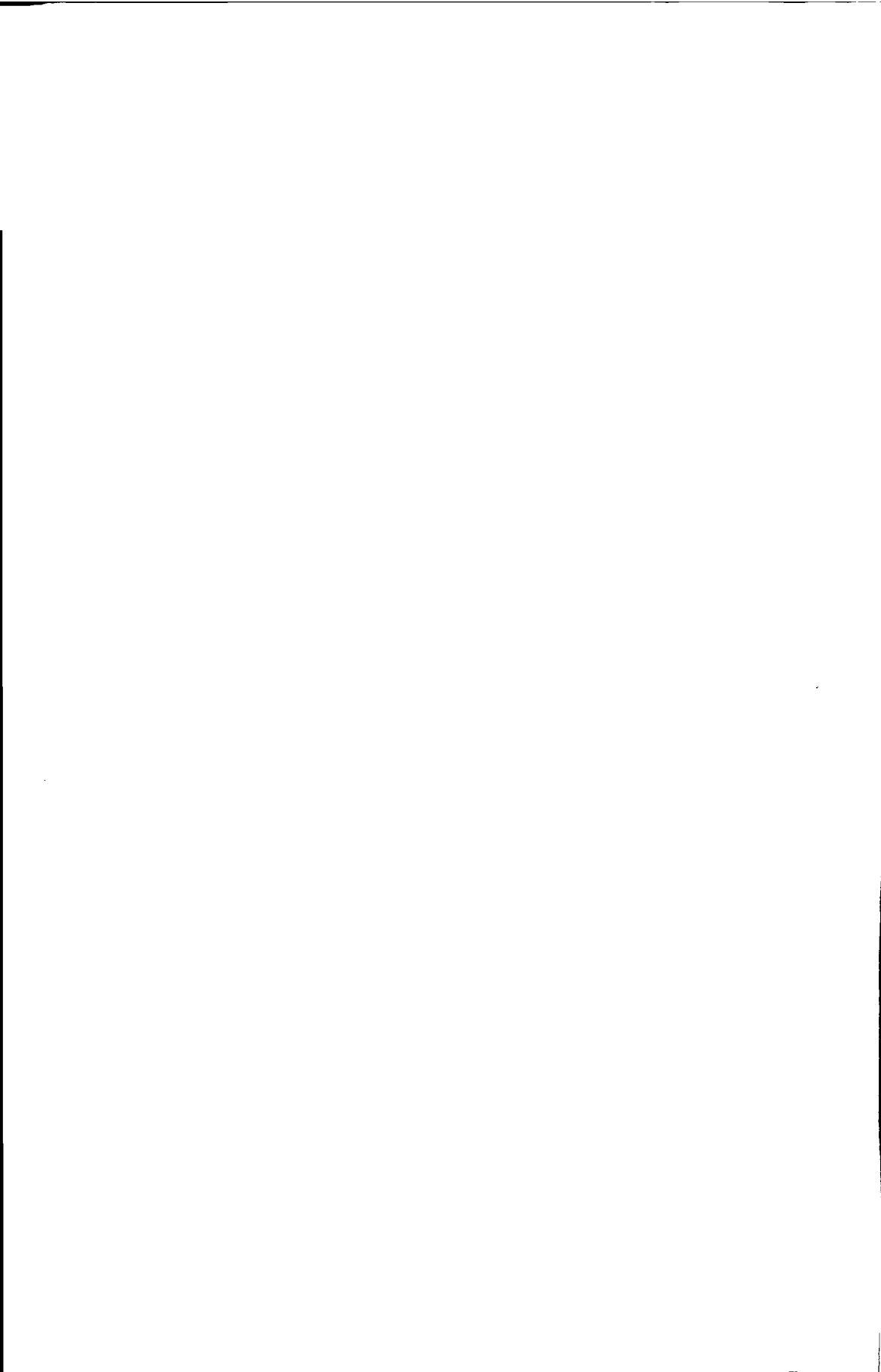
In Hoofdstuk 3 van dit proefschrift wordt de methode uitgebreid voor *P*-golf voortplanting bij een schuine hoek van inval op de gelaagdheid. Hierbij wordt een methode voorgesteld om de Thomsen anisotropie parameters (Thomsen, 1986) te berekenen wanneer de gelaagdheid van de aarde niet stationair is in de diepte richting. In deze gevallen worden de Thomsen parameters namelijk ook afhankelijk van de schaal. Een variatie van de Thomsen parameters in de orde van 100 % is gevonden. Daarom is de iteratieve methode als ontwikkeld in Hoofdstuk 2 uitgebreid voor *P*-golf propagatie onder een schuine hoek met de gelaagdheid. Het resultaat van deze iteratieve procedure is een geregulariseerde anisotropische snelheid op een bepaalde schaal voor vlakke golven die zich voortplanten onder schuine hoeken met de gelaagdheid. Deze geregulariseerde snelheid is een eerste orde correctie voor het effect van niet-stationaire fijngelaagdheid op de voortplantingssnelheid van *P*-golven. De resultaten van deze methode werden vergeleken met resultaten verkregen met behulp van numerieke modelleren, waarbij de resultaten vergelijkbaar waren.

De schaal-afhankelijke geregulariseerde snelheden kunnen in de praktijk gebruikt worden voor verschillende doelen. De snelheden kunnen gebruikt worden voor de tijd-naar-diepte of de diepte-naar-tijd conversie bij het verbinden van boorgatmetingen met de seismische metingen (“well-tieing”), bij het seismisch modelleren en bij inversie. Het gebruik van de snelheden verkregen met deze methode zal het verschil van de looptijden tussen seismische gegevens en boorgatmetingen wezenlijk

verminderen. De anisotrope snelheid kan gebruikt worden als achtergrond model bij pre-stack inversie. Wegens het niet-lineaire effect van de achtergrondsnelheid op de uiteindelijke inversieresultaten, kunnen zelfs relatief beperkte anisotropie en schaal-effecten een grote invloed hebben op de inversie resultaten.

Het tweede onderwerp behandeld in dit proefschrift, gaat over seismische interpretatie. De behoefte aan meer gedetailleerde interpretaties in de reservoirmanagement fase van een reservoir is stijgend. Enkele van de oorzaken hiervan zijn de steeds hoger wordende sedimentologische ingewikkeldheid van de petroleum reservoirs in productie, het toenemende gebruik van gevorderde productie methodes (bijvoorbeeld horizontale putten, gas en/of water injectie) en het feit dat een groot aantal van de belangrijke velden in bijvoorbeeld de Noordzee aan het einde van hun plateau fase komen en overgaan tot een afname van de productie. Al deze factoren zorgen voor een toenemende vraag voor gedetailleerde interpretaties op de schaal van individuele zandlichamen of een stapeling van zandlichamen. In Hoofdstuk 4 wordt een methode beschreven en toegepast die het mogelijk maakt om op een stabiele manier seismische attributen te bepalen. Als de omstandigheden gunstig zijn, dan kan uit deze attributen zelfs bepaald worden wat voor type zandlichaam er aanwezig is. Door een aannname te maken over de vorm van het wavelet en de verwachte golflengte, kunnen met behulp van de "matching pursuit" methode op een robuuste manier seismische attributen verkregen worden van ruis-gevoelige seismische metingen. Vergeleken met de konventionele methode van de respons-fase berekend van de analytische trace, laat het fase attribuut verkregen uit de "matching pursuit" methode 6 tot 9 dB extra ruis toe voor dezelfde nauwkeurigheid.

In gevallen met slechts weinig reservoirzanden in een kleimatrix, met relatief dikke zanden (tussen 0,5 en 1,25 keer de dominante golflengte van de seismische golf) en met een lateraal onveranderlijke kleimatrix (bijvoorbeeld een mariene klei) is het mogelijk om het verkregen fase-attribuut te koppelen aan het type van zandlichaam. Deze informatie is meteen bruikbaar voor reservoir ingenieurs om het reservoir model bij te werken, en bij het ontwerp van nieuwe boorputten. Het amplitude-attribuut dat ook uit de "matching pursuit" methode wordt verkregen, is tevens erg gevoelig voor de fluïda inhoud van de porieën en kan dus gebruikt worden als een indicator. De "matching pursuit" methode is toegepast op een 3-D dataset uit de Golf van Mexico. Het bleek in dit geval mogelijk te zijn om consistente geologische eenheden te bepalen. Het bleek tevens mogelijk om uit het fase-attribuut het type zandlichaam te bepalen. In een ander, moeilijker, voorbeeld uit Noord-Europa konden de resultaten slechts kwalitatief worden gebruikt.



Curriculum vitae

Frédéric Verhelst was born in Sint-Niklaas (Belgium) on July 24, 1968. He attended “Sint-Thomascollege” in Antwerp for his primary and secundary education. He received his “Humaniora - wetenschappelijke A” diploma (sciences & mathematics) in 1986.

Subsequently he became an engineering student at “Katholieke Universiteit Leuven” (K.U.Leuven, Belgium) and graduated in 1992 “magna cum laude” as mining engineer (“Ir.”). The subject of his MSc thesis was “Sediment-petrological and petrophysical characterisation of the Westphalian D sandstone in borehole KS-161 (Campine Basin-NE Belgium)” and was carried out partly at Delft University of Technology (with an Erasmus mobility scolarship) under supervision of Prof. ir. K. J. Weber, and partly at K.U.Leuven under supervision of Prof. dr. R. Swennen. His MSc thesis was awarded the “K VIV studentenprijs 1992” by the Flemish association of academical engineers (K VIV) as the best MSc thesis in Flanders in the field of mining, civil and architectural engineering.

After his graduation he joined K.U.Leuven civil and mining engineering department as a teaching and research assistant. His research was on the influence of heterogeneities in rock samples on its properties and included the use of a medical X-ray CT-scanner. He supervised several MSc students and taught different topics in the field of mining and civil engineering.

In 1996 he was asked through the intermediation of Prof. ir. K. J. Weber to join the DELPHI-consortium headed by Prof. dr. ir. A. J. Berkhout at Delft University of Technology. His research on seismic characterisation and integration of well-log and seismic data is reported in this thesis.

In 1999 he joined Saga Petroleum in Oslo (Norway) as a senior geophysicist in the reservoir development division. In 2000 he joined the measurement systems and data interpretation unit of TNO TPD in Delft (The Netherlands) as a research scientist.

Acknowledgment/Dankwoord

To all people who contributed directly or indirectly to the realisation of this thesis I am indebted. At the international side, the financial support of the sponsors of the DELPHI-consortium is gratefully acknowledged. The sponsors not only provided the financial support, but they also encouraged me during discussions and visits. Most notably, I would like to mention Walter Rietveld, Kurt Marfurt, Susan Nissen and Norman Haskell with Amoco and Dave Wilkinson with Chevron, for allowing me to visit their offices. I thank Tury Taner for his invitation to give a talk during the Seismic Attributes consortium meeting. At that occasion, Norman Neidell pointed me to some of his related earlier work. Furthermore, I am obligated to Gary Mavko, Tapan Mukerji, André Journel, Jef Caers and Felix Herrmann for the hospitality during my visits at Stanford University. The preprint of the Rock Physics Handbook and the reprints of the laboratory measurements were very helpful Gary. Saga Petroleum, Schlumberger Geco-Prakla and Mobil are specially thanked for providing the data sets used in this thesis. Leon Thomsen (BP-Amoco) is thanked for his comments on the concept version of my thesis.

Aan de Nederlandse kant ben ik veel dank verschuldigd aan prof. Berkhout en Kees Wapenaar voor hun gezamenlijke begeleiding en voor het verschaffen van de mogelijkheden binnen het DELPHI consortium. Ik vind het ook een hele eer om de veertigste promovendus te zijn van prof. Berkhout. Alle mede-promovendi en alle studenten van de afgelopen vier jaar wil ik bedanken voor de uitstekende tijd die ik met hen in de groep heb gehad. De staf van de vakgroep zorgde voor de infrastructurale ondersteuning.

Speciale dank gaat uit naar de wavelet-mannen, te weten Felix Herrmann, Frank Dassing, Joes Staal en Edo Hoekstra. Ze hebben me ingeleid en ook vele ideeën en aanmoedigingen gegeven. Ook een speciale vermelding voor de andere karakterisatie-man, Aart-Jan van Wijngaarden. Samen met Jan Thorbecke hebben we niet enkel de marathon uitgelopen, maar ook tijdens het oefenen hele werkbesprekkingen gehouden. Waarvoor mijn grote dank. Ook de andere collega's van de vroegere "hinnik-kamer", Riaz Ala'i en Alexander Koek: bedankt voor de goede sfeer. Gelukkig was er ook Johan Vos, zodat we soms steun konden vinden bij elkaar als twee Belgen in Nederland. De nieuwe collega's van D 208 (Barbara Cox, Kees

Hindriks en Paul Zwartjens), bedankt voor de gastvrijheid en het tolereren van mijn rommel. En natuurlijk, dank aan John Bolte voor de lol, aan Karin Schalkwijk voor de rake opmerkingen en aan Ewoud van Dedem. Aan Arno Volker, Maurits van de Heiden, Gerrit van Dijk en Alexander Koek, dank voor het gezellige “werkbesprekingen” op vrijdagmiddag.

For my former colleagues at Saga Petroleum: takk for flotte arbeidsmiljøet. Jeg savner dere alle !

Aan mijn huidige arbeidsgever, TNO TPD, bedankt voor de getoonde flexibiliteit en voor de steun in deze drukke tijden.

Dank uiteraard ook aan al mijn vrienden. Ik besef dat ik wat in te halen heb van de afgelopen tijd. De komende tijd zal ik terug moeten wennen aan het begrip “vrije tijd”.

Aan mijn moeder en Olivier: bedankt voor de steun door alle jaren heen.

Dank aan de hele familie Staal voor alle hulp bij het klussen aan onze nieuwe woning.

De rol van Liesbeth kan moeilijk overschat worden. Zonder haar (bijna) onvoorwaardelijke steun, en hulp in vele praktische aangelegenheden had het allemaal nog moeilijker geweest. Het samenwonen moet nu eigenlijk nog maar beginnen ...